ROLE OF REDOX-ACTIVE RELAY RESIDUES IN PROTEIN ELECTRON TRANSFER

A Dissertation

Presented to the Faculty of the Graduate School

of Cornell University

in Partial Fulfillment of the Requirements for the Degree of

Doctor of Philosophy

by

Estella Yee

August 2018

ROLE OF REDOX-ACTIVE RELAY RESIDUES IN PROTEIN ELECTRON TRANSFER

Estella Yee, Ph.D.

Cornell University 2018

Protein electron transfer reactions are essential in biological and bioenergetic systems. They are capable of mobilizing charges over vast distances through the use of relay residues, which behave as intermediary sites for electron localization and hopping. The electron transfer rate is primarily determined by driving force, reorganization energies, and electronic coupling between the donor and acceptor species, as modeled by the Marcus equation. However, these parameters are not readily obtained by *in vitro* experiments and the reaction may be further complicated by proton transfer events. Thus, systems amenable to facile manipulation of these parameters are highly advantageous for *in vitro* studies.

Tyrosine and tryptophan are among the most prevalent relay residues in electron transfer systems, but despite their similarities, one can not easily replace the functionality of the other. In our first protein model system, yeast cytochrome *c* peroxidase:cytochrome *c*, we substituted the conserved tryptophan electron hopping site with a tyrosine residue, allowing us to gain insight into the behavior of tyrosyl radicals in electron transfer and the effect of its local environment on activity. Our findings evince that inclusion of a basic side chain that coordinates to the phenolic proton is essential for augmenting electron transfer rates through the hopping site.

Other relay amino acids also play significant roles in proteins, including methionine and cysteine residues. In our second protein model, we use a flavoprotein photosensor (VIVID) variant that is devoid of an active-site cysteine residue essential for generating the canonical light-oxygen-voltage domain flavin signaling state. We demonstrated that this protein vari-

ant is surprisingly capable of *in vivo* signaling and light-dependent conformational changes. From spectroscopic investigations, we identified the elusive electron donors responsible for the formation of this signaling state and show the importance of methionine residues in transferring electrons.

Herein, I have disseminated our findings on these two projects, furthering our understanding of the intricacies of protein electron transfer and the necessary properties of relay residues for facilitating electron transfer reactions. Firstly, in Chapter 2 and Appendix A, I discuss our findings on intermolecular electron transfer through a tyrosyl hopping site in the cytochrome *c* peroxidase complex and recovery of activity through manipulation of the tyrosyl environment. Following this, I relate investigations of a photoactive model system comprised of internal electron donors. In Chapter 3, I evaluate the ability of the active-cysteine-less VIVID variant to induce a biologically relevant signaling response in blue light, and in Chapter 4, I describe continued investigations on the intrinsic electron transfer mechanism involved in photoactivation, with some burgeoning discoveries on an analogous photoactive system presented in Appendix B.

BIOGRAPHICAL SKETCH

Estella Fay-May Yee was born in 1990 to Raymond and Pearl Yee in Salem, Oregon where she developed an early fascination with science and technology. It wasn't until she attended secondary school that she expanded upon her love and appreciation for biology, chemistry, and computer programming. Subsequently, she earned a Bachelor of Arts degree from Willamette University in 2012, majoring in chemistry with a mathematics minor. Under her two research advisors, Drs. Andrew Duncan and Chuck Williamson, she gained expertise in synthetic organic chemistry and experimental physical chemistry. During the summer months, she participated in several enriching internship experiences through the Behavioral Research Advancements In Neuroscience (BRAIN) Program in Atlanta, Georgia, the Science Collaborative Research Program (SCRP) at Willamette University, and the Amgen Scholars program at UCSD, learning essential biochemistry techniques in the Parent lab, developing synthetic organic compounds in the Duncan group, and preparing silica nanoparticles in the Sailor lab, respectively. Armed with an array of interests and techniques, she was inspired to attend graduate school and foray into the interdisciplinary field of biophysics to learn about underlying mechanisms in biological processes. So, she finally left her hometown and journeyed to Cornell University to work under Dr. Brian Crane. There, she studied protein electron transfer mechanisms in metalloenzymes and circadian clock proteins while gaining proficiency in teaching through mentoring and outreach opportunities.

To my family

ACKNOWLEDGEMENTS

Through the past six years of graduate school, I have had the privilege of making some truly exceptional acquaintances. This work was made possible by each of these individuals who have impacted and shaped my journey. Here I shall endeavor to express my endless gratitude to the many who contributed to the successful completion of this dissertation.

Firstly, I would like to thank my PI and advisor **Brian Crane** for providing me with the opportunity and support to foray into the fields of protein electron transfer and biophysical characterization. Despite initially feeling immensely overwhelmed and uncertain due to my lack of expertise in the subject matter, his patience, guidance, and mentorship have been invaluable. On top of the many administrative and academic responsibilities on his shoulders, Brian was still able to spend numerous hours with me, helping me scrutinize data, develop theoretical models, and revise chapters. It is with thanks to his diligence and mentorship that I have become a better scientist and scholar.

To my committee members, **Poul Petersen** and **Sol Gruner**, thank you for your constructive feedbacks, critiques, and advice as I refined my dissertation projects. Both Poul and Sol have enriched and expanded my research focuses and future interests, providing me with valuable insight on prospective job searches.

Thank you to the people of the Crane research group. **Tom Payne** was an excellent mentor and provided me with a strong foundation to take over his electron transfer project. He patiently taught me everything from basic lab protocols to using our homebuilt transient absorption spectroscopy instrument. To my office mates **Michael Lynch**, **Sophie Ruff**, **Angela Picciano**, and **Zach Maschmann**, thank you for being wonderful sources of support and camaraderie through the long days and nights. Thanks of course to the rest of the group (**Siddarth Chandrasekaran**, **TK Chua**, **Karen Conrad**, **Rob Dunleavy**, **Kritika Dusad**, **Anna Greenswag**, **Changfan Lin**, **Craig Manahan**, **Greg Merz**, **Alise Muok**, **Dipanjan Samanta**, **Connor Schneps**, **Ria Sircar**, **Bee Sukomon**, **Daniyal**

Tariq, and **Joanne Widom**) for insight discussions, keeping the lab up and running, and showing me various protein purification, characterization, and mutagenesis techniques.

Some of the experiments that have been critical to the studies presented here would not have been possible without dedicated collaborators. **Jon Caranto**, **Avery Vilbert**, and **Meghan Smith** in the Lancaster group were instrumental in helping prepare and troubleshoot rapid freeze quench ESR samples. They patiently set aside time each week to assist me in meticulously packing frozen protein "snow" into fragile ESR tubes. Also, **Min Dong** in the Lin group kindly helped me get started with yeast expression systems. Furthermore, **Boris Dzikovski** and **Peter Borbat** in the Freed group assisted me in the collection of numerous ESR spectra.

In my time at Cornell, I have had the privilege of working with some amazing undergraduate students. **Sam Rodriguez**, **Laura Pineda-Bermudez**, and **Theo Esantsi** purified many protein constructs for me and helped with crystallizing some novel complexes. Thanks for allowing me to be your mentor.

To my chemistry cohort who entered the graduate program together with me in 2012, thanks for the camaraderie in the early years of graduate school and willingness to work together on problem sets, spending endless nights delving into the abyss of organic chemistry, quantum mechanics, and statistical mechanics. In addition, thanks to the Chemistry and Chemical Biology department at Cornell for providing me with the resources and opportunity to pursue a graduate degree and also to Pat Hine for all the wonderful work she does for the department. Moreover, I am grateful for the support and training the Molecular Biophysics Training Grant Program provided me.

I would be remiss not to acknowledge the impactful advisors I have had the pleasure of learning under before attending Cornell. To the chemistry and biology professors in my undergraduate studies, specifically to my advisors **Chuck Williamson**, **Andrew Duncan**, and **David Craig**, thank you for the inspiration and experiences as I learned and developed

the skills and wisdom needed to become a well-versed scientist. Their encouragement and advice ultimately inspired me to pursue a doctoral degree. Thanks are also due to my high school teachers **Karen Koepl** and **Dan Heer**. Both of them convinced me to continue pursuing my ambitions of conducting research and mentoring students.

To my dear friends **Sarah Nathan**, **Katy Hoth**, and **Ben Binder**, thank you for the support and love throughout these years of graduate school. I will always cherish the memories of our time together.

Last but not least, I would like to acknowledge my family – **Raymond**, **Pearl**, **Victor**, **Susan**, and my niece and nephews. I made it this far because of their continued support and enduring compassion. Many thanks for providing me with moments of joy, respite, and encouragement in times of stress and uncertainty.

TABLE OF CONTENTS

LIST OF TABLES

LIST OF FIGURES

CHAPTER 1

ELECTRON TRANSFER PARAMETERS IN PROTEIN SYSTEMS

1.1 Reliance of biological systems on efficient electron transfer

Electron transfer is arguably one of the key fundamental processes in chemistry and physics and plays an integral role in many biological systems. Two of the most important biological reactions for aerobic life as we know it, respiration and photosynthesis, both require rapid and precise electron transport for oxidative phosphorylation and glucose synthesis, respectively. Rapid electron transfer is additionally crucial for signal transduction and signaling pathways that are essential for the survival of an organism in its environment [1, 2]. In non-biological applications, an understanding of electron transfer events is also instrumental, such as for the generation of new materials for energy conversion and storage, including solar/fuel cell devices and artificial photosynthesis [3–5], development of long-lived fluorescent reporter molecules for imaging [6–8], and optimization of radical-based organic molecule and polymer syntheses [9, 10]. Hence, the underlying factors of electron transfer are of wide interest to many fields and disciplines, which ultimately desire to improve and control electron transfer rates to better suit the applications.

Research conducted on electron transfer mechanisms in small molecules have been critical for developing an understanding of rudimentary theory. Studies have utilized photoinducible, small molecule or peptide systems comprised of a covalently linked, photoactive ruthenium or rhenium complex. Upon laser excitation, the photo-excited complex oxidizes the appended amino acid on a nanosecond time scale, providing the necessary time resolution to observe early electron transfer events [11–14]. The use of these models allow for facile tuning of electron transfer parameters, though in the context of more complicated and relevant systems, components such as the protein matrix can be difficult to account for in

these systems [11]. Hence, we focus our attention on biological systems and protein models in order to ascertain how local environments can play a role on redox properties.

Fast, directed electron transfer in proteins is vital for biological processes and bioenergetics, as these mechanisms typically require electron transfer rates in the sub-millisecond regime [15, 16], and at times, electrons must traverse a long distance to reach the acceptor. A single tunneling step is at most 20 Å, but longer distances are accessible by multiple, coupled tunneling steps [15]. In the case of ribonucleotide reductase, electrons tunnel over 35 Å through a path of tyrosine residues to transfer radicals from an iron sulfur cluster to a transient cysteine radical and eventually generate the DNA-precursor deoxyribonucleotides [17–19]. Similarly, the di-heme *c* MauG enzyme is able to transfer electrons more than 40 Å away from the high-spin iron heme center by hole hopping through a tryptophan to oxidatively modify a precursor of methylamine dehydrogenase (preMADH) [20, 21]. Long-range electron transfer can also serve in the robustness of proteins. Hole hopping through tyrosine and tryptophan chains can protect proteins from oxidative damage [22, 23], and in other proteins, such as cryptochrome, electron transfer through these chains aids in maintaining a population of the signaling state [24].

Studying complex, multistep electron transfer systems is not without challenges. The rates of electron transfer reactions are dependent on various intrinsic factors, including driving forces and reorganization energies, however, they are not necessarily straightforward to measure or tune in the confines of a protein matrix [25]. Indeed, reorganization energies are typically calculated *in silico* due to high degrees of uncertainty in the *in vitro* measurements [26, 27]. Investigating these parameters *in vitro* typically requires a well-behaved protein system that is amenable to replacing residues important for radical localization. To this extent, some studies engineered a model protein by introducing an electron transfer mechanism into an alpha helical bundle devoid of redox-active side chains [28]. Yet, other factors,

such as the local environment of the hole hopping sites and proton transfer events, can be difficult to analyze in these models. Herein, we further examine the parameters that mediate electron transfer in proteins and their behavior in long range electron transfer mechanisms.

1.2 Principles of electron transfer mechanisms

1.2.1 Electron transfer models by Marcus theory

Rates of electron transfer reactions were approached theoretically by Rudolph Marcus in 1956 [29]. The rates were modeled as a function of donor/acceptor characteristics and solvent reorganization energies. Marcus theory treats a system as a combination of inner and outer sphere processes. In the outer sphere, non-bonded reactions induce no large structural alterations, and changes in charge from the electron transfer occur through space between redox species. By comparison, the inner sphere contributions are described as covalent, chemical bond formation/breakage and geometric changes [27, 29, 30].

Marcus theory is based off of transition state theory, and as such, assumes that rate constants are free energy surfaces along a reaction coordinate proportional to $\exp[-\Delta G^{\ddagger}/RT]$. $\Delta G^{\ddagger}$ is derived from the intersection of the donor and acceptor, with the free-energy surfaces modeled as simple harmonic oscillators, or two equivalent parabolas. For a single, outer-sphere electron transfer, donor and acceptor surfaces are weakly interacting; electron transfer occurs non-adiabatically and under Franck-Condon conditions, where the highest probability for electron transfer corresponds to the minimum difference in nuclear coordinates between the donor and acceptor states. The energy λ needed to attain this nuclear configuration is dependent on solvent and protein matrix reorganization as well as changes in the bond lengths and angles of the initial states, and so can be considered a sum of outer

and inner sphere contributions $\lambda = \lambda_o + \lambda_i$ [31, 32].

Thus, from the intersection of the two parabolas, $\Delta G^{\ddagger} = \frac{(\Delta G^{\circ}+\lambda)^2}{4\lambda}$, and from the Eyring equation, the rate constant is $k_{\mathrm{ET}} = A \cdot \exp\left[-\frac{(\Delta G^{\circ}+\lambda)^2}{4\lambda k_{\mathrm{B}}T}\right]$. Yet, electrons are capable of tunneling through barriers and this quantum nature is not accounted in this classical equation. To describe the quantum phenomenon, application of Fermi's Golden rule yields $k_{ET} = 4\pi^2/\hbar * |H_{DA}|^2 \cdot FC$, where $|H_{DA}|^2 = |\langle \Psi_A | \hat{H} | \Psi_D \rangle|^2 = H_0^2 \cdot \exp[-\frac{\beta}{2}(r_{DA} - r_0)]$ and FC is the Franck-Condon weighted density of states [33–36].

The $|H_{DA}|^2$ term is a measurement of the electronic coupling strength between the donor and acceptor orbitals and is expected to be small for non-adiabatic electron transfer reactions. Notably, $|H_{DA}|^2$ exponentially decays with greater donor-acceptor distances [37], with β being an attenuation parameter that is dependent upon the intervening medium. Hence, a single electron transfer is typically limited to no more than 20 Å [15]. With weak coupling, electrons must tunnel or "hop" through the medium or protein matrix in order to reach the acceptor moiety.

The Franck-Condon weighted density of states term constitutes a sum of overlap integrals of the donor-acceptor nuclear wave functions at the same energies. At a high temperature limit where vibrational frequencies are small ($h\nu/2k_{\mathrm{B}}T \leq 1$), FC is approximated to be $(4\pi\lambda k_{\mathrm{B}}T)^{-1/2} \exp\left[-\frac{\Delta G^{\circ}+\lambda)^2}{4\lambda k_{\mathrm{B}}T}\right]$. The exponential portion of FC is identical to that predicted by the classical derivation using parabolic energy surfaces and the Eyring equation. [33–36].

Hence, the semiclassical Marcus equation is as follows:

$$k = \frac{2\pi}{\hbar}\langle H_{\mathrm{AB}}^2 \rangle (4\pi\lambda k_{\mathrm{B}}T)^{-1/2} \cdot \exp\left[-\frac{(\Delta G^{\circ}+\lambda)^2}{4\lambda k_{\mathrm{B}}T}\right]$$

where k is the observed electron transfer rate constant, λ is the reorganization energy, and ΔG° is the Gibbs free energy change of the reaction [33, 38].

Perhaps the most well-known conclusion from Marcus theory is the prediction of the

inverted region. In the normal region, as the driving force increases, the rate of electron transfer increases until $-\Delta G^\circ = \lambda$. Once the amplitude of the driving force exceeds the reorganization energy, the barrier reforms and electron transfer rates decrease as the driving force increases. This has been observed in small molecule systems [39] and in chemiluminescence [38].

1.2.2 Proton-coupled electron transfer

Proton transfer can accompany electron transfer, requiring an additional level of theory to model these reactions. Proton-coupled electron transfer (PCET) can occur via either a concerted mechanism (coupled proton-electron transfer; CPET) or stepwise (either proton transfer followed by electron transfer (PTET) or vice versa (ETPT)); for the latter, either the proton or electron transfer can be rate-limiting [13, 40]. Thermodynamically, it is arguably more favorable for both transfers to be concerted as it allows for the avoidance of high energy species, however, a step-wise mechanism can occur if the oxidant has a high enough oxidation potential [41].

PCET theory was initially developed by Cukier and colleagues and expanded upon by Hammes-Schiffer. By combining aspects of proton transfer and electron transfer reactions, PCET is essentially a multidimensional analogue of Marcus theory. Energy surfaces are represented two-dimensionally by two solvent coordinates (one for proton transfer and the other for electron transfer) as paraboloids, with the surfaces describing whether reactions will occur in a concerted or sequential mechanism. Instead of two charge transfer states, there are four: both the proton and electron localized on either the acceptor or donor, proton on the donor and electron on the acceptor, and electron on the donor and proton on the acceptor. Owing to the coupling of proton and electron transfer, these states must be diabatic as nuclear and electronic motions are no longer separable [42].

For fixed proton donor-acceptor distances, the rate constant is

$$k = \sum_{\mu} P_{\mu} \sum_{\nu} \frac{|V^{\mathrm{el}} S_{\mu\nu}^{(0)}|^2}{\hbar} \sqrt{\frac{\pi}{\lambda_{\mu\nu} k_{\mathrm{B}} T}} \exp\left[-\frac{(\Delta G_{\mu\nu}^{0} + \lambda_{\mu\nu})^2}{4 \lambda_{\mu\nu} k_{\mathrm{B}} T} \right]$$

where summations are done over the vibronic states, P_{μ} is the Boltzmann probability for state μ, V^{el} is the electronic coupling, and S is the proton vibrational wave function overlap [43]. Notably, driving force and reorganization energy terms are no longer one dimensional [42, 44, 45]. Due to the inherent challenges in obtaining these multidimensional parameters required to fully describe a PCET reaction, oftentimes researchers incorporate solvent isotope effects and pH dependencies into their electron transfer rate measurements in order to garner more insights into the type of mechanism at play [46].

1.2.3 Relay amino acids in multistep electron transfer

Long range electron transfer require relay residues, which behave as stepping stones for multistep reactions, but in order to carry out this function, the side chain must be reversibly oxidized/reduced and the environment needs to be capable of stabilizing a transient charge. As such, the most widely known relay residues are tyrosine and tryptophan, which have relatively low oxidation/reduction potentials and allow for delocalization of the charge [47]. Recent work by Giese and coworkers have also identified cysteine and methionine side chains to be effective at relaying electrons, with the cysteine undergoing a PCET mechanism with the solvent [48]. Methionine residues in isolation have a high redox potential of 1.66 V, but the authors claim that neighboring group effects can actually lower the potential down to 0.85 V [48, 49]. Giese and colleagues have also hypothesized that redox-inactive side chains may be able to behave as relay amino acids. In the case of phenylalanine, the arene radical cation can be stabilized by the lone pairs of the adjacent carbonyl amide, which would not only increase the thermodynamic stability of the residue but also significantly reduce

its oxidation potential [47]. Similarly, polyprolines have been found to be able to transfer electron charge [50]. (It is worth noting that most of these experiments are accomplished with small peptide systems in solvent, so the conformations required for a neighboring group effect may be limited in a protein.) Additionally, glycine radicals have also be reported to be able to store radicals on the protein backbone through the generation tertiary radical species, which can then be stabilized by electron density donation from its neighbors [51–53].

1.2.4 Investigation of the tyrosyl hopping site in the cytochrome *c* peroxidase : cytochrome *c* complex

Cytochrome *c* peroxidase (CcP) and cytochrome *c* (Cc) were first discovered in 1939 in the inter- mitochondrial membrane of *Saccharomyces cerevisiae*. These two redox partners were later found to reduce hydrogen peroxide to water [54, 55] as part of an oxidative stress response and possibly as a peroxide sensing mechanism [55–57]. The catalytic cycle has been established to comprise four steps. Firstly, peroxide binds at the distal heme pocket and is stabilized by Arg48, Trp51, and His52; His52 has been determined to be essential for deprotonation of the peroxide and fast CcP oxidation [58–62]. After peroxide oxidizes CcP to Compound I ($Fe^{4+} = O$; $Trp^{+\bullet}$), one reduced equivalent of bound Cc donates an electron across the interface of the complex ($\sim$ 26 Å; heme iron to iron distance) to Compound I to generate the ferric state. Residue Trp191 oxidizes ferric heme to Fe^{4+}, which is subsequently reduced by a second equivalent of reduced Cc to reform the active protein (Scheme 1.1).

The catalytic mechanism of CcP:Cc has been investigated through various spectroscopic methods that have also been used for studying heme proteins, including spectrophotometric assays that indirectly determine the activity of CcP by measuring the rate of Cc oxidation, electron spin resonance (ESR) spectroscopy to characterize the iron center and the organic

$$\text{Fe(III)CcP} + \text{HOOH} \longrightarrow \text{Fe(IV)=O,W}^{\bullet+}\text{CcP} + \text{H}_2\text{O}$$
$$\text{Fe(IV)=O,W}^{\bullet+}\text{CcP} + \text{Fe(II)Cc} \longrightarrow \text{Fe(IV)=O,W}^{0}\text{CcP+Fe(III)Cc}$$
$$\text{Fe(IV)=O,W}^{0}\text{CcP+H}^{+} \longrightarrow \text{Fe(III)-OH,W}^{\bullet+}\text{CcP}$$
$$\text{Fe(III)-OH,W}^{\bullet+}\text{CcP+Fe(II)Cc+H}^{+} \longrightarrow \text{Fe(III),W}^{0}\text{CcP+Fe(III)Cc+H}_2\text{O}$$

Scheme 1.1: Proposed mechanism of WT CcP:WT Cc reaction upon initiation of reaction with H_2O_2.

radicals of Compound I, and infrared and resonance Raman spectroscopy to study porphyrin and ligand interactions [63]. Despite its fairly straightforward mechanism, measuring rate constants in the peroxide-initiated reaction can be complicated by several factors, such as mixing of the peroxide in solution and Cc binding and dissociation rates. Hoffman and colleagues developed an analogous, photoinducible system to measure the rate of electron transfer between the hole hopping site and the CcP prosthetic group [64–66]. By replacing the CcP ferriheme with a zinc porphyrin, the system can be excited by laser light, affording time resolutions down to the microseconds. The photoexcited zinc porphyrin generates the triplet state ($E^{\circ\prime} \sim +0.64$), which then either reverts back to ground state or ejects an electron across the CcP:Cc interface to ferriheme cytochrome *c*. Charge recombination is accelerated by the electron hole hopping site, returning the system to ground state [64–66]. Time-resolved measurements on the crystallized system has further eliminated Cc exchange reactions from interfering with the observed electron transfer rates [67, 68].

The electron hole hopping site Trp191 is highly conserved among peroxidases [69]. Its function and significance has been identified spectroscopically and by site-directed mutagenesis [70]. Moreover, ESR spectra of Compound I with the cationic tryptophanyl radical demonstrate an intriguing shoulder feature owing to anti-ferromagnetic coupling between Trp191 and the oxyferryl heme species [59, 71]. Substitution of Trp191 with a redox-inactive phenylalanine residue results in an inactive variant. Miller and coworkers discovered that this replacement also caused an alternate mechanism to occur wherein peroxide preferentially

reacted with the ferryl species directly to oxidize Cc(Fe^{2+}) [72]. Other mutations at site 191 involved substituting Trp191 with a glycine, thus generating a cavity where the aromatic side chain previously resided. Goodin and colleagues proceeded to use this cavity to bind substituted imidazoles with high affinity, demonstrating that the cavity favorably interacts with positively-charged substrates [73], however, later studies show that these surrogate hopping sites are unable to restore activity [74].

Substitution of particular residues near the heme pocket and at the surface in CcP and Cc have been found to alter the reduction potential. In general, the redox potentials of heme proteins are affected by protein fold, porphyrin type, and axial ligands [61, 75]. Many of the reported mutations alter the polar environment of the heme pocket region, with a few surface mutations affecting the accessibility of peroxide into the pocket and the binding of CcP to Cc [61]. Similarly, residue substitutions in Cc are aimed at affecting the heme environment and changing the stability of the oxidized and reduced forms [76]. Note that these mutations in the heme pocket likely only affect the heme iron reduction potential and have little influence on the hole hopping site.

As the intermediary tryptophan hole hopping site has been fairly well-studied, we replaced Trp191 with a tyrosine residue in order to further study the functionality of tyrosyl radicals. Tyrosyl hopping sites are of particular interest due to their key roles in the function of prostaglandin H synthase, ribonucleotide reductase, and photosystem II, among others [22, 77–80]. Recently, we have investigated the mutant W191Y CcP, which exhibited little to no activity (see Appendix A). The crystal structure of this variant in complex with Cc revealed no significant structural perturbations compared to the native structure (Figure 1.1), further indicating that the lack of activity was because of the tyrosyl radical. By using this robust, manipulable, model system, we have endeavored to study the properties of tyrosyl hopping sites to further determine the effects of driving force and the local environment on activity

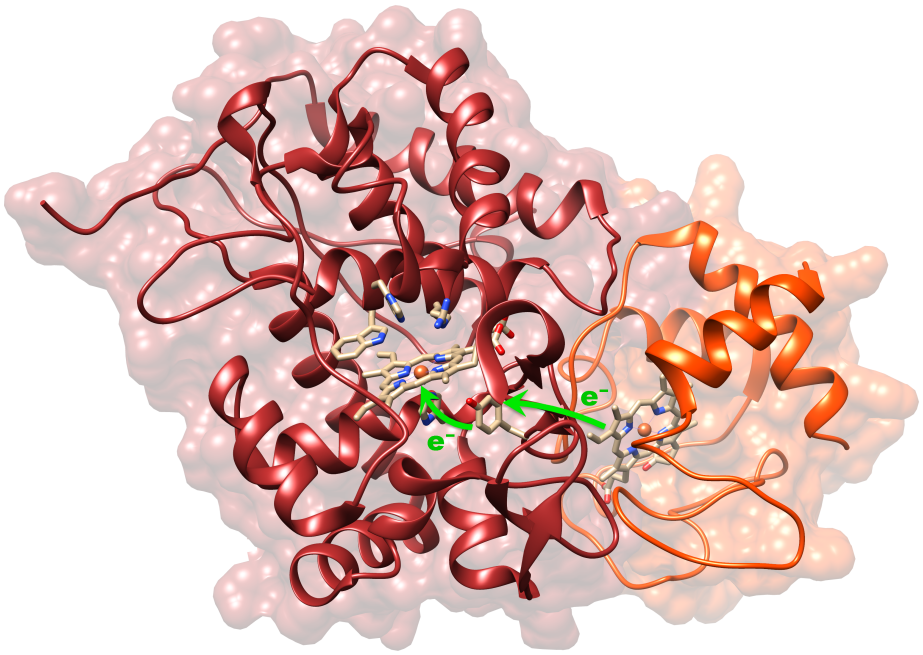

Figure 1.1: Structure of W191Y CcP:Cc complex (PDB 5CIH) CcP is in brown and Cc in red-orange. Green arrows illustrate the general path electrons take to reduce CcP to its ferric state. Figure generated by Chimera [81].

and the general electron transfer mechanism (see Chapter 2).

1.2.5 Internal electron transfer mechanisms of flavin binding domains

Flavin is a ubiquitous light and redox sensing cofactor owing to the broad range of redox and protonation states. The flavin cofactor (typically the riboflavin (RF), flavin mononucleotide (FMN), or flavin adenine dinucleotide (FAD) molecule) exists in one of four forms: the fully oxidized flavoquinone, the single electron reduced anionic semiquinone (ASQ), the single electron reduced neutral semiquinone (NSQ), and the fully reduced flavohydroquinone. Each form possesses distinguishable, characteristic features observable by UV-vis spectroscopy [82, 83]. In solution, the reduced flavin states are transient and rapidly

oxidized by oxygen; however, when bound in a protein matrix, their lifetimes can be extended to several days or more [84, 85]. Curiously, depending on the protein system and environment, each of these reduced forms exhibits signaling capabilities.

The flavin cofactor is found in a multitude of blue-light photoreceptor domains and proteins. They are loosely characterized into one of three families: the blue light receptors using FAD (BLUF) proteins, cryptochromes, and a subclass of the Per-Arnt-Ser (PAS) domains known as light-oxygen-voltage (LOV) domains [24]. These photosensory domains can either exist as isolated domains or covalently linked to effector domains. Upon photoactivation, they can elicit a host of different biological responses by propagating changes from the chromophore and its environment via electron transfer, bond rearrangements, and isomerizations. The various photochemical effects instigate conformational changes that promote interactions with other proteins or small molecules that are important in signal transduction and downstream signaling [86, 87].

For instance, BLUF proteins are predominantly found in prokaryotes and are essential for photoadaptation responses, including phototaxis, gene regulation, and virulence [88, 89]. Excitation by blue light curiously causes minimal conformational changes in the FAD cofactor and the signaling state is generated on a sub-nanosecond timescale [86]. The final signaling state is characterized by a subtly red-shifted spectrum of the fully oxidized FAD cofactor and changes in the hydrogen-bond network between the FAD and its environment. To date, the proposed mechanisms for the formation of the signaling state is contentious with different models, primarily in regards to the roles of tyrosine and glutamine residues, though a conserved methionine and partially-conserved tryptophan have also been deemed essential for signaling [89]. One theory postulates that photoactivation results in PCET from a conserved tyrosine residue to the flavin cofactor to generate a transient radical pair. Subsequent rotation of a conserved glutamine leads to recombination of the radical pair, hydrogen

bond rearrangement, and structural changes to generate the signaling state [86, 88]. Yet, an alternate mechanism proposes that an isomerization reaction occurs upon photoactivation. Rather than rotating, the conserved glutamine tautomerizes and the resultant hydrogen-bonding network then allows for rapid radical recombination [90]. Still other studies have highlighted the significance of the conserved tyrosine in dark state recovery; by altering the pK_{a} of the conserved residue with non-natural fluorotyrosines, researchers were able to affect the lifetime and stability of the light state [91, 92]. Efforts continue to be aimed at clarifying the photocycle mechanism and dynamics of the conserved, essential side chains to form a unifying theory that combines experimental and theoretical findings.

In the cryptochrome class, the protein domain fold is related to that of DNA photolyases. In general, cryptochrome (Cry) photoreduction requires a nearby chain of three conserved tryptophan residues. The Trp triad allows for the transfer of electrons from the surface of the protein to the flavin cofactor [93]. Upon photoreduction though, the biochemical output signals vary widely depending on the host organism. Cryptochromes found in *Drosophila*, *Arabidopsis*, *Synechocystis*, and *Homo* bind to DNA under UV irradiation and can repair cyclobutane-pyrimidine-dimer lesions [86, 94]. In *Drosophila*, cryptochrome photoreduction results in the flavin reduction to the ASQ and ensuing protonation of a neighboring His residue, which ultimately releases the C-terminal tail and facilitates interaction with its protein partners [95, 96]. By contrast, the photochemistry of plant cryptochromes involves generation of the NSQ ($\mathrm{FADH}^{\bullet}$) under blue light. Further excitation by green light then fully reduces the cofactor to the inactive hydroquinone state [97]. The output signals from plant Cry are less well-understood, with postulations that the C-terminal tail constitutes the effector domain and protein-protein dimerization important for downstream effects [86, 98].

And finally, the third class of flavin-binding domains, the LOV domains, comprise of a

FAD cofactor bound in a PAS domain fold. These domains were first discovered in phototropins, which are plant photoreceptors important for chloroplast movement, stomatal opening, and phototropism [87, 99, 100]. Phototropins consist of two LOV domains, LOV1 and LOV2, along with a serine/threonine kinase effector domain [99, 101]. The isolated LOV2 domains behaves in a canonical fashion: flavin excitation by blue light results in triplet state formation and a subsequent cysteinyl-flavin covalent bond formation between a strictly conserved cysteine residue and the C4a carbon of the isoalloxazine ring [102–105]. The fully reduced adduct state causes unfolding of the Jα helix and diminishes kinase inhibition [87, 106]. In other LOV domain systems, light activation can cause rearrangement of the Jα helices and linked effector domains, resulting in unfolding and dimerization, as in the case of YtvA, a stress response protein in *Bacillus subtilis* [107, 108]. Activation of the LOV domain can also lead to an assortment of different responses in other organisms, such as photoentrainment of circadian clocks [101, 109]. Specifically, in the protein VIVID (VVD) from *Neurospora crassa*, adduct formation is followed by release of the N-cap, allowing for a rapidly exchanging homodimer that purportedly inhibits the activity of the primary photosensory protein White Collar-1 [84, 110, 111] and confers photoadaptation to the organism [112, 113]. Of the LOV domains, our primary focus is on the short circadian clock protein VVD, as this blue-light receptor protein is comprised almost entirely of a single LOV domain, which is stable in aqueous conditions [112].

An increasing number of studies on the LOV domain have substituted the conserved cysteine residue with a redox-inactive one, which causes the photocycle to halt at the NSQ state instead of the fully reduced flavohydroquinone [85, 114–116]. Recently, we have demonstrated that this protonated flavin species is sufficient for eliciting *in vivo* signaling (see Chapter 3). To date, the electron donor that contributes to the formation of this state is unknown, but the variety of redox-active residues present in the LOV domain provides a tantalizing puzzle to be solved. Through an assortment of mutagenesis and spectroscopic methods, we have

narrowed down the potential residues that may contribute to internal electron transfer and signal state formation (see Chapter 4).

1.3 Biotechnology applications

Protein engineering efforts have been aimed at utilizing blue-light sensing proteins as fluorescent reporters for imaging applications. Rather than static, fluorescent probes, photoreceptors have the added advantages of being able to report on the dynamics of protein-protein interactions, can reversibly cycle between the dark and light states, and can be genetically encoded [117]. Researchers have successfully created permanently fluorescent reporter proteins by abolishing the natural photochemistry of photosensory proteins. For LOV domains, this was accomplished through site-directed mutagenesis and replacement of the active-site cysteine with either an alanine or serine, thus inhibiting fluorescence quenching caused by adduct formation [118, 119].

These applications can be taken one step further in optogenetics [120]. Initially, these studies were accomplished with naturally occurring photoreceptors and were limited to neuroscience applications. With the use of light-gated ion channels and ion pumps, such as channelrhodopsins, action potentials could be induced by light, allowing researchers to control and modulate cellular activity noninvasively through heterologous expression in the target organism or tissue. Optogenetics also affords high spatial and temporal resolution provided the photoinducible domains have rapid on/off kinetics and the resultant biological responses are fast. Advances in the field have now allowed studies to branch out and probe other cellular events, such as transcription, enzymatic processes, and cell motility [117]. To this effect, researchers have fused photoswitchable domains to effector modules that control the activity of interest [121]. For example, photoactivated adenyl cyclase has been used to

regulate cyclic AMP production and in turn, affect neuronal activation and regulate gene expression [87]. Continued advances in the field and improvements in photoreceptor engineering will require careful tuning of photocycles and understanding of electron transfer mechanisms in order to generate effective systems for optogenetic control.

BIBLIOGRAPHY

(1) Mullineaux, P.; Karpinski, S. *Curr. Opin. Plant Biol.* **2002**, *5*, 43–48.

(2) Hynes, N. E.; Ingham, P. W.; Lim, W. A.; Marshall, C. J.; Massagué, J.; Pawson, T. *Nat. Rev. Mol. Cell Biol.* **2013**, *14*, 393–398.

(3) Kirubakaran, A.; Jain, S.; Nema, R. K. *Renew. Sustain. Energy Rev.* **2009**, *13*, 2430–2440.

(4) Asim, N.; Sopian, K.; Ahmadi, S.; Saeedfar, K.; Alghoul, M. A.; Saadatian, O.; Zaidi, S. H. *Renew. Sustain. Energy Rev.* **2012**, *16*, 5834–5847.

(5) Whang, D. R.; Apaydin, D. H. *ChemPhotoChem* **2017**, *2*, 148–160.

(6) Ntziachristos, V. *Annu. Rev. Biomed. Eng.* **2006**, *8*, 1–33.

(7) Christie, J. M.; Hitomi, K.; Arvai, A. S.; Hartfield, K. A.; Mettlen, M.; Pratt, A. J.; Tainer, J. A.; Getzoff, E. D. *J. Biol. Chem.* **2012**, *287*, 22295–22304.

(8) Jullien, L.; Gautier, A. *Methods Appl. Fluoresc.* **2015**, *3*, 1–12.

(9) Matyjaszewski, K.; Xia, J. *Chem. Rev.* **2001**, *101*, 2921–2990.

(10) Matyjaszewski, K. *Macromolecules* **2012**, *45*, 4015–4039.

(11) Westerlund, K.; Berry, B. W.; Privett, H. K.; Tommos, C. *Biochim. Biophys. Acta - Bioenerg.* **2005**, *1707*, 103–116.

(12) Glover, S. D.; Parada, G. A.; Markle, T. F.; Ott, S.; Hammarstrom, L. *J. Am. Chem. Soc.* **2017**, *139*, 2090–2101.

(13) Mayer, J. M. *Annu. Rev. Phys. Chem.* **2004**, *55*, 363–390.

(14) Warren, J. J.; Mayer, J. M. *Biochemistry* **2015**, *54*, 1863–1878.

(15) Gray, H. B.; Winkler, J. R. *Proc. Natl. Acad. Sci. U. S. A.* **2005**, *102*, 3534–9.

(16) Shamir, M.; Bar-On, Y.; Phillips, R.; Milo, R. *Cell* **2016**, *164*, 1302–1302.

(17) Mulliez, E.; Fontecave, M.; Gaillard, J.; Reichard, P. *J. Biol. Chem.* **1993**, *268*, 2296–2299.

(18) Greene, B. L.; Taguchi, A. T.; Stubbe, J.; Nocera, D. G. *J. Am. Chem. Soc.* **2017**, *139*, 16657–16665.

(19) Song, D. Y.; Pizano, A. A.; Holder, P. G.; Stubbe, J.; Nocera, D. G. *Chem. Sci.* **2015**, *6*, 4519–4524.

(20) Tarboush, N. A.; Jensen, L. M. R.; Yukl, E. T.; Geng, J.; Liu, A.; Wilmot, C. M.; Davidson, V. L. *Proc. Natl. Acad. Sci. U. S. A.* **2011**, *108*, 16956–61.

(21) Yukl, E. T.; Williamson, H. R.; Higgins, L.; Davidson, V. L.; Wilmot, C. M. *Biochemistry* **2013**, *52*, 9447–9455.

(22) Gray, H. B.; Winkler, J. R. *Proc. Natl. Acad. Sci. U. S. A.* **2015**, *112*, 10920–10925.

(23) Winkler, J. R.; Gray, H. B. *Q. Rev. Biophys.* **2015**, *48*, 411–420.

(24) Zoltowski, B. D.; Gardner, K. H. *Biochemistry* **2011**, *50*, 4–16.

(25) Formaneck, M. S.; Li, G.; Zhang, X.; Cui, Q. *J. Theor. Comput. Chem.* **2002**, *01*, 53–67.

(26) Sharp, K. A. *Biophys. J.* **1998**, *74*, 1241–1250.

(27) Gray, H. B.; Winkler, J. R. *Q. Rev. Biophys.* **2003**, *36*, 341–372.

(28) Warren, J. J.; Winkler, J. R.; Gray, H. B. *FEBS Lett.* **2012**, *586*, 596–602.

(29) Marcus, R. A. *J. Chem. Phys.* **1956**, *24*, 966–978.

(30) Gray, H. B.; Winkler, J. R. *Annu. Rev. Biochem.* **1996**, *65*, 537–561.

(31) Eberson, L. *Adv. Free Radic. Biol. Med.* **1985**, *1*, 19–90.

(32) Stubbe, J. A.; Nocera, D. G.; Yee, C. S.; Chang, M. C. *Chem. Rev.* **2003**, *103*, 2167–2201.

(33) Marcus, R.; Sutin, N. *Biochim. Biophys. Acta-Reviews Bioenerg.* **1985**, *811*, 265–322.

(34) Moser, C. C.; Keske, J. M.; Warncke, K.; Farid, R. S.; Dutton, P. L. *Nature* **1992**, *355*, 796–802.

(35) *Protein electron transfer*; Bendall, D. S., Ed.; Bios Scientific Publishers: 1996, p 300.

(36) *The Exploration of Supramolecular Systems and Nanostructures by Photochemical Techniques*; Ceroni, P., Ed.; Lecture Notes in Chemistry, Vol. 78; Springer Netherlands: Dordrecht, 2012.

(37) Olshansky, L.; Stubbe, J.; Nocera, D. G. *J. Am. Chem. Soc.* **2016**, *138*, 1196–1205.

(38) Marcus, R. A. *J. Electroanal. Chem.* **1997**, *438*, 251–259.

(39) Closs, G. L.; Miller, J. R. *Science (80-.).* **1988**, *240*, 440–447.

(40) Pagba, C. V.; McCaslin, T. G.; Chi, S. H.; Perry, J. W.; Barry, B. A. *J. Phys. Chem. B* **2016**, *120*, 1259–1272.

(41) Dempsey, J. L.; Winkler, J. R.; Gray, H. B. *Chem. Rev.* **2010**, *110*, 7024–7039.

(42) Hammes-Schiffer, S. *Acc. Chem. Res.* **2001**, *34*, 273–281.

(43) Hammes-Schiffer, S. *Acc. Chem. Res.* **2009**, *42*, 1881–1889.

(44) Soudackov, A.; Hammes-Schiffer, S. *J. Chem. Phys.* **2000**, *113*, 10438–10450.

(45) Hammes-Schiffer, S.; Stuchebrukhov, A. A. *Chem. Rev.* **2010**, *110*, 6939–6960.

(46) Huynh, M. H. V.; Meyer, T. J. *Chem. Rev.* **2006**, *107*, 5004–5064.

(47) Nathanael, J.; Gamon, L.; Cordes, M.; Rablen, P.; Bally, T.; Fromm, K.; Giese, B.; Wille, U. *ChemBioChem* **2018**, *19*, 922–926.

(48) Wang, M.; Gao, J.; Müller, P.; Giese, B. *Angew. Chemie - Int. Ed.* **2009**, *48*, 4232–4234.

(49) Giese, B.; Wang, M.; Gao, J.; Stoltz, M.; Müller, P.; Graber, M. *J. Org. Chem.* **2009**, *74*, 3621–3625.

(50) Monney, N. P.; Bally, T.; Giese, B. *J. Phys. Org. Chem.* **2015**, *28*, 347–353.

(51) Copeland, E. S.; Sanner, T.; Pihl, A. *Eur. J. Biochem.* **1967**, *1*, 312–316.

(52) Backman, L. R.; Funk, M. A.; Dawson, C. D.; Drennan, C. L. *Crit. Rev. Biochem. Mol. Biol.* **2017**, *52*, 674–695.

(53) Shisler, K. A.; Broderick, J. B. *Arch. Biochem. Biophys.* **2014**, *546*, 64–71.

(54) Poulos, T.; Kraut, J. *J. Biol. Chem.* **1980**, *255*, 10322–10330.

(55) Volkov, A. N.; Nicholls, P.; Worrall, J. A. R. *Biochim. Biophys. Acta* **2011**, *1807*, 1482–1503.

(56) Charizanis, C.; Juhnke, H.; Krems, B.; Entian, K. D. *Mol. Gen. Genet.* **1999**, *262*, 437–447.

(57) Kathiresan, M.; English, A. M. *Chem. Sci.* **2017**, *8*, 1152–1162.

(58) Erman, J. E.; Vitello, L. B.; Miller, M. A.; Shaw, A.; Brown, K. A.; Kraut, J. *Biochemistry* **1993**, *32*, 9798–9806.

(59) Houseman, A. L. P.; Doan, P. E.; Goodin, D. B.; Hoffman, B. M. *Biochemistry* **1993**, *32*, 4430–4443.

(60) Erman, J. E.; Vitello, L. B. *Biochim. Biophys. Acta* **2002**, *1597*, 193–220.

(61) DiCarlo, C. M.; Vitello, L. B.; Erman, J. E. *J. Inorg. Biochem.* **2007**, *101*, 603–613.

(62) DiCarlo, C. M.; Vitello, L. B.; Erman, J. E. *J. Inorg. Biochem.* **2011**, *105*, 532–537.

(63) Jung, C.; Vries, S. D.; Schünemann, V. *Arch. Biochem. Biophys.* **2011**, *507*, 44–55.

(64) Shing Ho, P.; Sutoris, C.; Liang, N.; Margoliash, E.; Hoffman, B. M. *J. Am. Chem. Soc* **1985**, *107*, 1070–1071.

(65) Liang, N.; Kang, C.; Ho, P. S.; Margoliash, E.; Hoffman, B. M. *J. Am. Chem. Soc.* **1986**, *108*, 4665–4666.

(66) Nocek, J.; Zhou, J.; De Forest, S.; Beratan, D.; Priyadarshy, S.; Onuchic, J.; Hoffman, B. *Chem. Rev* **1996**, *96*, 2459–2490.

(67) Kang, S. A.; Marjavaara, P. J.; Crane, B. R. *J. Am. Chem. Soc.* **2004**, *126*, 10836–10837.

(68) Kang, S. A.; Hoke, K. R.; Crane, B. R. *J. Am. Chem. Soc.* **2006**, *128*, 2346–2355.

(69) Zámocký, M.; Dunand, C. *FEBS Lett.* **2006**, *580*, 6655–6664.

(70) Sivaraja, M.; Goodin, D. B.; Smith, M.; Hoffman, B. M. *Science (80-.).* **1989**, *245*, 738–740.

(71) Huyett, J. E.; Doan, P. E.; Gurbiel, R.; Houseman, A. L. P.; Sivaraja, M.; Goodin, D. B.; Hoffman, B. M. *J. Am. Chem. Soc.* **1995**, *117*, 9033–9041.

(72) Miller, M.; Vitello, L.; Erman, J. E. *Biochemistry* **1995**, *34*, 12048–58.

(73) Fitzgerald, M. M.; Churchill, M. J.; McRee, D. E.; Goodin, D. B. *Biochemistry* **1994**, *33*, 3807–3818.

(74) Putnam, A.-M. M. A.; Lee, Y. T.; Goodin, D. B. *Biochemistry* **2009**, *48*, 1–3.

(75) Hosseinzadeh, P.; Lu, Y. *Biochim. Biophys. Acta - Bioenerg.* **2016**, *1857*, 557–581.

(76) Lett, C. M.; Guillemette, J. G. *Biochem. J.* **2002**, *362*, 281–287.

(77) Karthein, R.; Dietz, R.; Nastainczyk, W.; Ruf, H. H. *Eur. J. Biochem.* **1988**, *171*, 313–320.

(78) Stubbe, J. A. *Annu. Rev. Biochem.* **1989**, *58*, 257–285.

(79) Aubert, C.; Mathis, P.; Eker, A. P. M.; Brettel, K. *Proc. Natl. Acad. Sci.* **1999**, *96*, 5423–5427.

(80) Barry, B. A. *J. Photochem. Photobiol. B Biol.* **2011**, *104*, 60–71.

(81) Pettersen, E. F.; Goddard, T. D.; Huang, C. C.; Couch, G. S.; Greenblatt, D. M.; Meng, E. C.; Ferrin, T. E. *J. Comput. Chem.* **2004**, *25*, 1605–1612.

(82) Liu, B.; Liu, H.; Zhong, D.; Lin, C. *Curr. Opin. Plant Biol.* **2010**, *13*, 578–586.

(83) Kao, Y. T.; Saxena, C.; He, T. F.; Guo, L.; Wang, L.; Sancar, A.; Zhong, D. *J. Am. Chem. Soc.* **2008**, *130*, 13132–13139.

(84) Zoltowski, B. D.; Vaccaro, B.; Crane, B. R. *Nat. Chem. Biol.* **2009**, *5*, 827–834.

(85) Vaidya, A. T.; Chen, C.-h. H.; Dunlap, J. C.; Loros, J. J.; Crane, B. R. *Sci. Signal.* **2011**, *4*, ra50.

(86) Möglich, A.; Yang, X.; Ayers, R. A.; Moffat, K. *Annu. Rev. Plant Biol.* **2010**, *61*, 21–47.

(87) Losi, A.; Gärtner, W. *Annu. Rev. Plant Biol.* **2012**, *63*, 49–72.

(88) Mathes, T.; Van Stokkum, I. H. M.; Stierl, M.; Kennis, J. T. M. *J. Biol. Chem.* **2012**, *287*, 31725–31738.

(89) Mathes, T.; Götze, J. P. *Front. Mol. Biosci.* **2015**, *2*, 62.

(90) Domratcheva, T.; Grigorenko, B. L.; Schlichting, I.; Nemukhin, A. V. *Biophys. J.* **2008**, *94*, 3872–3879.

(91) Gil, A. A.; Laptenok, S. P.; Iuliano, J. N.; Lukacs, A.; Verma, A.; Hall, C. R.; Yoon, G. E.; Brust, R.; Greetham, G. M.; Towrie, M.; French, J. B.; Meech, S. R.; Tonge, P. J. *J. Am. Chem. Soc.* **2017**, *139*, 14638–14648.

(92) Gil, A. A. et al. *J. Am. Chem. Soc.* **2016**, *138*, 926–935.

(93) Müller, P.; Yamamoto, J.; Martin, R.; Iwai, S.; Brettel, K. *Chem. Commun.* **2015**, *51*, 15502–15505.

(94) Pokorny, R.; Klar, T.; Hennecke, U.; Carell, T.; Batschauer, A.; Essen, L.-O. *Proc. Natl. Acad. Sci.* **2008**, *105*, 21023–21027.

(95) Ozturk, N.; Selby, C. P.; Zhong, D.; Sancar, A. *J. Biol. Chem.* **2014**, *289*, 4634–4642.

(96) Ganguly, A.; Manahan, C. C.; Top, D.; Yee, E. F.; Lin, C.; Young, M. W.; Thiel, W.; Crane, B. R. *Proc. Natl. Acad. Sci.* **2016**, *113*, 10073–10078.

(97) Banerjee, R.; Schleicher, E.; Meier, S.; Viana, R. M.; Pokorny, R.; Ahmad, M.; Bittl, R.; Batschauer, A. *J. Biol. Chem.* **2007**, *282*, 14916–14922.

(98) Partch, C. L.; Clarkson, M. W.; Özgür, S.; Lee, A. L.; Sancar, A. *Biochemistry* **2005**, *44*, 3795–3805.

(99) Christie, J. M.; Reymond, P.; Powell, G. K.; Bernasconi, P.; Raibekas, A. A.; Liscum, E.; Briggs, W. R. *Science (80-.).* **1998**, *282*, 1698–1701.

(100) Christie, J. M.; Corchnoy, S. B.; Swartz, T. E.; Hokenson, M.; Han, I. S.; Briggs, W. R.; Bogomolni, R. A. *Biochemistry* **2007**, *46*, 9310–9319.

(101) Crosson, S.; Rajagopal, S.; Moffat, K. *Biochemistry* **2003**, *42*, 2–10.

(102) Crosson, S.; Moffat, K. *Proc. Natl. Acad. Sci.* **2001**, *98*, 2995–3000.

(103) Conrad, K. S.; Manahan, C. C.; Crane, B. R. *Nat. Chem. Biol.* **2014**, *10*, 801–9.

(104) Zayner, J. P.; Sosnick, T. R. *PLoS One* **2014**, *9*, e87074.

(105) Losi, A.; Gärtner, W. *Photochem. Photobiol.* **2017**, *93*, 141–158.

(106) Harper, S. M.; Neil, L. C.; Gardner, K. H. *Science (80-.).* **2003**, *301*, 1541–1544.

(107) Ávila-Pérez, M.; Hellingwerf, K. J.; Kort, R. *J. Bacteriol.* **2006**, *188*, 6411–6414.

(108) Herrou, J.; Crosson, S. *Nat. Rev. Microbiol.* **2011**, *9*, 713–723.

(109) Crane, B. R.; Young, M. W. *Annu. Rev. Biochem.* **2014**, *83*, 191–219.

(110) He, Q. et al. *Science (80-.).* **2002**, *297*, 840–843.

(111) Chen, C.-H.; DeMay, B. S.; Gladfelter, A. S.; Dunlap, J. C.; Loros, J. J. *Proc. Natl. Acad. Sci.* **2010**, *107*, 16715–16720.

(112) Heintzen, C.; Loros, J. J.; Dunlap, J. C. *Cell* **2001**, *104*, 453–464.

(113) Schwerdtfeger, C.; Linden, H. *EMBO J.* **2003**, *22*, 4846–4855.

(114) Kay, C. W. M.; Schleicher, E.; Kuppig, A.; Hofner, H.; Rüdiger, W.; Schleicher, M.; Fischer, M.; Bacher, A.; Weber, S.; Richter, G. *J. Biol. Chem.* **2003**, *278*, 10973–10982.

(115) Kopka, B.; Magerl, K.; Savitsky, A.; Davari, M. D.; Röllen, K.; Bocola, M.; Dick, B.; Schwaneberg, U.; Jaeger, K. E.; Krauss, U. *Sci. Rep.* **2017**, *7*, 1–16.

(116) Magerl, K.; Stambolic, I.; Dick, B. *Phys. Chem. Chem. Phys.* **2017**, *19*, 10808–10819.

(117) Ziegler, T.; Möglich, A. *Front. Mol. Biosci.* **2015**, *2*, 30.

(118) Chapman, S.; Faulkner, C.; Kaiserli, E.; Garcia-Mata, C.; Savenkov, E. I.; Roberts, A. G.; Oparka, K. J.; Christie, J. M. *Proc. Natl. Acad. Sci.* **2008**, *105*, 20038–20043.

(119) Drepper, T.; Eggert, T.; Circolone, F.; Heck, A.; Krauß, U.; Guterl, J. K.; Wendorff, M.; Losi, A.; Gärtner, W.; Jaeger, K. E. *Nat. Biotechnol.* **2007**, *25*, 443–445.

(120) Deisseroth, K.; Feng, G.; Majewska, A. K.; Miesenbock, G.; Ting, A.; Schnitzer, M. J. *J. Neurosci.* **2006**, *26*, 10380–10386.

(121) Möglich, A.; Moffat, K. *Photochem. Photobiol. Sci.* **2010**, *9*, 1286.

CHAPTER 2

OPTIMIZATION OF PROTON COUPLED ELECTRON TRANSFER VIA STUDIES OF AN ENGINEERED TYROSINE HOLE-HOPPING SITE IN YEAST CYTOCHROME *C* PEROXIDASE

2.1 Abstract

The recovery of electron transfer rates to near wild-type levels of an inactive yeast cytochrome *c* peroxidase (CcP) variant W191Y has been accomplished by the introduction of a basic side chain that coordinates to the redox-active Tyr191 residue. Previous studies on W191Y CcP suggested that the tyrosine hole-hopping site was too low in reduction potential to accelerate electron transfer from a bound unit of reduced cytochrome *c* (Cc). Modification of the hopping site with higher potential fluorotyrosines was surprisingly not effective at improving electron transfer rates. In an effort to mimic protein systems that rely on tyrosyl hopping sites for electron transfer, an adjacent glutamate or histidine residue was positioned to hydrogen bond with the phenolic proton of Tyr191, resulting in upwards of a four-fold increase in Cc oxidation rates. Hydrogen bond formation was confirmed by crystallization of the CcP:Cc complex and continuous-wave electron spin resonance (ESR) spectroscopy studies. The reactivity of the tyrosyl radical was further investigated by rapid freeze quench ESR, with the hydrogen-bonded tyrosine demonstrating a diminished rate of re-oxidation by neighboring redox-active residues, thus implicating an upshift in redox potential due to the coordinating basic side chain. To characterize the proton-coupled electron transfer mechanism, we implemented kinetic isotope exchange and pH dependency studies, which suggest a stepwise process that has a rate-limiting proton transfer step. A combination of the kinetics data provided an approximation of the shift in redox potential and change in reorganization energy engendered by the coordinating base.

2.2 Introduction

Proteins involved in long range electron transfer (ET) play an integral role in a multitude of biologically relevant processes, from respiration and photosynthesis to the design of biocatalysts and artificial biomimetic systems [1–3]. The net rate of electron transfer often relies heavily on redox-active cofactors and tunneling via intermediate hole-hopping sites. As electron transfer decelerates exponentially with distance, systems often require appropriately placed redox-active relay amino acids to permit charge localization and to facilitate coupled, multistep tunneling for long distances >10 Å [4–6]. Additional parameters dictate the rate and distance of a single electron transfer, many of which have been studied through photosensitive small molecules, engineered peptides, and protein models [7–9]. Tyrosine residues are among one of the most common intermediate sites and have been determined to play key roles in electron transfer reactions of ribonucleotide reductase, prostaglandin synthase, DNA photolyase, and photosystem II [10–14]. However, tyrosine oxidation and reduction necessitate both proton transfer and electron transfer via either a stepwise or concerted mechanism in order to maintain its neutral charge [15]. Cationic tyrosyl radicals have an elevated redox potential of +1.4 eV and a very low pK_a of ~ -2 [9, 16], making this species highly reactive and transient in biological systems and impractical for stable, charge localization.

Many models have been generated in the past decades to explore biological electron transfer parameters [8], typically involving significant modifications to proteins, such as directly altering the primary and secondary coordination spheres of the cofactors [17] and introduction of a single electron transfer path into an "all-Phe" protein in which all redox tyrosine and tryptophan residues were replaced by phenylalanine residues [9]. Few have analyzed the effects of changing an intermediate site in the context of a fully functioning protein, specifically for the case of tyrosyl radicals, which play key roles in the enzymatic activity of crucial proteins [10, 11, 18–20].

Here we aim to further explore the ability of the lower-potential tyrosine residue to replicate the functionality of a highly conserved hole-hopping tryptophan residue in yeast cytochrome *c* peroxidase (CcP). Cytochrome *c* peroxidase and its redox partner cytochrome *c* (Cc) is a well-studied system that reduces hydrogen peroxide via a proposed two-electron mechanism, wherein Trp191 acts as an electron hole-hopping site (Scheme 2.1). The proper orientation of Trp191 and its ability to form a stable cationic radical is due in part to hydrogen bonding interactions between Trp191, Asp235, and His175 [21–24]. Hydrogen

$$\text{Fe(III)CcP} + \text{HOOH} \longrightarrow \text{Fe(IV)=O,W}^{\bullet+}\text{CcP} + \text{H}_2\text{O}$$
$$\text{Fe(IV)=O,W}^{\bullet+}\text{CcP} + \text{Fe(II)Cc} \longrightarrow \text{Fe(IV)=O,W}^{0}\text{CcP+Fe(III)Cc}$$
$$\text{Fe(IV)=O,W}^{0}\text{CcP+H}^{+} \longrightarrow \text{Fe(III)-OH,W}^{\bullet+}\text{CcP}$$
$$\text{Fe(III)-OH,W}^{\bullet+}\text{CcP+Fe(II)Cc+H}^{+} \longrightarrow \text{Fe(III),W}^{0}\text{CcP+Fe(III)Cc+H}_2\text{O}$$

Scheme 2.1: Proposed mechanism of WT CcP:WT Cc reaction upon initiation of reaction with H_2O_2.

peroxide oxidizes CcP to Compound I after which the ferryl species abstracts an electron from neighboring Trp191. Two equivalents of reduced Cc sequentially bind to CcP and proceed to reduce the peroxidase back to the ferric state through the $Trp191^{+\bullet}$ hopping site. In our previous studies, we found that replacement of Trp191 with tyrosine does not elicit any major structural alterations (PDB 5CIH), but significantly curtails $Cc(Fe^{2+})$ oxidation in a manner similar to that seen by replacing Trp191 with redox-inactive phenylalanine [21, 25]. The inactivity of the W191Y variant suggests that the tyrosyl radical ($Y^{\bullet}$) rapidly oxidizes an equivalent of $Cc(Fe^{2+})$ but either reoxidation of the tyrosyl by the ferryl is hindered (rate-limiting step 3; Scheme 2.1) or the potential of $Y^{\bullet}$ is too low to oxidize $Cc(Fe^{2+})$ at appreciable rates (rate-limiting step 2; Scheme 2.1) [26].

Proteins dependent on an active tyrosine hopping site typically employ an adjacent basic residue to facilitate PCET [8, 14], with studies reporting lack of activity once the base is removed [9, 27–29]. However, to our knowledge, the effects of coordinating bases on tyrosyl

reduction potential and reorganization energies in a modified protein system have not been explored extensively. Herein, we attempt to recover the activity of W191Y CcP to WT levels through substitution of hopping sites with higher potential non-natural amino acids and by the addition of coordinating bases. Kinetics experiments and spectroscopy provide a means to establish bounds on the electron transfer parameters in this system.

2.3 Results

2.3.1 Increasing Cc^{2+} oxidation activity of W191Y mutants

We hypothesized that the redox potential of $Y^{\bullet}$ is too low to accelerate long range electron transfer between Cc(Fe^{2+}) and CcP. To improve activity and probe the electron transfer mechanism, variant proteins were designed to raise the tyrosine reduction potential and reduce the possibility of radical migration from the 191 hole-hopping site.

Tyrosine and tryptophan residues with a redox potentials of $\sim 0.6 - 1.4$ V at pH 6 [9, 30] can be readily oxidized in CcP in the presence of peroxide [31]. Electron holes can thus delocalize by migrating to other redox-active residues. As the reduction of the tyrosyl intermediate by Cc(Fe^{2+}) is slow in W191Y, nearby tyrosine and tryptophan residues may compete as reductants for $Y191^{\bullet}$. To address this possibility, four adjacent tyrosine residues (187, 203, 229, and 236) that are each $\sim$10 Å from residue 191 were substituted with redox-inactive phenylalanine residues (W191Y-IV) to inhibit hole migration from Tyr191 (Figure 2.1).

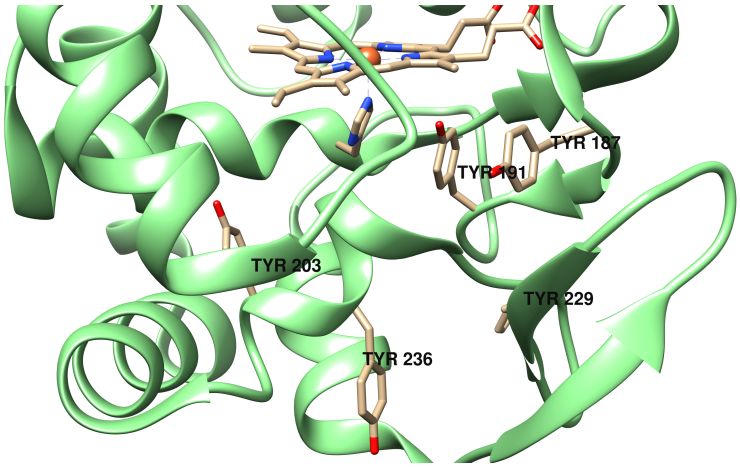

Figure 2.1: Tyrosine side chains within 10 Å of Tyr191 in W191Y CcP (PDB: 5CIH). Figure was prepared with Chimera [32].

Tyrosyl radical formation in solution typically results in the neutral deprotonated radical [9, 30]. Due to the low pK_a of the tyrosine radical cation, tyrosine residues coordinated to an adjacent proton acceptor, such as His, Asp, or Glu, have a higher propensity for a proton-coupled electron transfer (PCET) mechanism, as this environment provides a general base to encourage deprotonation and a resulting acid group to stabilize the radical [9, 14]. Thus, to localize a proton beside Y191 and potentially raise the redox potential of the tyrosyl radical, Leu232 was replaced with either His or Glu (W191Y:L232H and W191Y:L232E, respectively). An alternative approach to tune the redox potential of site 191 involved incorporation of non-natural fluorotyrosine residues. 2,3,5-trifluorotyrosine was synthesized by tyrosine phenol lyase, purified, and incorporated using an E3 aminoacyl-tRNA synthetase to replace the intermediate hopping site tyrosine [33, 34]. Further mutagenesis in these protein variants were conducted by replacing the four adjacent tyrosine residues with phenylalanine residues (W191Y-IV:L232E and W191(2,3,5)F_3Y-IV).

2.3.2 Cc(Fe^{2+}) oxidation rates in single/multiple turnovers

We employed single turnover reactions to assess the reactivity of CcP in the presence of two equivalents of Cc(Fe^{2+}) and peroxide. The activity of CcP was indirectly determined by monitoring the rate of Cc(Fe^{2+}) oxidation at the heme Q bands ($Abs_{550\ nm\ -\ 540\ nm}$ (baseline)) and changes in the CcP ferryl species ($Abs_{434\ nm}$; Cc Fe^{2+}/Fe^{3+} isosbestic point). Cc oxidation traces were fit with monoexponential curves after removal of the first five seconds where concentrations were in flux. WT CcP unsurprisingly exhibits the fastest oxidation of Cc(Fe^{2+}), and the resulting Compound I is highly stable, as observed when reacting only CcP with two equivalents of H_2O_2. Spectral changes at 562 nm corresponding to the Q band of CcP(Fe^{4+}=O) illustrate the steady persistence of CcP(Fe^{4+}=O) (Supplemental Figure 2.9c), with an expected half-life of $\sim$ 4.2 hrs at 23 °C [24, 35, 36].

The tyrosine CcP variants are slow to oxidize Cc in comparison to WT and many have similar rates as the inactive variant W191G (Figure 2.2a). Surprisingly, replacement of Tyr191 with a hotter oxidant (2,3,5-trifluorotyrosine) does not significantly accelerate the electron transfer rate, despite a $\sim$ 200 mV higher reduction potential for 2,3,5-trifluorotyrosine [33]. Although, addition of a His residue capable of coordinating to Tyr191 causes little change to the behavior of CcP at pH 6, a coordinating Glu yields similar Cc oxidation characteristics as WT CcP. The rate of Cc oxidation for both His and Glu variants also exhibits a pH dependency not observed in WT, with maximal rate constants at pH 7 and 6, respectively (Supplemental Table 2.4). Further modifications by removing four nearby tyrosine residues (W191Y-IV, W191Y-IV:L232E, W191(2,3,5)F_3Y-IV) result in similarly slow Cc oxidation traces compared to the parent (Figure 2.1). Interestingly, the Cc oxidation rate of W191Y-IV:L232E is much lower than W191Y:L232E and signify that these Phe variants perturb CcP activity.

We also tested the variants under multiple turnover conditions, in which one equivalent of

CcP was reacted with 30 equivalents of Cc(Fe^{2+}) and 10 equivalents of H_2O_2 (Supplemental Figure 2.9d). Of the five variants, WT CcP is the fastest at reacting with Cc(Fe^{2+}) and has a transient Compound I signal at $Abs_{434\ nm}$. In contrast, W191Y exhibits a slow decay at 550 nm (Cc) and a long-lived 434 nm signal that gradually increases over the time course of Cc(Fe^{2+}) oxidation; W191(2,3,5)F_3Y is barely two-fold faster than W191Y. The behavior of W191Y is reminiscent of that of inactive W191F CcP, where the ferryl species appear to react directly with the peroxide. Addition of a coordinating His residue (W191Y:L232H) converts the typical monoexponential Cc oxidation behavior to a biexponential decay at pH 6, with the slower phase becoming evident after approximately 30 seconds. Lowering the pH to 5 results in similar kinetics as at pH 6, while conducting the reaction at pH 7 converts Cc oxidation behavior into a monoexponential decay and increases the rate constant by nearly three-fold (Supplemental Figure 2.9d). Replacement of residue 232 with Glu (W191Y:L232E) gives the fastest reactivity of all of the W191Y-type CcPs and increases the Cc oxidation rate to just half that of WT CcP. Compound I build up and decay is markedly faster than W191Y (Supplemental Table 2.6) and approaches that of WT CcP. As in the single turnover experiments, both His and Glu variants exhibit diminished rates at higher pH (Supplemental Figure 2.10).

Titrations of peroxide into these systems (data not shown) confirm that the rate of Cc(Fe^{2+}) oxidation is not affected by repeated exposures to peroxide as long as excess Cc(Fe^{2+}) is available. In the absence of Cc(Fe^{2+}), W191Y-type Compound I shows a decrease in stability over time, gradually dissipating over the course of 20 minutes, with W191Y:L232E and W191Y:L232H rapidly reverting to ferric CcP within minutes (Supplemental Figure 2.9c). W191Y(2,3,5)F_3Y has the longest lived ferryl species, persisting for five minutes before sharply declining to the ferric state. Exposure to peroxide without Cc also generates higher order oligomers that is thought to render the protein inactive (Supplemental Figure 2.8). In the presence of Cc, CcP oxidation is negligible. Proteomics results of W191Y

CcP:Cc complex undergoing a two-minute single turnover reaction with two equivalents of peroxide depict minor changes in the percentage of oxidized Tyr and Trp in CcP after the reaction (data not shown).

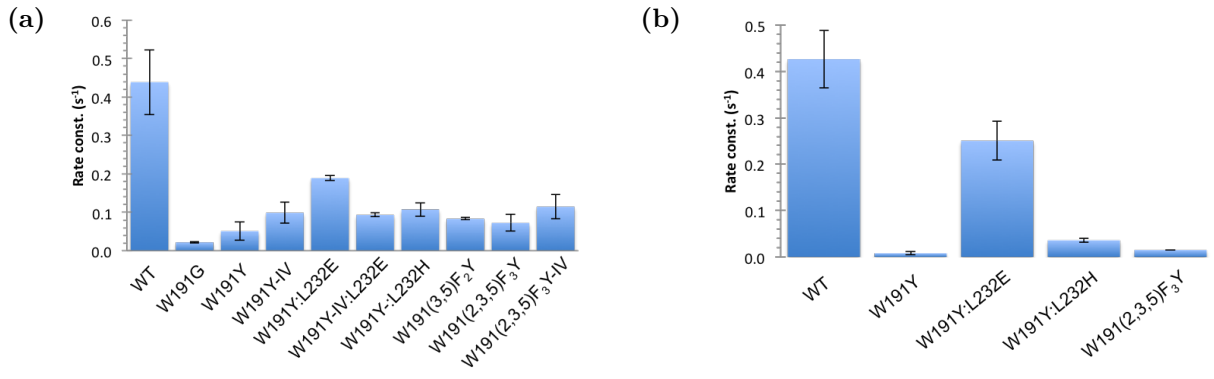

Figure 2.2: (a) Single turnover rate constants were obtained by reacting 1 μM CcP : 2 μM Cc(Fe^{2+} with 2 μM H_2O_2 in 100 mM KP_i, pH 6. Cc oxidation traces ($Abs_{550nm\ -\ 540\ nm}$) were fit to monoexponential curves after omitting data points in the first five seconds. (b) Rate constants of multiple turnover reactions were acquired with 1 μM CcP : 30 μM Cc : 10 μM H_2O_2 in 100 mM KP_i, pH 6, except for W191Y:L232H, which was in pH 7 buffer. Rate constants were determined by fitting oxidation decays (550 nm − 540 nm) with monoexponential functions.

2.3.3 Evidence of low tyrosyl radical redox potential

To monitor the progress of $Y^{\bullet}$ over time, we implemented rapid freeze quench (RFQ) experiments by flash freezing samples at time points over the course of a single turnover reaction. All X-band cw-ESR spectra were acquired at 12 K and quantified by subtracting a linear baseline, followed by numerical integration. Owing to variations in sample preparation and packing within ESR tubes, absorption signals were normalized to the integrated intensity of an internal standard: Er^{3+} chelated by diethylenetriaminepentaacetic acid (DTPA). This unreactive lanthanide-based species has a well-resolved, sharp signal at $g = 11.77$ and few features elsewhere. Samples were collected in repetition, signals integrated and averaged,

and fit to a sequential kinetics equation (2.1).

$$f(x) = A_0 \frac{k_1}{k_2 - k_1}(e^{-k_1 * x} - e^{-k_2 * x}) \tag{2.1}$$

which assumes that the initial Tyr191 radical is rapidly quenched by pre-bound Cc(Fe^{2+}) at rates that can not be resolved and the second oxidizing equivalent gradually drifts to adjacent redox-active residues. Data were further fit to kinetics traces generated by Kinetiscope [37]. The reaction scheme and parameters are delineated in Supplemental Table 2.2. As a control, W191Y CcP in the absence of Cc was similarly reacted with peroxide. Signals normalized to the internal standard were invariant over the first 30 seconds, indicating that Compound I radical formation is rapid and unresolved over this timescale (data not shown).

Figure 2.3a illustrates the slow quenching kinetics of the W191Y tyrosyl radical by Cc(Fe^{2+}). After the first equivalent of Cc has been oxidized, $Y^{\bullet}$ signal begins to rise gradually and exhibits maximal accumulation at approximately 15 seconds, followed by a slow decay afterwards. The tyrosyl quenching behavior by RFQ coincides with UV-vis kinetics under identical conditions, which demonstrate a similar build up of the ferryl species at 434 nm (Supplemental Figure 2.9b). W191Y:L232E illustrates a more gradual rise in $Y^{\bullet}$ (Figure 2.3b) and the signal maxes at approximately 30 seconds, but is maintained for the duration of the reaction. This variant may be more reactive than the parent W191Y to a second equivalent of peroxide, allowing radicals to continue building up as Cc(Fe^{2+}) reacts with Compound I.

Nevertheless, co-occurrence of both a tyrosyl radical and the ferryl species after the initial reduction in both W191Y and W191Y:L232E verifies that ferric CcP abstracts an electron from nearby Tyr191 in order to form Compound I. RFQ studies also provide positive identification of the radical species as they form over the course of the reaction. ESR signals are higher in intensity than baseline (i.e. the signal of inactive W191G CcP) and line shapes are similar to those of photogenerated tyrosyls in solution [26], thus confirming the presence

of the tyrosyl radical. As no other tyrosine residues are within van der Waals distance of the heme cofactor, residue 191 likely remains the primary hopping site for these W191Y variants.

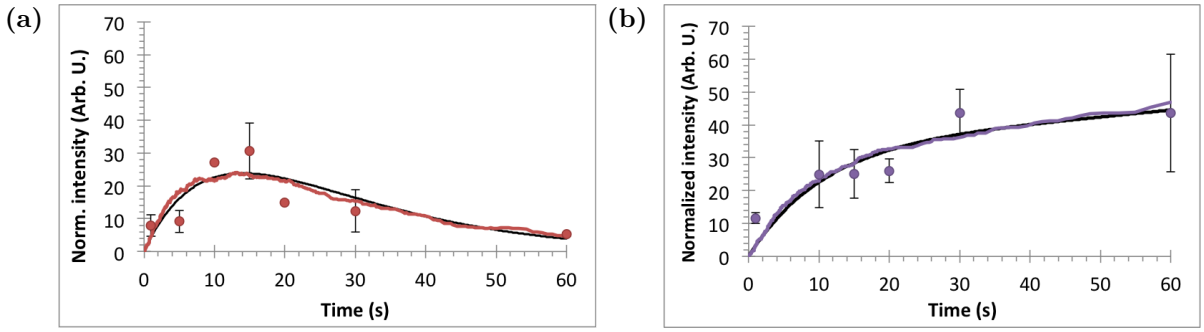

Figure 2.3: Rapid freeze quench X-band ESR tyrosyl signals were integrated and normalized to an Er^{3+} internal standard signal. $Y191^{\bullet}$ was generated under single turnover conditions by reacting 0.15 mM CcP with 0.3 mM H_2O_2 and quenched by 0.3 mM $Cc(Fe^{2+})$. Integrated, averaged, and normalized signals were fit with a sequential kinetics function (black line) and simulated by chemical kinetics models (red and purple lines). Comparison between (a) W191Y and (b) W191Y:L232E demonstrate differences in radical formation rates, which are reflected in the development of the ferryl species by UV-vis kinetics (Supplemental Figure 2.9b).

2.3.4 Crystal structure of W191Y:L232E

To elucidate structural effects of the L232E mutant and better define the basic side chain interaction with Tyr191, the W191Y:L232E : WT Cc complex was crystallized and the structure determined to 2.8 Å resolution. The structure was determined by molecular replacement using the parent W191Y : WT Cc structure as the probe. Structural comparison between W191Y (PDB 5CIH; Figure 2.4a) and W191Y:L232E (Figure 2.4b) reveals an identical interface between CcP and Cc in the two structures, along with similar placements of side chains. There is a noticeable displacement of Tyr191 by an RMSD of 1.04 Å in W191Y:L232E, yet, the heme to Tyr191 distance is not altered remarkably (6.90 − 7.20 Å in W191Y:L232E versus 6.53 − 6.74 Å in W191Y) nor is the distance between the heme

iron atom in Cc and Tyr191 changed significantly (21.53 − 21.79 Å in W191Y:L232E versus 20.91 − 21.03 Å in W191Y). Notably, the carboxyl group of Glu232 and the hydroxyl oxygen of Tyr191 are separated by 3.2 Å and are bridged by electron density at the 1σ level in the $2F_o - F_c$ electron density map. Presence of a hydrogen bond is not observed in the second CcP:Cc complex; no electron density exists between Glu232 and Tyr191 in this second complex contained within the asymmetric unit (ASU) though the distance between the carboxylic moiety and phenolic hydroxyl group is similar to that in the first CcP:Cc complex (Figure 2.4). Regardless, replacement of Leu232 with Glu perturbs the hopping site and encourages hydrogen bonding interactions between Tyr191 and Glu232, as indicated by the shift in Tyr191 position and direct interaction with the Glu carboxylate in one of the two CcP:Cc complexes.

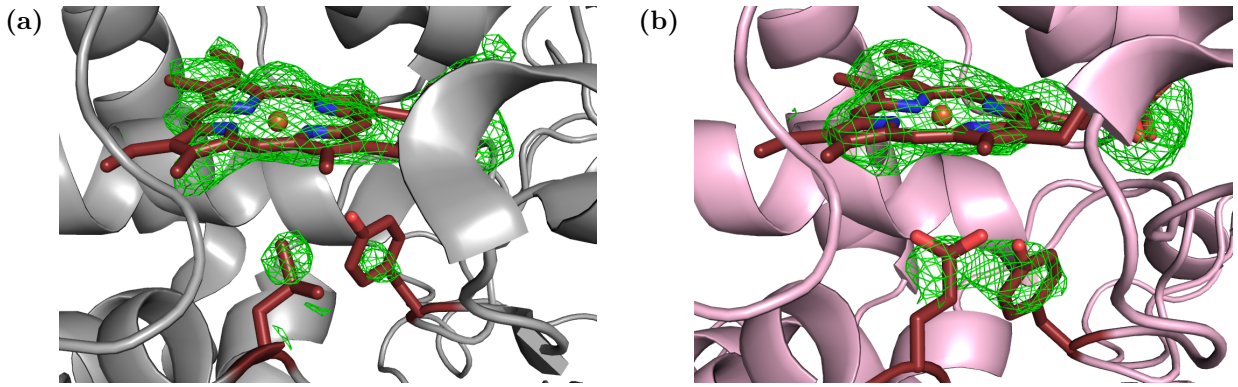

Figure 2.4: $F_o - F_c$ difference maps of (a) W191Y CcP and (b) W191Y:L232E CcP were calculated by omitting the heme center and residues 191 and 232. Maps are displayed at a contour level of 2.5σ. Substitution with Glu232 results in a 1.04 Å displacement of Tyr191 and electron density between the Glu232 and Tyr191 side chains in one of the complexes.

2.3.5 ESR characterization of Tyr191 radical species

Coordination to the hydroxyl proton of Tyr191 by the Glu residue evidently alters its ability to facilitate electron transfer from Cc whereas solely increasing the reduction potential of residue 191 with a fluorotyrosine has a lesser effect on activity. These effects on the tyrosyl

	W191Y:L232E
Data Collection	
space group	$P2_1$
a, b, c (Å)	45.80, 112.07,88.33
β (deg)	104.64
no. of unique reflections	19848
resolution (Å)[a]	$2.8/2.9 - 2.8$
completeness (%)	82.52/45.66
I/σ	8.6/3.9
R_{merge}[b]	0.184
Refinement	
R_{work}[c] (%)	25.8/39.5
R_{free}[c] (%)	30.7/47.2
no. of atoms	6527
no. of water molecules	5
mean B value (Å^2)	72.97
B value (waters) (Å^2)	60.41
B value (ligand) (Å^2)	77.40
rmsd for bonds (Å)	0.006
rmsd for angles (deg)	0.98
ϕ/ψ stats (%)	
most favored	93.89
outliers	0.13

Table 2.1: Diffraction Data Collection and Structure Refinement Statistics

[a]Highest-resolution range for compiling statistics follows slash.
[b]$R_{merge} = (\Sigma_i \Sigma_j |I_j - \langle I_i \rangle I)/[\Sigma_i(\Sigma_j I_j)]$, where I_j is the intensity of the j^{th} observation of reflection i, $\langle I_j \rangle$ is the average intensity of reflection i, and N_i is the redundancy of reflection i.
[c]R_{work} or $R_{free} = (\Sigma |F_{obs} - F_{calc}|)/(\Sigma |F_{obs}|)$.

moiety were examined by X-band cw-ESR.

X-band cw-ESR spectra of the fluorotyrosyl and tyrosyl radicals in CcP demonstrate line shape broadening (Figure 2.5a) that is likely due to an increase in anisotropy and hyperfine interactions from the fluorine moieties, though these effects are not as prominent as observed for free fluorotyrosyls in aqueous solution [33, 38]. ESR samples collected 30 s after reacting CcP with two equivalents of H_2O_2 (data not shown) show no spectral differences compared to those collected several minutes after Compound I formation, confirming that the fluorotyrosyl species are not gradually oxidizing nearby amino acids.

Addition of a coordinating His residue (W191Y:L232H) at pH 6 resulted in mild line broadening effects and minor differences that can be attributed to the Tyr191 interaction between either the δ or ϵ His nitrogens and the tyrosine hydroxyl proton. Raising the pH to 7.5 causes His to deprotonate to the neutral imidazole moiety and results in a broadened line shape for $Y^{\bullet}$. These spectral features are similar to those observed with Glu (W191Y:L232E) at pH 6. The change in line shape and hyperfine interactions signify a different coupling environment of the tyrosyl radical in the presence of these coordinating bases. The coupling strength of the basic proton to Tyr191 is dependent on the pK_a of the basic side chains. [Given the much lower pK_a of the glutamate side chains (4.4) compared to either of the pK_a's for histidine (His-δ: 6.5 and His-ϵ: 7.1), the glutamic acid proton likely has a stronger interaction with the tyrosyl radical at pH 6[39]].

Interestingly, when the four adjacent tyrosine residues are replaced, the signal intensity of the organic radical was similar to that of inactive W191G with peroxide (Figure 2.5b). Of the four substituted tyrosine residues, solvent-exposed Tyr236 may contribute some secondary radical species to the major Tyr191 signal [40, 41], and thus, the Phe variants were expected to have a slightly lower intensity than the parent. Instead, the signal amplitudes were barely one tenth of the parent's, which implies that these variants are unable to generate Compound

I in appreciable amounts.

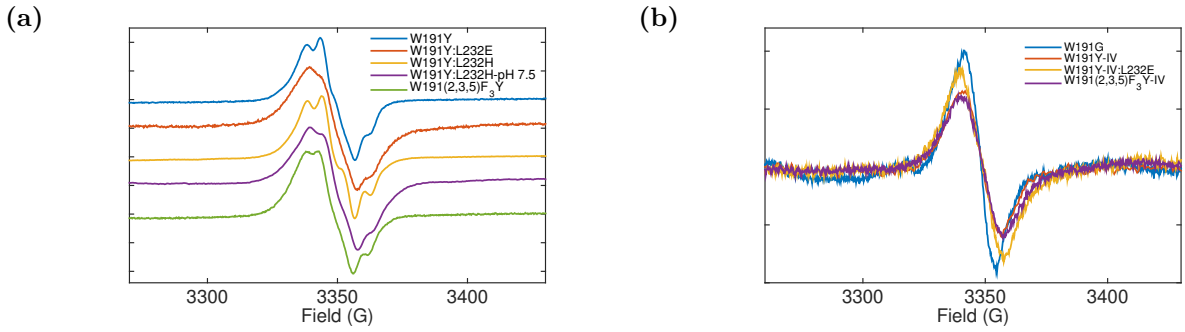

Figure 2.5: (a) X-band cw-ESR spectra of Compound I species acquired at 12 K. All variants were acquired in pH 6 buffer, except for where indicated. W191Y:L232H at pH 7.5 was acquired with 4 G modulation, and all others were collected with $1.5-2$ G modulation. (b) Replacement of four adjacent tyrosine with phenylalanine residues results in similar line shapes and intensities as inactive W191G CcP.

2.3.6 D_2O Effects on Protonation of Tyr191

Hydrogen bonding in W191Y:L232E/H CcP appears to boost Cc oxidation activity and points to the involvement of a PCET mechanism, which may manifest in a solvent isotope effect. Overnight incubation of W191Y CcP : Cc in a deuterium-rich phosphate buffer resulted in minor changes to the Cc(Fe^{2+}) oxidation rate ($k_H/k_D \simeq 1.2-1.4$; Supplemental Table 2.5), but the differences in rate constants between deuterated and protonated buffers are not significant ($p = 0.80$; $N = 4$). W191Y:L232E CcP : Cc shows a slightly larger solvent isotope effect. When reacted with peroxide, the D_2O-treated complex had a slower rate ($k_{obs}= 0.09 \pm 0.04$ s^{-1}) than its counterpart in a H_2O buffer ($k_{obs}= 0.166 \pm 0.007$ s^{-1}); thus, $k_H/k_D \simeq 1.7$, and the differences between rate constants are statistically significant ($p = 4.6 \times 10^{-7}$; $N = 12$). Moreover, X-band cw-ESR measurements of D_2O-treated CcP reacted with two equivalents of H_2O_2 show evidence of increased hyperfine splitting and narrowing of line shapes. W191Y:L232E gave the most prominent effects, evincing that deuterium exchange does occur on this time scale (∼12 hr) and hydrogen bonding between

Glu232 and Tyr191 is significant in the formation of Compound I.

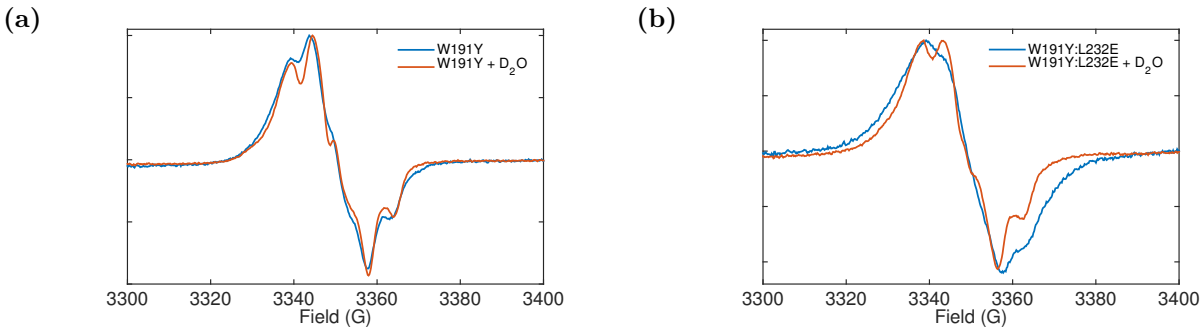

Figure 2.6: cw-ESR spectra of D_2O-treated (a) W191Y Compound I and (b) W191Y:L232E Compound I. Hyperfine splittings are better resolved and line shapes are narrower in comparison to Compound I in water (blue traces).

2.4 Discussion

Previous studies show W191Y CcP of *Saccharomyces cerevisiae* is unable to support rapid electron transfer activity when complexed to Cc and exposed to peroxide [26]. Here we attempt to recover the activity of this variant through use of a higher reduction potential hopping site and coordination of a basic side chain to the phenolic proton.

2.4.1 Identifying the source of Tyr191 inactivity

W191Y inactivity is evident by spectroscopic methods. Under single turnover conditions, Cc is slow to oxidize and suggests Tyr191 is incapable of accelerating electron transfer to the heme center of CcP. W191Y CcP may additionally become irreversibly damaged by peroxide over the course of the reaction. In general, W191Y CcP in the absence of Cc oligomerizes in minutes when exposed to peroxide (Supplemental Figure 2.8) and is known to oxidize extensively [42]. Compound I formation is thought to initiate radical migration to the surface and subsequently form dityrosine crosslinks, particularly at the highly exposed

Tyr36, Tyr39, and Tyr42 residues that lie at the interface between CcP and Cc [42, 43]. Complex formation with Cc inhibits CcP oligomerization by blocking the accessibility of these tyrosine residues to other CcP molecules and may suppress irreversible oxidation of the residues, as supported by proteomics results (data not shown). Hence, we postulate that the sluggish nature of W191Y CcP-mediated Cc oxidation is a direct result of the inability of Tyr191 to maintain a high enough redox potential for rapid electron transfer. Consequentially, Cc oxidation occurs via a side reaction involving a direct reaction between the CcP ferryl species, peroxide, and Cc [25].

This alternate ferryl-based mechanism was further observed in multiple turnover methods, which involved 10 equivalents of peroxide and 30 equivalents of reduced Cc. Under these conditions, W191Y-mediated oxidation of Cc is slow and the major oxidizing species is thought to be the CcP ferryl species (Fe^{4+}=O;$P^{\bullet+}$) [26]. In the case of W191F, the steady rise of ferryl is caused by Compound I reacting with Cc and becoming replenished by peroxide, instead of CcP returning to the ferric state (Equation 2.2) [25].

$$\text{CcP}(\text{Fe}^{4+}\text{= O}) + \text{H}_2\text{O}_2 + \text{Cc}(\text{Fe}^{2+}) \longrightarrow \text{CcP}(\text{Fe}^{4+}\text{= O}) + \text{Cc}(\text{Fe}^{3+}) \qquad (2.2)$$

Rapid freeze quench X-band ESR spectroscopy confirms that the formation of W191Y Compound I ferryl state relies on abstraction of an electron from a neighboring tyrosine residue. W191Y CcP Compound I initiation by peroxide (without Cc) exhibits a prominent organic radical signal that steadily persists over the first 30 seconds, indicating that Compound I radical formation is rapid and undetectable on this timescale (data not shown). When $Cc(Fe^{2+})$ is included in the reaction mixture, there is an immediate quench in radical followed by its gradual accumulation. The low radical signal over the first five seconds is likely the tail end of $Y^{\bullet}$ reduction by the first electron supplied from pre-bound $Cc(Fe^{2+})$, which appears concomitantly with the early phase of Cc oxidation. Slow growth and decay of the radical signal happens during $Cc(Fe^{2+})$ oxidation and follows decay of the ferryl species

at $Abs_{434\ nm}$, as observed spectrophotometrically under similar single turnover conditions. Use of stochastic kinetics simulation software allowed us to generate a model that represents the experimental data reasonably well (Scheme 2.2; Figure 2.3) [37]. Our model indicates that slow radical migration to neighboring redox-active amino acids contributes to accumulation of the radical signal. Owing to similar reduction potentials between these amino acids and Tyr191, electron holes can facilely return to site 191 and proceed to react with $Cc(Fe^{2+})$. Quenching is however limited by the rate of $Cc(Fe^{3+})$ exchange with $Cc(Fe^{2+})$.

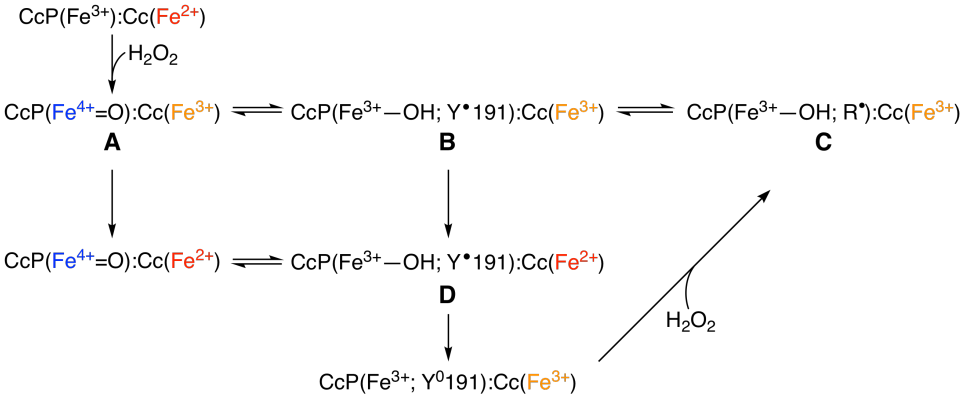

Scheme 2.2: Proposed mechanism of W191Y CcP:WT Cc reaction upon initiation of reaction with H_2O_2.

2.4.2 Tuning the hole-hopping site

The redox potential of residue 191 has a prominent effect on Cc oxidation. Replacing 191 with higher potential 3,5-difluorotyrosine (E° = 755 mV [33] compared to the deprotonated natural tyrosine Y^- E° = 680 mV [44]) results in Cc oxidation rates slower than with natural tyrosine (Supplemental Figure 2.9a). By comparison, increasing the redox potential of 191 with (2,3,5)-trifluorotyrosine (E° = 853 mV; [33]) augments the rate of Cc oxidation under multiple turnover conditions, but does not fully recover activity. The inability of these non-natural amino acids to recover function led us to consider the introduction of coordinating bases, specifically glutamate and histidine, which are known for their supporting roles in

tyrosine electron transfer pathways [9, 45–49]. Under typical experimental conditions (100 mM KP_i, pH 6), Glu is fully deprotonated and able to hydrogen bond to the phenolic proton of Tyr191, resulting in rapid activity with reduced Cc and similar behavior to WT CcP (Supplemental Figure 2.9d). To further prove that hydrogen bonding has a key effect on the increased activity, residue 232 was replaced with a histidine, which has fewer acidic protons than Glu. At pH 5 and 6, Cc oxidation rates mirrored that of the non-hydrogen-bonded Tyr191. Raising the pH to 7 showed rapid, monoexponential Cc oxidation behavior, but surprisingly, at pH 8, rates slowed significantly. Similarly, at pH 7 and 8, W191Y:L232E exhibited diminished Cc oxidation rates. Evidently, coordination of the tyrosine phenolic proton is highly effective for increasing the electron transfer rate from $Cc(Fe^{2+})$ to Tyr191, albeit higher pHs likely result in deprotonation of the hydrogen-bonded proton. Thus, the observed pH dependency reflects the pK_a of the base-coordinated tyrosyl complex.

Introduction of these mutations results in faster electron transfer between Tyr191 and Cc, but do they affect Tyr oxidation by the ferric heme of CcP? Owing to their concurrence, the rate of Tyr oxidation can be followed by tracking the formation of $CcP(Fe^{4+} = O)$ at 434 nm using spectrophotometric methods. The effects are clearest under multiple turnover reactions (Supplemental Figure 2.9d), where the rate of ferryl build up is fast when the Tyr phenolic proton is coordinated by a deprotonated basic side chain (W191Y:L232H/E). A proposed model suggests that base coordination causes the hydrogen-bonded proton to "rock" between the tyrosine and the base depending on the redox state of tyrosine [50, 51], effectively tuning the Tyr potential. Regardless of the variant, ferryl recycling still outcompetes its dissipation to the ferric state. The maxima of ferryl species accumulation coincides with the transition from fast to slow Cc oxidation kinetics. Long-lived ferryl species indicate that reaction of the ferryl with peroxide outcompetes its return to the ferric state by Cc (Equation 2.2). In the case of WT CcP, electron transfer is highly efficient and the ferryl state is transient. Hence, a majority of the electron transfer occurs between Trp191 and Cc. Similarly in W191Y:L232E,

reaction with Cc is significantly faster than the other W191Y variants, and the ferryl species are quickly consumed.

Further exploration of the mechanism by RFQ X-band ESR reveals not only a slow rise in the initial accumulation of the radical but also its continued development over the course of the reaction with Cc. Such behavior is indicative of radical migration from the 191 site to adjacent Tyr residues that can not be readily reduced by Cc. The initial rise in radical is similar to that of the parent W191Y, though we would expect faster radical migration with a hotter oxidant. This observation may indicate that deprotonation of the adjacent tyrosine residues limits their oxidation rate to some extent. Moreover, once radicals migrate to nearby amino acids, the rate of return to Tyr191 will depend on its relative potential. In the case of W191Y:L232E, the increased Tyr191 potential hinders return of the radical to the 191 position where it can then be reduced by Cc(Fe^{2+}). To account for the continued increase in radical signal, we can assume that either the second equivalent of the electron hole permanently migrates away into the recesses of CcP and stays unreduced, or the remaining equivalent of peroxide reacts with the regenerated CcP(Fe^{3+}); as both equivalents of reduced Cc are depleted, the resultant radicals remain unquenched.

2.4.3 Coordinating base effects on Tyr position and environment

Further analysis of base coordination with Tyr191 was accomplished by crystallization of the complex W191Y:L232E and WT Cc. The difference maps calculated after omission of the heme center and residues 191 and 232 clearly show interaction between the carboxylic moiety of the glutamate side chain and the phenolic proton of Tyr191 in one of the two CcP:Cc complexes in the ASU. The 1.04 Å shift of the Tyr191 position relative to Tyr191 confirms that interaction with Glu contributes to the differences in reactivity observed by single and multiple turnover reactions. Other than dissimilarities in the vicinity of 191, few

differences are found between the two mutants and the interface between CcP and Cc is preserved, which is essential for long distance electron transfer between the two proteins. Residue substitution also has little impact on the active site of the heme center, where the positions of Arg48, Trp51, and His52 are important for peroxide binding and Compound I generation [21, 52–56]. Crystallization of W191Y:L232H was attempted but has not yet yielded any diffraction quality crystals.

Compound I formation in W191Y variants results in characteristic tyrosine radical line shapes by X-band cw-ESR. Hyperfine splittings are identical for all variants except for those with a coordinating base, of which Tyr191 likely experiences a different microenvironment [57–62]. W191Y:L232E exhibits a broad line shape that is thought to result from rotation of the methylene hydrogens (H_β and $H_{\beta 2}$) in conjunction with the phenolic ring, which alters the magnitude of the coupling [57]. Hyperconjugation between the C−H σ bonds of the methylene protons and the phenolic π orbitals increases spin density on H_β and $H_{\beta 2}$, the magnitude of which is dependent upon the dihedral angles between the methylene C−H σ bonds and the plane of the phenolic ring [59, 63]. Simulations by DeGray and colleagues illustrate widening of the singlet features as the dihedral angles between the H_β protons and the axis of the phenol ring are displaced by just 12.5° [63]. However, these changes in dihedral angle are not reflected in the crystal structures of W191Y and W191Y:L232E. Measurements of the dihedral angles of the side chains using Avogadro are relatively similar between the two structures [64, 65]. This is unsurprising as the resolutions are not high enough to precisely place the tyrosine side chain in the electron density maps nor can we assume these dihedral angles are identical to those in the solution state. Yet, we can exploit the higher pK_a protons of His232 in W191Y:L232H to demonstrate the effects of hydrogen bonding on the line shape of Tyr191. At low pH's, the cw-ESR spectrum of W191Y:L232H resembles that of the parent W191Y CcP without a hydrogen-bonded phenolic proton. At pH's greater than 7, the spectrum begins to broaden and is remarkably similar to that of

W191Y:L232E.

Replacement with heavy water buffer sharpens the cw-ESR spectra and allows us to more clearly identify hyperfine coupling effects. Notably, W191Y:L232E in deuterated buffer has a similar ESR signal to other W191Y-type radicals (narrow singlet) and all broadening effects have vanished. We postulate that under these conditions, the hydrogen bond between Tyr and Glu is disrupted and the environment about Tyr191 is similar to that of the parent W191Y CcP. Consequently, W191Y:L232E CcP samples in deuterated buffer have Cc oxidation rate constants approaching that of W191Y in water-based buffer (Supplemental Table 2.5). The sensitivity of the Cc oxidation rates to deuterium exchange suggests that Tyr191 is likely dependent on proton exchange with the bulk solvent in the event of electron transfer.

2.4.4 Mechanistic implications in W191Y:L232E/H

Two major differences arise from the kinetics model fit of the RFQ data between W191Y and W191Y:L232E. The first involves back electron transfer from Tyr191 to nearby redox-active amino acids. Compared to the parent, W191Y:L232E Tyr191 exhibits an overall slower rate of electron transfer to these neighboring side chain radicals to regenerate the tyrosyl 191 electron hole. Secondly, the organic radical signal intensity at later time points is remarkable, illustrating that the radical in W191Y:L232E continues to develop after complete oxidation of Cc, whereas W191Y shows signs of decreasing radical levels as it continues to slowly be reduced by Cc. These rudimentary kinetics parameters will serve to approximate the change in reduction potential owing to coordination of the Tyr191 phenolic proton with a basic side chain. We begin by assuming the simplest case in which proton and electron transfer are not kinetically concerted. Most proposed models describing PCET reactions require intrinsic-barrier parameters in addition to the reorganization energy, providing a more adequate description of proton transfer [1]; however, these parameters are not easily

obtained experimentally [66, 67], so we will investigate whether an analysis using Marcus theory alone is capable of rationalizing the results.

The semiclassical Marcus equation is as follows

$$k = k_{\max} \times \exp\left[-\frac{(\Delta G^\circ + \lambda)^2}{4\lambda k_B T}\right]$$

where k is the observed rate constant of electron transfer, $k_{\max}$ is the pre-exponential factor $2\pi/\hbar\langle H_{\mathrm{DA}}^2\rangle(4\pi\lambda k_B T)^{-1/2}$, λ is the reorganization energy, and ΔG° is the Gibbs free energy change for the electron transfer reaction [68]. From the kinetics model of RFQ data, we can approximate the change in redox potential anticipated by the introduction of the glutamate side chain. Reorganization energies are assumed to be ~ 0.5 eV for most organic molecules [66, 69]) and 0.9 eV for ET from a tyrosinate anion [70]. However, use of the Born model describing a spherical particle in a classical dielectric continuum predicts a reorganization energy of approximately 0.72 eV [71, 72]

$$\lambda_{\mathrm{sol}} = (\Delta e)^2 \left(\frac{1}{2r_A} + \frac{1}{2r_B} - \frac{1}{R}\right)\left(\frac{1}{\epsilon_{\mathrm{op}}} - \frac{1}{\epsilon_{\mathrm{st}}}\right)$$

where ϵ_{op} and ϵ_{st} are the optical and static dielectric constants, respectively, r_{A} and r_{B} are the radii of the donor/acceptor, and R is the distance between the two molecules. Here, we assume $\epsilon_{\mathrm{op}} = n^2 = (1.6)^2$ for the refractive index of a protein[73], $\epsilon_{\mathrm{st}} = 4$, $r_{\mathrm{A}} = r_{\mathrm{B}} = 3.5$ Å for phenols [74], and $R = 10$ Å as the approximate distance between Tyr191 and an adjacent Tyr. At this reorganization energy, we can estimate the difference in reduction potential $\Delta\Delta G^\circ$ assuming $\Delta G^\circ_{\mathrm{ex}} \sim 0$ given facile electron transfer between Tyr191 and an adjacent tyrosine, using the relation

$$4k_{\mathrm{B}}T\ln\left(\frac{k_1}{k_2}\right) = \frac{-\left(\Delta G^\circ_{\mathrm{ex}} + \lambda_1\right)^2}{\lambda_1} + \frac{\left(\Delta G^\circ_{\mathrm{ex;\ L232E}} + \lambda_2\right)^2}{\lambda_2}$$

where $\Delta G^\circ_{\mathrm{ex}} = E^\circ(\mathrm{Y191}) - E^\circ(\mathrm{Y}^\bullet_{\mathrm{adj}})$ and $\Delta G^\circ_{\mathrm{ex;\ L232E}} = E^\circ(\mathrm{Y191{:}L232E}) - E^\circ(\mathrm{Y}^\bullet_{\mathrm{adj}})$. As-

suming the $k_{\max}$ and λ's are sufficiently similar between variants

$$\begin{aligned}\Delta\Delta G^{\circ} &= (E^{\circ}(\text{W191Y:L232E}) - E^{\circ}(\text{W191YCcP})) \\ &= \Delta G^{\circ}_{\text{ex; L232E}} - \Delta G^{\circ}_{\text{ex}} \\ &= \left(\pm\sqrt{4\lambda k_{\text{B}}T\ln(k_1/k_2) + (\Delta G - \Delta G^{\circ}_{\text{ex}} + \lambda)^2} \mp \lambda\right) - \Delta G^{\circ}_{\text{ex}}\end{aligned}$$

Given the 45-fold slower back electron transfer rate in the W191Y:L232E variant (relative to the parent), figure 2.7a predicts a minimum difference in reduction potentials of 0.17 eV. Fixing $\Delta\Delta G^{\circ}$ at 0.17 eV, we find the reorganization energies to be quite similar in the range of $\Delta G^{\circ}_{\text{ex}} \sim 0$.

If we assume $\Delta\Delta G^{\circ}$ between these mutants is invariant regardless of the reaction, we can utilize single turnover rate constants to approximate the redox potential of the Y$^{\bullet}$191 in CcP Compound I. Figure 2.7c shows that the only parameters capable of generating a similar redox potential difference are $\Delta G^{\circ}_1 = E^{\circ}(\text{Cc}) - E^{\circ}(\text{W191Y}) \approx -130$ meV and $\lambda_{\text{ave}} \approx 360$ meV, which would then imply that $E^{\circ}(\text{W191Y}) \approx 420$ meV. Likewise, if we set $-\Delta\Delta G^{\circ}$ to 0.17 eV, λ's appear to be fairly similar between the variants. Curiously, electron transfer between CcP and Cc has a calculated reorganization energy of $\lambda = 0.7$ eV, so it is likely our models are too simplistic for this system [75, 76]; however, even at this higher reorganization energy value, $-\Delta\Delta G^{\circ} = 0.34$ eV and $\Delta G^{\circ}_1 = -0.38$ eV, which would give an upper bound of W191Y CcP reduction potential of 670 meV. Critically, our models indicate that Compound I of W191Y must have a lower reduction potential than that of WT (~ 1 V).

Overall, our models and experimental data show that the reduction and oxidation of W191Y and W191Y:L232E must reside in the normal Marcus regime ($|\Delta G^{\circ}_1| < \lambda$), unlike in the WT CcP:Cc system [77]. Indeed, when using a higher reduction potential Cc (Y48K; 407 mV; [78]), the rate of Cc oxidation by W191Y:L232E drops from $k_{\text{obs}} = 0.189 \pm 0.006$ to 0.156 ± 0.005 s^{-1} ($p = 4.44 \times 10^{-5}$; $N = 4$ and 5, respectively), demonstrating that the rates we observe are sensitive to ΔG°. This suggests that the increase in electron transfer

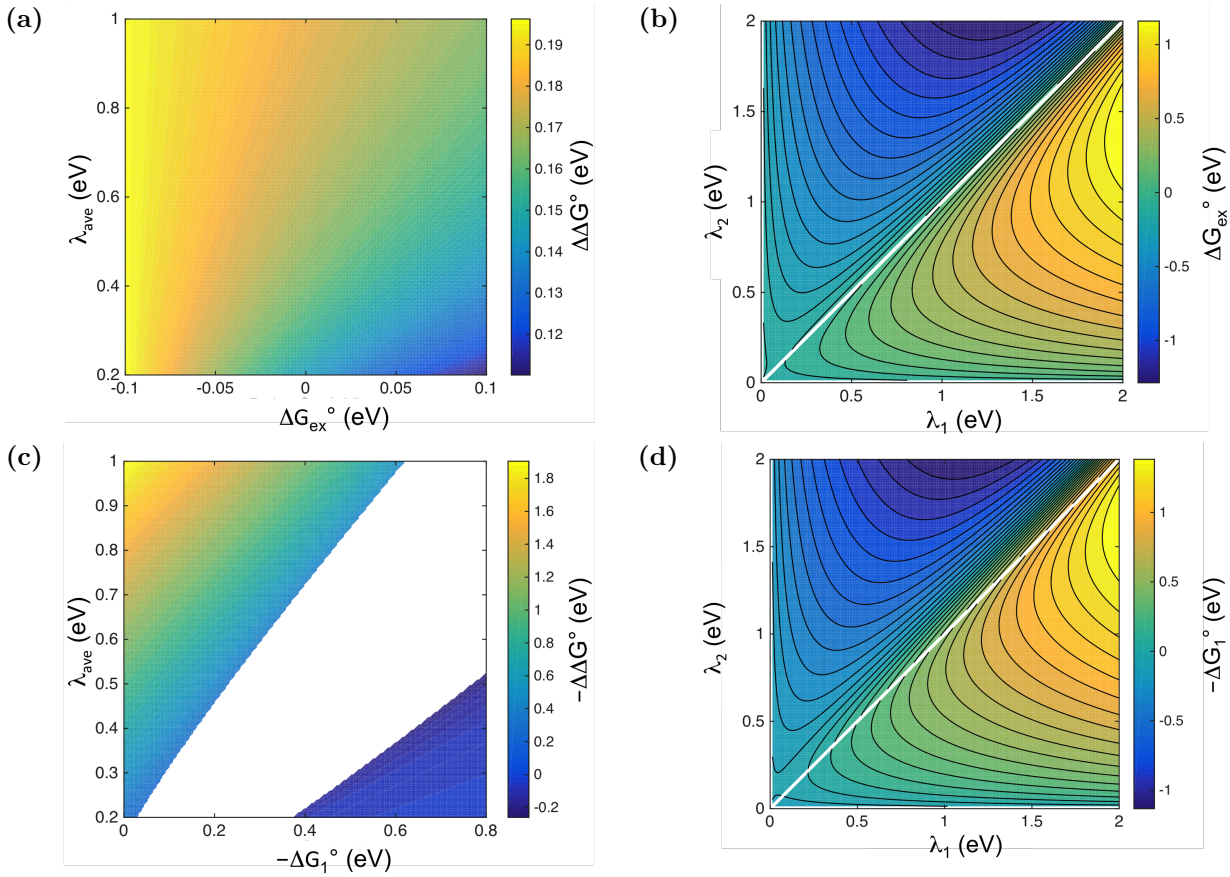

Figure 2.7: Heat maps relating reduction potential, reorganization energies, and change in driving force. (a−b) Self-exchange reactions between Tyr$^{\bullet}$191 and neighboring redox active amino acids. Rate constants for reoxidation of Tyr191 are acquired from kinetics modeling of RFQ data ($k_1 = 0.045$ s^{-1} and $k_2 = 0.001$ s^{-1} for W191Y and W191Y:L232E CcP, respectively). $\Delta G^{\circ}_{ex} = E^{\circ}(\text{Y191}) - E^{\circ}(\text{Y}^{\bullet}_{adj})$. For W191Y, ΔG°_{ex} is assumed to be close to 0 eV given similar forward and reverse electron transfer rate constants. $\Delta\Delta G^{\circ} = E^{\circ}(\text{W191Y:L232E}) - E^{\circ}(\text{W191Y})$ is approximately 170 meV at $\lambda = 0.7$ eV and $\Delta G^{\circ}_{ex} = 0$ from plot (a). Setting $\Delta\Delta G^{\circ}$ to 170 meV, plot (b) demonstrates the identical reorganization energies corresponding to $\Delta G^{\circ}_{ex} = 0$ between variants. (c−d) Cc oxidation by CcP under single turnover reaction conditions. Rate constants used for derivations are $k_1 = 0.05$ s^{-1} and $k_2 = 0.2$ s^{-1} for W191Y and W191Y:L232E CcP, respectively. $\Delta G^{\circ}_1 = E^{\circ}(\text{Cc}) - E^{\circ}(\text{W191Y CcP})$, and $-\Delta\Delta G^{\circ}$ is the change in reduction potential of CcP after perturbation. In plot (c), reorganization energy λ_{ave} is assumed to be similar between variants. Approximating $-\Delta\Delta G^{\circ} = 170$ meV from plot (a), $\Delta G^{\circ}_1 \approx -130$ meV and $\lambda_{ave} \approx 360$ meV, which signifies a reduction potential of W191Y CcP of 420 meV. (d) At $-\Delta\Delta G^{\circ} = 170$ meV, reorganization energies to appear similar.

rate of W191Y:L232E is due to an upshift in reduction potential from W191Y CcP owing to the formation of partially protonated cationic tyrosyl, which for a fully protonated species, exhibits a 1.4-V higher potential than the neutral protonated tyrosine [9]. Further analysis on the increase in activity first necessitates classification of the electron transfer process. PCET can occur either in a concerted or step-wise mechanism. Thermodynamic arguments often favor the concerted pathway in order to avoid high energy intermediates, however, a sequential mechanism is plausible given an oxidant with high enough redox potential [8]. Provided similar forward rate constants for the reduction of Tyr191$^{\bullet}$ in W191Y:L232E and W191Y from RFQ data fits, electron transfer does not seem to be the rate-limiting factor in the forward exchange reaction to remote Tyr residues, but rather the deprotonation of the adjacent non-hydrogen-bonded tyrosine residues. In the parent W191Y, electron exchange requires deprotonation and reprotonation of tyrosine residues, the rate of which is governed by the basicity of the proton. Deprotonation of neutral, protonated tyrosine in aqueous solution is generally rapid, resulting in a drop of pK_{a} from 10 down to -2 [79], however, in a protein environment, solvent accessibility may be limited. Introduction of a coordinating basic side chain has been established to lower the pK_{a} of the tyrosine, thus resulting in faster proton transfer [29]. Here, however, the formation of the Tyr191$^{\bullet}$ is not rate limiting, rather the reduction of the radical by Cc(Fe^{2+}). If this were not the case, the W191-F_3Y variant would not be expected to increase the reaction rate. Hence, the coordinating base and Tyr191$^{\bullet}$ form an ion pair that effectively increases the potential of Tyr191$^{\bullet}$. Loss of the proton from this pair at high pH greatly diminishes the rate of electron transfer from Cc(Fe^{2+}).

2.5 Conclusion

Many models have been employed to elucidate the parameters governing tyrosine electron hopping sites in biological systems, from small molecules in solvent to engineered protein systems, though not many have explored local environmental effects on tyrosine-mediated electron transfer [9, 70, 80]. Here we present our findings on a well-studied electron transfer process in the cytochrome *c* peroxidase : cytochrome *c* complex comprised of a single, primary hole-hopping site that we have replaced with tyrosine, which was unable to accelerate Cc oxidation. In this system, we have improved the electron transfer rate to nearly WT levels by introduction of a neighboring coordinating basic side chain that forms a hydrogen bond with the adjacent phenolic proton of tyrosine 191. Our results corroborate several other reports that identified the importance of a hydrogen-bonded phenol for mediating redox processes; removal of the basic side chain often results in loss of activity [9, 27]. Our kinetics studies further support our theory that hydrogen bond formation to the phenolic proton augments the electron transfer rate by upshifting the redox potential of Tyr191. By applying a simple Marcus model to the experimental data, we have approximated bounds on the parameters governing electron transfer in the W191Y:L232E CcP:Cc system. The increase in reduction potential from the addition of Glu232 is likely no greater than 200 meV; hence, the potential of W191Y Compound I is limited to 400 meV and confirms our suspicions on its low reactivity with Cc.

Unsurprisingly, proteins have naturally evolved to minimize reorganization energies and maximize reduction potentials for the purposes of efficient electron transport. Evidently, incorporation or modification of a radical hopping site is no trivial matter, and characterizing the parameters that enable such reactions will be critical in developing a relevant model for future protein engineering and electron transfer studies.

2.6 Materials and Methods

2.6.1 Protein purification

Cytochrome *c*

Wild-type yeast iso-1-Cc from *Saccharomyces cerevisiae* in a PBTR1 vector was used to transform *E. coli* BL21 (DE3) cells. Cells were grown in LB-Miller media for 20 h at 37 °C with 125 μg/mL ampicillin and $50-100$ μg/mL δ-aminolevulenic acid to improve heme incorporation. Harvested cells were resuspended in 50 mM sodium phosphate (NaP_i), pH 8 and lysed by sonication. Lysate was centrifuged at 20,000 RPM for 1 h at 4 °C and the supernatant was directly loaded onto an equilibrated HiPrep CMFF 16/10 column. After washing with one column volume (40 mL) of 50 mM NaP_i, a linear gradient of 50 mM NaP_i, 500 mM sodium chloride (NaCl), pH 8, was applied over 100 mL to elute the bound protein. Protein fractions were pooled and further purified by size-exclusion chromatography (HiLoad Superdex 75 26/60). Colored fractions were combined, concentrated, aliquotted, and stored at −80 °C. Concentrations were measured at $\text{Abs}_{550\text{ nm}} - \text{Abs}_{540\text{ nm}}$, $\epsilon = 19.2\ \text{mM}^{-1}\ \text{cm}^{-1}$.

Cytochrome *c* peroxidase

Cytochrome *c* Peroxidase (CcP) constructs from *Saccharomyces cerevisiae* in the pp-SUMO vector with an N-terminal His-tag followed by SUMO protein [26] were used to transform BL21(DE3) cells, which was grown at 37 °C in LB-Miller media with 50 μg/mL kanamycin. Cells were induced with 100 μM isopropyl β-D-1-thiogalactopyranoside (IPTG; 25 μg/mL) once O.D._{600} reached $0.8-1.2$ and overexpressed at room temperature for ∼18 h. Cells were harvested and resuspended in lysis buffer (50 mM HEPES, pH 7.0, 150 mM

NaCl, and 5 mM imidazole). Cells were lysed by sonication and centrifuged at 20,000 RPM for 1 h at 4 °C. CcP was purified with Ni-NTA resin column (Qiagen) and concentrated. SUMO-His_6 tag was cleaved with ULP-1 protease and dialyzed into 100 mM potassium phosphate (KP_i), pH 6, overnight at 4 °C. Eluent was flowed through a Ni-NTA column to remove the tags. To improve heme incorporation, the eluent was incubated with one molar equivalent of hemin dissolved in 500 μL 0.1 M sodium hydroxide (NaOH) overnight at 4 °C. The reaction was quenched with an equal amount of 0.1 M acetic acid. Unreacted hemin and precipitated protein were removed by centrifugation at 3,000 RPM for 10 min. The soluble portion was purified by size-exclusion chromatography (HiLoad Superdex 75 26/60) in 100 mM KP_i, pH 6. Protein fractions were combined and loaded directly onto an equilibrated HiPrep Q XL 16/10 column. A linear gradient of 500 mM KP_i, pH 6, was applied over 160 mL to elute the protein and separate the apo-CcP from the Fe-CcP. All fractions with high heme incorporation ($Abs_{408\ nm}/Abs_{280\ nm} > 1$) were pooled, concentrated, aliquotted, and stored at −80 °C. All preparations of the enzyme conformed to the purity criteria previously described [81]. Concentrations were determined at 408 nm, $\epsilon = 96\ mM^{-1}\ cm^{-1}$.

2.6.2 Mutagenesis

Single residue substitutions in CcP were produced by the overlap extension PCR method on the CcP construct within the ppSUMO vector. For fluorotyrosine derivatives, site 191 was replaced with a TAG amber stop codon.

Tyrosine phenol lyase

Tyrosine phenol lyase (TPL) in pET23b (generous gift from the Tonge lab, Stony Brook University) was overexpressed in BL21(DE3)pLysS cells (Novagen) in LB-Miller media with

chloramphenicol and ampicillin at room temperature for 18 h. Cells were harvested, re-suspended in lysis buffer (50 mM NaP_i, pH 7, 150 mM NaCl, 5 mM DTT), and lysed by sonication. Cell detritus was removed by centrifugation at 20,000 RPM, 1 h, 4 °C, and the resulting lysate was purified by Ni-NTA resin. The eluted protein was then further purified by size-exclusion chromatography (HiLoad Superdex 75 26/60) in 50 mM NaP_i, pH 7, 150 mM NaCl. Protein fractions were pooled and 10% glycerol added to aid in stability. Samples were stored at −80 °C and used within one week of preparation to avoid loss of activity. Final yield was ∼200 mg per 8 L culture.

Fluorotyrosine preparation and purification

Fluorotyrosine residues were prepared as described [33, 82]. Pyridoxal 5′ phosphate and 2,6-difluorophenol were purchased from Oakwood Chemicals; 2,3,6-trifluorophenol was acquired from Alfa Aesar. (Note that the numbering changes when converting the fluorophenol into fluorotyrosine.)

In a 1-L bottle, 30 mM ammonium acetate, pH 8, 60 mM sodium pyruvate, 40 μM pyridoxal 5′ phosphate, and 50 mM β-mercaptoethanol were combined. The solution was filtered through a 0.22 μm filter and 10 mM fluorophenol was added, adjusting the final pH to 8. Approximately 150 units (∼80 mg) of purified TPL were added to the mixture drop-wise while stirring, after which, the reaction was covered in foil and remained stirring at room temperature. Every two days, 30 units (∼16 mg) of TPL were added to the reaction mixture for a total of ∼1 week. The mixture was quenched by acidifying to pH ∼2.5, and precipitated protein was removed by filtration or centrifugation. The solution was extracted twice with 500 mL of ethyl acetate to remove unreacted phenols. The aqueous layer was run through a column (inner diameter ∼4 in) of activated Dowex 50W-X8 (50 − 100 mesh; Beantown Chemical Corporation) equilibrated in Nanopure water. The column was washed

with 1 L of filtered Nanopure water to remove impurities, and the fluorotyrosines were eluted with 10% ammonium hydroxide in ∼7 mL fractions. Fractions were spotted on a silica thin-layer chromatography plate and visualized by ninhydrin stain (0.19% (w/v) ninhydrin, 95% ethanol, 0.5% acetic acid, 4.5% water). Fractions containing the amino acid were combined, concentrated by roto-evaporation, and lyophilized to dryness. Fluorotyrosines were confirmed by ^{1}H NMR and ^{19}F NMR in D_2O [33]. Yield: ∼50%.

Fluorotyrosine incorporation into site 191 of CcP

BL21(DE3) cells were co-transformed with CcP (with site 191 replaced by TAG in pp-SUMO) and with E3 aminoacyl-tRNA synthetase (generous gift from the Stubbe group, MIT). Cells were grown in LB-Miller media with kanamycin (25 μg/mL) and chloramphenicol (12 μg/mL) at 37 °C until reaching an O.D.$_{600}$ of ∼0.4, after which 1 mM fluorotyrosines dissolved in 0.1 M NaOH was added to the culture and incubated for 10 minutes. Subsequently, E3 expression was induced with 0.05% (w/v) arabinose. After 1 h, CcP production was induced with 100 μM IPTG and overexpressed at 37 °C for 18 h. Cells were harvested and purified similarly as other CcP variants.

Single and multiple turnover measurements

Single turnover measurements were conducted with 1 μM CcP and 2 μM reduced Cc in 100 mM KP_i, pH 6 were reacted with 2 μM H_2O_2 at 20 °C with constant stirring (700 RPM). Multiple turnover experiments were conducted similarly, consisting of 1 μM CcP, 30 μM Cc, and 10 μM H_2O_2. Traces were collected at 550 nm, 540 nm, and 434 nm. $\mathrm{Abs}_{550\ \mathrm{nm}\ -\ 540\mathrm{nm}}$ corresponds to the concentration of Cc(Fe^{2+}) and $\mathrm{Abs}_{434\ \mathrm{nm}}$ follows CcP(Fe^{4+} = O). Exponential decays were fit to $y = a \cdot e^{-b \cdot x} + c$ with MatLab (Mathworks).

Solvent isotope effect on electron transfer rates

1 μM CcP and 1 μM Cc were combined in order to maintain the stability of CcP. The complex was diluted 500-fold into 100 mM KP_i, pH 6 deuterium-based buffer overnight at 4 °C. Due to overnight Cc oxidation in aerobic buffer, an additional 2 μM reduced Cc was added to the solution before initiating the reaction with 2 μM H_2O_2 at 20 °C with constant stirring. Data were acquired and processed similar to single turnover measurements. Statistically significant differences were determined by a two-tailed Student's t-test assuming equal variances.

Crystallization of CcP:Cc complex

CcP and Cc were combined in a 1:1 stoichiometric ratio and oxidized with potassium ferricyanide overnight. CcP:Cc were buffer exchanged into filtered Nanopure water and adjusted to 1 mM. Crystals formed by the hanging drop method appeared within a week (100 mM sodium acetate, pH $5.4 - 6$, 175 mM NaCl, 5 mM n-octyl-β-D-glucoside, 20% polyethylene glycol 3350). Crystals were soaked briefly in 20% ethylene glycol as a cryoprotectant, flash frozen, and diffracted at NE-CAT Advanced Photon Source 24ID-C beam line. All data were indexed, integrated, and scaled by HKL-2000. The structure was determined and refined by PHENIX [83]. Model building was performed with Coot [84].

Characterization of tyrosyl radical by electron spin resonance spectroscopy

Compound I samples were prepared by combining $0.1 - 0.2$ mM CcP and two molar equivalents of H_2O_2. Protein mixture was quickly loaded into an X-band ESR tube and flash frozen in liquid nitrogen within 1 min. Continuous-wave X-band spectra were acquired with a Bruker EleXSys II spectrometer at 9.39 GHz and 12 K with 100 kHz modulation

frequency, $1 - 4$ Gauss modulation amplitude, and $0.2 - 0.63$ mW power. Power was varied to check for characteristic saturation effects of tyrosyl signals.

Rapid freeze quench samples were prepared to quantify the Compound I radical species over the time of the reaction with Cc. As this method results in volume variations, instead of calculating a packing factor, an inert internal standard of Er:DTPA was prepared and added to the protein mixture. Er:DTPA was prepared by reacting a solution of 3 mM $Er_2(SO_4)_3 \cdot 8$ H_2O in 1 M HCl with 8 mM diethylenetriaminepentaacetic acid (DTPA; Sigma Chemical Company) in 0.1 M NaOH. The final pH was adjusted to 9.

Using a Bio-Logic SFM 300 machine, 0.3 mM CcP, 1.5 mM Er:DTPA, and 0.6 mM Cc in 100 mM KP_i, pH 6 were combined with 0.6 mM H_2O_2. After a time delay, the mixture was sprayed into liquid ethane-filled glass funnels that were coupled to X-band ESR tubes with heat shrink tubing. The resultant snow was immediately packed by hand into the bottom of an ESR tube with an aluminum rod. Spectra were collected with a Bruker EleXSys II spectrometer at 9.39 GHz and 12 K with 100 kHz modulation frequency, 4 dB modulation amplitude, and 0.6325 mW power. Data were processed by MatLab and EasySpin[85].

The organic radical signal at $g = 2$ was isolated and corrected by subtracting a linear baseline. Cumulative numerical integration (`cumtrapz`) followed by integration (`trapz`) were then implemented. The Er:DTPA signal at $g = 11.8$ was similarly truncated, baseline corrected, and integrated with `trapz`. Radical signals were normalized to that of Er:DTPA.

2.7 Acknowledgements

Thanks to Harry Gray (Caltech) for an insightful discussion; to Jon Caranto, Avery Vilbert, and Meghan Smith (Lancaster group; Cornell University) for help on rapid freeze

quench preparation; and to Agnieszka Gil (Tonge lab; Stony Brook University) for her guidance in fluorotyrosine preparation. Lastly, thanks to Boris Dzikovski (Freed group; ACERT; Cornell University) for assistance on cw-ESR spectroscopy and work on Er:DTPA internal standards. This work was financially supported by the NIH training grant T32 GM08267 (to E.F.Y.) and NSF grant 1715233 (to B.R.C.).

2.8 Supplemental Information

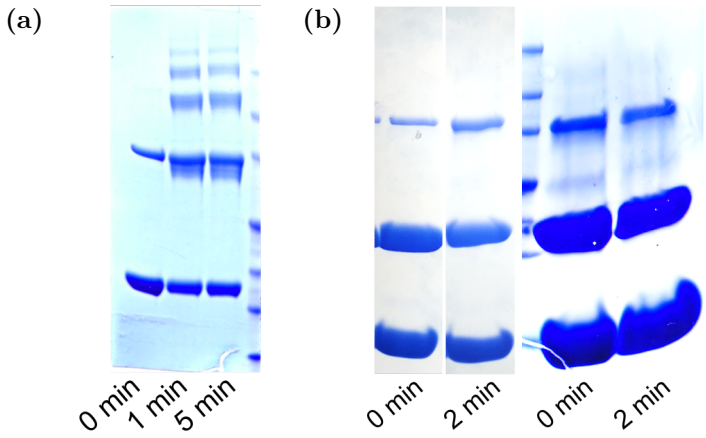

Supplemental Figure 2.8: Treatment of W191Y CcP (without Cc) with two molar equivalents of peroxide. Samples were prepared by incubating protein in freshly diluted peroxide for either 0 min, 1 min, or 5 min and immediately quenched with SDS loading buffer. After 1 min of peroxide exposure, higher order crosslinking bands were clearly apparent. (b) W191Y CcP and Cc(Fe^{2+}) ((left) samples were run nonadjacent on the same gel) or Cc(Fe^{3+}) ((right) gel was scaled for comparison) were combined in a 1:2 molar ratio and reacted with two equivalents of peroxide. After two minutes, no additional higher order or degradation bands developed. The CcP homodimer band at ~75 kDa showed a small increase in intensity over the course of this reaction. Notably, the oxidation state of Cc did not affect its ability to stabilize CcP. Molecular ladder markers from top to bottom: 150, 100, 75, 50, 35, 25, 15 kDa

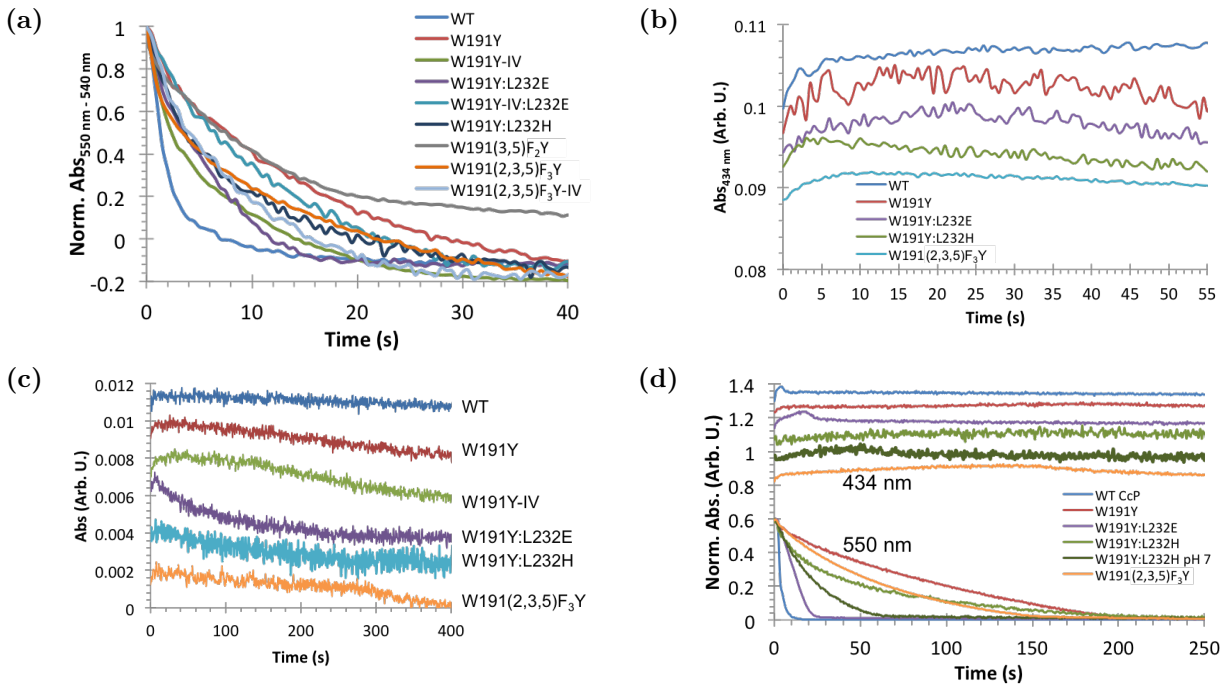

Supplemental Figure 2.9: Single turnover reactions (1 μM CcP : 2 μM Cc(Fe^{2+}) initiated with 2 μM H_2O_2 in 100 mM KP_i, pH 6). Cc oxidation was monitored by UV-vis at (a) $Abs_{550\ nm\ -\ 540\ nm}$ and at (b) $Abs_{434\ nm}$. Most variants oxidized Cc(Fe^{2+}) slowly relative to WT CcP (dark blue). W191Y:L232E (purple) initially exhibited linear kinetics followed by a monoexponential decay and was notably more effective than other tyrosine variants at Cc oxidation. Oxyferryl formation at 434 nm develops similarly to WT but slowly decreases after maximal build up. (c) Compound I stability assessed with 1 μM CcP in 100 mM KP_i, pH 6. Reaction was initiated with 2 μM H_2O_2. Q bands at 562 nm correspond to build up and decay of Compound I. Traces are stacked for clarity. WT CcP shows little variation over 10 minutes. W191Y, W191Y-IV, and W191(2,3,5)F_3Y exhibit stable features for several minutes before reverting back to the ferric state (408 nm), with W191(2,3,5)F_3Y lasting nearly five minutes. W191Y:L232E show rapid decay almost immediately upon reacting with peroxide. (d) Multiple turnover reactions with 1 μM CcP : 30 μM Cc : 10 μM H_2O_2 in 100 mM KP_i, pH 6. Traces at 550 nm and 434 nm are indicative of Cc oxidation and Compound I accumulation/decay, respectively. $Abs_{434\ nm}$ traces are stacked for clarity. W191Y:L232H at pH 6 exhibits a biexponential oxidation curve. When reacted with peroxide and Cc in pH 7 buffer, Cc oxidation follows a monoexponential trace. WT CcP and W191Y:L232E both rapidly oxidize Cc in a monoexponential fashion with transient Compound I signals.

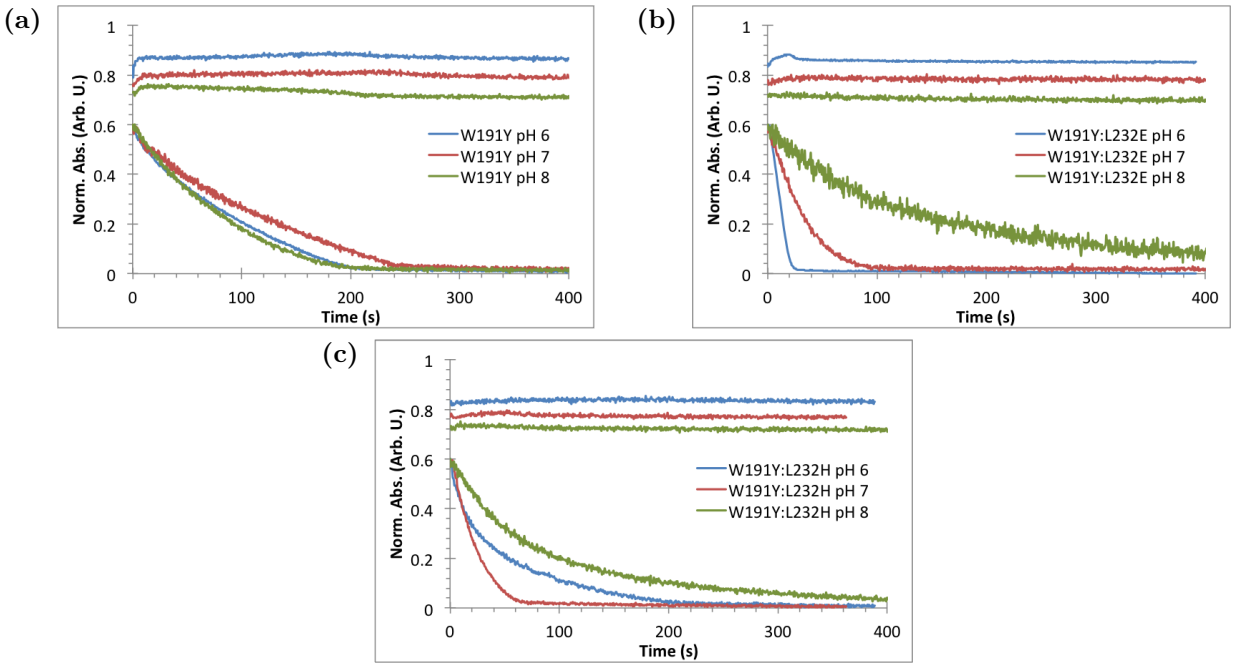

Supplemental Figure 2.10: Multiple turnover reactions (1 μM CcP : 10 μM H_2O_2 : 30 μM Cc) in 100 mM KP_i, pH 6, 7 or 8. (a) pH has little effect on the rate of Cc oxidation by W191Y, (b) while increasing the pH decreases the activity of W191Y:L232E. (c) W191Y:L232H exhibits maximal activity at pH 7, but the rate of Cc oxidation also decreases at high pH.

	W191Y		W191Y:L232E	
Rates(s^{-1})	k_1	k_{-1}	k_1	k_{-1}
A $\Leftrightarrow$ B	Rapid eq.	Rapid eq.	Rapid eq.	Rapid eq.
B $\Leftrightarrow$ C	0.06	0.045	0.04	0.001
B $\Rightarrow$ D	0.25	–	0.25	–
D $\Rightarrow$ C	–	–	0.003	–

Supplemental Table 2.2: Parameters for kinetic fits of rapid freeze quench cw-ESR in Figure 2.3. Assuming the first equivalent of Cc(Fe^{2+}) quickly oxidizes and quenches the radical, state *A*, CcP(Fe^{4+}), is in rapid equilibrium with *B*, CcP(Fe^{3+}=OH; $Y^{\bullet}$191). *C* represents the outward migration of the electron hole to nearby aromatic amino acids. *D* is the successful exchange of the complexed, oxidized Cc(Fe^{3+}) with the remaining equivalent of reduced Cc(Fe^{2+}) in solution. In the case of W191Y:L232E, the efficiency of Cc oxidation allows the remaining equivalent of peroxide to re-oxidize CcP back to its Compound I radical state.

Variant	A	k_1 [s^{-1}]
WT	0.034 ± 0.009	0.44 ± 0.08
W191G	0.0224 ± 0.0014	0.022 ± 0.002
W191Y	0.020 ± 0.008	0.05 ± 0.02
W191Y-IV	0.030 ± 0.008	0.10 ± 0.03
W191Y:L232E	0.044 ± 0.004	0.189 ± 0.006
W191Y:L232E + Y48K Cc	0.046 ± 0.006	0.156 ± 0.005
W191Y-IV:L232E	0.0450 ± 0.0019	0.093 ± 0.005
W191Y:L232H	0.024 ± 0.006	0.107 ± 0.018
W191(3,5)F_2Y	0.028 ± 0.003	0.083 ± 0.003
W191(2,3,5)F_3Y	0.021 ± 0.007	0.07 ± 0.02
W191(2,3,5)F_3Y-IV	0.033 ± 0.006	0.11 ± 0.03

Supplemental Table 2.3: Single turnover rate constants of 2 μM Cc(Fe^{2+}) oxidation by 1 μM CcP and 2 μM H_2O_2. Rate constants were obtained by monoexponential fits of $Abs_{550\text{ nm} - 540\text{ nm}}$ after truncation of the initial five seconds. Mutations to W191Y in an attempt to recover WT activity result in rate constants that are half that of WT. Curiously, despite the 200 mV higher redox potential of the 2,3,5-trifluorotyrosine, there is little effect on the rate of Cc oxidation.

CcP Variant	pH	A	k_1 [s^{-1}]
W191Y	pH 6	0.024 ± 0.008	0.026 ± 0.010
W191Y	pH 7	0.0231 ± 0.0002	0.0215 ± 0.0016
W191Y	pH 8	0.0336 ± 0.0011	0.024 ± 0.004
W191Y:L232E	pH 6	0.044 ± 0.004	0.189 ± 0.006
W191Y:L232E	pH 7	0.023 ± 0.002	0.101 ± 0.010
W191Y:L232E	pH 8	0.0491 ± 0.0016	0.0128 ± 0.008
W191Y:L232H	pH 6	0.024 ± 0.006	0.107 ± 0.018
W191Y:L232H	pH 7	0.044 ± 0.006	0.081 ± 0.018
W191Y:L232H	pH 8	0.027 ± 0.013	0.07 ± 0.02

Supplemental Table 2.4: Single turnover measurements (1 μM CcP : 2 μM Cc: 2 μM H_2O_2) in 100 mM KP_i, pH 6, 7, and 8. Increasing pH results in a decrease in Cc oxidation rate for W191Y:L232E. pH 6 parameters are the same as in Supplemental Table 2.3 except for W191Y. W191Y kinetics were acquired using a different stock and kinetics at pH 6 were remeasured.

CcP Variant	A	k_1 [s^{-1}]
W191Y	0.030 ± 0.011	0.033 ± 0.018
W191Y in D_2O	0.024 ± 0.005	0.030 ± 0.005
W191Y:L232E	0.058 ± 0.004	0.165 ± 0.011
W191Y:L232E in D_2O	0.046 ± 0.008	0.10 ± 0.03

Supplemental Table 2.5: Single turnover measurements (1 μM CcP : 2 μM Cc: 2 μM H_2O_2) after overnight incubation of CcP : Cc in either water-based or D_2O-based 100 mM KP_i buffer, pH 6. Due to overnight oxidation of Cc in aerobic buffer, before reaction initiation with peroxide, 2 μM Cc(Fe^{2+}) was freshly added to the mixture. Cc oxidation traces were acquired at $Abs_{550\ nm\ -\ 540\ nm}$ and fit to a monoexponential function after truncation of the initial five seconds.

Variant	A	k_1 [s^{-1}]	B	k_2 [s^{-1}]
WT	0.58 ± 0.10	0.43 ± 0.06	–	–
W191Y	0.66 ± 0.11	0.008 ± 0.003	–	–
W191Y:L232E	0.101 ± 0.018	0.25 ± 0.04	–	–
W191Y:L232H	0.340 ± 0.018	0.010 ± 0.003	0.180 ± 0.019	0.08 ± 0.03
W191Y:L232H (pH 7)	0.499 ± 0.011	0.036 ± 0.004	–	–
W191(2,3,5)F_3Y	0.554 ± 0.017	0.0149 ± 0.005	–	–

Supplemental Table 2.6: Multiple turnover rate constants of 1 μM CcP : 10 μM H_2O_2 : 30 μM Cc. Cc oxidation data were fit to monoexponential functions. In all tyrosine variants, data were truncated once inactivation occurred and a transition in rates was observed. The resultant data (the early phase) was fit to a monoexponential function.

BIBLIOGRAPHY

(1) Hammes-Schiffer, S.; Stuchebrukhov, A. A. *Chem. Rev.* **2010**, *110*, 6939–6960.

(2) Closs, G. L.; Miller, J. R. *Science (80-.).* **1988**, *240*, 440–447.

(3) Chang, C. J.; Chang, M. C.; Damrauer, N. H.; Nocera, D. G. *Biochim. Biophys. Acta - Bioenerg.* **2004**, *1655*, 13–28.

(4) Gray, H. B.; Winkler, J. R. *Annu. Rev. Biochem.* **1996**, *65*, 537–561.

(5) Gray, H. B.; Winkler, J. R. *Proc. Natl. Acad. Sci. U. S. A.* **2005**, *102*, 3534–9.

(6) Winkler, J. R.; Gray, H. B. *Philos. Trans. A. Math. Phys. Eng. Sci.* **2015**, *373*, 20140178.

(7) Wang, M.; Gao, J.; Müller, P.; Giese, B. *Angew. Chemie - Int. Ed.* **2009**, *48*, 4232–4234.

(8) Dempsey, J. L.; Winkler, J. R.; Gray, H. B. *Chem. Rev.* **2010**, *110*, 7024–7039.

(9) Warren, J. J.; Winkler, J. R.; Gray, H. B. *FEBS Lett.* **2012**, *586*, 596–602.

(10) Karthein, R.; Dietz, R.; Nastainczyk, W.; Ruf, H. H. *Eur. J. Biochem.* **1988**, *171*, 313–320.

(11) Stubbe, J. A. *Annu. Rev. Biochem.* **1989**, *58*, 257–285.

(12) Aubert, C.; Mathis, P.; Eker, A. P. M.; Brettel, K. *Proc. Natl. Acad. Sci.* **1999**, *96*, 5423–5427.

(13) Barry, B. A. *J. Photochem. Photobiol. B Biol.* **2011**, *104*, 60–71.

(14) Gray, H. B.; Winkler, J. R. *Proc. Natl. Acad. Sci. U. S. A.* **2015**, *112*, 10920–10925.

(15) Mayer, J. M.; Rhile, I. J.; Larsen, F. B.; Mader, E. A.; Markle, T. F.; DiPasquale, A. G. *Photosynth. Res.* **2006**, *87*, 3–20.

(16) Huynh, M. H. V.; Meyer, T. J. *Chem. Rev.* **2006**, *107*, 5004–5064.

(17) Hosseinzadeh, P.; Marshall, N. M.; Chacón, K. N.; Yu, Y.; Nilges, M. J.; New, S. Y.; Tashkov, S. A.; Blackburn, N. J.; Lu, Y. *Proc. Natl. Acad. Sci.* **2015**, *113*, 262–267.

(18) Aubert, C.; Brettel, K.; Mathis, P.; Eker, A. P. M.; Boussac, A. *J. Am. Chem. Soc.* **1999**, *121*, 8659–8660.

(19) Faller, P.; Goussias, C.; Rutherford, A. W.; Un, S. *Proc. Natl. Acad. Sci.* **2003**, *100*, 8732–8735.

(20) Stubbe, J. A.; Nocera, D. G.; Yee, C. S.; Chang, M. C. *Chem. Rev.* **2003**, *103*, 2167–2201.

(21) Wang, J. M.; Mauro, M.; Edwards, S. L.; Oatley, S. J.; Fishel, L. A.; Ashford, V. A.; Xuong, N.-h.; Kraut, J. *Biochemistry* **1990**, *29*, 7160–7173.

(22) Goodin, D. B.; McRee, D. E. *Biochemistry* **1993**, *32*, 3313–3324.

(23) Choudhury, K.; Sundaramoorthy, M.; Hickman, A.; Yonetani, T.; Woehl, E.; Dunn, M. F.; Poulos, T. L. *J. Biol. Chem.* **1994**, *269*, 20239–20249.

(24) Erman, J. E.; Vitello, L. B. *Biochim. Biophys. Acta* **2002**, *1597*, 193–220.

(25) Miller, M.; Vitello, L.; Erman, J. E. *Biochemistry* **1995**, *34*, 12048–58.

(26) Payne, T. M.; Yee, E. F.; Dzikovski, B.; Crane, B. R. *Biochemistry* **2016**, *55*, 4807–4822.

(27) Hays, A. M. A.; Vassiliev, I. R.; Golbeck, J. H.; Debus, R. J. *Biochemistry* **1998**, *37*, 11352–11365.

(28) Tommos, C.; Babcock, G. T. *Biochim. Biophys. Acta - Bioenerg.* **2000**, *1458*, 199–219.

(29) Narváez, A. J.; Kálmán, L.; LoBrutto, R.; Allen, J. P.; Williams, J. C. *Biochemistry* **2002**, *41*, 15253–15258.

(30) Harriman, A. *J. Phys. Chem.* **1987**, *91*, 6102–6104.

(31) Kathiresan, M.; English, A. M. *Chem. Sci.* **2017**, *8*, 1152–1162.

(32) Pettersen, E. F.; Goddard, T. D.; Huang, C. C.; Couch, G. S.; Greenblatt, D. M.; Meng, E. C.; Ferrin, T. E. *J. Comput. Chem.* **2004**, *25*, 1605–1612.

(33) Seyedsayamdost, M. R.; Reece, S. Y.; Nocera, D. G.; Stubbe, J. *J. Am. Chem. Soc.* **2006**, *128*, 1569–1579.

(34) Gil, A. A.; Laptenok, S. P.; Iuliano, J. N.; Lukacs, A.; Verma, A.; Hall, C. R.; Yoon, G. E.; Brust, R.; Greetham, G. M.; Towrie, M.; French, J. B.; Meech, S. R.; Tonge, P. J. *J. Am. Chem. Soc.* **2017**, *139*, 14638–14648.

(35) Erman, J. E.; Yonetani, T. *Biochem Biophys Acta* **1975**, *393*, 343–349.

(36) Erman, J. E.; Yonetani, T. *BBA - Protein Struct.* **1975**, *393*, 350–357.

(37) Hinsberg, W.; Houle, F. Kinetiscope: a stochastic kinetics simulator., 2017.

(38) Hulsebosch, R. J.; Van Den Brink, J. S.; Nieuwenhuis, S. A.; Gast, P.; Raap, J.; Lugtenburg, J.; Hoff, A. J. *J. Am. Chem. Soc.* **1997**, *119*, 8685–8694.

(39) Mongan, J.; Case, D. A.; McCammon, J. A. *J. Comput. Chem.* **2004**, *25*, 2038–2048.

(40) Bernini, C.; Arezzini, E.; Basosi, R.; Sinicropi, A. *J. Phys. Chem. B* **2014**, *118*, 9525–9537.

(41) Miner, K. D.; Pfister, T. D.; Hosseinzadeh, P.; Karaduman, N.; Donald, L. J.; Loewen, P. C.; Lu, Y.; Ivancich, A. *Biochemistry* **2014**, *53*, 3781–3789.

(42) Tsaprailis, G.; English, A. M. *J. Biol. Inorg. Chem.* **2003**, *8*, 248–255.

(43) Tsaprailis, G.; English, A. M. *Can. J. Chem.* **1996**, *74*, 2250–2257.

(44) Ishikita, H.; Knapp, E. W. *Biophys. J.* **2006**, *90*, 3886–3896.

(45) Diner, B. A.; Nixon, P. J.; Farchaus, J. W. *Curr. Opin. Struct. Biol.* **1991**, *1*, 546–554.

(46) Tommos, C.; Tang, X. S.; Warncke, K.; Hoganson, C. W.; Styring, S.; McCracken, J.; Diner, B. A.; Babcock, G. T. *J. Am. Chem. Soc.* **1995**, *117*, 10325–10335.

(47) Diner, B. A.; Force, D. A.; Randall, D. W.; Britt, R. D. *Biochemistry* **1998**, *37*, 17931–17943.

(48) Pace, C. N.; Horn, G.; Hebert, E. J.; Bechert, J.; Shaw, K.; Urbanikova, L.; Scholtz, J. M.; Sevcik, J. *J. Mol. Biol.* **2001**, *312*, 393–404.

(49) Carra, C.; Iordanova, N.; Hammes-Schiffer, S. *J. Am. Chem. Soc.* **2003**, *125*, 10429–10436.

(50) Babcock, G. T.; Barry, B. A.; Debus, R. J.; Hoganson, C. W.; Atamian, M.; Mcintosh, L.; Sithole, I.; Yocum, C. F. *Biochemistry* **1989**, *28*, 9557–9565.

(51) Rutherford, A. W.; Boussac, A.; Faller, P. *Biochim. Biophys. Acta - Bioenerg.* **2004**, *1655*, 222–230.

(52) Poulos, T.; Kraut, J. *J. Biol. Chem.* **1980**, *255*, 10322–10330.

(53) Edwards, S. L.; Poulos, T. L. *J.Biol.Chem.* **1990**, *265*, 2588–2595.

(54) Erman, J. E.; Vitello, L. B.; Miller, M. A.; Shaw, A.; Brown, K. A.; Kraut, J. *Biochemistry* **1993**, *32*, 9798–9806.

(55) Satterlee, J. D.; Alam, S. L.; Mauro, J. M.; Erman, J. E.; Poulos, T. L. *Eur. J. Biochem.* **1994**, *224*, 81–87.

(56) Bonagura, C. A.; Bhaskar, B.; Shimizu, H.; Li, H.; Sundaramoorthy, M.; McRee, D. E.; Goodin, D. B.; Poulos, T. L. *Biochemistry* **2003**, *42*, 5600–5608.

(57) Un, S.; Tang, X. S.; Diner, B. A. *Biochemistry* **1996**, *35*, 679–684.

(58) Debus, R. J. *Biochim. Biophys. Acta - Bioenerg.* **2001**, *1503*, 164–186.

(59) Svistunenko, D. A.; Cooper, C. E. *Biophys. J.* **2004**, *87*, 582–95.

(60) Svistunenko, D. A. *Biochim. Biophys. Acta - Bioenerg.* **2005**, *1707*, 127–155.

(61) Suarez, J.; Ranguelova, K.; Jarzecki, A. A.; Manzerova, J.; Krymov, V.; Zhao, X.; Yu, S.; Metlitsky, L.; Gerfen, G. J.; Magliozzo, R. S. *J. Biol. Chem.* **2009**, *284*, 7017–7029.

(62) Ferreira, J. C.; Marcondes, M. F.; Icimoto, M. Y.; Cardoso, T. H.; Tofanello, A.; Pessoto, F. S.; Miranda, E. G.; Prieto, T.; Nascimento, O. R.; Oliveira, V.; Nantes, I. L. *PLoS One* **2015**, *10*, 1–25.

(63) DeGray, J. A.; Lassmann, G.; Curtis, J. F.; Kennedy, T. A.; Marnett, L. J.; Eling, T. E.; Mason, R. P. *J. Biol. Chem.* **1992**, *267*, 23583–23588.

(64) Avogadro: an open-source molecular builder and visualization tool., 2017.

(65) Hanwell, M. D.; Curtis, D. E.; Lonie, D. C.; Vandermeerschd, T.; Zurek, E.; Hutchison, G. R. *J. Cheminform.* **2012**, *4*, 17.

(66) Rhile, I. J.; Markle, T. F.; Nagao, H.; DiPasquale, A. G.; Lam, O. P.; Lockwood, M. A.; Rotter, K.; Mayer, J. M. *J. Am. Chem. Soc.* **2006**, *128*, 6075–6088.

(67) Mayer, J. M. *J. Phys. Chem. Lett* **2011**, *2*, 1481–1489.

(68) Marcus, R. A. *J. Electroanal. Chem.* **1997**, *438*, 251–259.

(69) Larsen, H.; Pedersen, S. U.; Pedersen, J. A.; Lund, H. *J. Electroanal. Chem.* **1992**, *331*, 971–983.

(70) Sjödin, M.; Styring, S.; Åkermark, B.; Sun, L.; Hammarström, L. *J. Am. Chem. Soc.* **2000**, *122*, 3932–3936.

(71) Turró, C.; Zaleski, J. M.; Karabatsos, Y. M.; Nocera, D. G. *J. Am. Chem. Soc.* **1996**, *118*, 6060–6067.

(72) Matyushov, D. V. *J. Chem. Phys.* **2004**, *120*, 7532–7556.

(73) McMeekin, T. L.; Groves, M. L.; Hipp, N. J. *Adv. Chem.* **1964**, *44*, 54–66.

(74) Alfassi, Z. B.; Huie, R. E.; Marguet, S.; Natafwjan, E.; Neta, P. *Int. J. Chem. Kinet.* **1995**, *27*, 181–188.

(75) Summers, F. E.; Erman, J. E. *J. Biol. Chem.* **1988**, *263*, 14267–14275.

(76) Volkov, A. N.; van Nuland, N. A. J. *PLoS Comput. Biol.* **2012**, *8*, e1002807.

(77) Jiang, N.; Kuznetsov, A.; Nocek, J. M.; Hoffman, B. M.; Crane, B. R.; Hu, X.; Beratan, D. N. *J. Phys. Chem. B* **2013**, *117*, 9129–9141.

(78) Lett, C. M.; Guillemette, J. G. *Biochem. J.* **2002**, *362*, 281–287.

(79) Irebo, T.; Reece, S. Y.; Sjödin, M.; Nocera, D. G.; Hammarstrom, L. *J. Am. Chem. Soc.* **2007**, *129*, 15462–15464.

(80) Westerlund, K.; Berry, B. W.; Privett, H. K.; Tommos, C. *Biochim. Biophys. Acta - Bioenerg.* **2005**, *1707*, 103–116.

(81) Vitello, L. B.; Huang, M.; Erman, J. E. *Biochemistry* **1990**, *29*, 4283–4288.

(82) Gil, A. A. et al. *J. Am. Chem. Soc.* **2016**, *138*, 926–935.

(83) Adams, P. D. et al. *Acta Crystallogr. Sect. D Biol. Crystallogr.* **2010**, *66*, 213–221.

(84) Emsley, P.; Lohkamp, B.; Scott, W. G.; Cowtan, K. *Acta Crystallogr. Sect. D Biol. Crystallogr.* **2010**, *66*, 486–501.

(85) Stoll, S.; Schweiger, A. *J. Magn. Reson.* **2006**, *178*, 42–55.

CHAPTER 3

SIGNAL TRANSDUCTION IN LIGHT-OXYGEN-VOLTAGE RECEPTORS LACKING THE ADDUCT-FORMING CYSTEINE RESIDUE*

3.1 Abstract

Light-oxygen-voltage (LOV) receptors sense blue light through the photochemical generation of a covalent adduct between a flavin-nucleotide chromophore and a strictly conserved cysteine residue. Here we show that, after cysteine removal, the circadian-clock LOV-protein Vivid still undergoes light-induced dimerization and signalling because of flavin photoreduction to the neutral semiquinone (NSQ). Similarly, photoreduction of the engineered LOV histidine kinase YF1 to the NSQ modulates activity and downstream effects on gene expression. Signal transduction in both proteins hence hinges on flavin protonation, which is common to both the cysteinyl adduct and the NSQ. This general mechanism is also conserved by natural cysteine-less, LOV-like regulators that respond to chemical or photoreduction of their flavin cofactors. As LOV proteins can react to light even when devoid of the adduct-forming cysteine, modern LOV photoreceptors may have arisen from ancestral redox-active flavoproteins. The ability to tune LOV reactivity through photoreduction may have important implications for LOV mechanism and optogenetic applications.

*Reproduced with permission from E. F. Yee, R. P. Diensthuber, A. T. Vaidya, P. P. Borbat, C. Engelhard, J. H. Freed, R. Bittl, A. Möglich, and B. R. Crane. *Nat. Commun* **6**, 10079 (2015).

3.2 Introduction

Flavin-binding proteins widely occur across all kingdoms of life where they play vital roles in many different aspects of metabolism[1-3]. Beyond their crucial function in redox catalysis, flavin-binding proteins also serve as signal receptors for redox potential, partial oxygen pressure and blue light[1-3]. Flavin-based sensory photoreceptors fall into three major classes: light, oxygen and voltage sensing (LOV) proteins; BLUF proteins (sensors of blue light using flavin adenine dinucleotide (FAD)) and photolyases/cryptochromes (PL/CRY)[1-3]. The utility of flavin as a chromophore derives from the ability of light to facilitate interconversion between excited states and three ground oxidation states: namely the fully oxidized quinone, the partially reduced semiquinone radical and the fully reduced hydroquinone (HQ). Of these, the oxidized quinone-bound form often serves as the dark-adapted state because of its strong absorption in the blue spectral region.

LOV photoreceptors occur throughout archaea, bacteria, protists, fungi and plants, and regulate phototropism, chloroplast movement, stomatal opening, virulence, stress response, circadian rhythms and other physiological responses[1-4]. In the well-characterized LOV photocycle[1-3], blue-light absorption drives formation of a covalent adduct between a strictly conserved, active-site Cys residue and the C4a atom of the flavin isoalloxazine ring (either FAD; or flavin mononucleotide (FMN))[2,5] (Figure 3.1a). In at least one case, a neutral flavin semiquinone radical intermediate has been detected[6], suggesting that bond formation proceeds via rapid reduction of the flavin by the Cys thiol to form a neutral radical pair (FMNH−S-Cys) and subsequent radical recombination[5-7]; however, more recent spectroscopic studies could not identify build-up of such a species on the tens of ns-to-ms time scale and thereby concluded that if a flavin radical intermediate forms it must react faster than the rate by which it is produced[8]. Nonetheless, effective reduction of the flavin ring, by either adduct or radical formation greatly increases the pK_{a} of N5, thus promoting its

protonation[9]. In response to this protonation, a nearby glutamine residue, conserved in most LOV proteins, undergoes a 180° flip of its amide side chain to adjust hydrogen-bonding interactions[10-12]. Additional changes in hydrogen bonding propagate through the core α/β PAS-domain fold of the LOV domain to N-cap and C-cap regions that pack against the β-sheet on the side opposing the flavin-binding pocket[1-3]. Alteration of the structure and dynamics of these cap regions affect oligomeric state and the activity of output modules[1,3]. However, it is not clear whether adduct formation itself is the dominant factor in generating downstream signalling responses, or if N5 protonation alone can suffice. Despite the paramount importance of the conserved cysteine residue in the canonical LOV photocycle, at least some LOV photoreceptors apparently retain biological activity even after substitution of the Cys thiol for non-reactive side chains[12-15]. Although a rationalization of these findings has remained elusive, it is well-established that LOV domains devoid of this cysteine can undergo photoreduction to a neutral semiquinone (NSQ) state with N5 protonated[16-20], thus raising the question as to whether the NSQ triggers downstream signalling.

Taking the two well-characterized LOV photoreceptors Vivid (VVD)[12,13] and YF1[21], we demonstrate that the NSQ state indeed mediates wild-type (WT)-like signalling responses and that LOV photoreceptors devoid of the conserved adduct-forming cysteine are thus fully capable of light-dependent signal transduction. Furthermore, sequence analyses reveal natural LOV-like proteins that lack the adduct-forming cysteine residue. We demonstrate that one such protein from archaeal halobacteria binds flavin nucleotides and undergoes chemical- and photo-reduction processes that couple to changes in protein conformation. Our results lend new insight into photoreception and signal transduction by LOV photoreceptors, bear on LOV domain application as optogenetic tools[2,22] and suggest an intriguing possibility for the evolutionary origin of the widespread LOV photoreceptor family.

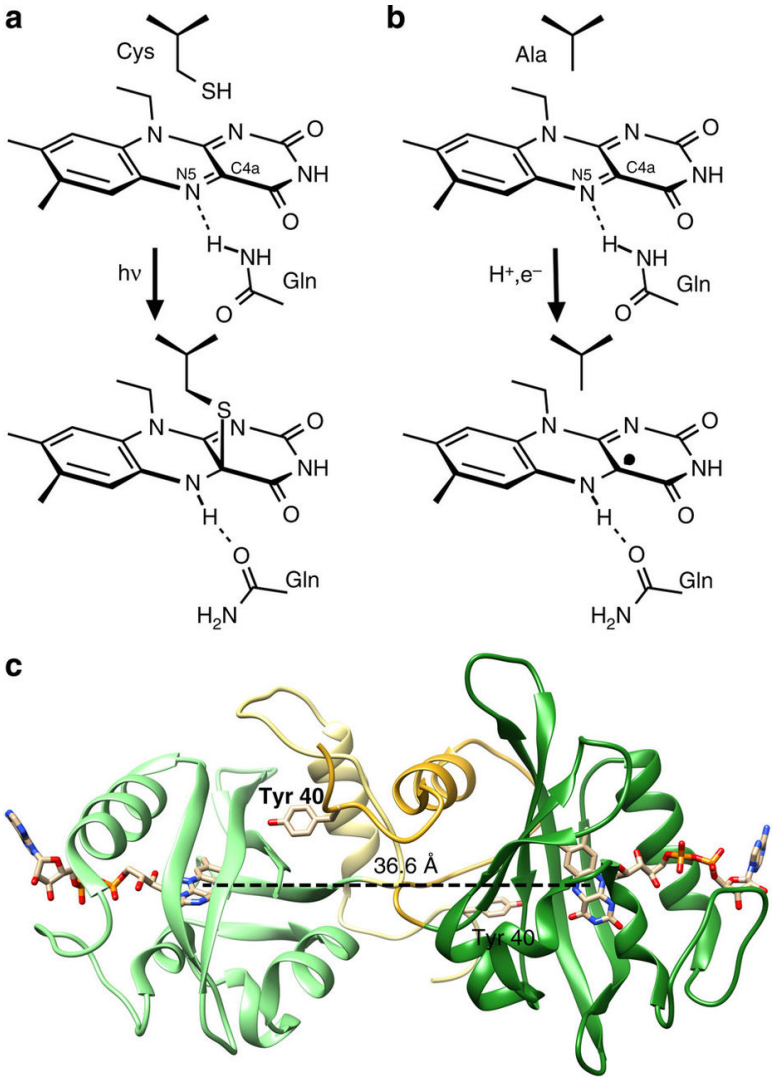

Figure 3.1: Photochemistry of LOV photoreceptors and structure of VVD. (a) In canonical LOV photoreceptors, light excitation of the flavin leads to a covalent adduct between the C4a atom of the flavin ring and an active-site Cys thiol (residues 108 and 62 in VVD and YF1, respectively). Coincident protonation of the flavin atom N5 induces a flip of the amide side chain of a conserved Gln residue (residues 182 and 123 in VVD and YF1, respectively). Resultant changes in hydrogen bonding propagate through the LOV photoreceptor, for example, to an N-cap region in the case of VVD. (b) The absence of the adduct-forming cysteine promotes photoreduction of the LOV flavin to the neutral semiquinone (NSQ). As N5 of the NSQ is also protonated, signals could be relayed in a manner corresponding to that in the cysteinyl adduct in a. (c) Structure of the light-adapted VVD dimer (3RH8)[12]. The flavin rings (tan) in the constituent subunits (dark and light green ribbons) are separated by ∼37 Å at their centroids. An exchange of N-terminal latches associates the N-caps (yellow), with Tyr40 making a key contact across the dimer interface.

3.3 Results

3.3.1 Photoconversion of VVD lacking the adduct-forming Cys

The replacement of the active-site Cys108 of VVD by Ala was produced in the context of VVD-II, which lacks the first 36 N-terminal unstructured residues and carries two other substitutions (M135I:M165I) that are known to stabilize the VVD light-adapted state[12,23]. The Met substitutions extend the adduct lifetime of VVD-II by 10-fold compared with WT VVD and upshift the flavin redox potential by removing two electron-rich sulfur residues that pack against the re-face of the flavin[12,23]. Accordingly, VVD-II purifies from over-expression in *Escherichia coli* as a pale green protein indicative of partial reduction to the NSQ (Supplementary Figure 3.6b). Introduction of the C108A substitution into VVD-II yielded VVD-III (VVD Δ36, C108A:M135I:M165I), which purifies as a much darker green protein than VVD-II (Supplementary Figure 3.6b). Different flavin redox states separate when the protein is passed through a size-exclusion chromatography (SEC) column (Supplementary Figure 3.6d), with the blue-coloured, NSQ-containing protein eluting as a dimer and the yellow-coloured, oxidized protein eluting as a monomer. Intriguingly, this behaviour is highly reminiscent of the homodimerization of WT VVD on blue-light-induced adduct formation[12,24]. On SEC, the adduct form of WT VVD elutes at a larger volume due to a rapidly exchanging equilibrium between dimer and monomer[24]. Light-induced VVD dimerization is critical for the protein to mediate photoadaptation in *Neurospora*[11,12].

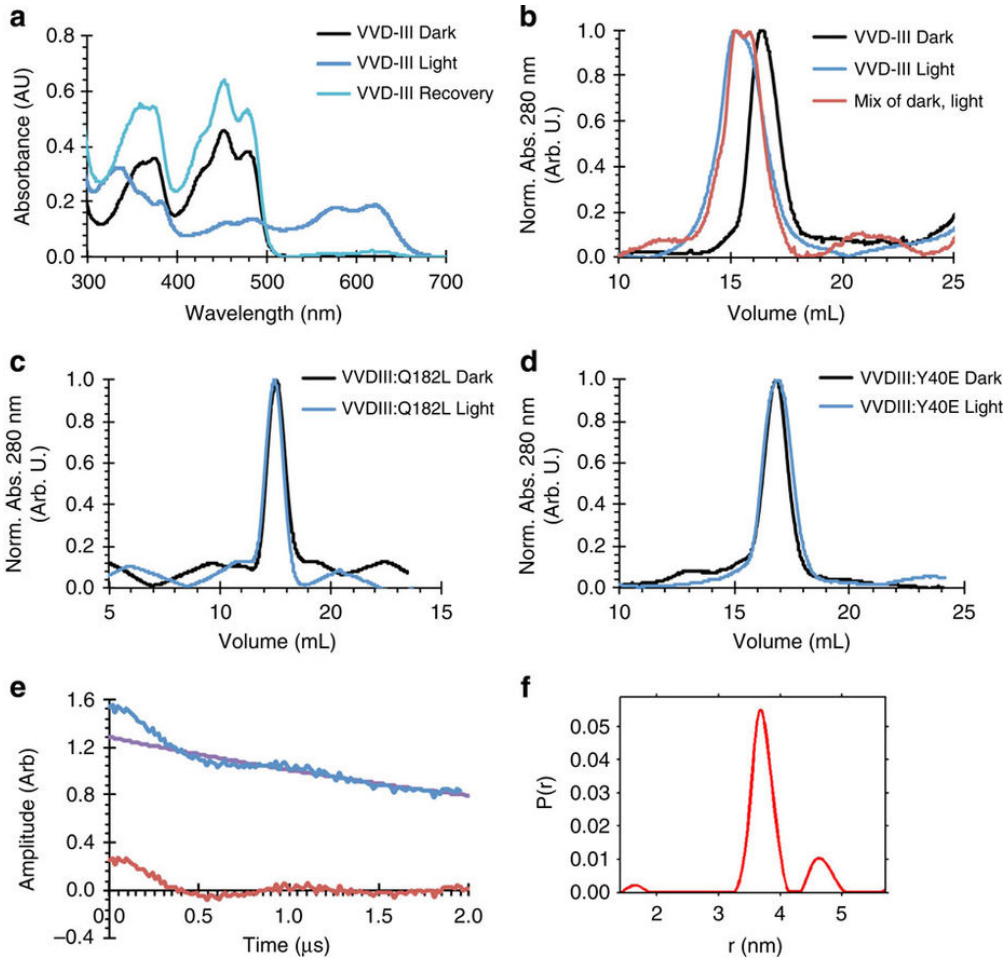

Figure 3.2: Photoreduced VVD-III forms the same light-adapted dimer as wild-type VVD. (a) Absorption spectra of VVD-III in its dark-adapted state (black) and neutral semiquinone state after photoreduction for 5 min with a 448-nm 30 mW laser (dark blue) followed by reoxidation after 170 min at ambient conditions (light blue). (b) Size-exclusion chromatography (SEC) of dark-adapted (black) and light-adapted VVD-III (blue) indicates dimer formation in the NSQ state. A 1:1 mixture of dark-adapted and light-adapted states produces intermediate peaks (red), indicative of the exchangeable nature of the VVD dimer and perhaps radical equilibration on the SEC time scale. (c,d) SEC traces of dark-adapted (black) and light-adapted (blue) VVDIII:Q182L (c) and VVD-III:Y40E (d) indicate no change in the oligomeric state of either protein on photoreduction to the NSQ. Q182L and Y40E traces have different baselines because different SEC columns were used. (e,f) Magnetic dipolar coupling between two radical flavin states was detected by DEER spectroscopy in illuminated VVD-III. (e) Raw time-domain DEER data (blue) with baseline (purple) and after baseline-subtraction (red) reveal a clear dipolar oscillation that produces a sharply peaked distance distribution $P(r)$ of the separated spins at ∼37 Å (f). The smaller peak in $P(r)$ at longer distance is a reconstruction artifact. The spin separation agrees well with that predicted by the light-adapted dimer of VVD (Figure 3.1c).

Exposure to a 448-nm laser (30 mW) reduces the VVD-III FAD quinone to the NSQ over the course of 5 min (Figure 3.2a and Supplementary Figure 3.7a). The FAD then recovers completely to the oxidized form within ∼3 h in the dark under aerobic conditions (Figure 3.2a and Supplementary Figure 3.7b). By following the loss of oxidized flavin fluorescence and formation of the NSQ by absorption spectroscopy, the relative quantum efficiency of reduction compared with adduct formation in WT VVD was determined to be 0.11 ± 0.07. The unprotonated anionic semiquinone was not observed on this time scale, and two isosbestic points (347 and 497 nm) in the forward photoreduction indicate the presence of only oxidized FAD and the NSQ (Supplementary Figure 3.7a). Formation of the NSQ implies that flavin N5 protonates readily on reduction of the isoalloxazine ring (Figure 3.1b). The mechanism for photoreductive quenching of VVD-III to the NSQ is currently unclear, but does not appear to require oxidation of aromatic residues within the protein as substitution of all aromatic residues to Phe has little effect on the rate of VVD-III photoreduction.

When subjected to SEC, the light-adapted NSQ state of VVD-III elutes as a dimer, whereas the dark-adapted oxidized quinone state remains monomeric (Figure 3.2b). Mixtures of the dark and light states elute at an intermediate volume, which suggests that either a NSQ subunit can associate weakly with a quinone subunit or that these oxidation states rapidly equilibrate within the population (Figure 3.2b). Substituting the conserved Gln182 that interacts with flavin N5 to Leu (cf. Figure 3.1a,b) does not affect photoreduction but completely prevents dimerization (Figure 3.2c). To confirm that the NSQ-containing VVD-III dimer has the same structure as that of the Cys-adduct dimer, we introduced the Y40E mutation (VVD-III:Y40E), which disrupts the dimeric interface necessary for signalling[12]. Indeed, introduction of Y40E in VVD-III:Y40E abrogates light-induced dimer formation, and both the light-adapted NSQ and dark-adapted oxidized quinone states elute from SEC as monomers (Figure 3.2d). To further investigate the structure of the VVD-III light-adapted dimer, we applied double electron-electron resonance (DEER) spectroscopy, which measures

the magnetic dipolar coupling between remote electron spins and hence their distance of separation. Modulation of the spin-echo amplitude in photoreduced VVD-III shows a substantial oscillation characteristic of two interacting spins (Figure 3.2e). The derived distance distribution features a sharp peak at ∼37 Å (Figure 3.2f), which matches the expected separation of the flavin radicals based on the crystal structure of the light-adapted VVD dimer[12] (cf. Figure 3.1c). Thus, photoreduction of VVD-III to the NSQ produces the same light-adapted dimer as the cysteinyl-flavin adduct in the WT protein.

3.3.2 Signal transduction in YF1 lacking the adduct-forming Cys

To assess whether the NSQ state can generally activate signalling in LOV proteins, we investigated photoreduction of the LOV histidine kinase YF1, which derives from the fusion of the LOV module of *Bacillus subtilis* YtvA to the histidine-kinase effector module of *Bradyrhizobium japonicum* FixL[21]. As a well-characterized paradigm, YF1 is emblematic of numerous natural proteins in which a LOV or PAS module regulates a histidine kinase[25,26]. Compared with VVD, YF1 is of different origin (prokaryotic versus eukaryotic), utilizes FMN instead of FAD, and possesses different effector output[27,28]. Like VVD, the C62A variant of YF1 undergoes photoreduction with blue light to the NSQ without population of the anionic semiquinone radical (Supplementary Figure 3.8a). Addition of reductants, such as TCEP (Tris(2-carboxyethyl)phosphine hydrochloride), greatly enhances the rate and yield of NSQ formation. Once blue-light illumination ceases, the NSQ oxidizes back to the quinone state in a largely monophasic process over the course of several hours (Supplementary Figure 3.8b).

To assess whether photoreduction of YF1 C62A to the NSQ suffices to elicit WT-like downstream signalling responses, we capitalized on efficient assays that allow probing YF1 signalling *in vivo* and *in vitro*. Combined with the cognate response regulator FixJ, YF1

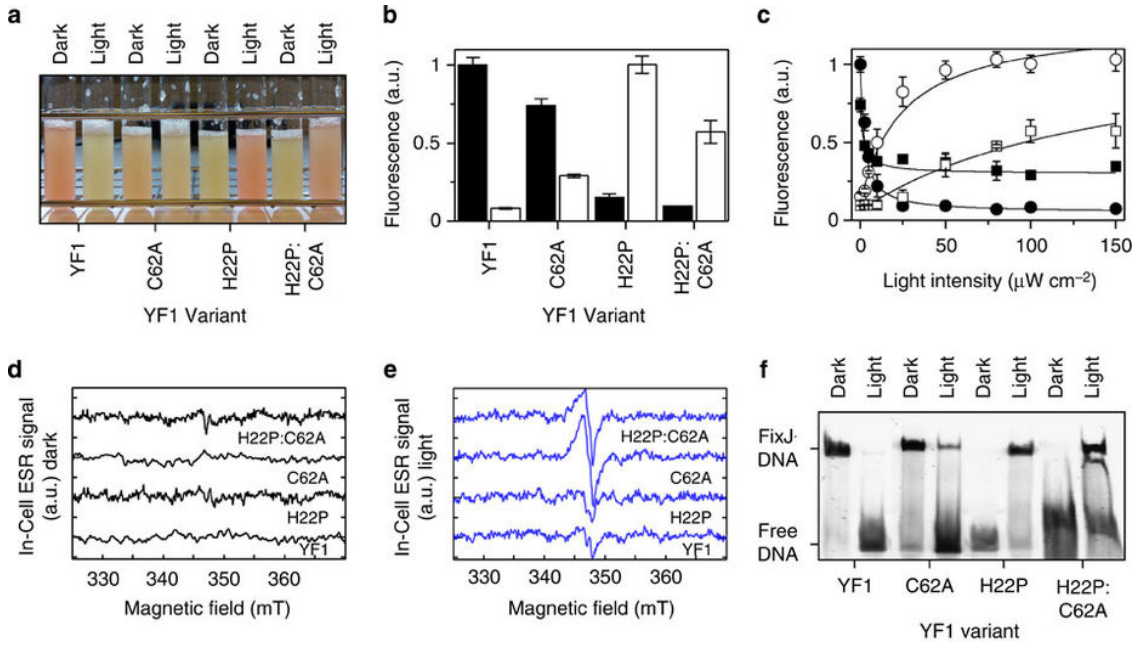

Figure 3.3: Activity measurements of YF1 variants. (a) Light-regulated activity of YF1 variants was assessed *in vivo* in the pDusk-DsRed reporter system[28]. Cultures of YF1 WT and variants C62A, H22P and H22P:C62A were grown in 5 ml under dark and blue-light conditions (470 nm, 100 mW cm^{-2}). DsRed expression is evident by red colouration of cultures. (b) DsRed fluorescence per OD_{600} was measured for the cultures in a under blue-light (white bars) and dark conditions (black bars). (c) The experiment in b was repeated at varying blue-light intensities (470 nm) between 0 and 150 mW cm^{-2}. YF1 (filled circle) and YF1 C62A (filled square) have nearly the same light-dose dependencies with half-maximal light doses, ED_{50}, of (2.1±0.6) mW cm^{-2} and (2.0±0.7) mW cm^{-2}, respectively. By contrast, YF1 H22P (empty circle) shows a higher half-maximal dose of (24.6±5.8) mW cm^{-2} that is increased to above 100 mW cm^{-2} for YF1 H22P:C62A (empty square). The precise ED_{50} value for YF1 H22P:C62A cannot be determined due to cytotoxicity of blue-light doses higher than 150 mW cm^{-2}. All data in b,c represent mean±s.d. of biological triplicates. (d,e) *E. coli* cultures from a were analysed by whole-cell ESR spectroscopy under the same conditions used in a-c. Spectra recorded for dark-adapted (d) or blue-light-adapted (e) cultures were corrected for the *E. coli* background ESR signal. Significant population of flavin radicals above background is only observed for the cysteine-devoid variants YF1 C62A and YF1 H22P:C62A under blue-light illumination. (f) *In vitro* activity measurements of YF1 variants by electrophoretic mobility shift assays (EMSA). In its dark-adapted state, YF1 phosphorylates FixJ, which then binds a rhodamine-labelled DNA substrate, retarding migration of the resultant phospho-FixJ:DNA complex in the polyacrylamide gel. In its light-adapted state, YF1 acts as a phosphatase, FixJ is not phosphorylated and no DNA upshift is observed. The inverter variant YF1 H22P shows the opposite behaviour with an upshift under blue light but not in the dark.

forms a two-component system that drives blue-light-repressed gene expression of the red-fluorescent reporter DsRed[21,28]. When incubated in the dark, *E. coli* cultures harbouring the pDusk plasmid[28] display readily discernible DsRed fluorescence due to FixJ phosphorylation by YF1; when cultures are incubated under saturating blue light (100 mW cm^{-2}, 470 nm), fluorescence is diminished by about 15-fold owing to dephosphorylation of FixJ by YF1 (Figure 3.3a,b). Replacement of Cys62 in YF1 by alanine slightly reduces DsRed expression in the dark; but, similar to WT, blue-light illumination induces a large (60%) repression of the DsRed fluorescence signal (Figure 3.3a,b). YF1 and YF1 C62A show remarkably similar light-dose dependencies with half-maximal light doses, ED_{50}, of (2.1±0.6) mW cm^{-2} and (2.0±0.7) mW cm^{-2}, respectively (Figure 3.3c). Evidently, the C62A variant of YF1 is still capable of mediating light-dependent signal transduction *in vivo*, albeit the response is partially attenuated.

Removal of the adduct-forming cysteine in LOV proteins not only promotes photoreduction and enhances the flavin fluorescence[29], but also renders the flavin a photosensitizer for the generation of singlet oxygen[30-32]. Blue-light-driven generation of reactive oxygen species (ROS) might thus interfere with the two-component system by causing rupture of the labile acid anhydride bond in phospho-FixJ and concomitant deactivation of gene expression. To confirm that YF1 C62A does not incapacitate FixJ through ROS production, we investigated the H22P mutant of YF1 that shows an inverted response to light[27,33]. In contrast to the WT, blue-light illumination of the H22P variant stimulates reporter gene expression by about 10-fold, that is, blue light induces a gain-of-function (Figure 3.3a-c). Introduction of the C62A mutation into the YF1 H22P inverter variant has no effect on the DsRed expression levels in the dark. When incubated under blue light, DsRed expression levels for YF1 H22P:C62A increase about sixfold to ∼60% of the value seen for YF1 H22P in the light. Interestingly, YF1 H22P:C62A showed a lower light sensitivity than YF1 H22P, and higher light doses were required for saturation (Figure 3.3a-c). Thus, YF1 H22P:C62A

is also capable of blue-light signal transduction without the active-site Cys residue, and because this variant increases gene expression, this effect cannot be due to ROS generation.

We sought evidence that regulation of gene expression by the cysteine-devoid YF1 variants correlates with population of the NSQ *in vivo*, and conducted whole-cell electron-spin resonance (ESR) spectroscopy on the above *E. coli* cultures. Dark-grown and light-grown cultures of YF1 and YF1 H22P, either with or without the adduct-forming cysteine residue, were rapidly frozen in liquid nitrogen. Continuous-wave ESR spectra were recorded and corrected for signals arising from endogenous *E. coli* cell constituents as determined from control cultures not expressing any YF1 variants (Figure 3.3d,e). The ESR spectra of YF1 and YF1 H22P with the adduct-forming Cys residues intact revealed no significant accumulation of flavin radicals above background under either dark or light conditions. By contrast, the cysteine-devoid variants YF1 C62A and YF1 H22P:C62A produced significantly elevated levels of flavin radical species under blue light but not in the dark. Note that the width of these signals ($\sim$10 G) is consistent with the broadening expected from the hyperfine interactions of flavin radicals (Figure 3.3e). These data suggest that photoreduction to the NSQ states of YF1 C62A and YF1 H22P:C62A readily takes place inside living *E. coli* cells and correlates with downstream signalling.

To further verify these *in vivo* effects, we also directly measured the ability of YF1 to regulate FixJ binding to DNA. Once YF1 phosphorylates FixJ, phospho-FixJ assembles into a homodimer and binds to the DNA substrate. In electrophoretic mobility shift assays (EMSA), the resultant complex migrates more slowly than the free DNA substrate (Figure 3.3f). In the dark, YF1 has net kinase activity, FixJ is phosphorylated and the DNA is in complex; by contrast, under blue light, YF1 has net phosphatase activity[21], FixJ is dephosphorylated, and no DNA gel shift is observed. For YF1 C62A, an upshift of the DNA band is seen in the dark, indicating activity as a net kinase. Under blue-light conditions,

most of the DNA is present in its free form and only a small portion is in complex with FixJ. As found *in vivo*, YF1 H22P shows the inverted signal response compared with YF1−an upshift of the DNA band indicative of FixJ phosphorylation under blue-light illumination, but not in the dark. Interestingly, DNA binding of FixJ induced by H22P:C62A was only observed in the light and in the presence of a ROS scavenger system (consisting of catalase, glucose and glucose oxidase). Apparently, under these conditions, YF1 H22P:C62A does generate ROS that can interfere with the FixJ response. Taken together, the *in vitro* results are in agreement with the *in vivo* findings and indicate that cysteine-devoid YF1 variants are capable of signal transduction on photoreduction to the NSQ.

3.3.3 Natural LOV-like proteins lacking the adduct-forming Cys

The observation that photoreduction elicits WT-like signalling responses in two different LOV proteins devoid of the adduct-forming Cys residue suggested that related proteins might occur naturally. A BLAST sequence search in Genbank for LOV-like proteins that contain all residues strictly conserved among LOV domains (see Methods) except for the adductforming cysteine revealed ca. 70 entries with this Cys replaced by one of several other residues, including Ala, His and Pro (Figure 3.4b and Supplementary Figure 3.9a). Cysteine-devoid LOV-like domains, denoted LOV*, are found in proteins with varied architectures (Supplementary Data 3.15). Among these proteins, we focused on a LOV* domain from a halobacterial archaea that has relatively close homology to VVD and contains an unreactive Pro residue in place of the adduct-forming Cys. This LOV* domain is a component of a much larger protein known as bacterio-opsin activator (BAT)[34], which also contains a response-regulator receiver domain, a GAF domain and a helix-turn-helix DNA-binding module. Notably, BAT-LOV* contains no Cys or Met residues, with the position of the adduct-forming Cys occupied by Pro (Figure 3.4b). When over-expressed in *E. coli*, BAT-

LOV* bound modest amounts of flavin but could be reconstituted with either FAD, FMN or riboflavin after incubation with excess cofactor (Supplementary Figure 3.10b). Although BAT-LOV* does not contain an insertion usually found to accommodate the adenosine moiety of FAD-binding LOV domains[11] (Figure 3.4b), reconstitution with FAD yielded no noticeable difference in photoreduction or behaviour on SEC compared with reconstitution with FMN (Supplementary Figures 3.10c and 3.11a). On photoreduction, reconstituted BAT-LOV* accumulated the NSQ with low yield compared with VVD-III (Figure 3.5a and Supplementary Figure 3.11a). Moreover, photoreduction is nearly two orders of magnitude slower than for VVD-III, and the corresponding rates can only be moderately increased by adding external reductive quenchers, such as dithiothreitol (DTT) (Figure 3.5a and Supplementary Figure 3.11a). A small lag phase for BAT-LOV* photoreduction, not seen with VVD-III, depends on the presence of oxygen (Supplementary Figure 3.11b). Low fluorescence quantum yields for BAT-LOV* compared with VVD-III (Table 3.1) indicate a much reduced lifetime of the initial S1 photo-excited state, possibly owing to rapid reversible reductive quenching from internal redox-active residues. Inspection of a BAT-LOV* homology model (Figure 3.4a) identified two Tyr residues and one Trp residue that reside closer to the flavin than any aromatic residues in VVD (Figure 3.4b). Substitution of the Tyr residues to Phe (BAT-II) produced little change in fluorescent yields or NSQ accumulation (Table 3.1). However, additional substitution of Trp172 to Phe (BAT-III) caused a large increase in fluorescent lifetime and photoreduction rates that are similar to those of VVD-III (Table 3.1, Figure 3.5b, Supplementary Figure 3.11a). Notably, most BAT-LOV* homologues contain a Phe at the position of Trp172 (Supplementary Figure 3.9a), and thus would be expected to have similar photoreduction yields as the BAT-III variant examined here.

Although photoreduction of WT BAT-LOV* is ineffective, the protein readily undergoes complete chemical reduction to the HQ (Figure 3.5a and Supplementary Figure 3.12). Reduced BAT-LOV* elutes on SEC with a profile shifted from that of the oxidized dark-

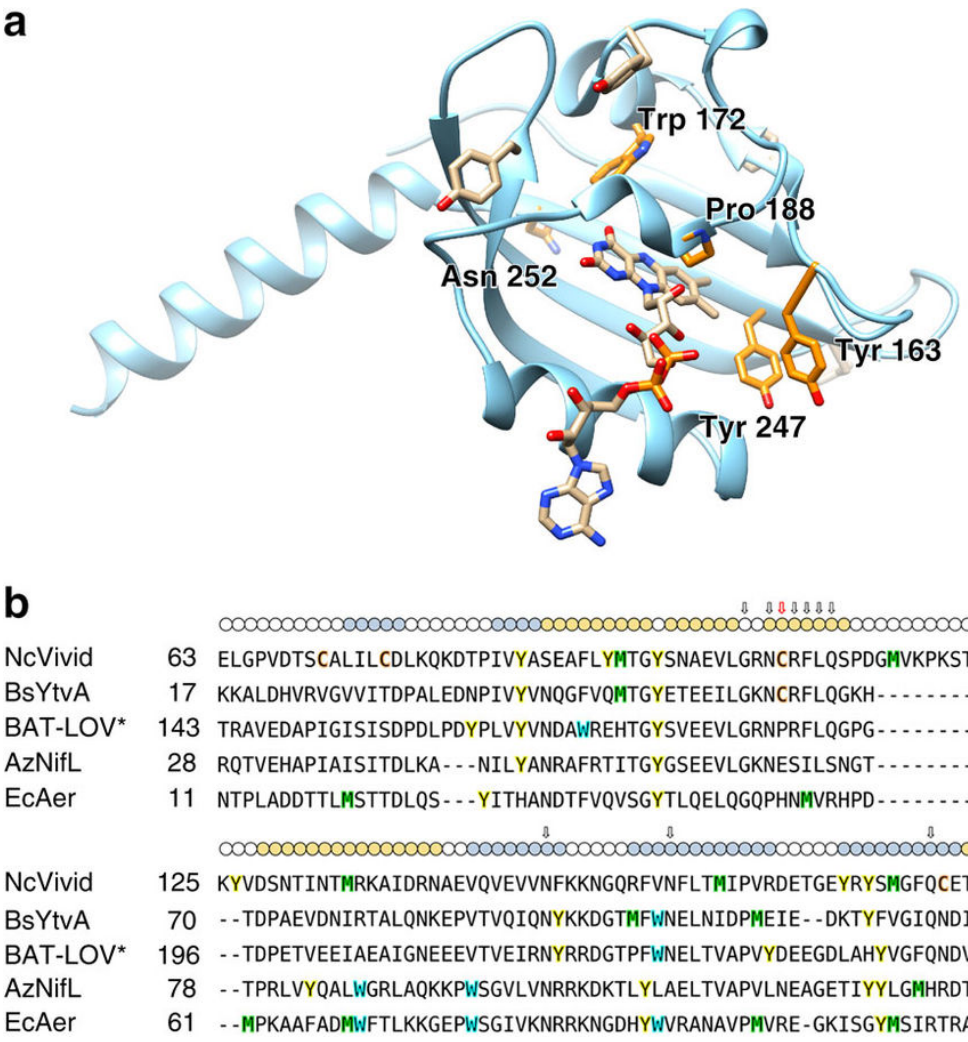

Figure 3.4: Structural model and sequence comparison for BAT-LOV*. (a) Homology model of BAT-LOV* bound to FAD based on sequence similarity to YtvA. Tyr163 and Tyr247 were changed to Phe in BAT-II, with Trp172 also changed to Phe in BAT-III. The P188C substitution (but not N252C) affects photoreduction yields. Three Tyr residues remote from the flavin are also shown. (b) Sequence alignment of VVD, BAT-LOV*, YtvA, *A. vinelandii* NifL and *E. coli* Aer. Tyr residues (yellow), Trp (blue), Cys (orange) and Met (green) are highlighted; circles above the alignment indicate the secondary structure in VVD with β sheets in blue and α helices in orange; arrows denote LOV-conserved residues, with the adduct-forming Cys in VVD and YtvA marked by a red arrow.

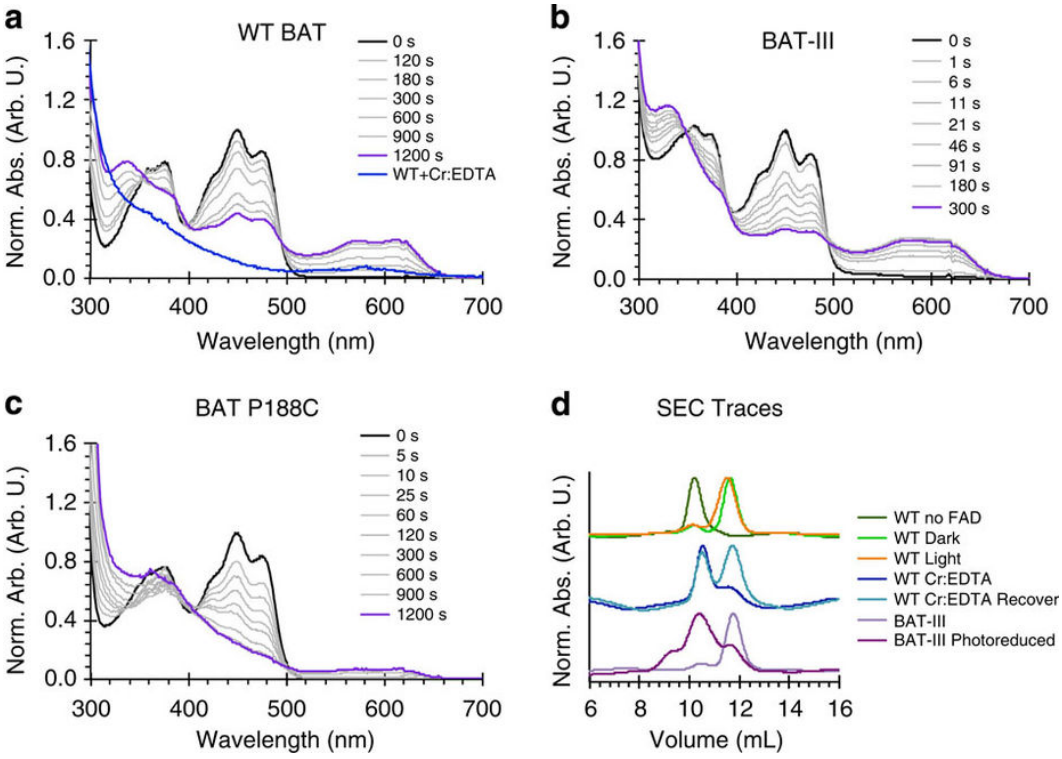

Figure 3.5: Photochemistry of BAT-LOV*. Photoreduction of recombinantly expressed, FAD-reconstituted (a) BAT-LOV* and (b) BAT-III (Y163F:W172F:Y247F). BAT-LOV* reduces slowly to the NSQ, whereas BAT-III reduces to the NSQ much more rapidly. Chemical reduction of BAT-LOV* with Cr:EDTA (blue) forms the HQ directly (a). (c) BAT P188C photoreduces to the HQ with little NSQ intermediate. Experiments in a-c were carried out on similar protein concentrations. See Supplementary Figure 3.11a for photoreduction rate constants. (d) SEC elution profile of BAT-LOV* and variants. Ambient light exposure of BAT-LOV* produces no shift on SEC (WT Dark compared with WT Light); however, chemical reduction (WT Cr:EDTA) results in a shift to an extended conformation that is similar to that of the protein stripped of flavin by anion exchange chromatography (WT no FAD). Reoxidation partially reforms the compact state (WT Cr:EDTA Recover). Photoreduction of BAT-III forms a state similar to that observed for reduced WT BAT-LOV* (BAT-III Photoreduced). Multi-angle light scattering confirmed that BAT-LOV* remained a monomer in the dark and with ambient light exposure; loss of FAD binding also does not alter the oligomeric state of BAT-III (Supplementary Figure 3.13a,b).

Variant	Rate constant [s^{-1}]
VVD-III	≡1.00
BAT-LOV*	0.08 ± 0.02
BAT-LOV* N252C	0.10 ± 0.02
BAT-II Y163F:Y247F	0.08 ± 0.03
BAT-III Y163F:Y247F:W172F	0.58 ± 0.13

BAT, bacterio-opsin activator; LOV, light-oxygen-voltage; VVD, vivid.

Table 3.1 Relative quantum yield of fluorescence for LOV variants.

state protein (Figure 3.5d). When flavin is removed from BAT-LOV*, a similar shift on SEC results, suggesting that reduction destabilizes flavin binding. Nevertheless, the reduced flavin remains loosely associated with BAT-LOV* as the compact state and spectrum for the quinone-bound protein partially recover after reoxidation in air (Figure 3.5d and Supplementary Figure 3.12). WT BAT-LOV* does not shift on SEC with light exposure owing to inefficient photoreduction; however, the more readily photoreduced BAT-III elutes at the same position as chemically reduced BAT-LOV*, while retaining a monomeric molecular mass (Figure 3.5d and Supplementary Figure 3.13a,b). Thus, both reduction processes influence protein conformation and destabilize flavin binding in the isolated LOV* domains. BAT-III recovers fully after reoxidation in aerobic solution, producing a spectrum for oxidized bound flavin (Supplementary Figure 3.11d).

We attempted to convert BAT-LOV* to a traditional LOV mechanism by mutating the active-site Pro residue to Cys. The P188C variant does not undergo conversion to a traditional adduct state with its characteristic 390-nm absorption peak, but the variant is much more readily photoreduced than WT, rivalling the reactivity of BAT-III (Figure 3.5c and Supplementary Figure 3.11a). Interestingly, the P188C appears to form the HQ directly with little NSQ intermediate observed on this time scale. Unlike the C4a adduct in canonical LOV domains, the light-adapted state of the P188C variant can be rapidly chemically oxidized to the quinone state, after which the flavin partially dissociates from the protein (Supplementary Figure 3.14). A control Cys substitution distant from the flavin

(N252C) increases photoreduction only marginally (Supplementary Figure 3.11a).

3.4 Discussion

Cysteine-adduct formation causes substantial changes to the LOV flavin pocket that include electronic redistribution in the cofactor, bond strain and protonation of the flavin N5 atom[2,3,35]. It has been challenging to assign the relative impact of these various factors on signal propagation. In this study, we partially separate these events and directly evaluate the role of the cysteinyl-flavin bond in signalling. As we show for the paradigm LOV photoreceptors VVD and YF1, blue light promotes reduction to the NSQ state in the absence of the adduct-forming cysteine. Corresponding photoreduction has been reported for several other LOV domains in which the adduct-forming cysteine has been replaced[16-18,20,36]. We now demonstrate that LOV NSQ states are biologically functional in that they elicit downstream signalling responses largely equivalent to those for the Cys-adduct states of the parental photoreceptors. In particular, photoreduced VVD-III associates into the same light-adapted dimer as WT VVD. Structural studies of VVD in its dark-adapted and signalling states indeed suggest that conformational changes important for promoting dimerization depend on N5 protonation[12]. These results are further borne out in YF1 C62A variants that on photoreduction show qualitatively the same light responses as the corresponding Cys-containing receptors, both in the original context and in the context of the H22P variant that inverts the light response. We thus conclude that flavin reduction and protonation of the flavin N5 are sufficient for signal transduction in these LOV domains. Our rather unexpected findings account for several puzzling observations in LOV photoreceptors. For example, the residual light responsiveness of the C108A variant of VVD in repressing downstream gene expression[13] can now be explained by photoreduction to the NSQ state. A similar mechanism is likely at play in variants of *Chlamydomonas reinhardtii* phototropin

1, which were found to elicit light responses even though the adduct-forming Cys residues of the two LOV domains had been replaced by mutagenesis (C57S:C250A)[14,15].

The present results also bear on mechanistic studies of LOV photoreceptors and their biotechnological application. Often, cysteine knock-out variants are used as negative controls in LOV photoreceptor studies; given the likelihood of activation by photoreduction, responses from these variants should be carefully considered. Similarly, LOV domains devoid of their adduct-forming cysteine have found frequent use as fluorescent protein tags and as photosensitizers for the generation of ROS[29,30]. As the present results reveal, these model LOV domains may still populate a signalling state through NSQ formation that could have functional consequences, even in heterologous hosts. By contrast, in other scenarios signal transduction by Cys-less LOV variants could be desirable: for example, removal of the adduct-forming cysteine will lower the absolute light sensitivity of LOV photoreceptors as shown for YF1 H22P:C62A (Figure 3.3c), which may be of use in optogenetic applications[22,37]. As demonstrated by BAT-III, photoreduction yields may be tuned by the location of residues capable of reductively quenching the flavin excited-state. Removal of the adduct-forming cysteine hence provides an avenue towards modulating the light-driven forward reaction, which is challenging to perturb in canonical LOV domains[38]. Nonetheless, we reiterate that cysteine-devoid LOV variants come with enhanced fluorescence and ROS generation[29,30].

Our results reveal commonalities among flavin-based photo- and redox receptors that could reflect evolutionary relationships among them. In the canonical LOV photocycle, a flavin excited triplet state reacts with the thiol group of a conserved cysteine residue[2,3,35]. Bond formation likely proceeds via a redox process, as supported by detection of a transient flavin NSQ in *C. reinhardtii* phot1 LOV1 [6], by indirect arguments from magnetic resonance experiments[39,40], and by the general efficacy of flavin photoreduction in the cysteine-devoid

variants[16-18,20,36]. Thus, the NSQ is a likely intermediate in generating the adduct. The BAT-LOV* P188C variant demonstrates that Cys at the adduct-forming position is an effective electron donor to the photo-excited flavin. LOV signalling through the NSQ state has intriguing parallels to signal transduction in the other flavin-based photoreceptor classes cryptochrome and BLUF[1-3]. Although controversial, there is strong evidence that the signalling state of cryptochromes involves reduction of the FAD to either the NSQ or anionic semiquinone states[1,3,41]. While the details of BLUF photochemistry are still under intense debate, a NSQ state may be populated transiently during the photocycle as part of a radical-pair intermediate between the flavin and a conserved Tyr (FADH−O-Tyr)[42]. Interestingly, removal of the conserved Tyr allows efficient photoreduction of the BLUF protein to the NSQ state[43]; moreover, this NSQ state regulates the activity of an adenylate-cyclase effector, albeit with inverted polarity and reduced dynamic range compared with WT.

Changes in flavin redox state affect conformation and flavin binding in the naturally Cys-less BAT-LOV*. BAT regulates expression of bacteriorhodopsin, a light-driven proton pump expressed in halobacteria under conditions of high light intensity and low oxygen levels[34]. A direct response to light by BAT has been suggested[34] but has not been definitively established. BAT-LOV* shares some relationship to the flavin-binding oxygen sensor proteins *E. coli* Aer[44] and *Azotobacter vinelandii* NifL, but its sequence is more similar to LOV domains, such as those of VVD or YF1 (Figure 3.4b). Aer, which senses O_2 indirectly by a redox response to the membrane potential[44], can also act as a photoreceptor[45]. BAT retains the conserved Gln for responding to protonation changes at N5 and indeed changes conformation on flavin reduction. The isolated BAT-LOV* domain studied here cannot be effectively photoreduced because its excited-state lifetime is too short, owing to reductive quenching by neighbouring aromatic residues. However, substitution of an unconserved Trp to its more typical occurrence of Phe generates photoreduction yields that rival those of VVD-III. Thus, for both BAT and possibly Aer, either chemical or light-driven flavin

reduction may trigger downstream signalling.

Our demonstration that the isolated BAT-LOV* domain binds flavin and conformationally responds to chemical or photoreduction lends strength to the assertion that this module acts as an integrated redox/light sensor in the regulation of bacteriorhodopsin production. The reactivity of BAT-LOV* also raises the question as to whether ancestral LOV proteins were redox sensors that bound flavin but did not contain an adduct-forming Cys. Introduction of such a reactive Cys would preserve the light-adapted state and thereby increase effective light sensitivity. Increased photoreduction yields made possible by a neighbouring Cys donor, as we observe with BAT-LOV* P188C, may have been an intermediate step in the generation of an adduct mechanism. Structural changes that then promoted bond formation would have made photoreception less susceptible to changes in redox potential. As a result, Cys incorporation could have rapidly disseminated due to its utility for photosensing. It may be no accident that the flavin chromophores of certain LOV photoreceptors have redox potentials in the physiologically relevant range[46]. Thus, the division between photosensor and redox sensor may be small, particularly for flavoproteins in which the polypeptide responds to changes in the flavin redox state, whether they be generated chemically or by light.

3.5 Materials and Methods

3.5.1 Molecular biology and protein expression

VVD constructs were cloned into pET28a vectors and over-expressed in *E. coli* BL21(DE3) cells as previously described[11,12]. Expression of VVD variants was induced with 100 mM isopropyl β-D-1-thiogalactopyranoside (IPTG) for 20 h at 17 °C under con-

stant light. Proteins were purified by Ni:NTA affinity chromatography, followed by SEC on HiLoad 26/60 Superdex 75 or 200 prep grade columns with 50 mM HEPES (pH 8), 150 mM NaCl, 10% (v/v) glycerol.

Site-directed mutants of YF1 were generated in the background of the expression plasmid pET-41a-YF1 [27] via the QuikChange protocol (Invitrogen, Life Technologies GmbH). For assaying YF1 activity *in vivo*, corresponding mutants were also introduced into the reporter plasmid pDusk-myc-DsRed[27,28]. Purification of YF1 WT and site-specific mutants was carried out as described previously[27]. Briefly, expression in *E. coli* BL21 CmpX13 cells[47] was induced with 1 mM IPTG for 4 h at 37 °C. Proteins were purified by Ni:NTA affinity chromatography and dialysed into storage buffer (10 mM Tris-HCl (pH 8.0), 10 mM NaCl, 10% (v/v) glycerol). Protein concentration was determined by absorption measurements with an Agilent 8453 UV-vis spectrophotometer (Agilent Technologies, Santa Clara, CA, USA) using an extinction coefficient at 450 nm of 12,500 M^{-1} cm^{-1}. Full-length FixJ was expressed and purified as previously[21], with the exception that the N-terminal His_6 affinity tag was not cleaved off. Protein concentration was calculated using an extinction coefficient of 4,860 M^{-1} cm^{-1} at 280 nm [21].

The gene from *Halorubrum hochstenium* (ATCC 700873) BAT, residues $141 - 275$, was synthesized by Biomatik in Bluescript (pBSK + Simple), and was cloned into pET28a via restriction with NdeI and XhoI. The protein was overexpressed with an N-terminal His_6 tag and purified from *E. coli* BL21(DE3) cells as described for VVD, except that after induction expression was executed at 37 °C for 3 h under constant light. After SEC, samples were further purified by HiPrep Q XL 16/10 to remove endogenous flavin. Samples were incubated with free flavin nucleotide in a buffer containing 0.5 M NaCl for at least 12 h. Unbound flavin was removed by buffer exchange through 10 kDa cutoff centrifugal filters (Amicon). Mutant variants of BAT were prepared by site-directed mutagenesis.

The identity of all constructs was confirmed by DNA sequencing at the Biotechnology Resource Center of Cornell University or by LGC Genomics (Berlin, Germany).

3.5.2 Absorption and fluorescence spectroscopy

Photoreduced species of VVD and BAT were monitored by irradiating dark-state samples with 448-nm diode laser light (30 mW; World Star Tech) perpendicular to the observation beam. Full spectra were collected on an Agilent 8453 diode-array spectrophotometer as a function of time. In kinetics mode, data were obtained by monitoring samples at 450 nm with a cycle time of $0.5 - 1.0$ s under temperature control. Traces were normalized and fit with MATLAB (The MathWorks Inc., Natick, MA, USA) to equation (1)

$$y(t) = A(1 - e^{-k_1(t-t_0)}) + B(1 - e^{-k_2(t-t_0)}) + y_0 \tag{3.1}$$

where A, B, y_0 are coefficients, t_0 is the x-axis offset, and k_1 and k_2 are rate constants. In the case of BAT-III and P188C, the data were fit to the triexponential version of equation (1).

Absorption spectra for YF1 variants were recorded with an Agilent 8453 spectrophotometer as described above except that samples were illuminated with 455-nm light (Royal Blue, Luxeon Star, 50 mW cm^{-2}) at 22 °C until the photostationary state was reached. Photobleaching and recovery kinetics were followed by recording absorption spectra. Data evaluation was carried out with Origin (OriginLab, Northampton, MA, USA).

Fluorescence measurements were carried out on a Varian Cary Eclipse fluorometer. For kinetic measurements of fluorescent quenching by photoreduction, samples were excited at 450 nm using a 10-nm bandwidth, and emission data were collected at 508 nm using a 5-nm slit width with 0.1 s averaging. Kinetic traces were normalized and fit by MATLAB

using equation (1) with $y_0 = 1$. Fluorescence intensities used for relative quantum yield measurements were collected at 525 nm over the first 5 s of excitation at 450 nm. Reoxidation spectra of P188C were recorded by treatment with $[Co(phen)_3](ClO_4)_3 \cdot 2H_2O$, which was prepared as described[48].

3.5.3 Analytical SEC

Purified samples of VVD and BAT-LOV* were verified to be in their dark state by absorption spectroscopy, as indicated by the absence of adduct- or NSQ-related features. Samples were immediately loaded onto equilibrated foil-covered Superdex 75 or 200 10/300 GL columns. Light-activated samples were obtained by irradiation on ice until a significant amount of adduct or NSQ built up. Samples were checked by UV-vis spectroscopy and immediately loaded onto the uncovered column, with constant external illumination throughout the run. Reduced BAT samples were prepared anaerobically with the addition of 12 mM chromium (II) EDTA complex (Cr:EDTA)[49] and immediately loaded onto the column with degassed buffer (50 mM HEPES (pH 7.5), 500 mM NaCl, 2 mM TCEP, 5 mM DTT). BAT-III samples were photoreduced in the same degassed buffer and loaded onto the column.

3.5.4 Multi-angle light scattering

A 5.0 mg ml^{-1} solution of Bovine Serum Albumin (BSA, Sigma) was injected onto a Phenomenex Bio Sep-SEC-s 300 column that had been equilibrated in GF buffer containing 50 mM Tris (pH 7.5) and 150 mM NaCl to normalize the light-scattering detectors and act as a calibration control for both peak alignment and molecular weight determinations. Purified protein samples ($1-10$ mg ml^{-1}) were then injected onto the same column. BAT-

III samples were run using degassed buffer (50 mM HEPES (pH 7.5), 500 mM NaCl, 2 mM TCEP, 5 mM DTT). The SEC (WTC050N5−Wyatt) is coupled to a static 18-angle light-scattering detector (DAWN HELEOS-II), a refractive index detector (Optilab T-rEX; Wyatt Technology) and dynamic light-scattering device (WyattQELS). Data were collected every second for 30 min at the flow rate of 1 ml min^{-1} at 25 °C. The ASTRA V software was used to extract the molar weight distribution, root-mean-square radius, radius of hydration and the polydispersity of each resolved peak, which were taken as averages across the elution peaks. Concentrations were determined by the refractive index indicator.

3.5.5 YF1 *in vivo* and *in vitro* activity assays

In vivo activity measurements of YF1 WT and variants were conducted in the pDusk-DsRed reporter system as described[28]. Briefly, for each construct, three 5-ml LB/Kan cultures were incubated overnight at 37 °C and 225 r.p.m. either in the dark or under constant blue light (470 nm, 100 mW cm^{-2}). OD_{600} and DsRed fluorescence were measured using black-walled 96-well mClear plates (Greiner BioOne, Frickenhausen, Germany) with a Tecan Infinite M200 PRO plate reader (Tecan Group Ltd. Mannedorf, Switzerland). Fluorescence excitation and emission wavelengths were set at 554±9 nm and 591±20 nm, respectively. Data were normalized to the fluorescence per OD_{600} for YF1 WT under dark conditions and represent the averages of three biological replicates±s.d. Light-dose experiments were conducted as above except that the intensity of 470-nm light was varied between 0 and 150 mW cm^{-2}. Light intensities were determined with a power meter (model 842-PE, Newport) and a silicon photodetector (model 918D-UV-OD3, Newport).

Net kinase activities of YF1 variants were assessed *in vitro* by monitoring the binding of phospho-FixJ to DNA using EMSA. A double-stranded DNA fragment containing part of the FixK2 promoter sequence was produced by heating to 95 °C

and then slowly cooling a mixture of 100 mM forward oligonucleotide primer (5' - GAGCGATATCTTAAGGGGGGTGCCTTACGTAGAACCC-3') labelled at its 5' -end with (5-and-6)-carboxytetramethylrhodamine (TAMRA) and 100 mM of the reverse complementary primer in 5 mM Tris-HCl (pH 8.0); the high-affinity FixJ binding site is underlined[50,51]. To analyse net kinase activities, 250 nM YF1 WT or variants were mixed with 1 mM ATP and 1.25 mM FixK2-DNA substrate in 10 mM HEPES (pH 8.0), 80 mM KCl, 2.5 mM MgCl2, 0.1 mM EDTA, 100 mg ml^{-1} BSA, 10% (v/v) glycerol, 4% (v/v) ethylene glycol and 10 mM Tris(2-carboxyethyl) phosphine. In case of YF1 variants harbouring the mutation C62A, a ROS scavenger system containing 0.5 mg ml^{-1} glucose oxidase, 5 mg ml^{-1} glucose and 30 U catalase was added to the reaction mixture, and the buffer concentration was raised to 200 mM HEPES. The mixture was either kept in the dark or incubated under constant blue light (455 nm, 50 mW cm^{-2}) at 30 °C for 15 min followed by addition of 30 mM FixJ. Samples were further incubated for 30 min and then run on a native 6% (w/v) acrylamide gel in TBE buffer (89 mM Tris, 89 mM borate, 2 mM ethylenediaminetetraacetic acid, pH 8.3) at 100 V for 45 min. DNA bands were visualized in a Fujifilm image reader FLA 3000 (Fujifilm Holdings K. K.) using excitation and emission wavelengths of 532 and 580 nm, respectively.

3.5.6 Electron spin resonance spectroscopy

For pulsed-dipolar ESR experiments, samples containing 350 mM VVD and 30% glycerol (v/v) were irradiated with 448-nm diode laser light on ice for several minutes until uniformly pale blue in colour and then were flash-frozen in liquid nitrogen. Four-pulse DEER experiments were conducted at 100 K on a 17.3 GHz Fourier Transform ESR spectrometer, which is modified to perform pulsed-dipolar ESR experiments[52,53]. $\pi/2$ and π pulses were 20 ns and 40 ns, respectively, with a frequency separation of 60 MHz. Pumping was applied

at the high-field side of the ESR spectrum, with detection on the opposite low-field slope. Data averaging time was 23 h. The baseline used for data processing was approximated by a single exponential function, which slightly deviates from a linear polynomial. Distance distributions of spin separations within the sample were calculated by the Tikhonov method and refined by the maximum entropy regularization[53].

For cw-ESR measurements on YF1 variants, E. coli cultures were transferred into quartz tubes (QSIL GmbH, Ilmenau, Germany; 3.0 mm/3.9 mm inner/outer diameter), were either kept in the dark or were illuminated with a 450 nm LED (LUXEON Lumiled, Phillips Lumileds, San Jose, CA, USA) for 5 min, and were then rapidly frozen in liquid nitrogen. cw-ESR spectra were recorded on a laboratory-built X-Band spectrometer, consisting of a microwave bridge ER 041 MR, microwave controller ER 048R, magnet power supply ER 081S, field controller BH 15 and cavity resonator ER 4122 SHQ E all from Bruker. For signal detection, a Stanford Research SR810 lock-in detector (Stanford Research, Sunnyvale, CA, USA) was used. Microwave frequency measurements were performed using an Agilent 53181A frequency counter (Agilent Technologies). The samples were measured with 4G modulation amplitude, 100 kHz modulation frequency and 100 ms lock-in time constant. The microwave power was 60 mW and the frequency was ∼9.38 GHz. For each measurement, the current microwave frequency was recorded. The spectra were then normalized to 9.6 GHz. During cw-ESR measurements, samples were maintained at 80 K with an Oxford ESR 910 cryostat and Oxford ITC503 temperature controller. The reported spectra are averages over 40 scans.

3.5.7 Sequence analysis and homology modelling

Using Biopython, a BLAST search was performed with the residues $1-127$ of B. subtilis YtvA (PHOT_BACSU) as the query sequence and with an E-value of 10 as cutoff. The

BLAST results were filtered for entries that lack the adduct-forming cysteine (corresponding to residue C62 in YtvA) but possess at least 9 out of the other 10 conserved amino acids in LOV domains (corresponding to residues G59, N61, R63, F64, L65, Q66, N94, N104 and Q123 in YtvA). The resultant list was manually curated to remove entries that correspond to proteins in which the active-site cysteine was deliberately removed by mutation, for example, in LOV domains used as fluorophores. Sequences were further filtered to remove closely similar entries (cutoff 90% sequence identity). All remaining entries were aligned to the sequences of VVD and YtvA using ClustalX54.

A homology model of BAT-LOV* was calculated using SWISS-MODEL[55] and YtvA as the template structure (PDB entry 2PR6), which possesses a sequence similarity of 45.2% compared with BAT-LOV*. Sequence alignment was achieved with Clustal Omega at EMBL-EBI54.

3.6 Acknowledgements

We thank members of the Crane and Möglich groups for discussion. Financial support from NIH grant R01 GM079679 (to B.R.C.), from NIH training grant T32 GM08267 (to E.F.Y.), NIH/NIGMS ACERT center grant P41GM103521 (to J.H.F.), from a Sofja-Kovalevskaya Award by the Alexander-von-Humboldt Foundation (to A.M.), from Deutsche Forschungsgemeinschaft (DFG) within the Cluster of Excellence Unifying Concepts in Catalysis 'UniCat' and grant BI 464/10 within priority program SPP 1601 (to R.B.) and from DFG grant MO 2192/3-1 within research group FOR 1279 (to A.M.) are all gratefully acknowledged.

3.7 Supplementary Information

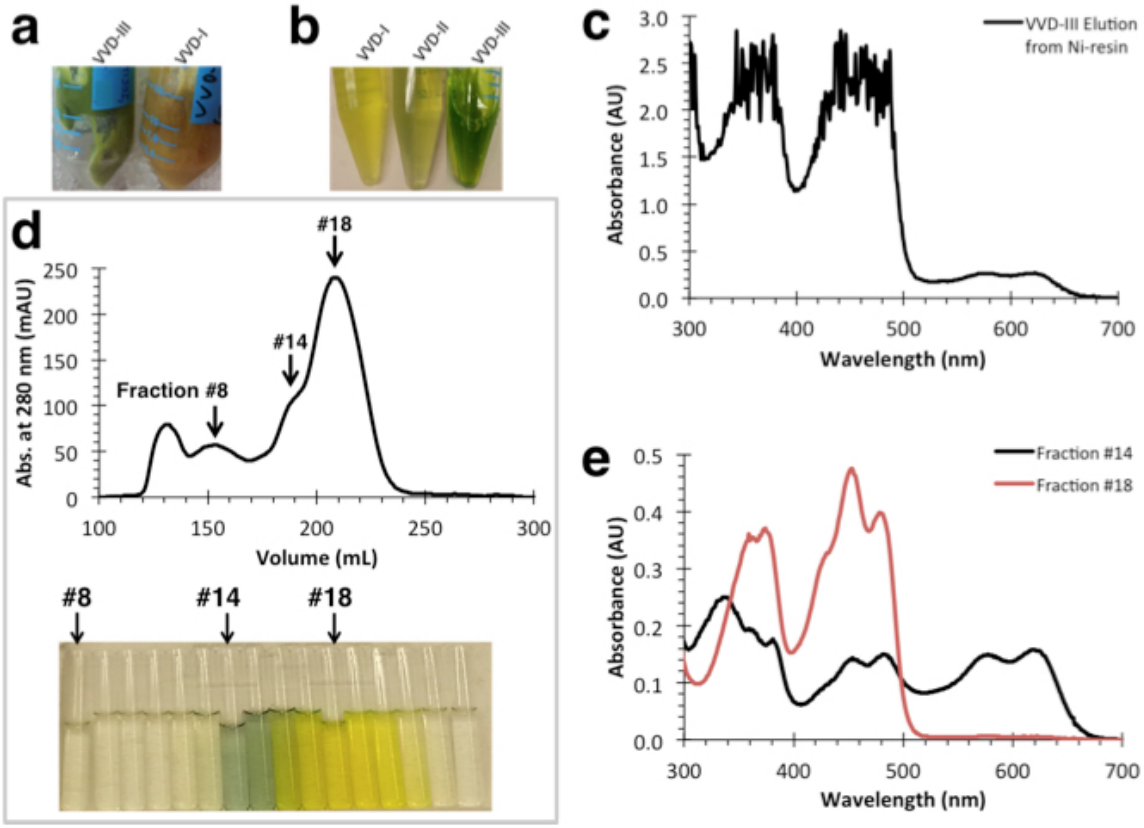

Supplementary Figure 3.6: VVD-III purifies in a reduced state. (a) The cell pellet of VVD-III (VVD Δ36 C108A:M135I:M165I) is green compared to VVD-I (wild type VVDΔ36) due to the accumulation of the neutral semiquinone radical. (b) Purified VVD-I is yellow, VVD-II (VVD Δ36 M135I:M165I) is pale green, while VVD-III is dark green. (c) Absorption spectrum of purified VVD-III, shown in (b), reveals a mixture of oxidized (450 nm) and neutral semiquinone (577 nm, 621 nm) states of FAD. (d) Size Exclusion Chromatography (SEC) profile of VVD-III shows that the different redox forms of VVD separate by size; fractions corresponding to the peaks are shown above. (e) Absorption spectra of fraction #14 (d), which elutes earlier than #18, contains a neutral semiquinone state of VVD-III, whereas #18 contains the oxidized form.

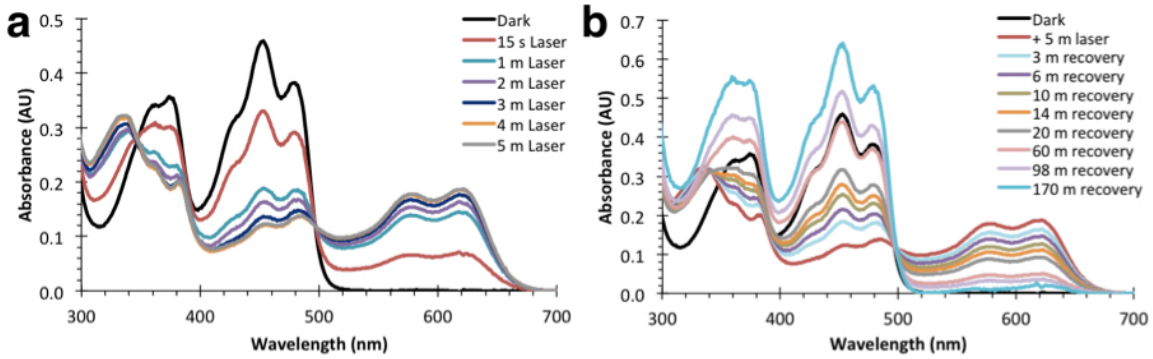

Supplementary Figure 3.7: Photoreduction of VVD-III. (a) Time course for photoreduction of VVD-III to a neutral semiquinone with a 30 mW 448-nm laser, as monitored by absorption spectroscopy (note the two isosbestic points at 347 nm and 497 nm). (b) Reoxidation of VVD-III under ambient aerobic conditions. Precipitation of some protein during the experiments causes light scattering and greater absorption at wavelengths <500 nm compared to the dark-adapted sample.

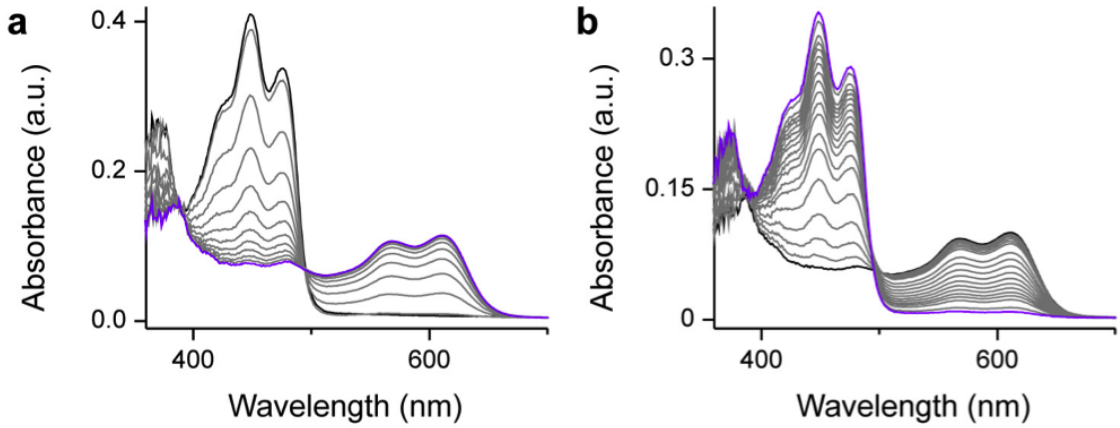

Supplementary Figure 3.8: Photoreduction of YF1 C62A.(a) Photoreduction of YF1 C62A in the presence of 10 mM TCEP was followed by absorption spectroscopy. The sample was continuously illuminated with 455-nm light (50 mW cm^{-2}), and absorption spectra were recorded using a diode-array spectrophotometer. To avoid excitation of the sample by probe light, spectra were recorded with the tungsten lamp only, with the deuterium lamp turned off; hence spectra below ∼370 nm suffer from poor signal-to-noise ratio. From top to bottom, spectra were recorded 1, 62, 122, 182, 242, 302, 362, 422, 482, 542, 602, and 662 s after onset of illumination. (b) Following saturating photoreduction to the NSQ state, the recovery was monitored in the dark under otherwise identical experimental settings. From top to bottom, spectra were recorded 0, 120, 240, 390, 570, 750, 930, 1440, 1800, 2160, 2520, 2880, 3240, 3600, 3960, 4320, 4750, 6190, and 7630 s after blue-light illumination ceased.

a

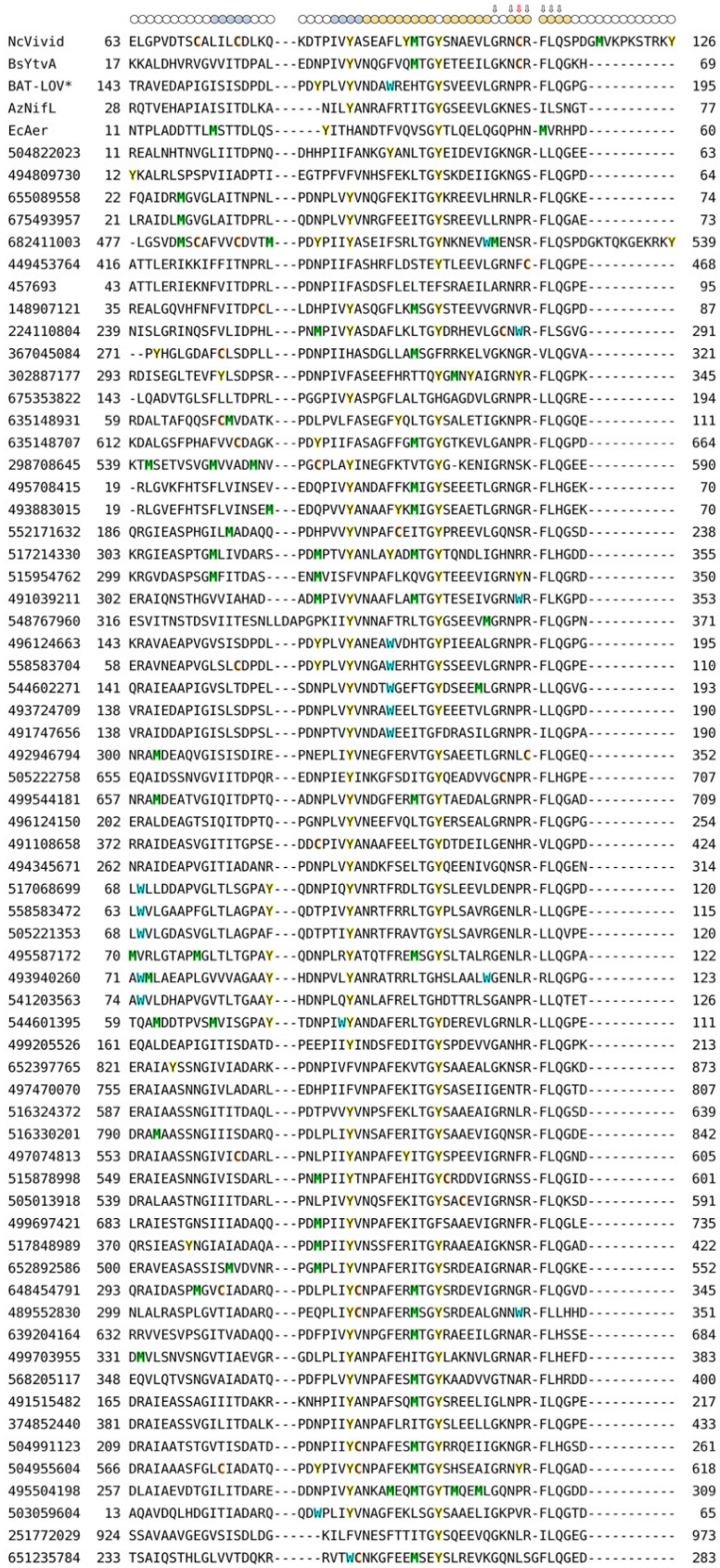
NcVivid 63 ELGPVDTSCALILCDLKQ---KDTPIVYASEAFLYMTGYSNAEVLGRNCR-FLQSPDGMVKPKSTRKY 126
BsYtvA 17 KKALDHVRVGVVITDPAL---EDNPIVYVNQGFVQMTGYETEEILGKNCR-FLQGKH---------- 69
BAT-LOV* 143 TRAVEDAPIGISISDPDL---PDYPLVYVNDAWREHTGYSVEEVLGRNPR-FLQGPG---------- 195
AzNifL 28 RQTVEHAPIAISITDLKA------NILYANRAFRTITGYGSEEVLGKNES-ILSNGT---------- 77
EcAer 11 NTPLADDTTLMSTTDLQS------YITHANDTFVQVSGYTLQELQGQPHN-MVRHPD---------- 60
504822023 11 REALNHTNVGLIITDPNQ---DHHPIIFANKGYANLTGYEIDEVIGKNGR-LLQGEE---------- 63
494809730 12 YKALRLSPSPVIIADPTI---EGTPFVFVNHSFEKLTGYSKDEIIGKNGS-FLQGPD---------- 64
655089558 22 FQAIDRMGVGLAITNPNL---PDNPLVYVNQGFEKITGYKREEVLHRNLR-FLQGKE---------- 74
675493957 21 LRAIDLMGVGLAITDPRL---QDNPLVYVNRGFEEITGYSREEVLLRNPR-FLQGAE---------- 73
682411003 477 -LGSVDMSCAFVVCDVTM---PDYPIIYASEIFSRLTGYNKNEVWMENSR-FLQSPDGKTQKGEKRKY 539
449453764 416 ATTLERIKKIFFITNPRL---PDNPIIFASHRFLDSTEYTLEEVLGRNFC-FLQGPE---------- 468
457693 43 ATTLERIEKNFVITDPRL---PDNPIIFASDSFLELTEFSRAEILARNRR-FLQGPE---------- 95
148907121 35 REALGQVHFNFVITDPCL---LDHPIVYASQGFLKMSGYSTEEVVGRNVR-FLQGPD---------- 87
224110804 239 NISLGRINQSFVLIDPHL---PNMPIVYASDAFLKLTGYDRHEVLGCNWR-FLSGVG---------- 291
367045084 271 --PYHGLGDAFCLSDPLL---PDNPIIHASDGLLAMSGFRRKELVGKNGR-VLQGVA---------- 321
302887177 293 RDISEGLTEVFYLSDPSR---PDNPIVFASEEFHRTTQYGMNYAIGRNYR-FLQGPK---------- 345
675353822 143 -LQADVTGLSFLLTDPRL---PGGPIVYASPGFLALTGHGAGDVLGRNPR-LLQGRE---------- 194
635148931 59 RDALTAFQQSFCMVDATK---PDLPVLFASEGFYQLTGYSALETIGKNPR-FLQGQE---------- 111
635148707 612 KDALGSFPHAFVVCDAGK---PDYPIIFASAGFFGMTGYGTKEVLGANPR-FLQGPD---------- 664
298708645 539 KTMSETVSVGMVVADMNV---PGCPLAYINEGFKTVTGYG-KENIGRNSK-FLQGEE---------- 590
495708415 19 -RLGVKFHTSFLVINSEV---EDQPIVYANDAFFKMIGYSEEETLGRNGR-FLHGEK---------- 70
493883015 19 -RLGVEFHTSFLVINSEM---EDQPVVYANAAFYKMIGYSEAETLGRNGR-FLHGEK---------- 70
552171632 186 QRGIEASPHGILMADAQQ---PDHPVVYVNPAFCEITGYPREEVLGQNSR-FLQGSD---------- 238
517214330 303 KRGIEASPTGMLIVDARS---PDMPTVYANLAYADMTGYTQNDLIGHNRR-FLHGDD---------- 355
515954762 299 KRGVDASPSGMFITDAS----ENMVISFVNPAFLKQVGYTEEEVIGRNYN-FLQGRD---------- 350
491039211 302 ERAIQNSTHGVVIAHAD----ADMPIVYVNAAFLAMTGYTESEIVGRNWR-FLKGPD---------- 353
548767960 316 ESVITNSTDSVIITESNLLDAPGPKIIYVNNAFTRLTGYGSEEVMGRNPR-FLQGPN---------- 371
496124663 143 KRAVAEAPVGVSISDPDL---PDYPLVYANEAWVDHTGYPIEEALGRNPR-FLQGPG---------- 195
558583704 58 ERAVNEAPVGLSLCDPDL---PDYPLVYVNGAWERHTGYSSEEVLGRNPR-FLQGPE---------- 110
544602271 141 QRAIEAAPIGVSLTDPEL---SDNPLVYVNDTWGEFTGYDSEEMLGRNPR-LLQGVG---------- 193
493724709 138 VRAIEDAPIGISLSDPSL---PDNPLVYVNRAWEELTGYEEETVLGRNPR-LLQGPD---------- 190
491747656 138 VRAIDDAPIGISLSDPSL---PDNPTVYVNDAWEEITGFDRASILGRNPR-ILQGPA---------- 190
492946794 300 NRAMDEAQVGISISDIRE---PNEPLIYVNEGFERVTGYSAEETLGRNLC-FLQGEQ---------- 352
505222758 655 EQAIDSSNVGVIITDPQR---EDNPIEYINKGFSDITGYQEADVVGCNPR-FLHGPE---------- 707
499544181 657 NRAMDEATVGIQITDPTQ---ADNPLVYVNDGFERMTGYTAEDALGRNPR-FLQGAD---------- 709
496124150 202 ERALDEAGTSIQITDPTQ---PGNPLVYVNEEFVQLTGYERSEALGRNPR-FLQGPG---------- 254
491108658 372 RRAIDEASVGITITGPSE---DDCPIVYANAAFEELTGYDTDEILGENHR-VLQGPD---------- 424
494345671 262 NRAIDEAPVGITIADANR---PDNPLVYANDKFSELTGYQEENIVGQNSR-FLQGEN---------- 314
517068699 68 LWLLDDAPVGLTLSGPAY---QDNPIQYVNRTFRDLTGYSLEEVLDENPR-FLQGPD---------- 120
558583472 63 LWVLGAAPFGLTLAGPAY---QDTPIVYANRTFRRLTGYPLSAVRGENLR-LLQGPE---------- 115
505221353 68 LWVLGDASVGLTLAGPAF---QDTPTIYANRTFRAVTGYSLSAVRGENLR-LLQVPE---------- 120
495587172 70 MVRLGTAPMGLTLTGPAY---QDNPLRYATQTFREMSGYSLTALRGENLR-LLQGPA---------- 122
493940260 71 AWMLAEAPLGVVVAGAAY---HDNPVLYANRATRRLTGHSLAALWGENLR-RLQGPG---------- 123
541203563 74 AWVLDHAPVGVTLTGAAY---HDNPLQYANLAFRELTGHDTTRLSGANPR-LLQTET---------- 126
544601395 59 TQAMDDTPVSMVISGPAY---TDNPIWYANDAFERLTGYDEREVLGRNLR-LLQGPE---------- 111
499205526 161 EQALDEAPIGITISDATD---PEEPIIYINDSFEDITGYSPDEVVGANHR-FLQGPK---------- 213
652397765 821 ERAIAYSSNGIVIADARK---PDNPIVFVNPAFEKVTGYSAAEALGKNSR-FLQGKD---------- 873
497470070 755 ERAIAASNNGIVLADARL---EDHPIIFVNPAFEKITGYSASEIIGENTR-FLQGTD---------- 807
516324372 587 ERAIAASSNGITITDAQL---PDTPVVYVNPSFEKLTGYSAAEAIGRNLR-FLQGSD---------- 639
516330201 790 DRAMAASSNGIIISDARQ---PDLPLIYVNSAFERITGYSAAEVIGQNSR-FLQGDE---------- 842
497074813 553 DRAIAASSNGIVICDARL---PNLPIIYANPAFEYITGYSPEEVIGRNFR-FLQGND---------- 605
515878998 549 ERAIEASNNGIVISDARL---PNMPIIYTNPAFEHITGYCRDDVIGRNSS-FLQGID---------- 601
505013918 539 DRALAASTNGIIITDARL---PNLPIVYVNQSFEKITGYSACEVIGRNSR-FLQKSD---------- 591
499697421 683 LRAIESTGNSIIIADAQQ---PDMPIIYVNPAFEKITGFSAAEVIGRNFR-FLQGLE---------- 735
517848989 370 QRSIEASYNGIAIADAQA---PDMPIIYVNSSFERITGYRAAEAIGKNSR-FLQGAD---------- 422
652892586 500 ERAVEASASSISMVDVNR---PGMPLIYVNPAFERITGYSRDEAIGRNAR-FLQGKE---------- 552
648454791 293 QRAIDASPMGVCIADARQ---PDLPLIYCNPAFERMTGYSRDEVIGRNGR-FLQGVD---------- 345
489552830 299 NLALRASPLGVTIADARQ---PEQPLIYCNPAFERMSGYSRDEALGNNWR-FLLHHD---------- 351
639204164 632 RRVVESVPSGITVADAQQ---PDFPIVYVNPGFERMTGYRAEEILGRNAR-FLHSSE---------- 684
499703955 331 DMVLSNVSNGVTIAEVGR---GDLPLIYANPAFEHITGYLAKNVLGRNAR-FLHEFD---------- 383
568205117 348 EQVLQTVSNGVAIADATQ---PDFPLVYVNPAFESMTGYKAADVVGTNAR-FLHRDD---------- 400
491515482 165 DRAIEASSAGIIITDAKR---KNHPIIYANPAFSQMTGYSREELIGLNPR-ILQGPE---------- 217
374852440 381 DRAIEASSVGILITDALK---PDNPIIYANPAFLRITGYSLEELLGKNPR-FLQGPE---------- 433
504991123 209 DRAIAATSTGVTISDATD---PDNPIIYCNPAFESMTGYRRQEIIGKNGR-FLHGSD---------- 261
504955604 566 DRAIAAASFGLCIADATQ---PDYPIVYCNPAFEKMTGYSHSEAIGRNYR-FLQGAD---------- 618
495504198 257 DLAIAEVDTGILITDARE---DDNPIVYANKAMEQMTGYTMQEMLGQNPR-FLQGDD---------- 309
503059604 13 AQAVDQLHDGITIADARQ---QDWPLIYVNAGFEKLSGYSAAELIGKPVR-FLQGTD---------- 65
251772029 924 SSAVAAVGEGVSISDLDG------KILFVNESFTTITGYSQEEVQGKNLR-ILQGEG---------- 973
651235784 233 TSAIQSTHLGLVVTDQKR------RVTWCNKGFEEMSEYSLREVKGQNLSGFLQGED---------- 283

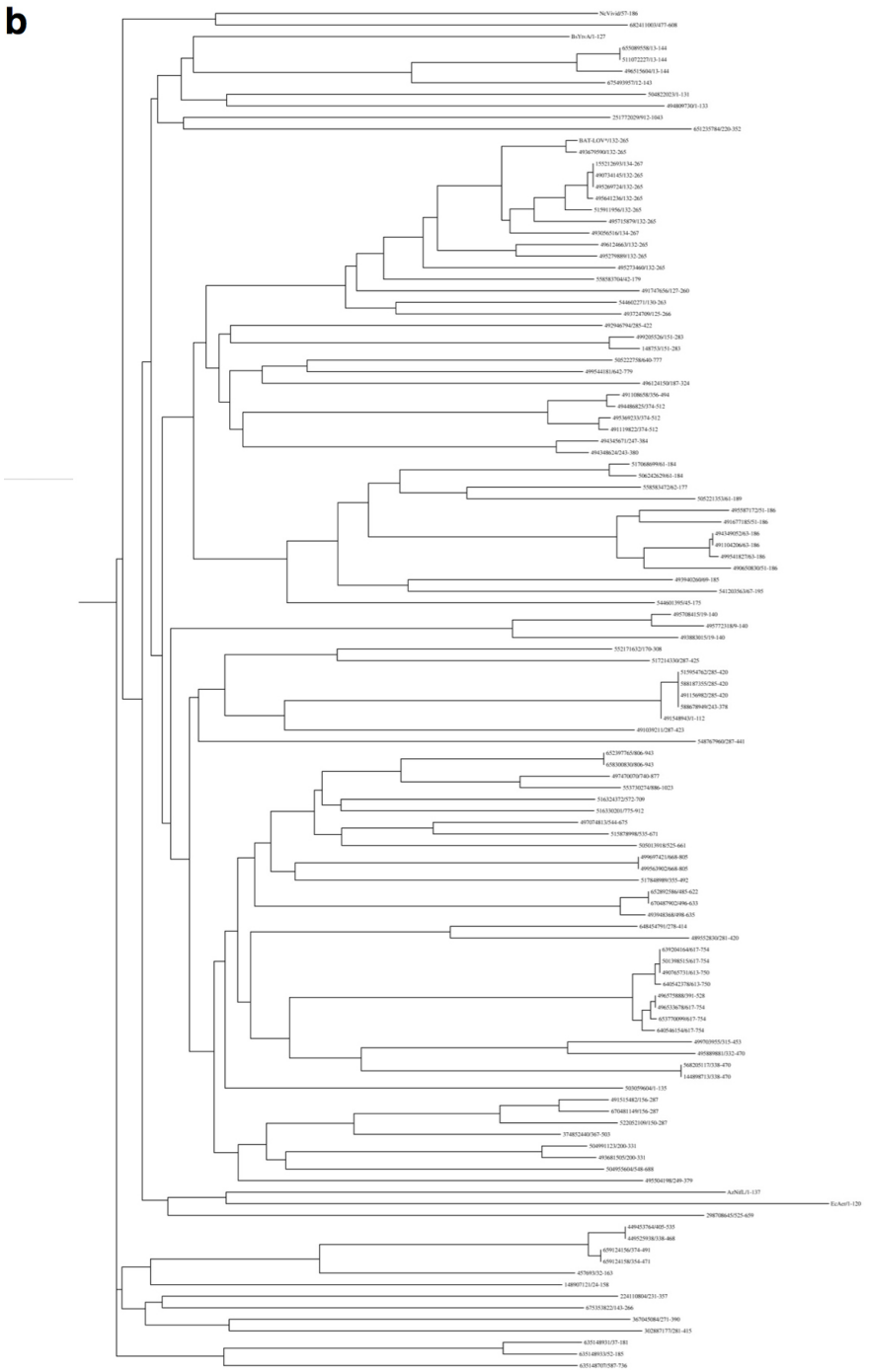

Supplementary Figure 3.9: Extended alignment of natural Cys-less LOV* domains. (a) Sequence alignment of VVD, BAT-LOV*, *B. subtilis* YtvA, *A. vinelandii* NifL, *E. coli* Aer, and LOV-like proteins lacking the adduct-forming cysteine. Tyr residues (yellow), Trp (blue), Cys (orange), and Met (green) are highlighted; circles above the alignment indicate the secondary structure in VVD with β sheets in blue and α helices in orange; arrows denote LOV-conserved residues, with the adduct-forming Cys in VVD and *B. subtilis* YtvA marked by a red arrow. (b) Dendrogram of the alignment shown in (a).

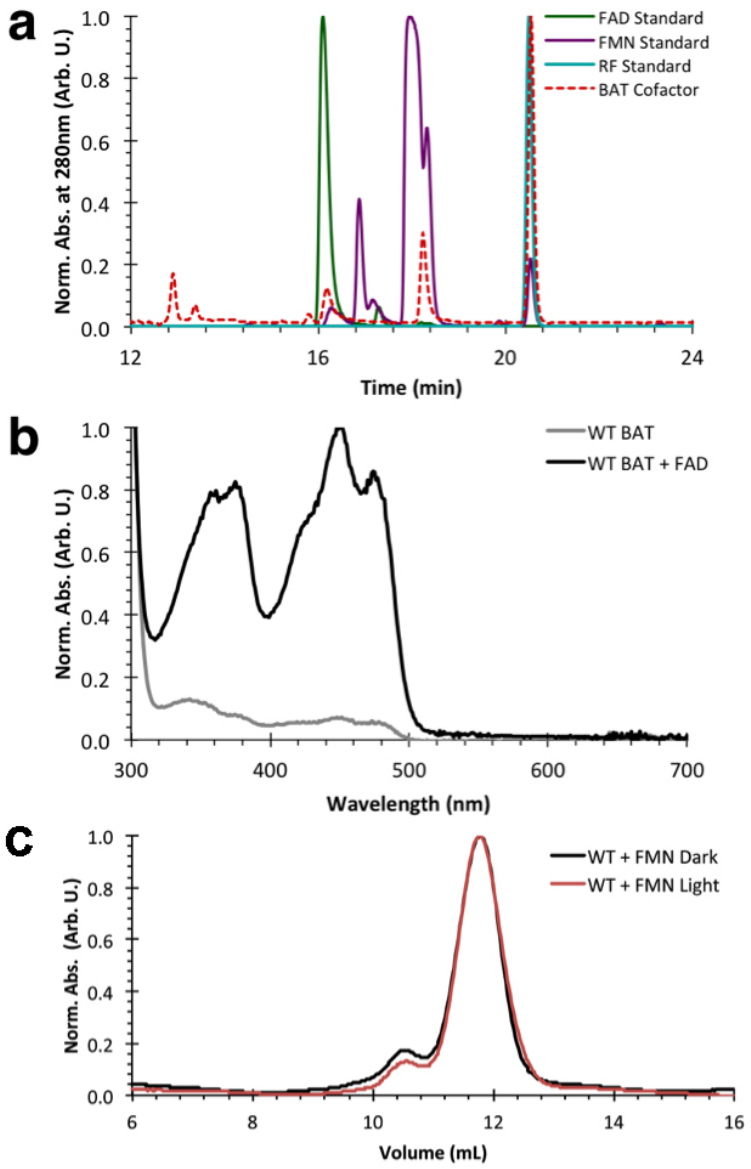

Supplementary Figure 3.10: Flavin binding and reconstitution of recombinantly expressed BAT-LOV*. (a) Reverse-phase HPLC trace of flavin moieties released from BAT-LOV* produced through recombinant expression in *E. coli*. BAT-LOV* primarily co-purifies with riboflavin, although small amounts of FMN and FAD are also bound. (b) Absorbance spectra of WT BAT-LOV* before (grey) and after (black) reconstitution with FAD. Apoprotein separates from the flavin-bound protein on SEC (see Fig. 3.5d), and from these elution profiles, we estimate that $85-90\%$ of BAT-LOV* can be reconstituted with either FAD or FMN. These estimates also match those based on flavin spectral quantification relative to protein absorption. (c) SEC traces of BAT-LOV* reconstituted with FMN in the dark and after broad-spectrum light exposure, as for the FAD-bound protein shown in Fig. 3.5d.

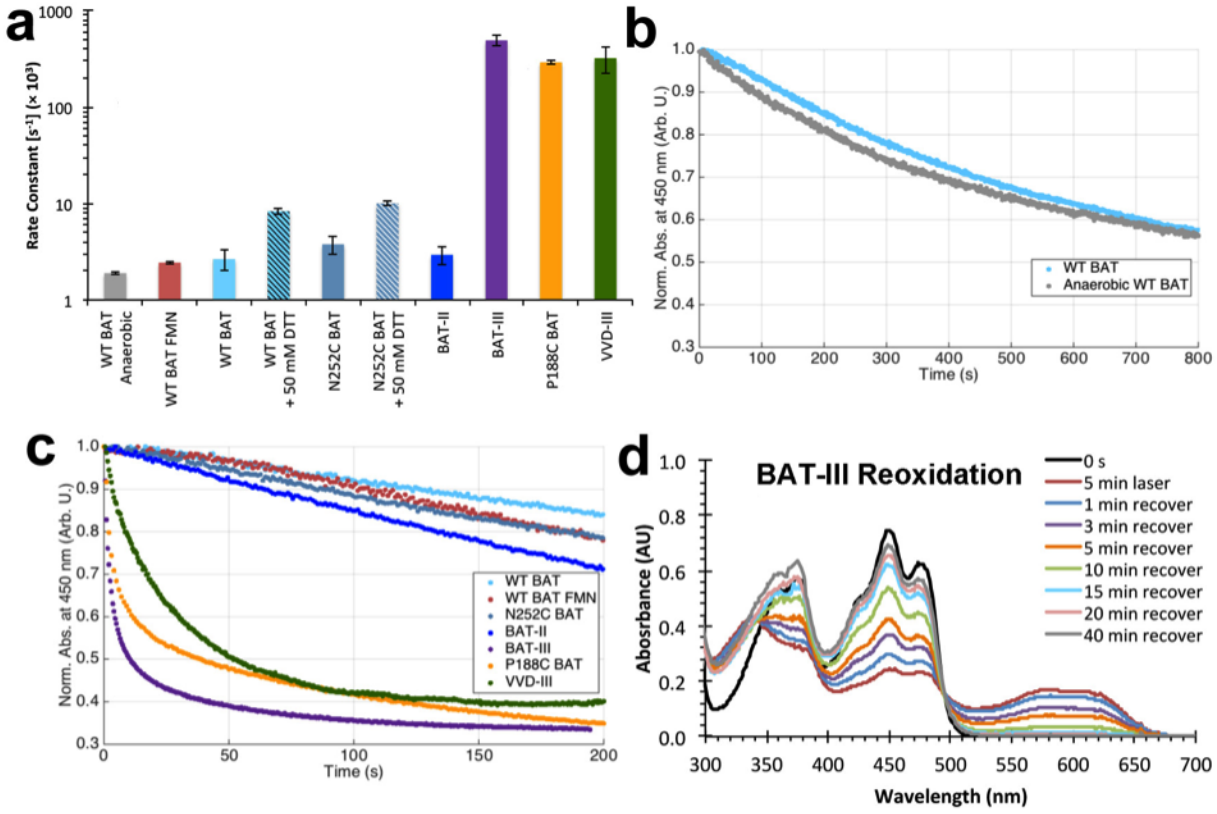

Supplementary Figure 3.11: Relative photoreduction yields of VVD-III and BAT-LOV*. (a) VVD-III reduces to the NSQ by orders of magnitude more rapidly than BAT-LOV* when exposed to 448-nm light. However, photoreduction yields of BAT-LOV* can be increased to rival those of VVD-III by either replacing the three flavin-proximal aromatic residues (BAT-III) with Phe or substituting the Pro residue that occupies the position which normally forms an adduct with a Cys residue (P188C). Addition of a Cys residue on Iβ ~13 Å from the flavin ring has only a small effect (N252C), as does addition of exogenous reductants. Reconstitution with FMN instead of FAD has an insignificant effect. (b) In the presence of air, there is a small lag phase for WT BAT-LOV* photoreduction that is not present under anaerobic conditions. (c) Time courses for photoreduction of VVD and BAT variants. (d) Recovery of photoreduced BAT-III to the oxidized state in aerobic solution.

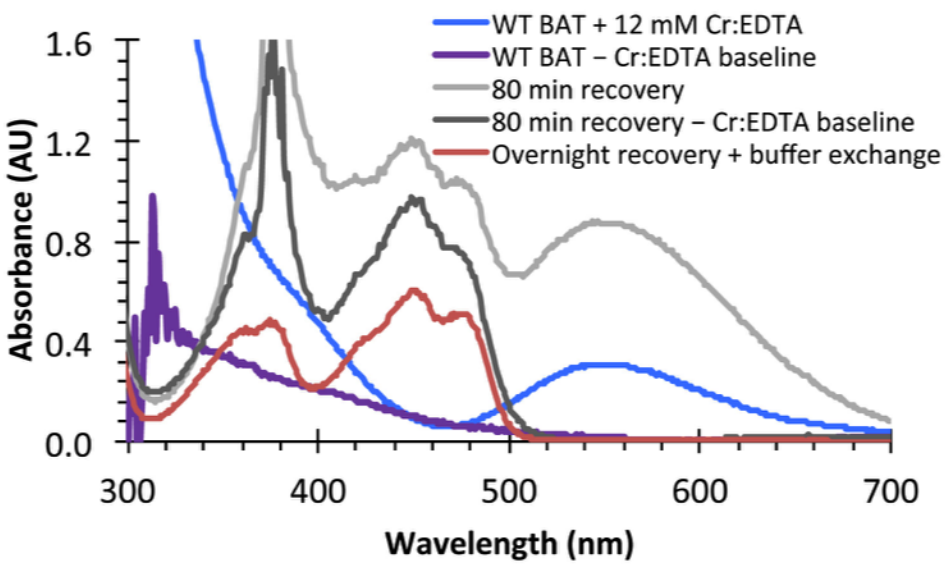

Supplementary Figure 3.12: Chemical reduction and recovery of BAT-LOV*. Treatment of BAT-LOV* with the low potential reductant Cr:EDTA generates a fully reduced flavin (blue line, broad absorption at 550 nm represents oxidation products of the Cr:EDTA reagent; purple line, with Cr:EDTA subtraction). Reoxidation after 80 min (shown with (dark grey) and without (light grey) Cr:EDTA subtraction) recovers the oxidized flavin, which is more evident after removal of the reductant by buffer exchange (red). A substantial amount of flavin remains bound to the protein after reoxidation.

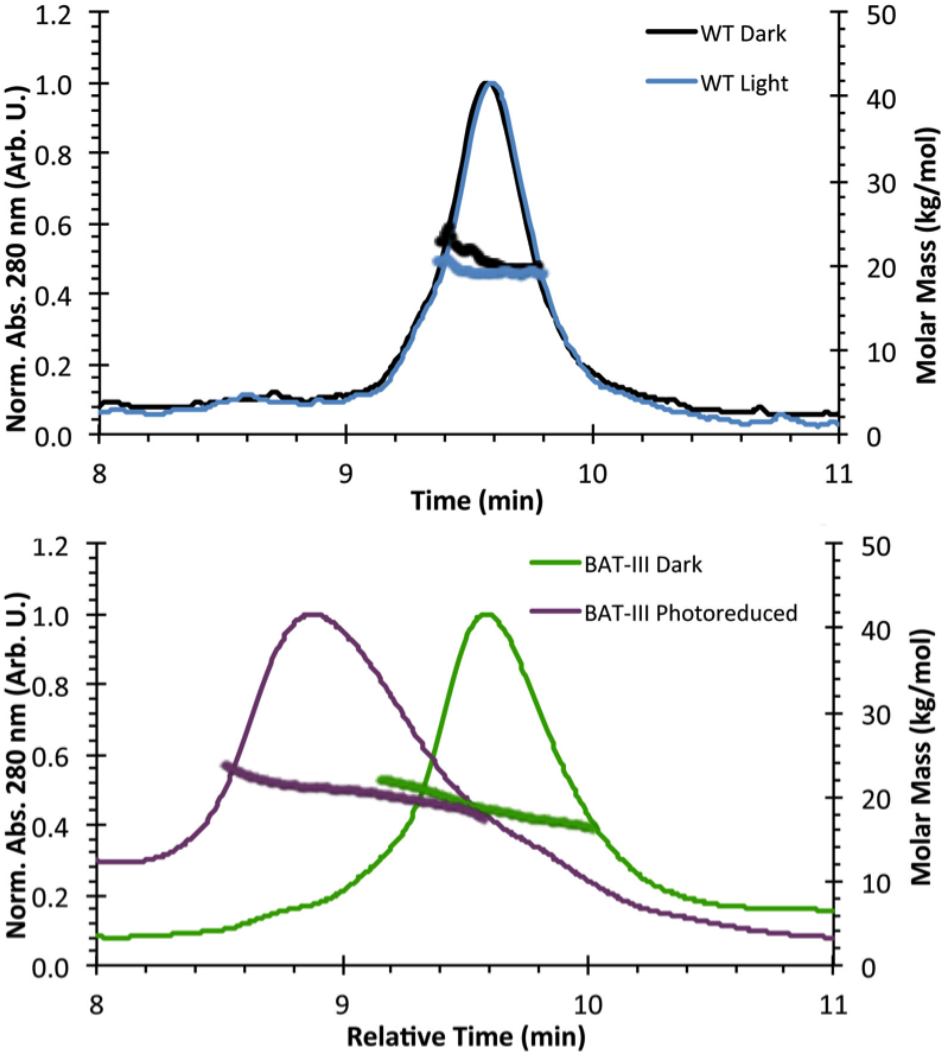

Supplementary Figure 3.13: Multi-angle light scattering of BAT-LOV* and BAT-III. (a) Molar mass measurements from MALS are shown across the SEC elution profiles for dark-adapted BAT-LOV*-FAD (black) and BAT-LOV* exposed to a 100 W broad-spectrum visible light source for 1.5 h prior to chromatography (blue). (b) MALS-SEC data of BAT-III in the dark-adapted and photoreduced state. The shift in BAT elution profile does not accompany a substantial change in molecular weight. Elution times are standardized to WT BAT-LOV*.

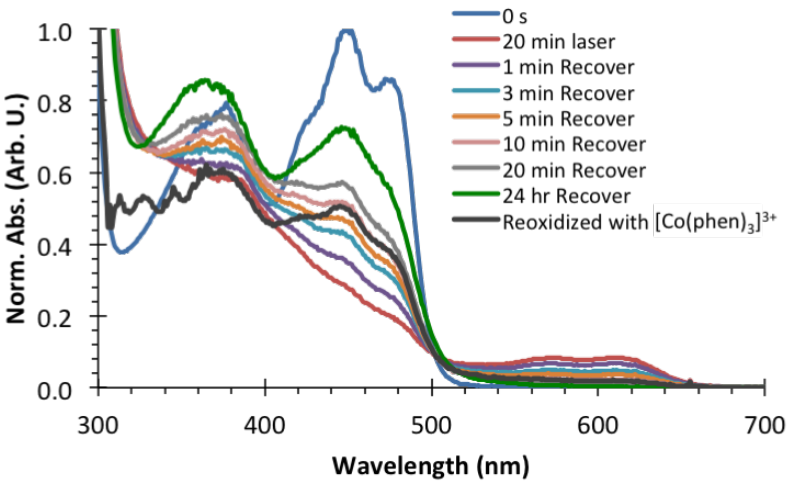

Supplementary Figure 3.14: Reoxidation of the BAT-P188C photoproduct. The spectrum of the light-excited protein strongly resembles that of a reduced HQ state. Furthermore, the light state can be rapidly converted to the oxidized flavin with the oxidant Co(III)phen$_3$. Over time, most of the reoxidized flavin dissociates from the protein (green trace). Some flavin is also unrecovered and presumably irreversibly photobleached. Unlike C4a adducts, the reduced state is also insensitive to bases, such as imidazole. In a 0.2-cm path length cuvette, 10 μL of 1 mM protein was photoreduced for 20 minutes under 448-nm laser light, after which, 1 μL of 1.2 mM [Co(phen)$_3$](ClO$_4$)$_3$ solution was immediately added. Spectra for the reoxidized species were collected within one minute (dark grey trace).

Supplementary Data 3.15: Overview of LOV-Like Proteins Lacking the Adduct-Forming Cysteine. The accompanying HTML File can be opened in a standard web browser and provides a graphical overview of the domain architecture of entries in GenBank that comprise LOV-Like domains lacking the adduct-forming cysteine residue.

BIBLIOGRAPHY

[1] Zoltowski, B. D. and Gardner, K. H. Tripping the light fantastic: blue-light photoreceptors as examples of environmentally modulated protein protein interactions. *Biochemistry* **50**, 4-16 (2011).

[2] Losi, A. and Gärtner, W. Old chromophores, new photoactivation paradigms, trendy applications: flavins in blue light-sensing photoreceptors. *Photochem. Photobiol.* **87**, 491-510 (2011).

[3] Conrad, K. S., Manahan, C. C. and Crane, B. R. Photochemistry of flavoprotein light sensors. *Nat. Chem. Biol.* **10**, 801-809 (2014).

[4] Briggs, W. R. The LOV domain: a chromophore module servicing multiple photoreceptors. *J. Biomed. Sci.* **14**, 499-504 (2007).

[5] Alexandre, M. T. et al. Primary reactions of the LOV2 domain of phototropin studied with ultrafast mid-infrared spectroscopy and quantum chemistry. *Biophys. J.* **97**, 227-237 (2009).

[6] Bauer, C., Rabl, C.-R., Heberle, J. and Kottke, T. Indication for a radical intermediate preceding the signalling state in the LOV domain photocycle. *Photochem. Photobiol.* **87**, 548-553 (2011).

[7] Pfeifer, A. et al. Time-resolved Fourier transform infrared study on photoadduct formation and secondary structural changes within the phototropin LOV domain. *Biophys. J.* **96**, 1462-1470 (2009).

[8] Kutta, R.-J., Magerl, K., Keny, U. and Dick, B. A search for radical intermediates in the photocycle of LOV domains. *Photochem. Photobiol. Sci.* **14**, 288-299 (2015).

[9] Lederer, F. Extreme pK_{a} displacements at the active sites of FMN-dependent alpha-hydroxy acid-oxidizing enzymes. *Protein Sci.* **1**, 540-548 (1992).

[10] Crosson, S. and Moffat, K. Photoexcited structure of a plant photoreceptor domain reveals a light-driven molecular switch. *Plant Cell* **14**, 1067-1075 (2002).

[11] Zoltowski, B. D. et al. Conformational switching in the fungal light sensor vivid. *Science* **316**, 1054-1057 (2007).

[12] Vaidya, A. T., Chen, C.-H., Dunlap, J. C., Loros, J. J. and Crane, B. R. Structure of a light-activated LOV protein dimer that regulates transcription. *Sci. Signal.* **4**, ra50 (2011).

[13] Chen, C.-H., DeMay, B. S., Gladfelter, A. S., Dunlap, J. C. and Loros, J. J. Physical interaction between VIVID and white collar complex regulates photoadaptation in Neurospora. *Proc. Natl Acad. Sci. USA* **107**, 16715-16720 (2010).

[14] Aihara, Y. et al. Mutations in N-terminal flanking region of blue light-sensing light-oxygen and voltage 2 (LOV2) domain disrupt its repressive activity on kinase domain in the *Chlamydomonas phototropin*. *J. Biol. Chem.* **287**, 9901-9909 (2012).

[15] Okajima, K., Kashojiya, S. and Tokutomi, S. Photosensitivity of kinase activation by blue light involves the lifetime of a cysteinyl-flavin adduct intermediate, S390, in the photoreaction cycle of the LOV2 domain in phototropin, a plant blue light receptor. *J. Biol. Chem.* **287**, 40972-40981 (2012).

[16] Kay, C. W. M. et al. Blue light perception in plants. Detection and characterization of a light-induced neutral flavin radical in a C450A mutant of phototropin. *J. Biol. Chem.* **278**, 10973-10982 (2003).

[17] Bittl, R., Kay, C. W. M., Weber, S. and Hegemann, P. Characterization of a flavin radical product in a C57M mutant of a LOV1 domain by electron paramagnetic resonance. *Biochemistry* **42**, 8506-8512 (2003).

[18] Kottke, T., Heberle, J., Hehn, D., Dick, B. and Hegemann, P. Phot-LOV1: photocycle

of a blue-light receptor domain from the green alga *Chlamydomonas reinhardtii*. *Biophys. J.* **84**, 1192-1201 (2003).

[19] Richter, G. et al. Photochemically induced dynamic nuclear polarization in a C450A mutant of the LOV2 domain of the *Avena sativa* blue-light receptor phototropin. *J. Am. Chem. Soc.* **127**, 17245-17252 (2005).

[20] Lanzl, K., Sanden-Flohe, M. V., Kutta, R.-J. and Dick, B. Photoreaction of mutated LOV photoreceptor domains from *Chlamydomonas reinhardtii* with aliphatic mercaptans: implications for the mechanism of wild type LOV. *Phys. Chem. Chem. Phys.* **12**, 6594-6604 (2010).

[21] Möglich, A., Ayers, R. A. and Moffat, K. Design and signalling mechanism of light-regulated histidine kinases. J. Mol. Biol. **385**, 1433-1444 (2009).

[22] Möglich, A. and Moffat, K. Engineered photoreceptors as novel optogenetic tools. *Photochem. Photobiol. Sci.* **9**, 1286-1300 (2010).

[23] Zoltowski, B. D., Vaccaro, B. and Crane, B. R. Mechanism-based tuning of a LOV domain photoreceptor. *Nat. Chem. Biol.* **5**, 827-834 (2009).

[24] Zoltowski, B. D. and Crane, B. R. Light activation of the LOV protein VIVID generates a rapidly exchanging dimer. *Biochemistry* **47**, 7012-7019 (2008).

[25] Purcell, E. B., Siegal-Gaskins, D., Rawling, D. C., Fiebig, A. and Crosson, S. A photosensory two-component system regulates bacterial cell attachment. *Proc. Natl Acad. Sci. USA* **104**, 18241-18246 (2007).

[26] Swartz, T. E. et al. Blue-light-activated histidine kinases: two-component sensors in bacteria. *Science* **317**, 1090-1093 (2007).

[27] Diensthuber, R. P., Bommer, M., Gleichmann, T. and Möglich, A. Full-length structure of a sensor histidine kinase pinpoints coaxial coiled coils as signal transducers and modulators. *Structure* **21**, 1127-1136 (2013).

[28] Ohlendorf, R., Vidavski, R. R., Eldar, A., Moffat, K. and Möglich, A. From dusk till dawn: one-plasmid systems for light-regulated gene expression. *J. Mol. Biol.* **416**, 534-542 (2012).

[29] Drepper, T. et al. Reporter proteins for *in vivo* fluorescence without oxygen. *Nat. Biotechnol.* **25**, 443-445 (2007).

[30] Qi, Y. B., Garren, E. J., Shu, X., Tsien, R. Y. and Jin, Y. Photo-inducible cell ablation in *Caenorhabditis elegans* using the genetically encoded singlet oxygen generating protein miniSOG. *Proc. Natl Acad. Sci. USA* **109**, 7499-7504 (2012).

[31] Pimenta, F. M., Jensen, R. L., Breitenbach, T., Etzerodt, M. and Ogilby, P. R. Oxygen-dependent photochemistry and photophysics of "MiniSOG," a protein-encased flavin. *Photochem. Photobiol.* **89**, 1116-1126 (2013).

[32] Westberg, M., Holmegaard, L., Pimenta, F. M., Etzerodt, M. and Ogilby, P. R. Rational design of an efficient, genetically encodable, protein-encased singlet oxygen photosensitizer. *J. Am. Chem. Soc.* **137**, 1632-1642 (2015).

[33] Gleichmann, T., Diensthuber, R. P. and Möglich, A. Charting the signal trajectory in a light-oxygen-voltage photoreceptor by random mutagenesis and covariance analysis. *J. Biol. Chem.* **288**, 29345-29355 (2013).

[34] Baliga, N. S., Kennedy, S. P., Ng, W. V., Hood, L. and DasSarma, S. Genomic and genetic dissection of an archaeal regulon. *Proc. Natl Acad. Sci. USA* **98**, 2521-2525 (2001).

[35] Alexandre, M. T., Arents, J. C., van Grondelle, R., Hellingwerf, K. J. and Kennis, J. T. A base-catalyzed mechanism for dark state recovery in the *Avena sativa* phototropin-1 LOV2 domain. *Biochemistry* **46**, 3129-3137 (2007).

[36] Song, S.-H., Dick, B., Penzkofer, A. and Hegemann, P. Photo-reduction of flavin mononucleotide to semiquinone form in LOV domain mutants of blue-light receptor phot from *Chlamydomonas reinhardtii. J. Photochem. Photobiol. B.* **87**, 37-48 (2007).

[37] Christie, J. M., Gawthorne, J., Young, G., Fraser, N. J. and Roe, A. J. LOV to BLUF: flavoprotein contributions to the optogenetic toolkit. *Mol. Plant* **5**, 533-544 (2012).

[38] Diensthuber, R. P. et al. Biophysical, Mutational, and Functional Investigation of the Chromophore-Binding Pocket of Light-Oxygen-Voltage Photoreceptors. *ACS Synth. Biol.* **3**, 811-819 (2014).

[39] Schleicher, E. et al. On the reaction mechanism of adduct formation in LOV domains of the plant blue-light receptor phototropin. *J. Am. Chem. Soc.* **126**, 11067-11076 (2004).

[40] Schleicher, E. and Weber, S. Radicals in flavoproteins. *Top. Curr. Chem.* **321**, 41-65 (2012).

[41] Langenbacher, T., Immeln, D., Dick, B. and Kottke, T. Microsecond light-induced proton transfer to flavin in the blue light sensor plant cryptochrome. *J. Am. Chem. Soc.* **131**, 14274-14280 (2009).

[42] Gauden, M. et al. Hydrogen-bond switching through a radical pair mechanism in a flavin-binding photoreceptor. *Proc. Natl Acad. Sci. USA* **103**, 10895-10900 (2006).

[43] Stierl, M., Penzkofer, A., Kennis, J. T. M., Hegemann, P. and Mathes, T. Key residues for the light regulation of the blue light-activated adenylyl cyclase from *Beggiatoa sp.* *Biochemistry* **53**, 5121-5130 (2014).

[44] Taylor, B. L. Aer on the inside looking out: paradigm for a PAS-HAMP role in sensing oxygen, redox and energy. *Mol. Microbiol.* **65**, 1415-1424 (2007).

[45] Wright, S., Walia, B., Parkinson, J. S. and Khan, S. Differential activation of *Escherichia coli* chemoreceptors by blue-light stimuli. *J. Bacteriol.* **188**, 3962-3971 (2006).

[46] Purcell, E. B., McDonald, C. A., Palfey, B. A. and Crosson, S. An analysis of the solution structure and signalling mechanism of LovK, a sensor histidine kinase integrating light and redox signals. *Biochemistry* **49**, 6761-6770 (2010).

[47] Mathes, T., Vogl, C., Stolz, J. and Hegemann, P. *In vivo* generation of flavoproteins with modified cofactors. *J. Mol. Biol.* **385**, 1511-1518 (2009).

[48] Warren, R. M. L., Lappin, A. G., Mehta, B. D. and Neumann, H. M. Electron transfer reactions of optically active tris(phenanthroline)cobalt(3+ /2-) and derivatives. *Inorg. Chem.* **29**, 4185-4189 (1990).

[49] Vaidya, A. T. et al. Flavin reduction activates *Drosophila* cryptochrome. *Proc. Natl Acad. Sci. USA* **110**, 20455-20460 (2013).

[50] Nellen-Anthamatten, D. et al. *Bradyrhizobium japonicum* FixK2, a crucial distributor in the FixLJ-dependent regulatory cascade for control of genes inducible by low oxygen levels. *J. Bacteriol.* **180**, 5251-5255 (1998).

[51] Kurashima-Ito, K. et al. Solution structure of the C-terminal transcriptional activator domain of FixJ from *Sinorhizobium meliloti* and its recognition of the fixK promoter. *Biochemistry* **44**, 14835-14844 (2005).

[52] Borbat, P. P. and Freed, J. H. Multiple-quantum ESR and distance measurements. *Chem. Phys. Lett.* **313**, 145-154 (1999).

[53] Borbat, P. P. and Freed, J. H. Pulse dipolar ESR: distance measurements. *Struct. Bond.* **152**, 1-82 (2014).

[54] Sievers, F. et al. Fast, scalable generation of high-quality protein multiple sequence alignments using Clustal Omega. *Mol. Syst. Biol.* **7**, 1-6 (2011).

[55] Biasini, M. et al. SWISS-MODEL: modelling protein tertiary and quaternary structure using evolutionary information. *Nucleic Acids Res.* **42**, W252-W258 (2014).

CHAPTER 4

ACTIVATION OF FLAVIN PHOTOSENSORY PROTEINS BY PHOTOINDUCED ELECTRON TRANSFER

4.1 Abstract

Relay residues in photoactive proteins are essential for generating the active state of the flavin cofactor and instigating subsequent conformational changes for *in vivo* signaling. In the light-oxygen-voltage photoreceptor VVD, when the adduct-forming cysteine is substituted to alanine, the resultant variant is still partially active *in vivo* owing to the formation of a flavin neutral semiquinone (NSQ) state and subsequent N5 nitrogen protonation under blue light irradiation. Yet, the mechanism of NSQ development remains elusive and the electron donor to the flavin has yet to be identified. Through a series of mutagenesis studies, we have isolated the relay residues suspected to be donors. X-ray Absorption Spectroscopy, Difference Fourier Transform Infrared Spectroscopy, Fluorescence and UV-vis kinetics all indicate that tyrosine, tryptophan, and cysteine residues play little or no role in photoactivity. Substituting methonines with selenomethionines aided in the determination of oxidation state changes and conversion of the sulfur/selenium atoms in the residues during excitation, successfully confirming that methionine residues were indeed primary electron donors for generation of the NSQ. These findings illustrate the numerous donors accessible to the flavin cofactor and the importance of their consideration for engineering of protein electron transfer.

4.2 Introduction

Blue-light photoreceptors that comprise of a subclass of Per-Arnt-Sim (PAS) domains bind to either flavin adenine dinucleotide (FAD) or flavin mononucleotide (FMN). This

cofactor confers the ability to chemically sense changes in the environment. In these light-oxygen-voltage (LOV) domains, excitation by light promotes flavin reduction and subsequent covalent bond formation between a conserved cysteine residue and the C4a carbon of the isoalloxazine ring. Formation of the adduct state leads to hydrogen bond rearrangement and ultimately changes in the oligomerization state of the protein [1–4]

Neurospora crassa's VVD is one of the smallest canonical LOV domain proteins and consists of only 184 amino acids. In conditions of prolonged and increasing light intensity, VVD is important for photoadaptation in the organism and for its ability to continue responding to light under high intensity light conditions. It has been proposed that activation of VVD causes its dimerization to another LOV domain in the principal light sensor of *Neurospora crassa* White Collar-1 (WC1) and repression of WC1 transcription activity [5].

VVD and other LOV domain proteins have been the target of modifications to study the underlying mechanism of photoactivation. Previous studies have removed the conserved cysteine residue from VVD to inhibit adduct formation, resulting in a partially active protein that forms the one electron reduced neutral semiquinone (NSQ) under light exposure instead of the cysteinyl-flavin adduct [5–7]. Our prior work established the importance of N5 protonation in flipping of Gln182 and subsequent conformational changes [7, 8], however, to date, the electron donor to flavin is unknown. Recently, the fluorescent protein iLOV (based off of the phototropin-2 LOV2 domain) was modified to instigate electron transfer through an intrinsic chain of highly conserved tryptophan and tyrosine residues by first stabilizing the neutral semiquinone [9]. Another study has found that introduction of an adjacent tyrosine that performs proton-coupled electron transfer with the flavin cofactor prevents adduct formation, despite the presence of the conserved cysteine [10]. Both studies argue for the importance of these aromatic side chains in the flavin photoreduction mechanism. Still other studies in small peptide systems have indicated the ability of cysteine and methionine

residues to conduct and transfer electrons [11], and several proteins rely on backbone glycyl radicals for functionality [12]. As there are many possible relay amino acids, it is essential to consider their potential roles in active-cysteine-less VVD.

Here we attempt to identify the electron donating residues that lead to the development of the NSQ state. Through mutagenesis and spectroscopic experiments, we have eliminated all aromatic and cysteine residues as possible electron donors. Backbone glycyl chains were investigated through studies of an analogous LOV-HK system. This work indicated presence of a nearby glycine had little effect on photoconversion. Replacement of all methionine residues with selenomethionine provided spectroscopic handles for us to establish how the sulfurs (or Se) in these side chains were behaving under blue light. Our results confirm that methionine residues are the prevalent electron donors in this active cysteine-less domain.

4.3 Results and Discussion

4.3.1 Search for the elusive electron donor in VVD photoreduction

To determine which redox active amino acids contributes to the formation of the neutral semiquinone (NSQ) state, active cysteine-less protein VVD-III (VVD-37 C108A:M135I:M165I) was modified by replacing all nine tyrosine residues, all of which are ∼16 Å from the center of the flavin isoalloxazine ring, with redox-inactive phenylalanine (Figure 4.1). Tyrosine and tryptophan residues have reduction potentials in the range of that of the flavin excited state and are widely proposed to be the electron donors [13]. This Tyr-less VVD-III variant did not affect protein stability and was easily purified from recombi-

nant expression in *E. coli* with high yields. However, under blue light, flavin photoreduction to the NSQ form was not perturbed. Subsequent removal of the cysteine residue closest to the flavin (Cys76; ~ 6 Å) resulted in much lower yields of soluble protein but also failed to inhibit photoreduction.

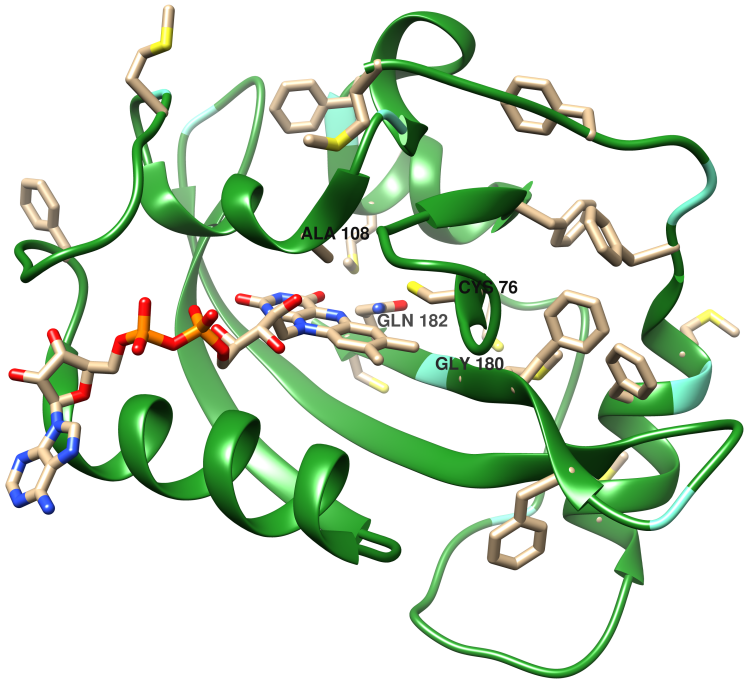

Figure 4.1: Homology model of Tyr-less VVD-III variant (template: 2PD7). Side chains for phenylalanine residue, methionine, and cysteine residues are displayed. Glycines are denoted in aquamarine ribbon sections. The cysteine and glycine residues closest to the flavin cofactor are labeled. Figure was generated with Chimera [14].

4.3.2 Glycyl radicals are unlikely to be involved in photoreduction

Glycyl radicals are known to form on peptide backbones and are capable of electron hole localization [12, 15, 16]. As such, in Tyr-less VVD-III a conserved glycine residue (Gly180) near the flavin was replaced by either serine or alanine. Unfortunately, introduction of these side chains likely interfered with the flavin cofactor binding, as the resultant, insoluble apoprotein was unable to be reconstituted *in vitro*, even after multiple refolding attempts.

Brucella abortus LOV-HK (histidine kinase) proteins possess one of the few studied LOV domains that does not have the highly conserved glycine next to the flavin isoalloxazine ring; in LOV-HK, this residue is a serine (Ser130). Compared to VVD, LOV-HK has a 22% sequence identity and a similar fold, with a few structural differences at the distal regions (PDB 3T50; [17]). Notably, the structure lacks an N-terminal cap, the loop connecting Eα to Fα is shorter, which probably restricts the size of the cofactor to the shorter FMN molecule, and Iβ is slightly displaced to accommodate the perturbation of Ser instead of Gly at position 180 (Figure 4.2a).

WT LOV-HK was highly sensitive to blue light and required an additional neutral density filter in order to collect UV-vis kinetics data. Moreover, the protein did not fully return to the oxidized state overnight despite care taken in keeping the sample in the dark, as evidenced by the 390 nm feature remaining in the UV-vis spectrum (Supplemental Figure 4.10a). However, we note that previous studies did observe full flavin oxidation of the protein under their laboratory conditions [17]. Replacement of Ser130 with glycine caused few changes in the flavin binding (as assessed by UV-vis) and photoreduction rate. This variant however returned to the fully oxidized flavoquinone state overnight (Supplemental Figure 4.10b). The mutation likely affected the stability of the protein, as observed by the sloped baseline in the photoreduction trace (Supplemental Figure 4.10b). The introduction of additional space in the flavin binding pocket from the removal of serine may have led to small instabilities that contribute to flavin loss. In contrast, the cysteine-less variant (C69A) behaved well and easily photoreduced to the NSQ state (Supplemental Figure 4.10b). However, even in the C69A background, removal of Ser130 did not affect flavin binding nor the photoreduction rate (Figure 4.2b and Table 4.1). Hence, for LOV-HK, both adduct formation and photoreduction does not require an adjacent glycine, and furthermore, its introduction does not augment photoactivity.

(a)

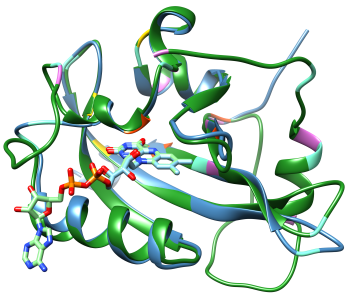

(b)

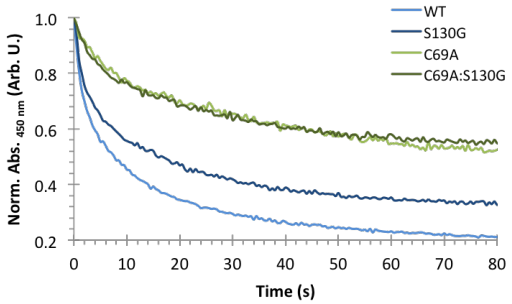

Figure 4.2: (a) Structure of LOV-HK (PDB 3T50; blue) versus VVD (PDB 2PD7; green). All methionine residues are in purple, cysteines in orange, glycines in aquamarine, and tyrosines/tryptophans in yellow. Figure was prepared with Chimera [14]. (b) Photoreduction of variants under 448-nm laser light. A neutral density of 1.6 was applied to attenuate the light source for WT and S130G. Comparisons between WT and S130G and C69A and C69A:S130G show few differences, thereby signifying the lack of importance of the conserved glycine residue.

Variants	a	k_1 [s^{-1}]	b	k_2 [s^{-1}]
WT	0.26 ± 0.03	0.61 ± 0.07	0.37 ± 0.05	0.061 ± 0.006
S130G	0.14 ± 0.04	0.58 ± 0.11	0.17 ± 0.05	0.056 ± 0.016
C69A	0.069 ± 0.018	0.31 ± 0.14	0.15 ± 0.03	0.031 ± 0.005
C69A:S130G	0.10 ± 0.02	0.24 ± 0.07	0.15 ± 0.02	0.031 ± 0.007

Table 4.1: Photoreduction rates of LOV-HK variants: WT, S130G WT, C69A, and C69A:S130G. Traces at 450 nm were fit to biexponential curves.

4.3.3 Replacing methionine residues alters the properties of photoreduction

Methionine residues in VVD were evaluated as potential flavin redox donors as all other Tyr-less VVD-III mutations resulted in minute changes to the photoreduction rates. Of the six methionines, Met95 and Met179 are the closest to the isoalloxazine ring center at a distance of 10.9 Å and 12.2 Å, respectively, which is short enough for rapid single step electron tunneling to the flavin excited state [18]. To probe their relevance in photoactivation, Tyr-less VVD-III proteins were substituted with selenomethionine (SeMet) by expressing

them in an auxotrophic *E. coli* cell line to which selemethionine was provided as the sole "methionine" source. (The reduction potential of selenomethionine has not been reported, but measurements on selenocysteine illustrate the effect of selenium substitution at sulfur by causing a two-fold decrease in reduction potential; E°(Cys) = 0.92 V vs E°(SeCys) =0.43 V; [19]). The SeMet Tyr-less VVD-III variant was approximated to be > 95% incorporated with selenomethionine using mass spectrometry-based proteomics, and assessment by circular dichroism (CD) indicated that the protein was properly folded in buffer and exhibited similar stability compared to the parent Tyr-less VVD-III (Supplemental Figure 4.7). Curiously, between the parent and SeMet variant, there were only small differences in photoreduction rates and no major differences in the final yield of NSQ under blue light. To account for the possibility that the SeMet residues had become oxidized and incapable of electron donation to the flavoquinone, both Met and SeMet proteins were incubated with a reductant (5 mM reduced glutathione (GSH) has been reported to reduce oxidized SeMet residues [20–23]) or in oxidizing conditions (5 mM hydrogen peroxide (H_2O_2)). Similar changes in rate constants were observed for both variants, suggesting that GSH likely behaves as an extrinsic reductant (Figure 4.3 and Supplemental Figure 4.8). Oxidizing conditions did not significantly lower the photoreduction rate compared to the untreated samples, though the SeMet protein appears to have a diminished sensitivity to blue light and slower generation of the NSQ in comparison to the Met variant. It is important to note that neither treatment in glutathione or peroxide affected the protein stability, as determined by UV-vis spectroscopy and SDS-PAGE (data not shown), though the SeMet variant had a greater percentage of apoprotein upon expression (Supplemental Figure 4.8a and 4.8b).

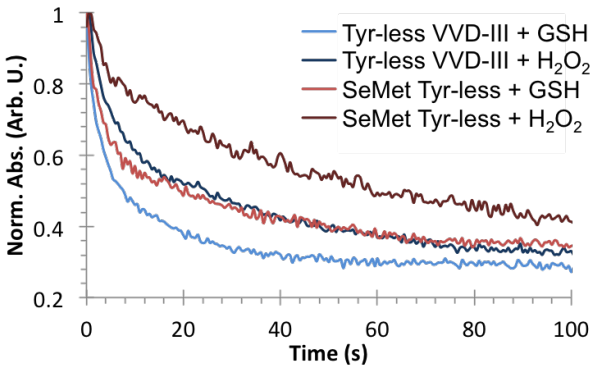

Figure 4.3: Photoreduction of VVD variants with 448-nm laser light in the presence of 5 mM reduced glutathione or 5 mM H_2O_2. GSH-treated samples exhibit similar photoreduction traces. SeMet protein incubated in peroxide reduces to the NSQ state slower than the normal Met variant.

To determine the oxidation state of selenomethionine residues in SeMet proteins, we attempted to use mass spectrometry-based proteomics and intact protein analysis. Unfortunately, tryptic cleavage of proteins resulted in facile oxidation of SeMet residues, leading to false positives, and intact proteins were poorly ionized. Thus, we characterized the selenium oxidation state using the K-edge energy from X-ray Absorption Near Edge Spectroscopy (XANES; C1 beam line, CHESS, Cornell University). XANES K-edge features are highly sensitive to local coordination environment and the oxidation state of target elements. The binding energy of the core electrons increase with higher oxidation states owing to the increase in the effective nuclear charge, thus resulting in a shift of the edge energy [24–26], and local environments about the atom contribute to distinctive oscillations in the post-edge region [27]. The most straightforward method to interpret XANES data is to compare to known standards and determine composition by linear combination analysis. Hence, we collected data on solution standards of L-selenomethionine treated with either GSH, H_2O_2, or peroxynitrite ($ONOO^-$). Hydrogen peroxide is thought to oxidize SeMet residues to selenone [25], whereas peroxynitrite has been found to rapidly oxidize the amino acid to selenoxide [28]. In general, selenium K-edge signals arise from a 1s to 4p transition, with the selenium

oxides exhibiting an intense, sharp white line feature as the electrons are withdrawn from the 4p level by oxo moieties [24, 29].

Figure 4.4 displays spectra of the SeMet standards and protein samples. Linear combination analyses by Athena [30] show that overnight incubation of SeMet Tyr-less with 5 mM GSH or 5 mM H_2O_2 does not affect the percentage of oxidized selenium. Treatment with $ONOO^-$ resulted in destabilization and release of flavin (observed by UV-vis), which likely increased solvent accessibility to the core of the protein and oxidized more SeMet residues. Interestingly, the photoreduction of SeMet Tyr-less protein caused a change in the percentage of selenium oxides, suggesting that some selenomethioine residues may become oxidized by photoreduction of the flavin cofactor (Supplemental Table 4.3).

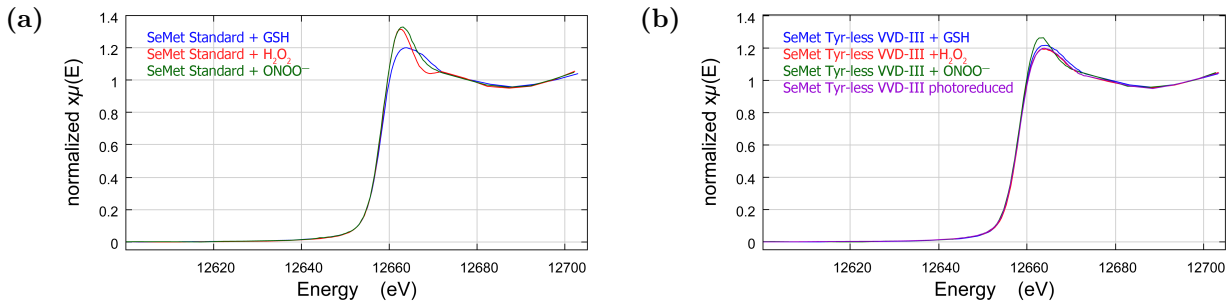

Figure 4.4: X-ray absorption Near Edge spectroscopy of SeMet Tyr-less VVD-III. (a) SeMet standards in buffer incubated in glutathione, H_2O_2, or peroxynitrite overnight. Glutathione treatment resulted in broad features between $\sim 12660 - 12670$ eV. Oxidation with H_2O_2 or peroxynitrite was discernible by a sharp white line feature centered at ∼12663 eV along with an additional small feature at ∼12674 eV. (b) SeMet Tyr-less VVD-III contained reduced selenium regardless of reduction or oxidation conditions. Only peroxynitrite generated a small amount of oxidation (dark green). Photoreduction by blue light slightly oxidized the selenium, as determined by linear combination analyses (Supplemental Table 4.3).

Flavin fluorescence provides an additional means to investigate the effect of SeMet residues on the photoactivation of the variant and lifetime of the excited singlet S_1 state. The initial intensity of the fluorescence emission from the S_1 to S_0 transition is dependent on adjacent quenchers, including tyrosine, tryptophan, phenylalanine, cysteine, and histidine residues, with the lifetime shortening as the quantity of quenchers increase [31]. For

the canonical LOV domain, fluorescence kinetics can be indicative of the quenching of the singlet state, usually through intersystem crossing to the triplet T_1 state followed by rapid formation of the cysteinyl-flavin bond [32], and thus is a direct measure of the efficiency of adduct development. In LOV domain proteins lacking the active cysteine, formation of the NSQ is thought to proceed from the T_1 triplet state [33, 34]. The NSQ state has little to no fluorescence at 502 nm [35], so the fluorescence signal is expected to decrease accordingly during photoreduction. Indeed, the Tyr-less VVD-III protein after photoreduction by laser light exhibits 1/7th of the original signal amplitude from the remaining unreduced flavoquinone (data not shown).

Analysis of flavin fluorescence emission intensities indicate that the quantum yield of the cofactor is not affected by the introduction of SeMet. For equal amounts of chromophore ($Abs_{450\ nm} = 0.15$, 1 cm path length), excitation at 450 nm results in similar emission profiles and amplitudes at 502 nm (Figure 4.5a). Neither replacing tyrosines nor methionines appears to significantly alter the S_1 state. However, fluorescence quenching kinetics differ remarkably between the Met and SeMet proteins; for the latter, fluorescence intensities remain constant over the course of an hour (Figure 4.5b). Owing to the lower intensity of excitation light from the fluorimeter (compared to the 30-mW blue laser light used in UV-vis kinetics), the SeMet variant demonstrates an extremely low sensitivity to blue light, which supports UV-vis kinetics observations on the slower reactivity of this protein. Likely, the Met residues are either directly involved in quenching or replacement with SeMet residues has affected the placement of other unknown amino acid quenchers, though the latter is unlikely due to the prevalence of using SeMet as an isosteric replacement for structure determination in protein crystallography [36–38].

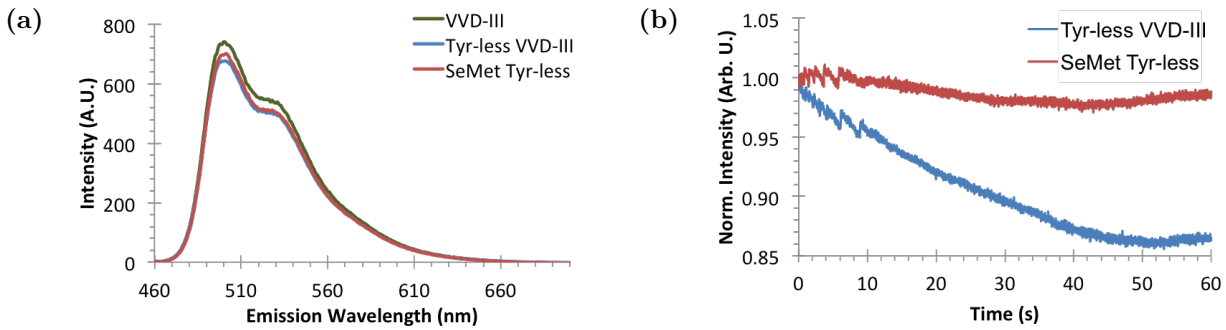

Figure 4.5: (a) Fluorescence emission of VVD mutants excited at 450 nm. (b) Fluorescence quenching kinetics normalized to 1 at $t = 0$ s. Excitation was set at 450 nm and emission at 502 nm.

4.3.4 Transient difference FTIR of VVD variants

The conformational behavior of VVD mutants was probed by difference Fourier Transform Infrared (FTIR) spectroscopy to gain further insight into the role of SeMet residues in the variant. Firstly, WT VVD was compared to the reference protein aureochrome LOV domain (modified construct has the A'α helix but lacks the C-terminal Jα helix; termed LOV-A'$\alpha\Delta$Jα) which has been studied and well-characterized by FTIR [39, 40]. Characteristic bands from aureochrome were used to help assign the signals corresponding to dimerization after adduct formation. In WT VVD, formation of the cysteinyl-flavin bond is observed at 1552 and 1538 cm^{-1}, which is accompanied by other large changes at 1648 cm^{-1} and 1682 cm^{-1} that reflect alterations in α helical content and turn structure, respectively (Supplemental Figure 4.9a).

As a secondary control, Glu182 was replaced with Leu in VVD-III to inhibit photoactivation, conformational changes, and oligomerization from occurring during reduction [7, 8]. In comparison to WT, the signature bands corresponding to secondary structure and dimerization (1648 cm^{-1}, 1656 cm^{-1}, and 1682 cm^{-1}) are absent. Similarly, the Tyr-less VVD-III variant lack these signals and confirm its photoinactivity. The absence of these

structural changes allows for clear observation of the chromophore signal (1547 cm^{-1} and 1532 cm^{-1}) in the protein amide II region, which arises from flavin C4a-N5 and C10a=N1 stretches [40, 41] (Figure 4.6a).

However, photoreduction of this sample exhibited an NSQ signal at 1532 cm^{-1} after two minutes of irradiation, and then surprisingly, the sample continued to convert in the dark to a fully reduced state (1519 cm^{-1} and 1412 cm^{-1}) (Supplemental Figure 4.9d). This behavior is further verified in the VVD-III Q182L variant (Supplemental Figure 4.9c). Photoreduction to a fully reduced hydroquionone has not been observed by UV-vis kinetics and may suggest the presence of an internal reductant in the experiments. Importantly, in the Tyr-less VVD-III, cysteine residues are not likely to be involved in the photoreduction of FAD to the NSQ state, as the thiol band at 2561 cm^{-1} remains unaltered during illumination (Supplemental Figure 4.9b).

Difference spectra of Tyr-less VVD-III and SeMet Tyr-less were compared to unmask the thiol signatures of methionine residues during photoreduction. These data indicate photoconversion of methionine residues that is absent in the SeMet-substituted variant owing to the lack of S−C−H bending modes (1279 cm^{-1}; Figure 4.6b) [42, 43]. A similar vibrational band is seen in bacteriorhodopsin at 1284 cm^{-1} that is present in the WT and absent in the SeMet-bacteriorhodopsin [43]. Additionally, flavin vibrational stretch bands at 1547 cm^{-1} and 1532 cm^{-1} appear upon photoreduction in both VVD samples, indicating NSQ formation and confirming that the methionine conversion is indeed linked to the development of the NSQ state.

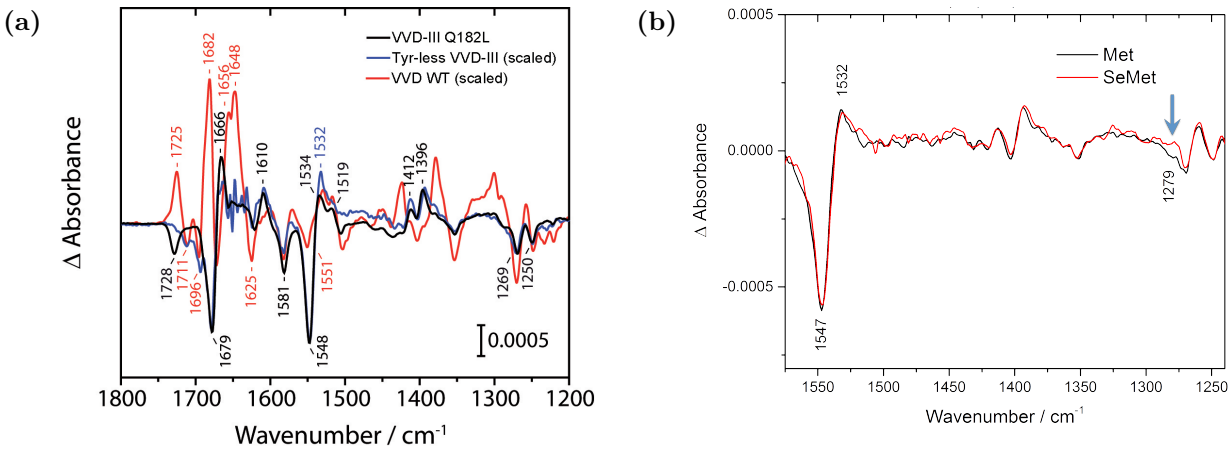

Figure 4.6: (a) Difference Fourier Transform Infrared spectra of WT VVD, VVD-III Q182L, and Tyr-less VVD-III. (b) Comparison between Tyr-less VVD-III and SeMet Tyr-less. Note the presence of the 1279 cm^{-1} band in the Met-containing variant, which indicates conversion of methionine under illumination.

4.4 Conclusion

Previous reports on active cysteine-less VVD (see Chapter 3) reveal its partial photoadaptation capability *in vivo* and photoreduction to the NSQ state under blue light irradiation [5–7]. The electron donor(s) to the flavin cofactor in these type of LOV systems has/have been elusive. Establishing their identity is significant not only for generating null variants *in vivo*, but also for augmenting the fluorescence lifetime of LOV domain reporter molecules. Moreover, these findings may contribute toward the general understanding of how electrons flow in proteins. Here, we report that tyrosine, tryptophan, cysteine, and glycine residues are likely not the active electron donors in this system. WT VVD without tryptophan and tyrosine residues exhibited no attenuation in photoreduction rate, and cysteine residues have been determined spectroscopically to not convert under blue light irradiation. Glycine residues could potentially behave as transient electron donors, but due to their importance in structuring the flavin binding pocket, it is difficult to substitute them. However, extensive spectroscopic probing of the methionine residues and the effects upon their replacement by

SeMet residues gives credence to our suspicions that these residues are the key reductants for generating the NSQ. Additionally, methionine residues can be potent flavin reductants under anaerobic conditions and capable of increasing the photoreduction rate of riboflavin in solution upon exposure to light [44–46]. Interestingly, if Met residues are the sole reductants, replacement with SeMet should have increased photoreduction rates. Yet, the reduction potential of excited state flavin is quite high, rising from -0.3 V to $+1.9$ V upon excitation to the triplet state [47–49], and thus, the increased oxidation potential of the electron donors would have minute effects on the observed rate of electron transfer. Interestingly, based upon fluorescence emission and kinetics data, there may be another intermediary relay residue that bridges the electron donation from the methionine residues to the flavin cofactor. This residue may be the Gly180 that we have yet to successfully replace or even phenylalanine, which has been shown to stabilize electron charges by the contribution of electron density from a neighboring carbonyl-amide to the arene radical [50]. Overall, our findings highlight the prevalence of relay residues and their underlying functionalities in LOV domain proteins. Future protein designs should pay careful consideration to possible electron donation from other redox-active side chains and not only tyrosine and tryptophan residues.

4.5 Materials and Methods

4.5.1 Mutagenesis

VVD-37 from *Neurospora crassa* was mutated to VVD-III (C108A:M135I:M165I) in the pET-28a vector. The construct was further modified with Q182L to remove the coordinating glutamine to the N5 nitrogen of flavin (VVD-III Q182L). The Tyr-less VVD-III (all-Phe) variant was generated from VVD-III by replacing all nine Tyr with Phe

(Y:40,45,50,87,94,98,126,175,177:F). Tyr-less VVD-III was further modified by overlap PCR with either C76V or G180A/S (Tyr-less C76V, Tyr-less G180A/S, respectively).

LOV-HK constructs were generously gifted to us by the Goldbaum group (Leloir Institute Foundation, Argentina). Mutations were implemented by overlap extension PCR to generate the following three variants: S130G, C69A, and C69A:S130G. All constructs were placed in the pET-24d vector.

4.5.2 Protein expression and purification

VVD constructs in a pET-28a vector was used to transform a CmpX13 strain modified from *E. coli* C41 (DE3) with mannose permease gene manX exchanged to flavin transporter RibM to improve flavin incorporation and protein yield [51] or to transform auxotrophic B834 cells for the SeMet variant. Cells were grown either in LB-Miller or LeMaster media with SeMet at 37 °C with 100 mg of riboflavin until OD_{600} ∼0.8. Temperature was lowered to 17 °C and protein expression was induced with 100 μM IPTG. After 18 h of expression, cells were pelleted at 5000 G and either stored temporarily at −20 °C until ready for purification or immediately resuspended in buffer (50 mM HEPES, 150 mM NaCl, 10% glycerol, pH 8) and lysed. Resuspended cells were sonicated for three cycles of 2 min (2 s on, 2 s off) until homogenous. Lysed cells were centrifuged at 20,000 RPM for 1 h at 4 °C, and the supernatant loaded onto a Ni-NTA resin column. The bound protein was washed with buffer +20 mM imidazole and eluted with buffer +200 mM imidazole. Elution was concentrated with a 10 kDa cut-off filter and loaded onto an equilibrated preparatory HiLoad 26/600 Superdex 75. Colored fractions corresponding to ∼17 kDa were collected, concentrated, aliquoted, and stored at −80 °C.

LOV-HK proteins were expressed in *E. coli* C41 (DE3) + RibM transporter [51] in LB-

Miller media with 100 mg of riboflavin at 28 °C overnight. Cells were harvested and lysed in 20 mMTris, pH 8.0, 500 mM NaCl, 0.1% v/v Triton X-100, and 1 mM DTT. After removal of detritus by centrifugation at 20,000 RPM for 1 h at 4 °C, proteins were purified by Ni-NTA affinity chromatography, as delineated above.

4.5.3 Circular dichroism

Purified protein samples were buffer exchanged into 50 mM sodium phosphate, pH 8, 100 mM NaCl, and 10% glycerol. Stock concentrations were determined by Bradford assay and diluted to ∼30 μM. Wavelength scans were collected from $200 - 260$ nm at 25 °C. Thermal melts were acquired at $\lambda = 220$ nm from 25 °C to 95 °C at +2 °C increments. All measurements were acquired using Aviv Model 202-01. Thermal melt traces were fit with a sigmoidal curve to quantify the melting temperatures more accurately.

$$f(x) = \frac{a}{1 + e^{b \cdot (-x+c)}} - d$$

4.5.4 UV-vis photoreduction kinetics

Samples were buffer exchanged into 50 mM HEPES, pH 8, 150 mM NaCl, 10% glycerol and concentrated to $A_{450\ nm}$ ∼0.1 to 0.2. Kinetic traces were collected every 0.5 s at 20 °C while irradiating 10 μL of sample in a 0.2 cm path length cuvette using a 30-mW blue laser (World Star). Exponential decays were fit to $y = a \cdot e^{-b \cdot x} + c$ with MatLab (Mathworks).

4.5.5 Fluorescence emission spectroscopy

Samples at $A_{450\ nm}$ ~0.1 were prepared and added to quartz cuvettes of 0.3 cm path length. Samples were measured in triplicate using a Varian Cary Eclipse coupled to a Quantum Northwest temperature controller at 20 °C. Excitation wavelength was set to 450 nm with a bandwidth of 10 cm, and emission wavelength was 460 nm − 700 nm with a bandwidth of 5 cm.

4.5.6 Difference Fourier Transform Infrared spectroscopy

Samples were purified and buffer exchanged into 50 mM sodium phosphate, 100 mM NaCl, 10% glycerol, and 10 mM DTT, pH 8. Data were acquired by Elena Helman, Sabine Oldemeyer, and Tilman Kottke (Bielefeld University, Germany).

4.5.7 Selenium K-edge X-ray Absorption Near Edge Spectroscopy

Standards were prepared by diluting 10 mM L-selenomethionine (Aldrich) into buffer (50 mM HEPES, 150 mM NaCl, 10% glycerol, pH 8). Protein samples were concentrated to ~ 0.6 mM and buffer exchanged into fresh buffer (50 mM HEPES, 150 mM NaCl, 10% glycerol, pH 8). To these stocks, 5 mM or 10 mM of either reduced glutathione (GSH), H_2O_2, or 5 mM peroxynitrite ($ONOO^-$) was added and allowed to incubated overnight at 4 °C. As $ONOO^-$ was stored in NaOH, an equivalent molar of HCl was added to neutralize the basicity. Owing to the concentration of $ONOO^-$, the selenomethionine standard was diluted to 5 mM and the protein sample had to be concentrated down to ~ 0.6 mM the following morning. Protein samples were loaded into MiTeGen MicroRT capillaries (~ 40 μL), stored in cryovials with punctured holes, and flash frozen in liquid nitrogen.

At the C1 beam line station (CHESS, Cornell University), capillaries were mounted into a cold finger in a vacuum chamber and cooled to 100 K. Samples were translated and centered in the beam for highest signal-to-noise and irradiated from 12.6 to 12.72 keV. Fluorescence data were collected perpendicular to the incident beam using a Vortex detector over the following ranges with 10 s averaging times per point: $12.6-12.645$ (5 eV steps); $12.645-12.675$ (0.5 eV steps); $12.675-12.705$ (5 eV steps). Data were subsequently merged, calibrated to 12568 eV, and normalized in Athena [30]. As edges shifted randomly and inconsistently by several eV (likely due to inhomogeneities) despite the use of an internal standard of selenium-doped graphite, all edges were aligned and spectra analyzed qualitatively.

4.5.8 Proteomics - intact protein analysis

Purified protein in 50 mM HEPES, 150 mM NaCl, 5% glycerol, pH 8 were treated with either $10-20$ mM glutathione or H_2O_2 overnight at 4 °C and subsequently diluted into 5% acetonitrile and 0.1% formic acid. Samples were run on a Thermo UltiMate3000 RSLC on a Thermo Scientific BioBasic-4 column at a flow rate of 200 μL/min in a solvent system of 0.1% formic acid and 95% acetonitrile and 0.1% formic acid and a gradient of $15-75-95-15$ %B. The Orbitrap Elite was operated in ESI positive ion FT mode with Ion Max-S API source under Xcalibur 2.2. All analyses were conducted with the Xcalibur 2.2 software package. Samples were alternatively analyzed by positive electrospray ionization time-of-flight mass spectrometry using a Synapt HDMS. To reduce selenomethionine oxidation, reduced samples were treated with L-methionine and the trap column was flushed with EDTA and HPLC-grade water before equilibrating in 5% acetonitrile and 0.1% formic acid [52].

4.6 Acknowledgements

Thanks to Ken Finkelstein for assistance at C1 beam line at CHESS, Cornell University. Also, thanks to Sheng Zhang and Robert Sherwood (Cornell University Biotechnology Resource Center (BRC)) for running and analyzing proteomics samples. Lastly, thanks to Sabine Oldemeyer, Elena Herman, and Tilman Kottke for difference FTIR collection and analyses. This work was financially supported by the NIH training grant T32 GM08267 (to E.F.Y.) and NSF grant 1715233 (to B.R.C.).

4.7 Supplemental Information

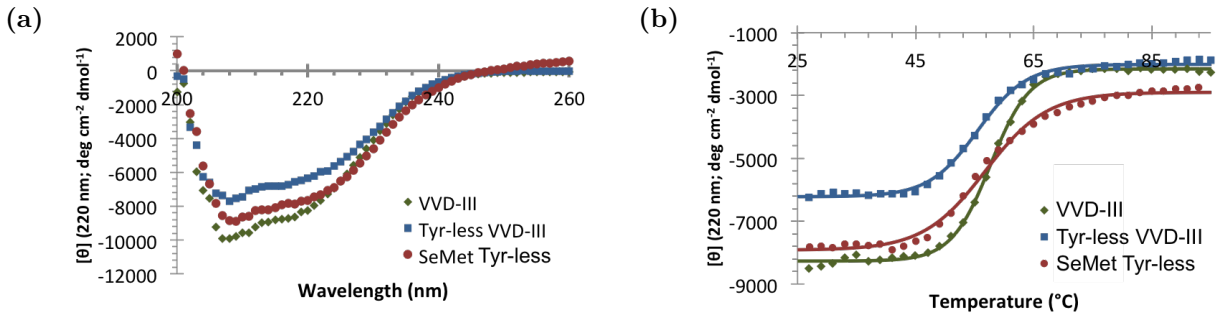

Supplemental Figure 4.7: Comparisons by circular dichroism (CD) of structural stability. All samples were at similar concentrations, as quantified by Bradford assay. (a) CD spectra illustrate few differences in molar ellipticity between variants. (b) Thermal melts conducted at $\lambda = 220$ nm exhibit similar melting temperatures, though VVD-III appears to melt more homogeneously.

Variant	a [θ]	b [°C^{-1}]	c [°C]	d [θ]
VVD-III	6113	0.302	57.7	8271
Tyr-less VVD-III	4210	0.242	55.5	6224
SeMet Tyr-less	5022	0.191	56.8	7923

Supplemental Table 4.2: Circular dichroism thermal melt fits using the sigmoidal function $f(x) = \frac{a}{1+e^{b\cdot(-x+c)}} - d$. Parameter c is the melting temperature, which varies little between protein samples, and a corresponds to the melting homogeneity.

Sample	% Std + GSH	% Std + H_2O_2	% Std + $ONOO^-$
SeMet Tyr-less + GSH	90.4 ± 4.7	–	9.6 ± 7.6
SeMet Tyr-less + H_2O_2	90.5 ± 7.1	0.0 ± 9.0	9.5 ± 11.4
SeMet Tyr-less + $ONOO^-$	49.9 ± 1.4	25.9 ± 1.8	24.2 ± 2.2
SeMet Tyr-less + photoreduced	78.3 ± 10.4	0.0 ± 13.1	21.7 ± 16.7

Supplemental Table 4.3: Linear combination analysis results of SeMet Tyr-less XAS spectra. Components are XAS spectra of selenomethionine solution standards treated with either GSH, H_2O_2 or $ONOO^-$. The flavin core appears to be fairly solvent inaccessible and not easily oxidized by peroxide. Addition of $ONOO^-$ causes destabilization and flavin release. Irradiation of protein sample with blue light appears to cause a small amount of Se oxidation.

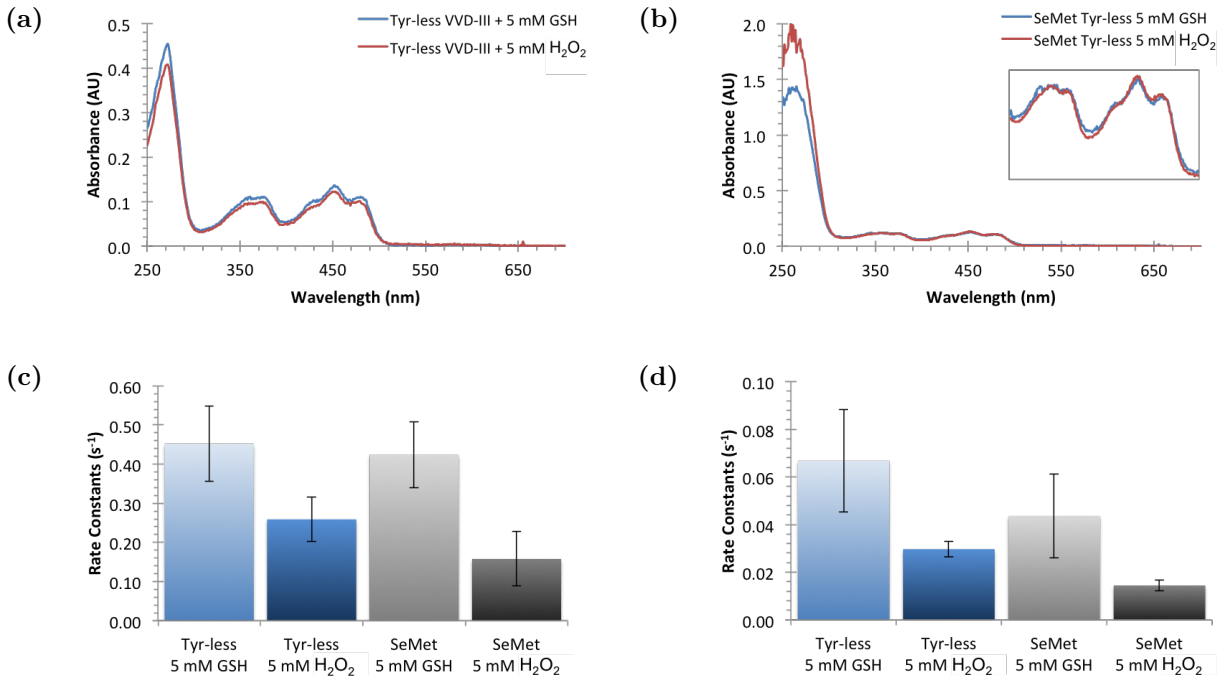

Supplemental Figure 4.8: (a–b) VVD-III samples after overnight incubation with 5 mM reduced glutathionine or hydrogen peroxide in buffer. Neither conditions resulted in destabilization of the proteins nor release of the flavin, as observed by the distinctive features of bound flavin. (c–d) Kinetic traces were obtained at 450 nm while irradiating samples with 448-nm laser light at $T = 20$ °C and subsequently fit to biexponential curves. Graph (c) compares the fast phase k_1 rate constants, and graph (d) illustrates the differences in slow phase k_2.

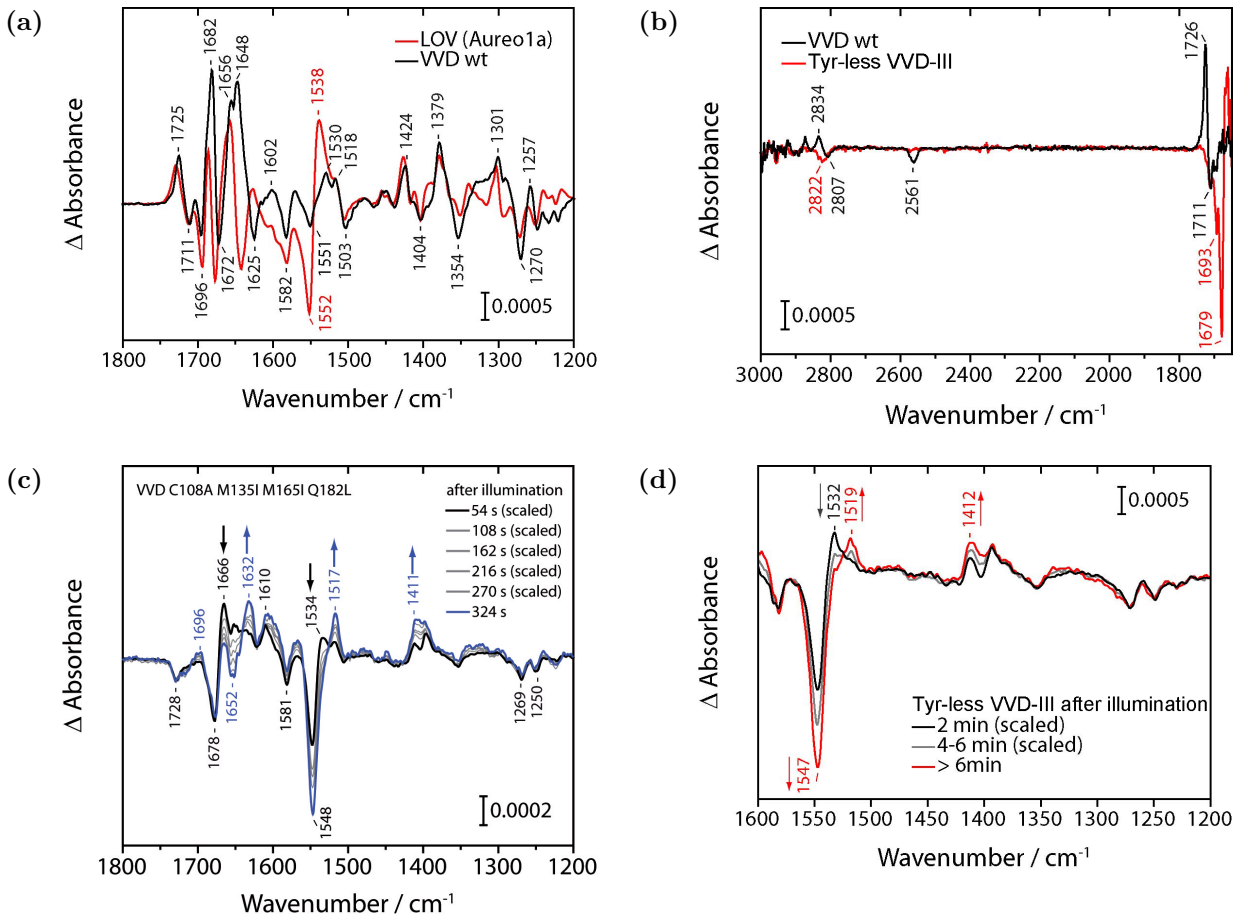

Supplemental Figure 4.9: Difference Fourier Transform Infrared spectra. (a) Comparison of WT VVD photoconvertion to that of aureochrome LOV-A'$\alpha\Delta$Jα domain. (b) Lack of cysteine adduct formation in the Tyr-less VVD-III variant is observed by the absence of the 2561 cm^{-1} band. (c–d) Photoreduction of VVD-III (C108A:M135I:M165I) Q182L and Tyr-less VVD-III. Proteins continue to convert to the fully reduced state in the dark in the absence of an external reductant.

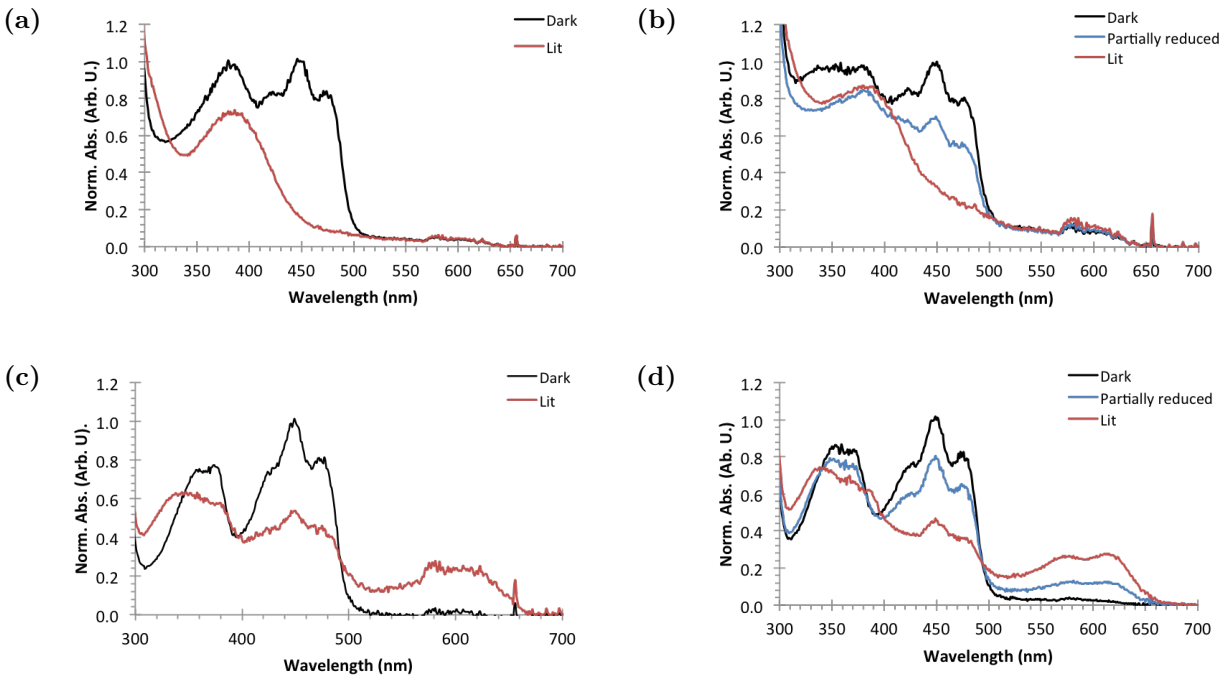

Supplemental Figure 4.10: UV-vis spectra of photoreduced LOV-HK proteins under 448-nm laser light at $T = 20$ °C. WT and S130G variants were irradiated through a neutral density filter of 1.6.

BIBLIOGRAPHY

(1) Crosson, S.; Moffat, K. *Proc. Natl. Acad. Sci.* **2001**, *98*, 2995–3000.

(2) Cheng, P.; He, Q.; Yang, Y.; Wang, L.; Liu, Y.; Briggs, W. R. *Proc. Natl. Acad. Sci. U. S. A.* **2003**, *100*, 5938–43.

(3) Zoltowski, B. D.; Crane, B. R. *Biochemistry* **2008**, *47*, 7012–7019.

(4) Herrou, J.; Crosson, S. *Nat. Rev. Microbiol.* **2011**, *9*, 713–723.

(5) Chen, C.-H.; DeMay, B. S.; Gladfelter, A. S.; Dunlap, J. C.; Loros, J. J. *Proc. Natl. Acad. Sci.* **2010**, *107*, 16715–16720.

(6) Vaidya, A. T.; Chen, C.-h. H.; Dunlap, J. C.; Loros, J. J.; Crane, B. R. *Sci. Signal.* **2011**, *4*, ra50.

(7) Yee, E. F.; Diensthuber, R. P.; Vaidya, A. T.; Borbat, P. P.; Engelhard, C.; Freed, J. H.; Bittl, R.; Möglich, A.; Crane, B. R. *Nat. Commun.* **2015**, *6*, 10079.

(8) Ganguly, A.; Thiel, W.; Crane, B. R. *J. Am. Chem. Soc.* **2017**, *139*, 2972–2980.

(9) Kopka, B.; Magerl, K.; Savitsky, A.; Davari, M. D.; Röllen, K.; Bocola, M.; Dick, B.; Schwaneberg, U.; Jaeger, K. E.; Krauss, U. *Sci. Rep.* **2017**, *7*, 1–16.

(10) Magerl, K.; Stambolic, I.; Dick, B. *Phys. Chem. Chem. Phys.* **2017**, *19*, 10808–10819.

(11) Wang, M.; Gao, J.; Müller, P.; Giese, B. *Angew. Chemie - Int. Ed.* **2009**, *48*, 4232–4234.

(12) Backman, L. R.; Funk, M. A.; Dawson, C. D.; Drennan, C. L. *Crit. Rev. Biochem. Mol. Biol.* **2017**, *52*, 674–695.

(13) *Flavins: Photochemistry and Photobiology*; Silva, E., Edwards, A. M., Eds.; Comprehensive Series in Photochemical; Royal Society of Chemistry: 2007.

(14) Pettersen, E. F.; Goddard, T. D.; Huang, C. C.; Couch, G. S.; Greenblatt, D. M.; Meng, E. C.; Ferrin, T. E. *J. Comput. Chem.* **2004**, *25*, 1605–1612.

(15) Mulliez, E.; Fontecave, M.; Gaillard, J.; Reichard, P. *J. Biol. Chem.* **1993**, *268*, 2296–2299.

(16) Stubbe, J.; van der Donk, W. A. *Chem. Rev.* **1998**, *98*, 705–762.

(17) Rinaldi, J.; Gallo, M.; Klinke, S.; Paris, G.; Bonomi, H. R.; Bogomolni, R. A.; Cicero, D. O.; Goldbaum, F. A. *J. Mol. Biol.* **2012**, *420*, 112–127.

(18) Gray, H. B.; Winkler, J. R. *Proc. Natl. Acad. Sci. U. S. A.* **2005**, *102*, 3534–9.

(19) Nauser, T.; Steinmann, D.; Grassi, G.; Koppenol, W. H. *Biochemistry* **2014**, *53*, 5017–5022.

(20) Krause, R. J.; Elfarra, A. A. *Biochem. Pharmacol.* **2009**, *77*, 134–140.

(21) Misra, S.; Peak, D.; Chen, N.; Hamilton, C.; Niyogi, S. *Comp. Biochem. Physiol. - C Toxicol. Pharmacol.* **2012**, *155*, 560–565.

(22) Reich, H. J.; Hondal, R. J. *ACS Chem. Biol.* **2016**, *11*, 821–841.

(23) Carroll, L.; Pattison, D. I.; Fu, S.; Schiesser, C. H.; Davies, M. J.; Hawkins, C. L. *Redox Biol.* **2017**, *12*, 872–882.

(24) Pickering, I. J.; Brown, Jr, G. E.; Tokunaga, T. K. *Environ. Sci. Technol.* **1995**, *29*, 2456–2459.

(25) Smith, J. L.; Thompson, A. *Structure* **1998**, *15*, 815–819.

(26) Sharff, A. J.; Koronakis, E.; Luisi, B.; Koronakis, V. *Acta Crystallogr. Sect. D Biol. Crystallogr.* **2000**, *56*, 785–788.

(27) Ryser, A. L.; Strawn, D. G.; Marcus, M. A.; Johnson-Maynard, J. L.; Gunter, M. E.; Möller, G. *Geochem. Trans.* **2005**, *6*, 1–11.

(28) Padmaja, S.; Squadrito, G.; Lemercier, J.-N.; Cueto, R.; Pryor, W. A. *Free Radic. Biol. Med.* **1996**, *21*, 317–322.

(29) Holton, J. M. *J. Synchrotron Radiat.* **2007**, *14*, 51–72.

(30) Ravel, B.; Newville, M. *J. Synchrotron Radiat.* **2005**, *12*, 537–541.

(31) Penzkofer, A.; Bansal, A. K.; Song, S. H.; Dick, B. *Chem. Phys.* **2007**, *336*, 14–21.

(32) Kennis, J. T. M.; Crosson, S.; Gauden, M.; Van Stokkum, I. H. M.; Moffat, K.; Van Grondelle, R. *Biochemistry* **2003**, *42*, 3385–3392.

(33) Sakai, M.; Takahashi, H. *J. Mol. Struct.* **1996**, *379*, 9–18.

(34) Kutta, R. J.; Magerl, K.; Kensy, U.; Dick, B. *Photochem. Photobiol. Sci.* **2015**, *14*, 288–299.

(35) Kao, Y. T.; Saxena, C.; He, T. F.; Guo, L.; Wang, L.; Sancar, A.; Zhong, D. *J. Am. Chem. Soc.* **2008**, *130*, 13132–13139.

(36) Hendrickson, W. A.; Horton, J. R.; LeMaster, D. M. *EMBO J.* **1990**, *9*, 1665–1672.

(37) Usón, I.; Sheldrick, G. M. *Curr. Opin. Struct. Biol.* **1999**, *9*, 643–648.

(38) Ealick, S. E. *Curr. Opin. Chem. Biol.* **2000**, *4*, 495–499.

(39) Herman, E.; Sachse, M.; Kroth, P. G.; Kottke, T. *Biochemistry* **2013**, *52*, 3094–3101.

(40) Herman, E.; Kottke, T. *Biochemistry* **2015**, *54*, 1484–1492.

(41) Abe, M.; Kyogoku, Y.; Kitagawa, T.; Kawano, K.; Ohishi, N.; Takai-Suzuki, A.; Yagi, K. *Spectrochim. Acta Part A Mol. Spectrosc.* **1986**, *42*, 1059–1068.

(42) Grunenberg, A.; Bougeard, D. *J. Mol. Struct.* **1987**, *160*, 27–36.

(43) Bergo, V.; Mamaev, S.; Olejnik, J.; Rothschild, K. J. *Biophys. J.* **2003**, *84*, 960–6.

(44) Frisell, W. R.; Chung, C. W.; Mackenzie, C. G. *J. Biol. Chem.* **1958**, *234*, 1297–1302.

(45) Enns, K.; Burgess, W. H. *J. Am. Chem. Soc.* **1965**, *87*, 1822–1823.

(46) Ninnemann, H. *Photochem. Photobiol.* **1982**, *35*, 391–398.

(47) Losi, A. *Photochem. Photobiol.* **2007**, *83*, 1283–1300.

(48) Arents, J. C.; Perez, M. A.; Hendriks, J.; Hellingwerf, K. J. *FEBS Lett.* **2011**, *585*, 167–172.

(49) Losi, A.; Gärtner, W. *Photochem. Photobiol.* **2017**, *93*, 141–158.

(50) Nathanael, J.; Gamon, L.; Cordes, M.; Rablen, P.; Bally, T.; Fromm, K.; Giese, B.; Wille, U. *ChemBioChem* **2018**, *19*, 922–926.

(51) Mehlhorn, J.; Steinocher, H.; Beck, S.; Kennis, J. T. M.; Hegemann, P.; Mathes, T. *PLoS One* **2013**, *8*, e79006.

(52) Kang, P.; Mezhebovsky, T.; Chen, W.; McCardle, J. A.; Zhang, S.; Sullivan, E. P.; Sass, P. M.; Routhier, E. *Rapid Commun. Mass Spectrom.* **2016**, *30*, 1734–1742.

APPENDIX A

CONSTRAINTS ON THE RADICAL CATION CENTER OF CYTOCHROME *C* PEROXIDASE FOR ELECTRON TRANSFER FROM CYTOCHROME *C* *

A.1 Abstract

The tryptophan 191 cation radical of cytochrome *c* peroxidase (CcP) compound I (Cpd I) mediates long-range electron transfer (ET) to cytochrome *c* (Cc). Here we test the effects of chemical substitution at position 191. CcP W191Y forms a stable tyrosyl radical upon reaction with peroxide and produces spectral properties similar to those of Cpd I but has low reactivity toward reduced Cc. CcP W191G and W191F variants also have low activity, as do redox ligands that bind within the W191G cavity. Crystal structures of complexes between Cc and CcP W191X (X = Y, F, or G), as well as W191G with four bound ligands reveal similar 1:1 association modes and heme pocket conformations. The ligands display structural disorder in the pocket and do not hydrogen bond to Asp235, as does Trp191. Well-ordered Tyr191 directs its hydroxyl group toward the porphyrin ring, with no basic residue in the range of interaction. CcP W191X (X = Y, F, or G) variants substituted with zinc-porphyrin (ZnP) undergo photoinduced ET with Cc(III). Their slow charge recombination kinetics that result from loss of the radical center allow resolution of difference spectra for the charge-separated state [ZnP^+, Cc(II)]. The change from a phenyl moiety at position 191 in W191F to a water-filled cavity in W191G produces effects on ET rates much weaker than the effects of the change from Trp to Phe. Low net reactivity of W191Y toward Cc(II) derives either from the inability of ZnP^+ or the Fe-CcP ferryl to oxidize Tyr or from the low potential of

*Reproduced with permission from T. M. Payne, E. F. Yee, B. Dzikovski, and B. R. Crane. *Biochemistry* **2016** *55* (34), 4807-4822.

the resulting neutral Tyr radical.

A.2 Introduction

The electron transfer (ET) partners cytochrome *c* peroxidase (CcP) and cytochrome *c* (Cc) provide an important model system for understanding interprotein ET, protein−protein interactions, and heme−oxygen chemistry.[1-6] The catalytic mechanism of CcP:Cc proceeds as follows: Peroxide reacts with the Fe(III) heme of CcP to form compound I (Cpd I), which consists of an Fe(IV) iron oxo species [Fe(IV)=O] and a radical cation localized on neighboring Trp191 ($W^{\bullet+}$). Two Fe(II) Cc proteins sequentially reduce CcP Cpd I back to Fe(III) and water. In the first step, $W^{\bullet+}$ is directly reduced by Cc(II). In the second step, the remaining Fe(IV)=O center reoxidizes Trp191, which is subsequently reduced by Cc(II)[7-10] (Scheme A.1). Thus, $W^{\bullet+}$ is the key electron acceptor for oxidation of Cc(II). Hoffman and colleagues developed CcP:Cc as a model ET system by incorporating Zn-porphyrin (ZnP) into either CcP or Cc in place of heme.[2, 11-16] The photoexcited ZnP triplet state injects an electron across the molecular interface to reduce the Cc Fe(III) heme. ZnP^+ and Cc(II) then recombine to regenerate the ground state. Similar to the native reaction, back ET between ZnP^+ and Cc(II) is greatly accelerated by Trp191, which acts as a hole-hopping site by localizing the cation radical closer to the Cc Fe(II) heme[3, 17-19] (Figure A.1). Little of the charged separated state builds up in ZnCcP:Cc because the rate constant for back ET (k_{eb}) is much greater than the rate constant for forward ET (k_e). However, the W191F substitution slows ET by at least 2 orders of magnitude and allows resolution of a ZnP^+ Cc(II) intermediate.[17, 20] In fact, charge recombination in W191F is slow enough to compete with complex dissociation, which produces a second kinetic phase at long times.[20] Recent theoretical studies support the involvement of Trp191 oxidation in ZnCcP:Cc reaction kinetics.[3, 19] Importantly, the back reaction of the $ZnP/W^{\bullet+}$ center with Fe(II)Cc involves

donor-acceptor states, redox potentials, and coupling pathways similar to those of the natural ET reaction between Cpd I and Fe(II)Cc.[3]

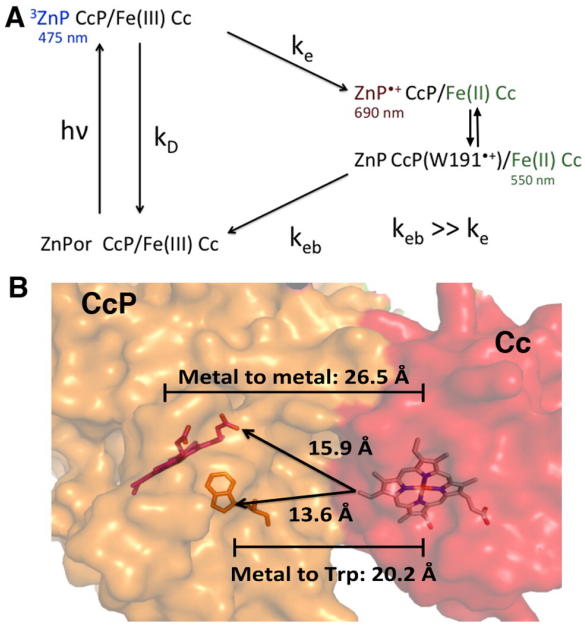

Figure A.1: Photoinduced ET by ZnCcP:Cc. (A) The triplet state of zinc-porphyrin (ZnP) bound to CcP (^{3}ZnP) is produced by an 8 ns pulse of 532-560 nm light. ^{3}ZnP CcP will then either decay back to the ground state (rate constant k_D in the absence of Cc) or reduce Fe(III)Cc to Fe(II)Cc (rate constant k_e) to produce a porphyrin radical cation (ZnP^+). The cation radical rapidly equilibrates between ZnP^+ and a nearby aromatic side chain at position 191. The charge-separated state will then recombine with rate constant k_{eb}. Dissociation and reassociation of the charge-separated complex are not included in the scheme. (B) Residue 191 resides between the CcP ZnP and Cc heme in the protein complex.

$$\text{Fe(III)CcP} + \text{HOOH} \longrightarrow \text{Fe(IV)=O,W}^{\bullet+}\text{CcP} + \text{H}_2\text{O}$$
$$\text{Fe(IV)=O,W}^{\bullet+}\text{CcP} + \text{Fe(II)Cc} \longrightarrow \text{Fe(IV)=O,W}^{0}\text{CcP+Fe(III)Cc}$$
$$\text{Fe(IV)=O,W}^{0}\text{CcP+H}^{+} \longrightarrow \text{Fe(III)-OH,W}^{\bullet+}\text{CcP}$$
$$\text{Fe(III)-OH,W}^{\bullet+}\text{CcP+Fe(II)Cc+H}^{+} \longrightarrow \text{Fe(III),W}^{0}\text{CcP+Fe(III)Cc+H}_2\text{O}$$

Scheme A.1: Peroxidase Activity of CcP and Cc

Conformational processes and dynamic docking of the CcP:Cc complex have also attracted much interest.[5, 9, 21-30] Photoinduced ET reactions in crystals confirm that the

crystal association mode has ET kinetics similar those observed in solution.[18, 31, 32] Nonetheless, conformational dynamics within the ZnCcP:Cc complex likely generate ET competent states both in solution and in crystals.[5, 18, 31, 33, 34] Altered binding interactions between CcP and Cc cause changes in ET kinetics that can be explained by accounting for Trp191 radical formation, electron coupling between donor and acceptor sites, redox potentials, and reorganization energies.[3]

Electron-hole hopping through aromatic residues is an important process in many redox systems such as photosystem II, ribonucleotide reductase (RR), photolyase enzymes, and cryptochromes.[35-41] Protein ET rate constants are exponentially dependent on the distance of separation between electron donor (D) and acceptor (A) sites.[42] Thus, if the acceptor can oxidize an intervening residue (the "hole"), one long ET step can be broken into two shorter "hops".[37, 43-45] Introduction of appropriately placed Trp and Tyr residues into modified blue copper proteins [44-46] and model systems [36, 47] demonstrates the ability of aromatic residues to accelerate long-range ET. Incorporation of non-natural variants of Tyr into RR has also probed the effects of redox potential on multistep tunneling reactions.[40] ZnCcP:Cc provides another system for exploring residue oxidation in ET with the potential advantage of widening the reactivity of the hole-hopping site beyond Tyr and Trp residues. In particular, Goodin and colleagues have demonstrated that the Trp191Gly variant (W191G) produces a cavity in CcP within which heterocyclic cationic compounds will bind.[48-51] One such compound, 2-aminothiazole, acts as a reductant of the peroxide-oxidized heme.[50] Replacement of a segment of the CcP polypeptide with a surrogate peptide allows for substitution of Trp191 with benzimidazole.[52] Despite being a good structural mimic for the native residues, the surrogate peptide renders CcP inactive because the benzimidazole moiety cannot form a stable radical upon reaction with peroxide.[52] Herein, we extend this general approach of CcP cavity complementation to examine the ability of residue substitutions and exogenous compounds to support peroxidase activity

and hole hopping in ZnCcP:Cc. Determinations of the structures of modified CcP:Cc complexes provide constraints for the interpretation of reactivity. We find that despite wild-type (WT)-like conformations and suitable redox potentials of various exogenous surrogates, only the native Trp191 residue supports peroxidase activity with Cc and rapid back ET in the ZnCcP system. Surprisingly, a Tyr191 variant also appears to form a Cpd I-like state but does not oxidize Cc in the natural reaction or accelerate the photoinduced recombination process.

A.3 Results

In the following experiments, CcP Trp191 was substituted with Phe,[68] Gly,[48] and Tyr. For the W191G variant, a series of small molecules were also introduced into the cavity created by removal of the residue 191 side chain. In all cases, crystal structures of the CcP:Cc complexes were determined to aid interpretation of reactivity data. We then examined the peroxidase activity of the variants, their ability to form Cpd I, and their photoinduced ET reactions in the context of ZnCcP:Cc.

A.3.1 Structures of W191(Y,F,G) CcP

The structures of W191(Y,F,G) CcP in complex with Fe(III)Cc were determined at resolutions that ranged from 2.0 to 2.4 Å (Table A.1). For each of the variants, both CcP and Cc retained conformations nearly identical to those seen in the WT complex (Figure A.2). In the absence of Cc, the W191G substitution causes enhanced flexibility in the 190−195 loop.[69] Because this loop resides at the binding interface with Cc, there was concern that increased flexibility would impact the formation of the crystal complex. Nonetheless, W191G

binds Cc in the expected position. The two copies of the CcP:Cc complex in the asymmetric unit are very similar to each other in structure (designated as chains A and C for CcP and chains B and D for Cc). Several of the Cc moieties were not well ordered in the complex structures. As observed previously,[18] the interfaces between CcP and Cc are generally well-defined, but electron density weakens at the periphery of the complexes, largely because of Cc conformational variability within the lattice. This disorder is difficult to model well and somewhat degrades the refinement statistics relative to those expected for an average structure of similar resolution (Table A.1).

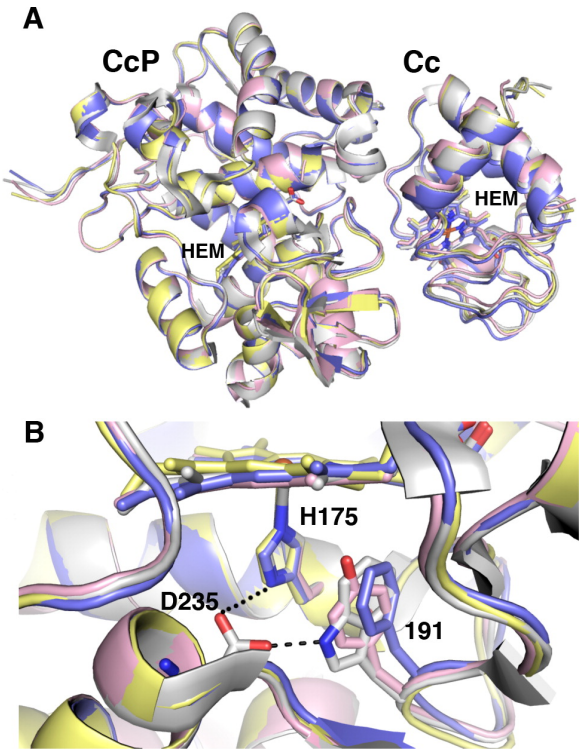

Figure A.2: Structures of CcP W191X variants with Cc. (A) Overlay of the CcP:Cc W191X structures with the WT complex showing a high degree of similarity (WT, Protein Data Bank entry 1U74, in white, W191Y in pink, W191F in blue, and W191G in yellow). One of the two unique complexes in the asymmetric unit is shown. (B) Superposition of residue 191 in the respective crystal structures showing that the aromatic side chains all hold approximately the same position in each variant, with each side chain oriented in the plane of coordinating His175. In WT CcP, Trp191 hydrogen bonds with Asp235. The side chains of Tyr191 and Phe191 have no polar contacts. The peptide backbone of Gly191 has the same conformation that Trp191 in WT does.

	W191F	W191Y	W191G	W191G with aniline
Data Collection				
space group	$P2_1$	$P2_1$	$P2_1$	$P2_1$
a, b, c (Å)	44.8, 113.8, 88.2	45.5, 110.2, 88.2	45.4, 117.1, 88.9	45.4, 110.3, 87.9
β (deg)	105.3	104.3	105.1	105.5
no. of unique reflections	51828	21533	52508	27854
resolution (Å)	2.01	2.4	2.06	2.5
last shell resolution[a] (Å)	2.03-2.01	2.44-2.40	2.13-2.06	2.54-2.5
completeness (%)	92.2/90.7	80.7/51.1	96.1/98.3	95.9/98.0
I/σ	14.9/3.8	8.4/2.0	9.2/2.7	7.3/2.0
R_{merge}[b]	0.222/0.488	0.135/0.670	0.121/0.46	0.158/0.537
Refinement				
R_{work}[c] (%)	21.5/23.4	22.3/28.9	28.1/33.8	25.0/31.1
R_{free}[c] (%)	26.7/37.6	30.9/43.9	29.7/34.6	29.4/43.5
no. of atoms	7052	6560	6912	6657
no. of water molecules	534	40	324	55
mean B value (Å^2)	33.6	70.5	43.3	66.4
B value (waters) (Å^2)	35.9	55.4	44.3	52.0
B value (ligand) (Å^2)	NA	NA	NA	59.9
rmsd for bonds (Å)	0.004	0.003	0.003	0.003
rmsd for angles (deg)	0.8	0.7	0.8	1.0
ϕ/ψ stats (%)				
most favored	97.6	94.5	96.8	96.1
outliers	0.13	0.25	0.25	0.0
Protein Data Bank entry	5CIF	5CIH	5CIG	5CIE

	W191G with *o*-toluidine	W191G with 24dma	W191G with 3abt
Data Collection			
space group	$P2_1$	$P2_1$	$P2_1$
a, b, c (Å)	45.4, 111.9, 87.9	45.4, 107.5, 87.2	45.3, 117.5, 88.5
β (deg)	104.3	104.5	104.4
no. of unique reflections	20376	15317	51366
resolution (Å)	2.76	3.0	2.10
last shell resolution[a] (Å)	2.59-2.76	3.05-3.00	2.14-2.10
completeness (%)	93.5/65.7	95.9/85.0	98.7/90.0
I/σ	17.1/3.2	17.2/3.4	14.2/4.7
R_{merge}[b]	0.092/0.388	0.123/0.512	0.096/0.402
Refinement			
R_{work}[c] (%)	21.4/26.9	23.5/27.8	19.2/24.8
R_{free}[c] (%)	26.8/34.8	31.3/37.8	22.8/29.1
no. of atoms	6613	6606	7076
no. of water molecules	9	0	496
mean B value (Å^2)	70.2	60.1	45.2
B value (waters) (Å^2)	54.4	NA	45.7
B value (ligand) (Å^2)	76.3	57.5	46.3
rmsd for bonds (Å)	0.005	0.003	0.005
rmsd for angles (deg)	1.0	0.8	0.9
ϕ/ψ stats (%) most favored	95.7	94.0	98.6
outliers	0.38	0.31	0.25
Protein Data Bank entry	5CID	5CIB	5CIC

Table A.1 Diffraction Data Collection and Structure Refinement Statistics

[a]Highest-resolution range for compiling statistics follows slash.
[b]$R_{merge} = (\Sigma_i \Sigma_j |I_j - \langle I_i \rangle I)/[\Sigma_i (\Sigma_j I_j)]$, where I_j is the intensity of the j^{th} observation of reflection i, $\langle I_j \rangle$ is the average intensity of reflection i, and N_i is the redundancy of reflection i.
[c]R_{work} or $R_{free} = (\Sigma |F_{obs} - F_{calc}|)/(\Sigma |F_{obs}|)$.

In the CcP:Cc complexes, the altered side chains of W191F and W191Y occupy nearly the same position as W191 in the WT (Figure A.2B), with the phenol group of W191Y and the phenyl group of W191F aligning with the imidazole of His175, which coordinates the heme and hydrogen bonds to Asp235.[70] There is no polar moiety within hydrogen bonding range of the Tyr191 hydroxyl group (Figure A.2B) (the Thr180 side chain is within 3.3 Å of the Tyr191 hydroxyl group, but the hydroxyl group hydrogen bonds with the backbone of Gly189). Instead, the Tyr191 hydroxyl proton may be stabilized by the π-electrons of the heme itself. In the W191G Cc complex, difference electron density confirms the presence of ordered water molecules in the cavity created by the loss of the W191 indole. However, the water positions differ somewhat from those of uncomplexed CcP[48, 49] and vary between chain A and chain C in these structures. No ordered water molecules were detected near the side chains of Tyr191 or Phe191 in the respective structures.

A.3.2 Complementation of the W191G Pocket with Small Molecules

To promote ligand binding in the W191G cavity, crystals were soaked with several redox-active compounds at concentrations of 30 mM (Figure A.3). These compounds were selected considering their structural similarity to aniline or indoline, each of which is a ligand demonstrated to bind the pocket that has a solution redox potential similar to that of Trp.[71, 72] Although the affinities of these compounds for W191G have not been measured, we reasoned

that they would be in a range similar to those found for aniline and indoline (30 and 160 μM for CcP W191G, respectively[58]). Of the compounds tested, four bound to W191G as evidenced by the presence of significant difference electron density in the cavity made vacant by the W191G substitution [$>2.0\sigma$ in a $F_o - F_c$ electron density difference map (Figure A.4)]. Although the difference densities are changed relative to that seen in the water-filled cavity of W191G, they are ambiguous in each case; hence, the compounds may bind with multiple configurations (Figure A.4). Despite the demonstrated affinity of indoline for the cavity, we did not observe any electron density for this compound in the crystal structures. Perhaps Cc association prevents movement of the 190−195 loop that is required for this larger ligand to access the pocket.[52, 69] A barrier to access may have also prevented binding of indole and tryptophan, which were also not detected in the crystallization experiments. Co-crystallization of the complex with these ligands was also unsuccessful. Indole binding was possibly limited by its low solubility in the crystallization solutions.

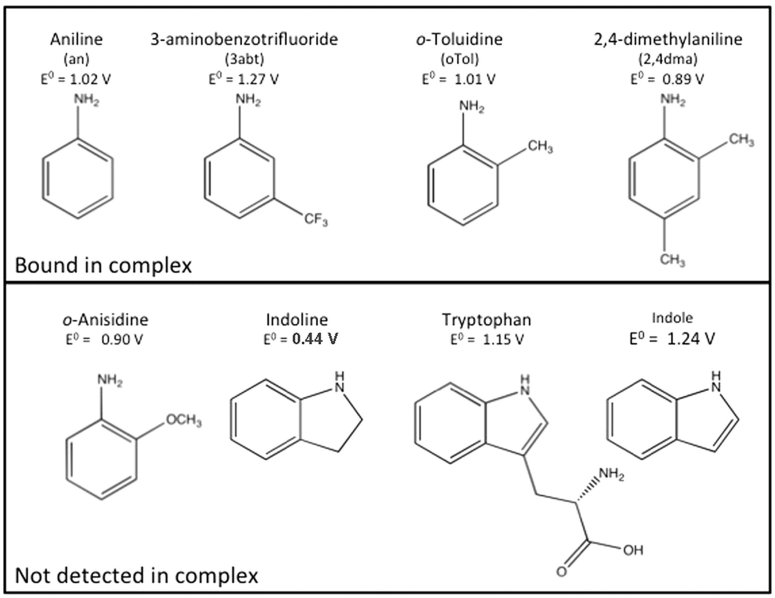

Figure A.3: Compounds targeted at the W191G cavity. Compounds tested for binding W191G cavity and their respective reduction potentials (tryptophan,[110] aniline,[111] indole,[111] and aniline derivatives[90]).

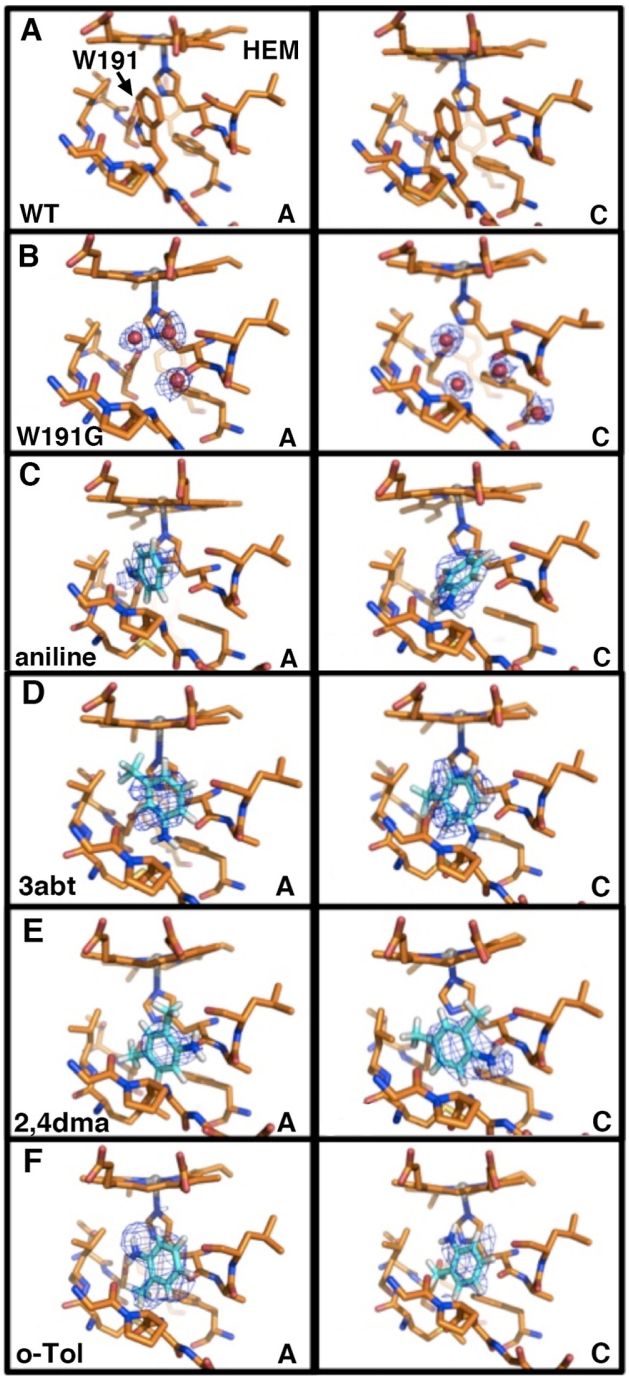

Figure A.4: Ligands bound in the W191G CcP cavity. The WT CcP:Cc structure compared to the W191G CcP:Cc structure soaked with (B) nothing, (C) aniline, (D) 3-aminobenzorufluoride, (E) 2,4-dimethylaniline, and (F) *o*-toluidine. Omit map difference electron density is shown at $2.2 - 2.5\sigma$ for both unique complexes in the asymmetric unit (chains A and C).

A.3.3 Saturation Kinetics

WT CcP displayed the expected high peroxidase activity and typical Michaelis−Menten behavior (V_{max}/E_0 = 1600 ± 100 s^{-1}; K_m = 30 ± 7 μM; 100 mM KP_i) with respect to Cc concentration at 100 mM KP_i, where complicating factors from second-site binding are negligible.[20, 73] (We note that the K_m value for WT is ∼5 times higher than those of previous studies,[63, 73, 74] perhaps because of the different buffer conditions used here.) As expected,[48, 66, 68] W191F and W191G had little detectable peroxidase activity, above that of Cc oxidation by hydrogen peroxide alone. The steady-state rate of Cc(II) oxidation by W191F has previously been shown to be at least 10^3-fold lower than that by WT and linear for only a few seconds.[66] We found similar behavior for both W191F and W191G, with the lack of linearity making rates difficult to determine. Under our conditions, W191Y also appeared to be largely inactive. V_{max}/E_0 was only 40 ± 20 s^{-1} but also showed a peroxide dependence (see below).

To determine if the small-molecule compounds that bound in the W191G CcP cavity can rescue peroxidase activity, the rate of Cc oxidation was measured for W191G and compared to the value of W191F under the same conditions. As both W191G and W191F are inactive and Phe191 blocks the cavity, any peroxidase activity of W191G above that seen for W191F should reflect ligand binding. At ligand concentrations at least 1 order of magnitude above the measured K_D values (2 mM [58]), no detectable peroxidase activity of W191G was observed in the presence of any of the compounds listed in Figure A.3. These results corroborate previous studies of W191G complementation.[48]

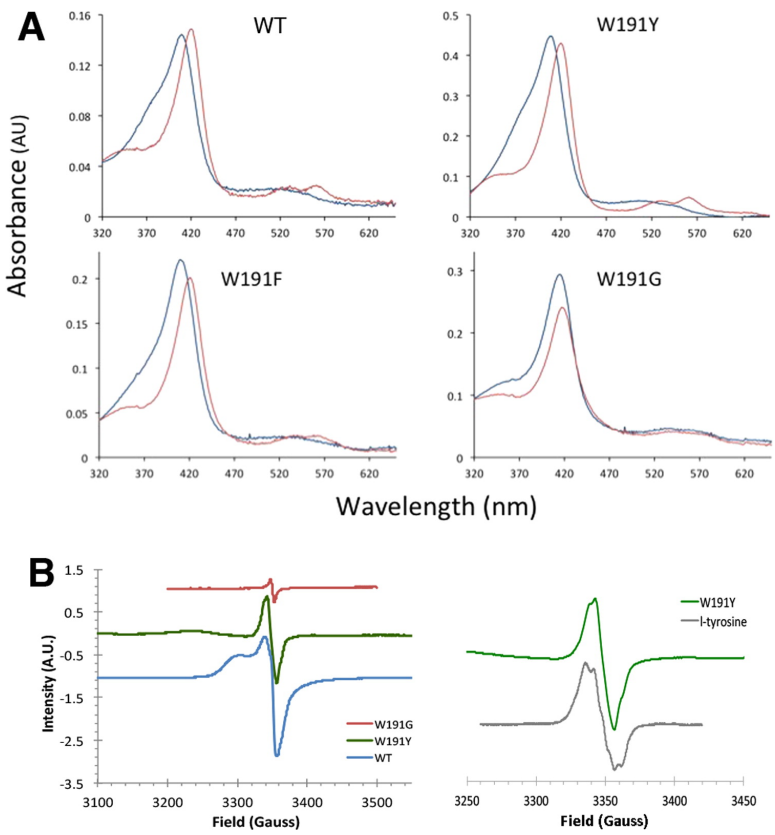

Figure A.5: Compound I formation in CcP by UV/vis. (A) UV/vis spectra of CcP before (blue) and after (red) introduction of hydrogen peroxide. WT, W191F, and W191Y show the typical Soret shift from 409 to 420 nm, and Q-bands indicative of Cpd I formation. W191G shows a shift from 414 to 417 nm, with broad Q-bands that move toward those seen in WT. (B) Peroxide-induced radicals in CcP. (Left) cw EPR spectra of CcP variants with peroxide. Both WT and W191Y radical signals are much larger than those seen in W191G or W191F (not shown). A small amount of organic radical is likely formed elsewhere in W191G. Spectra recorded at X-band (9 GHz) with a 1 G modulation amplitude, a 100 kHz modulation frequency, and a 25−30 dB modulation amplitude. Data were collected at 5, 12, and 50 K for each variant; WT is shown at 5 K, W191Y at 12 K, and W191G at 50 K. Temperature has no appreciable effect on the relative amplitudes of the signals. The origin of the broad feature for W191Y at 3235 G is unknown but gives different saturation behavior and is thus distinct from the main radical signal. (Right) Neutral tyrosyl radicals were generated by UV photolysis and collected at ∼100 K. The sample exhibits similar line shape features as in W191Y.

A.3.4 Species Formed upon Reaction with Peroxide

CcP compound I formation is evidenced in the UV/vis absorbance spectrum of WT and CcP W191Y by a shift in the Soret peak from 409 to 420 nm and the appearance of Q-bands characteristic of the oxo-ferryl species (Figure A.5).[75] W191F also produces a similar Soret peak shift, from 409 to 420 nm, but the Q-bands are less well-defined[50, 68] (Figure A.5A). W191G displays the most unique spectrum with a 414 nm Soret peak for the ferric state. Although previous studies of the W191G reaction with peroxide found pronounced ferryl formation as indicated by a well-defined 414 nm Soret peak and Q-bands at 530 and 560 nm,[48, 50] we find only a modest shift in the W191G Soret band to 417 nm with similarly small changes in the Q-bands (Figure A.5A). The reason for this difference is unknown but could reflect the heme incorporation process during protein expression.

We also tested for the ability of WT, W191Y, and W191F to produce cw EPR spectra characteristic of aromatic residue oxidation (Figure A.5B). As previously reported for W191G in CcP[50] and related peroxidases,[76] we observe a small amount of organic radical forms upon reaction with peroxide [$\sim$ 1/10 of the WT signal (Figure A.5B)], presumably because of the minor oxidation of aromatic residues remote from the active center.[50, 77-79] In contrast, W191Y produces a strong EPR signal characteristic of a neutral Tyr radical[80, 81] with an amplitude similar to that seen with WT (Figure A.5B). Thus, despite its inability to oxidize Cc(II), W191Y forms a Cpd I-like species containing an oxo-ferryl complex and a tyrosine radical. Features of the W191Y radical species correspond well with those of free tyrosyl radicals generated from UV photolysis (Figure A.5B).

A.3.5 Oxidation of Cc(II) by W191Y Cpd I

To further investigate the inactivity of W191Y in the steady-state oxidation of Cc(II), we examined the oxidation of W191Y Cpd I by Cc(II) under pseudo-first-order conditions and compared the results to those for W191F.[66] W191F does not form a radical species at position 191 upon reaction with peroxide and exhibits only very slow turnover under steady-state conditions.[66] Titration of W191Y with hydrogen peroxide indicated that ∼2 equiv of H_2O_2 was necessary to fully form Cpd I, which was then stable for at least 5 min on ice [it is unclear why 2 equiv of H_2O_2 is needed for the initial formation of Cpd I; under multiple turnovers by W191Y, one peroxide oxidizes two Cc(II) molecules (see below)]. Following the same procedure used previously for W191F,[66] 30 μM Cc(II) was mixed with 2 μM CcP and 4 μM H_2O_2 was added to initiate the reaction, which was then monitored at 550 nm [Cc(II)], 540 nm (an isosbestic point for Cc oxidation), and 434 nm [Fe(IV)=O]. During the initial buildup of the Fe(IV)=O species at 434 nm, there was an early phase of Cc(II) oxidation with a k_1 of 0.17 ± 0.03 s^{-1}. Following the maximal absorbance at 434 nm [Fe(IV)=O peak], the oxidation of Cc(II) was monophasic (Figure A.6A), giving a rate constant k_2 of 0.08 ± 0.03 s^{-1}. This behavior and value are similar to those for Cc(II) oxidation by the W191F ferryl species under analogous conditions, which also shows a slow phase of Fe(IV)=O oxidation with a k_2 of 0.14 s^{-1}.[66] Furthermore, the spectral changes at 550 nm indicate that for W191Y ∼1 equiv of Cc(II) (2.5 ± 0.5 μM) is oxidized by W191Y Cpd I on this time scale. An equivalent of Cc(II) was also oxidized during the buildup of Cpd I in the initial phase of the reaction.

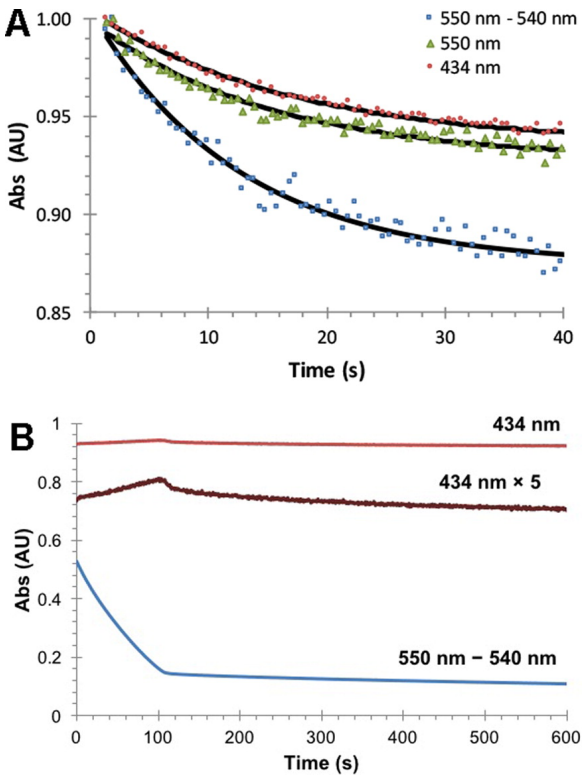

Figure A.6: Oxidation of Cc(II) by W191Y. (A) Single turnover of CcP W191Y Cpd I with excess Cc(II). Reaction was initiated by mixing 4 μM H_2O_2 with 2 μM CcP W191Y and 30 μM Cc(II). After an initial phase in which Fe(IV)=O builds up at 434 nm, CcP oxidizes 1 equiv of Cc(II) with a rate constant k_2 of 0.08 $\pm$ 0.03 s^{-1}. Normalized absorbances are shown for A_{434}, A_{550}, and $A_{550} - A_{540}$. (B) Multiple turnovers of Cc(II) oxidation by CcP W191Y. Reaction was initiated by mixing 10 μM H_2O_2 with 2 μM CcP and 30 μM Cc(II). Absorbance traces are shown at 434 nm [Fe(IV)=O] and $A_{550} - A_{540}$ [Cc(II)]. In the initial phase, 22 $\pm$ 2 μM Cc(II) is consumed where the amount of Fe(IV)=O increases, until the peroxide is depleted, at which point Fe(IV)=O is slowly reduced to Fe(III) by the remaining Cc(II). The rate of the early phase is peroxide-dependent and exceeds that of Fe(IV)=O reduction in a single turnover.

We then examined multiple turnovers of Cc(II) oxidation by reacting W191Y (1 μM) with a 10-fold excess of peroxide (10 μM) and 30 μM Cc(II) (Figure A.6B). The resulting reactions produced 2 equiv of oxidized Cc (22 $\pm$ 1 μM) and proceeded with a turnover number (V/E_0) of 0.29 $\pm$ 0.03 s^{-1},(1) which is greater than the rate constant for the analogous single-turnover condition (0.08 $\pm$ 0.3 s^{-1}). Notably, the amount of the ferryl species (434 nm) increases as Cc(II) decreases and then decays slowly when the peroxide is extinguished, concomitant

with a small amount of Cc(II) oxidation. This behavior is somewhat different from that seen with W191F, where the CcP ferryl species remains constant until peroxide is depleted.[66] For W191F, it was suggested that the ferryl species reacts directly with peroxide to oxidize Cc(II), perhaps through the formation of additional protein-based radicals.

$$\text{Fe(IV)=O CcP} + \text{HOOH} + 2\text{Cc(II)} + 2\text{H}^+ \longrightarrow \text{Fe(IV)=O CcP} + 2\text{Cc(II)} + 2\text{H}_2\text{O} \quad \text{(A.1)}$$

With W191Y, the ferryl appears to increase at 434 nm as the oxidation of Cc(II) slows, suggesting that in the early phase peroxide [and Cc(II)] reacts with an intermediate that precedes the ferryl in the reaction sequence. Furthermore, the multiple-turnover rate (0.29 s^{-1}) is considerably faster than the single-turnover rate (0.08 s^{-1}), and thus with excess peroxide present, the reaction is not rate-limited by oxidation of Cc(II) by Fe(IV)=O. The reaction rate did show a peroxide concentration dependence, but the relationship was complex and not proportional. Although this behavior requires further investigation, it is clear that the W191Y Cc(II) turnover rate is $10^3 - 10^4$ times slower than that of WT CcP[82-84] because of the altered reactivity of the Tyr radical.

Considering that W191Y does form a Tyr radical (Figure A.5B), there are two possibilities for the reactivity of W191Y Cpd I. In the first case, $Y^\bullet$ reacts quickly to oxidize 1 equiv of Cc(II), but the remaining ferryl cannot reoxidize Y191 (as per eq A.3). The second oxidation then involves reaction of the ferryl or some other intermediate with peroxide, which is fast compared to oxidation of Cc(II) by Fe(IV)=O (eq A.1). In the second case, the $Y^\bullet$ potential is too low to oxidize Cc(II) at rates that greatly exceed the rate of oxidation by Fe(IV)=O or reaction of an intermediate state with peroxide. If the $Y^\bullet$ were especially stable, it may be observable during the single-turnover experiment using EPR spectroscopy. However, no $Y^\bullet$ was observed in the presence of Cc(II) during decay of the ferryl species (20−30 s after reaction with peroxide). Thus, the $Y^\bullet$ species has reacted prior to the reduction of Fe(IV)=O. Further investigation of $Y^\bullet$ reactivity remains to be determined by methods with better time resolution.

A.3.6 Photoinduced ET of ZnCcP:Cc W191 Variants

We invoked the ZnCcP:Cc system to evaluate the ability of CcP position 191 to facilitate long-range ET[2, 11-16] (Figure A.1). Zinc-protoporphyin IX (ZnP) provides a reactive, long-lived triplet state (^{3}ZnCcP) when excited with 532−560 nm light. In isolation, ^{3}ZnCcP will decay back to the ground state with a rate constant k_D of ∼100 s^{-1},[14, 16, 32, 57] whereas in complex with oxidized Cc, ^{3}ZnCcP [Fe(III)Cc] is additionally quenched by heme-to-heme ET to Cc Fe(III) with rate constant k_e. The total quenching rate constant ($k_P = k_D + k_e$) is ∼260 s^{-1} for the 1:1 complex with yeast Cc, depending somewhat on ionic strength, temperature, and pH.[12, 14, 15, 17, 20, 57] The resulting charge-separated state containing the ZnP cation radical (ZnP^+) and reduced Fe(II)Cc then recombines in an ET process (k_{eb}) that involves oxidation of W191 to an indole cation radical [$W^{\bullet+}$ (Figure A.1)]. On the time scale of ET with Cc, the radical equilibrates extremely rapidly between ZnP and W191 or may be considered delocalized between the two centers.[3] In the WT system, k_{eb} greatly exceeds k_e, and as a result, the charge-separated intermediate forms in vanishingly small amounts. To characterize the ET reactivity of the ZnCcP:Cc complex, we employed a multichannel analyzer that allowed time resolution of complete difference spectra for the ZnCcP:Cc complex following photoexcitation. Global analysis of the data sets defined reactive states and their kinetic parameters. A typical difference spectrum for ^{3}ZnCcP in the absence of Cc is characterized by a broad, positive peak at 475 nm and two negative Q-bands at 555 and 592 nm[85] (Figure A.7). A strong negative peak at 432 nm also appears, consistent with triplet excited-state spectra of isolated Zn-porphyrins.[86] The 432, 555, and 592 nm features correspond to absorption maxima in the visible spectrum of ZnCcP (Figure A.7), and their diminished intensity reflects changes in the electronic state upon triplet formation.

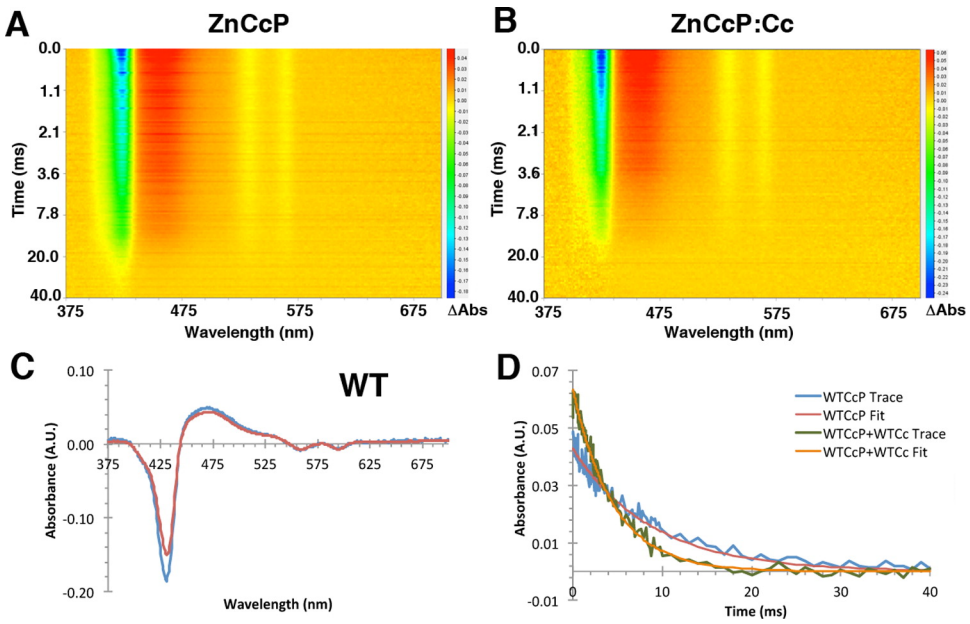

Figure A.7: Time-dependent difference spectra for photoexcited ZnCcP WT with and without Cc. (A) Difference spectra for ^{3}ZnCcP decay shown as a heat map. Red, orange, and yellow colors reflect positive changes in absorption, whereas blue and green colors reflect negative changes. The difference spectrum is strongest at $t = 0$ ms and decays over 40 ms to a flat line. Initial time points are spaced 50 μs apart, and the time interval between successive spectra increases over the course of the measurement. The exposure time for each spectrum is 50 μs. (B) Excited-state decay of WT CcP with Fe(III)Cc added. The ^{3}ZnCcP excitation is much shorter-lived with Cc. (C) Difference spectrum of the excited state of ZnCcP at time zero. Data are colored blue, with the component state extracted from the global fit colored red. (D) Time dependence of absorbance at 475 nm for ZnCcP with and without Cc. The fit for the decay rate of the principal state in panel C is superimposed. Data shown for 100 mM KP$_i$ conditions.

All spectral features of ^{3}ZnCcP alone decay with a rate constant k_D of 114 $\pm$ 4 s^{-1} (Table A.2). To study ET quenching of ^{3}ZnCcP by Fe(III)Cc, we used both 100 mM KP$_i$ ionic strength conditions that favor the 1:1 complex and limit secondary binding of an additional Fe(III)Cc and 10 mM KP$_i$ conditions that stabilize the complex against dissociation but permit some secondary-site binding.[20, 57] Although, both cases potentially bring complications, we find that changes in ionic strength do not greatly alter the kinetic parameters (Table A.2). Under 100 mM KP$_i$ conditions, addition of Fe(III)Cc in 2-fold excess increases the rate constant for triplet-state decay to $k_P = k_D + k_e = 230 \pm 12$ s^{-1} (Table A.2 and

Figure A.7). The increased level of quenching primarily results from ET to Fe(III)Cc[14, 15, 32] ($k_e = k_P - k_D = 116\ s^{-1}$), which is consistent with there being little change in rate constant ($<10\ s^{-1}$) when reduced Fe(II)Cc is added. For WT ZnCcP:Cc, the k_{eb} indeed exceeds k_e, and thus, an intermediate state could not be resolved (for individual acquisition times as low as 1 μs). Consequently, the system was best modeled with a single difference spectrum corresponding to the formation and decay of ^{3}ZnCcP. The kinetic parameters (Table A.2) are in line with those determined from single-wavelength measurements in other studies.[14, 15, 32, 57]

	k_P $(s^{-1})^a$	k_D $(s^{-1})^b$	k_e $(s^{-1})^c$	k_{eb} $(s^{-1})^d$	KP_i buffer
WT	230 ± 10	114 ± 4	116 ± 13	ND[e]	100 mM
W191F	160 ± 7	102 ± 5	60 ± 10	40 ± 5	100 mM
W191F	170 ± 20	108 ± 2	60 ± 20	70 ± 10	10 mM
W191Y	200 ± 10	100 ± 2	100 ± 12	50 ± 20	100 mM
W191Y	180 ± 10	100 ± 2	80 ± 30	50 ± 10	10 mM
W191G	186 ± 10	113 ± 6	70 ± 10	16 ± 5	100 mM

Table A.2: [a] k_P is the ^{3}ZnP decay constant in the presence of Cc(III).
[b] k_D is the ^{3}ZnP decay constant in the absence of Cc(III).
[c] $k_e = k_P - k_D$ (the forward ET rate constant).
[d] k_{eb} is the apparent back recombination ET rate constant. Note that under 100 mM conditions where complex dissociation may compete with back ET, k_{eb} may not be strictly first-order.
[e] Not determined.

In contrast to WT ZnCcP:Cc, W191F shows slower back ET[17, 20] (Table A.2). Here we resolve difference spectra for the charge-separated state [$ZnP^+/W^{\bullet+}$:Cc(II)]. Alone, W191F CcP produces difference spectra identical to those of WT CcP and decays uniformly at the same rate. However, in the presence of Fe(III)Cc, an additional spectral species is detected (Figure A.8). At ∼10 ms, positive features begin to appear at 416, 550, and 625−690 nm. The intensities of these absorption peaks increase while the intensity of the ^{3}ZnP signal diminishes and then subsequently decay back to zero (Figure A.8). Global analysis of the data reveals two distinct evolution-associated difference spectra, or EADS[87] (Figure A.8),

whose time-dependent linear combination effectively models the series of spectra.[87] EADS1 is identical to the triplet-state difference spectrum and fully describes the spectral features at $t = 0$ ms (Figure A.7). EADS2 replaces EADS1 and is visible between 10 and 40 ms (Figure A.8). EADS2 contains components characteristic of Fe(II)Cc (Soret peak at 416 nm and Q-bands at 522 and 550 nm) and a ZnP^+ π-cation radical (625−690 nm) (Figure A.8) and thus represents the charge-separated state. Global analysis predicts that the Fe(II)Cc and ZnP^+ features rise and fall with the same kinetics. Thus, forward ET between ^{3}ZnCcP(W191F) and Fe(III)Cc produces ZnP^+ and Cc(II), which then recombine charge on a slower time scale (Table A.2). To investigate the involvement of an additional intermediate, the data were modeled with three or more rate constants. However, any additional EADS was always degenerate to the first two and produced no new species of unique spectral quality or time evolution. Previous studies of W191F (performed at 10 mM KP_i) found a second slower kinetic phase for loss of ZnP^+:Cc(II) that results from dissociation of the complex.[17, 20] The overall time scale in our experiments (40 ms) is probably too short to characterize such dissociation well, and thus, k_{eb} for intraprotein ET in the associated complex may be slightly underestimated because the system does not account for this contribution. Complex dissociation at an ionic strength of >30 mM is rapid[27] and could influence the apparent k_{eb}, especially considering that the ∼10% yield of ET products in these experiments leaves a majority of competing unreacted proteins.[20, 27] We thus also investigated the reaction at a lower ionic strength (10 mM KP_i) where the W191F complex is known to be stable in the millisecond time range.[20] There was little change in the apparent rate constants between 100 and 10 mM KP_i conditions (Table A.2), with both the 10 and 100 mM apparent k_{eb} values (40−70 s^{-1}) matching well with previously reported values of 40−74 s^{-1}.[17, 20]

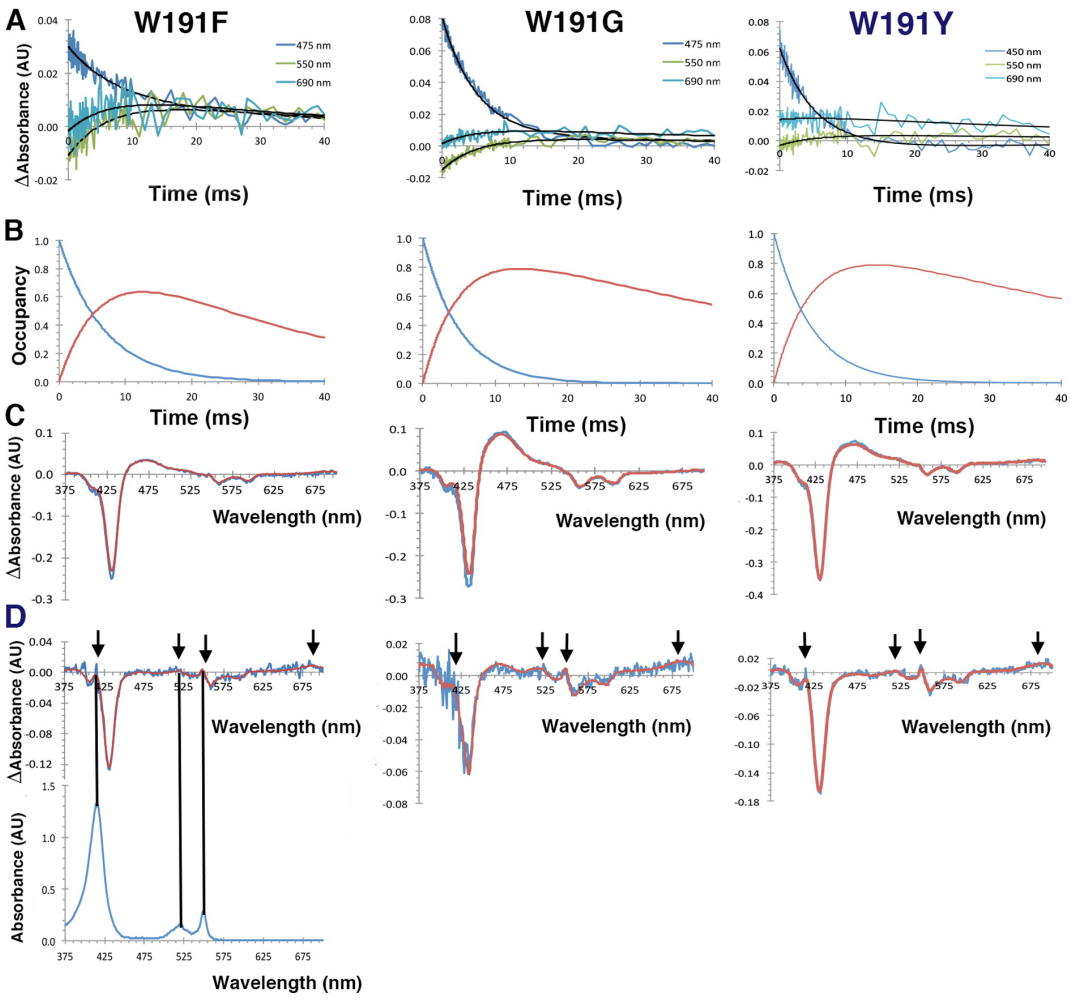

Figure A.8: Detection of a charge-separated state in W191F(G) ZnCcP:Cc. (A) Time plots of the difference spectra at various wavelengths for W191F, W191G, and W191Y; 475 nm reflects ^{3}ZnP, 550 nm Cc(II), and 690 nm ZnP$^+$. (B) Progress curves for the two principal states [^{3}ZnP and ZnP$^+$:Cc(II)] defined by single-value decomposition and global analysis of the data. Traces for ^{3}ZnP are colored blue, and those for the charge-separated state are colored red (C) Difference-state spectra at t = 10 ms superimposed with the fits of the associated EADS1 for ^{3}ZnCcP. Recorded changes in absorbance are colored blue and fits red. (D) Difference-state spectra at t = 18 ms superimposed with the fits of EADS2 for the additional charge-separated intermediate in W191F, -G, and -Y. New peaks at 416 and 550 nm (arrows) correspond to Fe(II)Cc [spectra of Fe(II)Cc below], and the broad peak at ∼680 nm (arrow) is characteristic of ZnP$^+$. Data shown for 100 mM KP$_i$ conditions.

The ET behavior of ZnCcP W191G is similar to that of W191F (Table A.2). ZnP^+:Cc(II) builds up and decays with similar kinetics (Figure A.8); both k_e and k_{eb} are smaller than for WT but comparable to those for W191F. Thus, substitution of an aromatic group for a water-filled cavity at position 191 has an only modest effect on the apparent forward and reverse ET processes; however, weaker binding between CcP and Cc for the W191G cavity mutant may increase dissociation kinetics, which could then contribute to the slightly lower observed k_{eb}.

Tyr at position 191 does not reductively quench ^{3}ZnP because the ^{3}ZnP excited-state decay rate is unaffected in the absence of Cc. Like W191F and W191G, Cc(III) produces a modest increase in the ^{3}ZnP decay rate (Table A.2), indicating quenching by ET to Cc(III). Global analysis of the transient spectra in the presence of Cc(III) reveals two major EADS, similar to that observed with W191F and W191G, with similar absorbance increases in the 625 nm range of EADS2 (Figure A.8). Consequently, there is no rate acceleration for the back ET reaction in W191Y, which reacts like W191F(G) (Table A.2). Like W191F, high-ionic strength (100 mM KP_i) and low-ionic strength (10 mM KP_i) conditions give very similar k_e and k_{eb} values (Table A.2). Unfortunately, we were unable to study how the substituted anilines affect photoinduced ET with ZnCcP W191G because the ligands quenched ^{3}ZnP in a manner independent of binding to the W191G cavity.

A.4 Discussion

Trp191 oxidation is a key feature of the CcP peroxidase mechanism and also of the ZnCcP photoinduced ET reactions. Here we report that Tyr, a similar redox-active residue at site 191, cannot support these activities, nor can a set of redox-active small molecules bound in the W191G cavity. The Tyr is unable to rescue these reactions despite the fact that it forms

a stable radical adjacent to the heme upon reaction with peroxide. The influence exerted by Trp or Tyr oxidation on back ET depends on the structural and electrochemical properties of the donor, acceptor, and hopping center. Indeed, the positioning and reduction potential of a hole-hopping site must fall within certain ranges to enhance long-range ET rates.[37, 45, 88] When Cc(III) oxidizes ^{3}ZnP, the resulting radical is distributed between ZnP^+ and $W^{\bullet+}$, with an equilibrium weighting (K_{ex}) that depends on the difference in reduction potentials (ΔE°).

$$K_{ex} = \frac{k_f^{ex}}{k_r^{ex}} = \frac{[ZnP^0W^{\bullet+}]}{[ZnP^+W^0]} = e^{-F\Delta E^\circ/RT} \tag{A.2}$$

ET to ZnP^+ from Cc(II) could conceivably take place with and without involvement of the 191 site:

$$ZnP^0Cc(III) \xleftarrow{k_{eb}^1} ZnP^0W^{\bullet+} \underset{k_f^{ex}}{\overset{k_r^{ex}}{\leftrightarrows}} ZnP^+W^0Cc(II)$$

$$ZnP^0Cc(III) \xleftarrow{k_{eb}^2} ZnP^+W^0Cc(II)$$

If the electron exchange reaction between ZnP^+ and W is much faster than the back electron transfer reactions (i.e., k_f^{ex}, $k_r^{ex} \gg k_{eb}^1$,k_{eb}^2) and the rate of ET to $W^{\bullet+}$ exceeds that to ZnP^+ ($k_{eb}^1 \gg k_{eb}^2$), the observed back ET rate constant (k_{obs}) will be the rate constant for transfer to $W^{\bullet+}$ weighted by the equilibrium constant for hole exchange between ZnP^+ and $W^{\bullet+}$ (eq A.3).

$$k_{obs} = k_{eb}^1 K_{ex} \tag{A.3}$$

Known parameters justify the assumption of eq A.3. ET from Cc(II) to $W^{\bullet+}$ is much faster ($k_{eb}^1 = 2 \times 10^6$ s^{-1})[8] than direct ET to ZnP^+ [$k_{eb}^2 \sim 10^1 - 10^2$ s^{-1} (Table A.2)].[17] Thus, k_{eb}^2 sets a lower limit for any involvement of W191 to enhance ET from Cc(II). If the equilibrium constant for hole exchange $K_{ex} < 10^{-4}$ [i.e., ΔE° >240 mV (eq A.2)], there will be little advantage to hole hopping through the 191 site. For solution and crystalline complexes of ZnCcP with Cc(III), $k_{obs} \geq 4000$ s^{-1},[12, 18, 89] and thus, eq A.2 implies that 120 mV < ΔE° < 180 mV. This difference in potential is consistent with measurements of the isolated

moieties: $E^{\circ}(\mathrm{ZnP}^{0}/\mathrm{ZnP}^{+}) = 1.2$ V,[15] whereas $E^{\circ}(\mathrm{W}^{0}/\mathrm{W}^{\bullet+}) = 1.1 - 1.4$ V.[45, 81, 90, 91] It is worth noting that the actual reduction potentials of $\mathrm{W191}^{\bullet+}$ and ZnP^{+} in CcP are likely less than these values. $\mathrm{W}^{\bullet+}$ potentials usually exceed 1 V,[45, 81, 90, 91] and most peroxidase Cpd II [Fe(IV)=O] potentials are >0.9 V;(92, 93) however, in WT CcP:Cc, the two-electron couple $E^{\circ}[\mathrm{W}^{\bullet+}\mathrm{Fe(IV)}/\mathrm{W}^{0}\mathrm{Fe(III)}] = 1/2\{E^{\circ}(\mathrm{W}^{\bullet+}/\mathrm{W}^{0}) + E^{\circ}[\mathrm{Fe(IV)}/\mathrm{Fe(III)}]\} = 0.740$ V.[94, 95] Thus, the protein environment may substantially lower the reduction potentials of the 191 side chain and the porphyrin moiety.[96, 97] Importantly, a lowered potential for $\mathrm{W}^{\bullet+}$ is still consistent with a very small population of the charge-separated intermediate in the WT ZnCcP:Cc system. Provided that the reduction potential of the hopping site remains more than ∼200 mV higher than that of the donor Cc(II) [E°(Cc) = 290 mV;[98, 99] i.e., $\Delta G = -200$ mV], the standard Marcus equation[42] $\{k \sim k_{\mathrm{eb}}(\mathrm{W}^{\bullet+})\exp[-(\lambda+\Delta G)^{2}/4\lambda kT]\}$ predicts that the back ET rate to a 191 radical will remain ∼100 times higher than the forward rate of Cc(III) reduction [$\sim 10^{2}$ s^{-1} (Table A.2)]. [This estimate is based on a reorganization energy (λ) of ∼0.7 V for ZnCcP:Cc back ET[3] and a $k_{\mathrm{eb}}(\mathrm{W}^{\bullet+})$ of 2×10^{6} s^{-1} for ET to $\mathrm{W191}^{\bullet+}$ that is close to activationless.[8]]

With the crystal structure of the W191Y complex ruling out any substantial structural perturbations caused by the substitution, the inability of Tyr191 to accelerate back ET like Trp may derive from one of the two considerations mentioned previously. First, although $E^{\circ}(\mathrm{Y}^{\bullet+}/\mathrm{Y}^{0})$ will likely be comparable to $E^{\circ}(\mathrm{W}^{\bullet+}/\mathrm{W}^{0})$,[43, 90, 91, 100-102] even a redox potential increase of 50-100 mV over that of Trp would decrease k_{eb}^{1} to the range of k_{eb}^{2}. Unlike Trp191, which hydrogen bonds to Asp235, there is no hydrogen bond acceptor for the Tyr hydroxyl, and thus, the Tyr redox potential may not be suitably reduced by the protein environment. In this case, during reaction of Fe(III) CcP with peroxide, Cpd I may react rapidly at $\mathrm{Y}^{\bullet}$ or $\mathrm{Y}^{\bullet+}$ to oxidize 1 equiv of Cc(II), but then the remaining ferryl species has insufficient potential to regenerate the Tyr radical. Oxidation of Cc(II) by the ferryl or another intermediate species would be slow relative to the reaction of this intermediate

with peroxide itself. In the case of ZnCcP, the potential of $ZnP^{\bullet+}$ would also be too low to produce any appreciable amount of $Y^{\bullet}$. In the second case, the potential of neutral $Y^{\bullet}$ could be too low to oxidize Cc(II) at appreciable rates. The low pK_a of $Y^{\bullet+}$ (~ -2)[43, 101] favors deprotonation to the neutral radical $Y^{\bullet}$. The $W^{\bullet+}$ pK_a is considerably higher than this at 3.2−4.5,[103] and furthermore, the CcP heme pocket is known to stabilize the $W^{\bullet+}$ cation[104] by favorable electrostatics[96, 105] and hydrogen bonding with the Asp235 carboxylate nitrogen.[96, 106] In support of this scenario, during several turnovers, the ferryl species does not build up until peroxide and Cc(II) are depleted (Figure A.6B), which suggests that direct reaction of peroxide with the ferryl is not rate-limiting (eq A.1). However, the situation is complex and involves reaction of peroxide with something other than the ferric enzyme because the multiple-turnover rate constant is faster than the single-turnover rate constant. At this stage, we view the first scenario as more likely because reduction of $Y^{\bullet}$ in single-turnover experiments precedes that of the ferryl, and $Y^{\bullet}$ is not stable in the presence of Cc(II), albeit on relatively long time scales. Experiments with faster time resolution will help resolve this issue. The inability of the W191F and W191Y ferryl species to oxidize Cc(II) at rates comparable to that of WT CcP I supports the assertion that for WT ET proceeds primarily to the $W191^{\bullet+}$ center after it has been re-formed by reduction of Fe(IV)=O (Scheme A.1).

The aniline derivatives do not rescue the peroxidase activity of the W191G CcP variant, even though they bind in the cavity and have potentials that should be in range of those of Trp. Furthermore, the pK_as of the resulting aniline cation radicals are likely higher than those of Trp and Tyr (by 2−3 pK_a units[71, 103]); hence, deprotonation of the radical cations does not explain their inactivity. The inability of the ligands to hydrogen bond with the Asp235 carboxylate may prevent the protein from sufficiently lowering their reduction potentials. That said, the bound ligands have a potential range of ∼0.3 V (Figure A.3), and thus, at least some of them should be susceptible to oxidation by ZnP^{+}. Thus, the

more likely explanation for their inactivity stems from disorder and/or weak binding in the pocket. In particular, reorientation of the ligands in the W191G cavity, as evidenced by their heterogeneous binding configurations in the crystals, may limit interactions conducive to oxidation or destabilize any resulting radicals by promoting side reactions. Moreover, the lack of covalent attachment to the protein may short circuit hopping as the ligands exchange to solvent on the overall ET time scales. Similar results were found with the CcP Asp235Asn substitution, which destabilizes the conformation of W191 and produces Cc turnover rates similar to those of W191F.[107-109]

The near equivalence of the WT, W191Y, and W191F structures in complex with Cc lends strong support to the involvement of Trp oxidation in the charge recombination reaction. Interestingly, complete loss of the side chain in W191G produces kinetics similar to that of W191F. Even if complex dissociation is enhanced in W191G (at 100 mM KP_i), the apparent k_{eb} values are not much less than those for W191F under conditions where the complex is stable (10 mM KP_i). Thus, when hopping is inoperative, the ET rates are largely insensitive to large changes in the structure intervening between the donor and acceptor sites. Calculations suggest that although many different bonding networks contribute to electron tunneling between the porphyrin centers, those that involve Trp oxidation are the most effective at accelerating long-rang ET.[3, 19] The W191F to W191G comparison supports the view that such effects are indeed large compared to those resulting from even quite substantial structural perturbations.

We conclude that a functional ET hopping site must not only meet requirements of potential and proton transfer but also maintain a degree structural stability that can be best accomplished by covalent attachment or tight binding to the protein. Moreover, there is a narrow redox potential range over which hopping will be effective at accelerating ET rates, and thus, stringent conditions must be met for multistep ET pathways to accelerate

net charge transfer in proteins.

A.5 Materials and Methods

A.5.1 Mutagenesis

Cytochrome *c* peroxidase (CcP) was subcloned into the ppSUMO vector,[53] a pET28 derivative vector that introduces a His-tagged version of the SUMO protein into the N-terminus of CcP (obtained from H. Sondermann, Department of Molecular Medicine, Cornell University). After a silent mutation (QuikChange, Agilent Technologies) was introduced to remove a natural BamHI site in CcP, the CcP gene was amplified via polymerase chain reaction and inserted between the BamHI and XhoI restriction sites of ppSUMO. Two N-terminal Met-Ile residues were added to generate the "MI" version of CcP.[24] Point mutations were introduced via QuikChange (Agilent Technologies).

A.5.2 Protein Purification

Cytochrome *c* was expressed and purified as described previously.[54] *Escherichia coli* BL21(DE3) cells were transformed with the Cc gene in a PBTR-1 vector and expressed overnight at 37 °C in lysogeny broth (LB) with 125 μg/mL ampicillin and 50 μg/mL Δ-aminolevulenic acid to increase heme production. The PBTR1 vector[54] contains the trc promoter, which is constitutively active and does not require induction. Cells were harvested by centrifugation at 8000 rpm, and pellets were resuspended in 50 mM sodium phosphate (pH 8.0). The resuspended pellets were either frozen for storage or lysed by sonication. The lysate was spun at 22000 rpm for 1 h to remove insoluble cell detritus, and the supernatant was

loaded directly onto a HiPrep CMFF cation exchange column (GE Healthcare Life Sciences) using an ÄKTA FPLC system (Amersham Pharmacia). The column was equilibrated and washed with 50 mM sodium phosphate (pH 8), and Cc was eluted by a 5 column volume gradient of a high-salt buffer [50 mM sodium phosphate (pH 8) and 500 mM NaCl]. All red-colored fractions were collected and concentrated using Millipore Amicon Ultra centrifugal concentrators (10 kDa cutoff) and then loaded onto a Superdex 75 size-exclusion column [50 mM sodium phosphate (pH 8) and 500 mM NaCl]. Red-colored fractions were concentrated, flash-frozen, and stored at −80 °C.

Cytochrome *c* peroxidase was expressed in BL21(DE3) cells and grown at 37 °C in LB with 50 μg/mL kanamycin. When the OD_{600} reached $0.8 - 1.2$, cells were induced with 100 μM isopropyl β-d-1-thiogalactopyranoside and overexpressed at 24 °C for ∼20 h. Cells were harvested by centrifugation at 8000 rpm, and the pellets were resuspended in lysis buffer [50 mM HEPES (pH 7.0), 150 mM NaCl, and 5 mM imidazole]. Cells were lysed by sonication. Insoluble cell detritus was separated out by centrifugation at 22000 rpm for 1 h. CcP was purified with a Ni-NTA column (Qiagen). To cleave the SUMO tag, the ULP-1 protease was added to the elution and incubated at 4 °C overnight. The eluent was then dialyzed into 100 mM potassium phosphate (KP_i, pH 6) buffer and passed over the Ni-NTA resin to separate the cleaved tag from the protein. CcP was loaded onto a HiPrep Q anion exchange column (GE Healthcare Life Sciences) using an ÄKTA FPLC system. A 10-column-volume gradient of 100 mM KP_i against 500 mM KP_i (pH 6.0) was used to separate the heme-containing CcP (FeCcP) from the apo-CcP. The apo-CcP was collected for zinc-protoporphyrin IX (ZnP) incorporation. FeCcP was concentrated and stored at −80 °C for enzymatic assays. To improve the yield of heme incorporation, SUMO-cleaved CcP in 100 mM KP_i (pH 6) was gently stirred with 1 molar equivalent of hemin (stock dissolved in 0.1 M NaOH) at 4 °C overnight. The reaction mixture was neutralized with 1 molar equivalent of 0.1 M acetic acid afterward and centrifuged to remove the precipitate. The solution was run through

an equilibrated Superdex 75 SEC column followed by anion exchange chromatography to separate the iron-containing protein from the apoprotein.[55]

For ZnP incorporation, the apo-CcP concentration was determined using the absorbance at 280 nm and a molar absorptivity coefficient ϵ_{280} of 53 mM^{-1} cm^{-1}.[56] A 5-fold excess of ZnP and carbonyl-diimidazole (1:1 molar ratio) was mixed with apo-CcP in THF or DMF for 2 h. The solvent was removed by rotovap and the activated ZnP resuspended in 500 μL of DMF. The ZnP solution was added to the apo-CcP and allowed to stir in the dark for 5 days at 4 °C. The solution was then centrifuged to remove protein and unbound ZnP that had precipitated. The sample was loaded onto the Superdex 75 size-exclusion column in 100 mM KP_i (pH 6.0) to increase purity and to remove nonspecifically bound ZnP. The colored fractions were concentrated and loaded onto the HiPrep Q column to separate the apoprotein from the ZnP-incorporated protein (ZnCcP) using the protocol described previously to separate the apo-CcP from FeCcP. ZnP incorporation was evaluated by comparing the UV−vis absorbance of the protein peak at 280 nm and the ZnCcP Soret peak at 432 nm (ϵ_{432} = 196 mM^{-1} cm^{-1}).[13, 57] Fractions with an A_{432}/A_{280} ratio of >2 were concentrated, flash-frozen, and stored at -80 °C for crystallization and spectroscopy. Yields of ZnCcP were 80−90% of the initial apoprotein.

A.5.3 Crystallography

Prior to crystallization, Fe(III)CcP and Cc were combined in a 1:1 molar ratio at a final concentration of 1 mM each. The protein mixture was buffer exchanged into H_2O to reduce the ionic strength and thereby increase the level of CcP/Cc binding. Initial crystal hits were obtained using the Phoenix robot (Art Robbins Instruments). Larger crystals were grown by vapor diffusion in either sitting or hanging drop trays against a reservoir containing 15−25% polyethylene glycol 3350, 175 mM NaCl, 5 mM n-octyl β-d-glucoside, and 100 mM sodium

acetate (pH 4.6−5.6). In some cases, streak seeding was used to increase size and crystal quality.

A.5.4 Structure Determination

Diffraction data were collected at the Cornell High Energy Synchrotron Source (CHESS) at beamlines A1 and F2 on an ADSC Quantum 210 CCD camera. A mixture of 4 parts reservoir and 1 part ethylene glycol was used as a cryoprotectant for crystals. In soaking experiments with CcP W191G crystals, the protocol described by Goodin et al.[58] was followed. Briefly, potential small-molecule ligands were dissolved in 50% ethanol to make a 100 mM stock solution, with the exception of indole, which was dissolved in 100% ethanol. The crystals were soaked in a drop of well solution with a final ligand concentration of 30 mM for 30 s prior to soaking with cryoprotectant. Longer ligand soaks proved to be detrimental to diffraction. All data were indexed and scaled with HKL2000.[59] All structures were phased using molecular replacement in PHENIX.[60] Structures of CcP W191G were refined using CNS,[61] and all other structures were refined with the PHENIX suite.[60] Building and adjustments were made with COOT.[62] Translation/libration/screw (TLS) parameters were applied in PHENIX to model Cc anisotropic disorder in the lattice.

A.5.5 Saturation Kinetics

The steady-state assay for CcP peroxidase activity was performed as previously described.[63] Stock solutions of Cc were reduced on ice in the glovebox by incubation with 10 mM DTT for 1 h. DTT was then removed by buffer exchange into 100 mM KP_i (pH 6.0), either by PD-10 desalting columns or 10 rounds of concentration and dilution using Millipore Amicon Ultra centrifugal filters (10 kDa cutoff). Samples containing 2 nM peroxidase,

100 mM KP_i (pH 6.0), and 0−75 μM Cc were then prepared anaerobically in a volume of 1800 μL in gastight cuvettes (StarnaCell). Samples were placed in a Hewlett-Packard 8909A Peltier sample cooler kept at 24 °C and stirred at 500 rpm. Spectra were recorded with an Agilent 8453 spectrophotometer. Samples were blanked prior to data acquisition to monitor the change in absorbance over time. The reaction was initiated by addition of hydrogen peroxide to a final concentration of 170 μM. Oxidation of Cc was monitored at 550 and 540 nm, and a constant baseline was set by normalizing to the absorbance at 750 nm. The kinetics were monitored for 60 s, with data collected every 0.5 s. The initial range of data in which the reaction progress is linear was chosen to represent the steady-state progress of the reaction, where the Cc concentration greatly exceeded the enzyme concentration. A linear fit was applied to this range, and the slope was taken as the reaction velocity (v_0) for that concentration. For every concentration of Cc, three samples were measured.

For measuring the effect of potential ligands on CcP activity, stock solutions of the ligands were prepared in 50% ethanol, or 100% ethanol in the case of indole. Samples were prepared as described above, with a Cc concentration of 30 μM, a ligand concentration of 2 mM, and a final ethanol concentration of <10 mM. To determine Michaelis−Menten constants $V_{\max}$ and K_{M}, the average v_0 was plotted versus concentration and fit to the equation $v = (V_{\max}[\mathrm{Cc}])/(K_{\mathrm{M}} + [\mathrm{Cc}])$ in Mathematica.[64] Steady-state parameters of W191G with ligands were compared to those of W191F with ligands to identify effects not attributable to cavity binding.

A.5.6 Cpd I Spectroscopic Characterization

For UV/vis spectroscopy, 30 μM CcP was prepared in 100 mM KP_i (pH 6.0), and hydrogen peroxide was added to a final concentration of 1 mM. Stock solutions were diluted in 100 mM KP_i (pH 6.0) to 1−4 μM for recording optical spectra on an Agilent 8453 spectropho-

tometer. For continuous wave EPR spectroscopy, CcP was prepared at a concentration of ∼0.5 mM to obtain stronger signals. Prior to data collection, samples were diluted into a buffer of 100 mM KP_i (pH 6.0), 2 mM hydrogen peroxide, and 30% glycerol. Samples were loaded into EPR tubes, flash-frozen minutes after addition of hydrogen peroxide, and measured with a Bruker EleXSys II spectrometer at 9 GHz with a 1.5 G modulation amplitude, a 100 kHz modulation frequency, and a 25−30 dB microwave attenuation.

The L-tyrosine EPR standard was prepared as described previously.[65] L-Tyrosine was dissolved in a sodium borate buffer (pH 10), degassed via three freeze−thaw cycles, and flame-sealed in a quartz EPR tube. While frozen in liquid nitrogen in a finger dewar, the sample was irradiated with a 600 W mercury lamp for 3−4 min to generate the free tyrosyl radical.

A.5.7 CcP Turnover Experiments

Following the method used for W191F,[66] Cc(II) was reduced with dithionite and buffer exchanged into 100 mM KP_i (pH 6). While the sample was being continuously stirred at 25 °C, 4 μM H_2O_2 was added to 2 μM CcP and 30 μM reduced Cc in 100 mM KP_i (pH 6), bringing the total volume to 1800 μL. Spectral changes were monitored at 550, 540, and 434 nm over 15 min with a single baseline set at 800 nm. The change in Cc(II) concentration was determined spectrally by monitoring $A_{550} - A_{540}$ and applying an extinction coefficient of 19.2 mM^{-1} cm^{-1}. Traces were fitted to a monoexponential equation using MATLAB (The MathWorks, Inc., Natick, MA)

The offset t_0 for the early phase was determined by an immediate drop in $A_{550} - A_{540}$ after addition of peroxide. For the slow phase, the offset was established at the maximum of A_{434}. Traces were truncated from the onset of the early phase to the onset of the slow

phase to obtain k_{obs} for the early phase. The k_{obs} for the latter phase was determined from data truncated from the onset of the slow phase to 40 s later. To determine the minimal amount of peroxide required for CcP ferryl generation, 8 μM CcP in 100 mM KP_i (pH 6) was titrated with 8−24 μM H_2O_2 and the reaction monitored at 434 nm. Once formed, the CcP ferryl was stable for at least 2 h on ice. The H_2O_2 concentration was determined by titration with permanganate. Stock peroxide was diluted 10-fold, and 1 mL was combined with approximately 30 mL of water and 10 mL of 3 M sulfuric acid. While the sample was being stirred, a 0.025 M solution of $KMnO_4$ was added by buret until the midpoint was observed. The concentration of H_2O_2 was calculated from the volume dispensed. For multiple-turnover experiments, Cc(II) was reduced with dithionite and buffer exchanged into 100 mM KP_i (pH 6). While the sample was being continuously stirred at 25 °C, $5 - 10$ μM H_2O_2 was added to 1 μM CcP and 30 μM reduced Cc in 100 mM KP_i (pH 6), bringing the total volume to 1800 μL. Initial rate values were determined by fitting the data to a monoexponential decay and then taking the first derivative at time zero. For examination by cw EPR, reduced Cc and CcP W191Y were combined in a 15:1 ratio, with the final concentration of CcP being ∼0.2 mM in a buffer of 100 mM KP_i (pH 6) and 25% glycerol. H_2O_2 was added to a final concentration of ∼0.4 mM, and the solution was rapidly mixed by stirring or vortexing. At 30 and 60 s, ∼70 μL of sample was transferred to an X-band EPR tube and flash-frozen in liquid nitrogen. Data were collected as described above.

A.5.8 Transient Absorption Spectroscopy

All preparations of spectroscopic samples were conducted under anaerobic conditions to avoid quenching of ^{3}ZnCcP by oxygen. ZnCcP was diluted into 10 or 100 mM KP_i (pH 7.0) to a concentration of 100−200 μM and combined with Fe(III)Cc in a 1:2 molar ratio. Drops (4 μL) were placed on siliconized glass coverslips (Hampton) and glued to glass

slides using a ring of epoxy to form a gastight seal, with an average path length of ∼0.5 mm. Samples were placed in the path of a probe light, provided by a 75 W Xe-arc lamp. Excitation light was provided either by an Opotek Opolette Nd:YAG laser tuned to 560 nm with approximately 2 mJ of power per 8 ns pulse or by a Continuum Surelight Nd:YAG laser providing light at 532 nm at approximately 5 mJ of power per 4 ns pulse. The fluorescent efficiency at various excitation wavelengths was measured by tracking the light emitted at 600 nm. Samples were preferentially excited in the Q-bands at 560 nm, although there was also sufficient cross section at 532 nm for sample excitation. The two excitation energies produced identical kinetics, with both lasers firing at 20 Hz. Exposure to excitation light was controlled by a Hamamatsu A6538 Optical Laser shutter, and the absorbance of the probe light was measured with a Hamamatsu Photonic Multichannel Analyzer (PMA). Unless otherwise specified, spectra recorded by the PMA were acquired from a $1-50$ μs exposure time and averaged $20-200$ times, depending on the strength of the signal. The laser Q-switch firing acted as the master trigger, with a Digital Delay Generator DG355 (Stanford Research Systems) controlling timing between the other elements. Detection of scattered laser light set t_0 (time = 0 s). Subsequent time points were then sampled randomly with an entire UV/vis spectrum collected for each exposure. The time delay points were acquired in a random order to mitigate the effects of any photobleaching during data collection. To record a given time point, N reference spectra were recorded at the specified delay time (relative to t_0), where N is the number of spectra being averaged. Next, the laser shutter opened, and N excited spectra were recorded at the same delay. Difference spectra were calculated as $\Delta A = \log(\text{excited/reference})$, accumulated, and averaged over N.

To process the data, data vectors across the wavelength range were reordered in time and subjected to global analysis by Glotaran.[67] Data below 375 nm were discarded because little light at those wavelengths was transmitted through the optics to the PMA, and data above 750 nm were discarded because of a lack of spectral features. A baseline correction at the

triplet-state isosbestic point of 546 nm was applied.[17] Single-value decomposition (SVD) of the multiwavelength data was conducted to reconstruct the minimal number of spectroscopic (difference) states sufficient to describe the kinetic progress. In general, sequential reaction kinetics were assumed, and as such, single- or double-exponential terms were used to connect the spectroscopic states in time.

A.5.9 Accession Codes

Deposited in the Protein Data Bank as entries 5CIF (W191F), 5CIH (W191Y), 5CIG (W1919G), 5CIE (W191G with aniline), 5CID (W191G with toluidine), 5CIB (W191G with 24dma), and 5CIC (W191G with 3abt).

A.6 Acknowledgements

We thank the Cornell High Energy Synchrotron Source (CHESS) and the National Biomedical Center for ESR Technologies for access to data collection facilities and Nancy Li for help with protein purification. We also thank the anonymous reviewers for very useful comments in the revision of the manuscript.

BIBLIOGRAPHY

[1] Erman, J. E., and Vitello, L. B. (**1998**) Cytochrome *c* peroxidase: A model heme protein, *J. Biochem. Mol. Biol.* 31, 307-327.

[2] Nocek, J. M., Zhou, J. S., DeForest, S., Priyadarshy, S., Beratan, D. N., Onuchic, J. N., and Hoffman, B. M. (**1996**) Theory and practice of electron transfer within protein-protein complexes: Application to the multidomain binding of cytochrome *c* by cytochrome *c* peroxidase, *Chem. Rev.* 96, 2459-2489.

[3] Jiang, N., Kuznetsov, A., Nocek, J. M., Hoffman, B. M., Crane, B. R., Hu, X. Q., and Beratan, D. N. (**2013**) Distance-independent charge recombination kinetics in cytochrome *c* - cytochrome *c* peroxidase complexes: Compensating changes in the electronic coupling and reorganization energies, *J. Phys. Chem. B* 117, 9129-9141.

[4] Millett, F., and Durham, B. (**2002**) Design of photoactive ruthenium complexes to study interprotein electron transfer, *Biochemistry* 41, 11315-11324.

[5] Nocek, J. M., Leesch, V. W., Zhou, J., Jiang, M., and Hoffman, B. M. (**2000**) Multidomain binding of cytochrome *c* peroxidase by cytochrome *c* : Thermodynamic vs. microscopic binding constants, *Israel J. Chem.* 40, 35-46.

[6] Millett, F., Miller, M. A., Geren, L., and Durham, B. (**1995**) Electron transfer between cytochrome *c* and cytochrome *c* peroxidase, *J. Bioenerg. Biomem.* 27, 341-351.

[7] Liu, R. Q., Hahm, S., Miller, M., Durham, B., and Millett, F. (**1995**) Photooxidation of Trp191 in cytochrome *c* peroxidase by ruthenium cytochrome *c* derivatives, *Biochemistry* 34, 973-983.

[8] Wang, K. F., Mei, H. K., Geren, L., Miller, M. A., Saunders, A., Wang, X. M., Waldner, J. L., Pielak, G. J., Durham, B., and Millett, F. (**1996**) Design of a ruthenium-cytochrome *c* derivative to measure electron transfer to the radical cation and oxyferryl heme in cytochrome *c* peroxidase, *Biochemistry* 35, 15107-15119.

[9] Mei, H. K., Wang, K. F., Peffer, N., Weatherly, G., Cohen, D. S., Miller, M., Pielak, G., Durham, B., and Millett, F. (**1999**) Role of configurational gating in intracomplex electron transfer from cytochrome *c* to the radical cation in cytochrome *c* peroxidase, *Biochemistry* 38, 6846-6854.

[10] Miller, M. A., Geren, L., Han, G. W., Saunders, A., Beasley, J., Pielak, G. J., Durham, B., Millett, F., and Kraut, J. (**1996**) Identifying the physiological electron transfer site of cytochrome *c* peroxidase by structure-based engineering, *Biochemistry* 35, 5948-5948.

[11] Zhou, J. S., Tran, S. T., McLendon, G., and Hoffman, B. M. (**1997**) Photoinduced electron transfer between cytochrome *c* peroxidase (D37K) and Zn-substituted cytochrome *c* : Probing the two-domain binding and reactivity of the peroxidase, *J. Am. Chem. Soc.* 119, 269-277.

[12] Wallin, S. A., Stemp, E. D. A., Everest, A. M., Nocek, J. M., Netzel, T. L., and Hoffman, B. M. (**1991**) Multiphasic intracomplex electron-transfer from cytochrome *c* to Zn cytochrome *c* peroxidase - Conformational control of reactivity, *J. Am. Chem. Soc.* 113, 1842-1844.

[13] Nocek, J. M., Stemp, E. D. A., Finnegan, M. G., Koshy, T. I., Johnson, M. K., Margoliash, E., Mauk, A. G., Smith, M., and Hoffman, B. M. (**1991**) Low-temperature, cooperative conformational transition within Zn-cytochrome *c* peroxidase, cytochrome *c* complexes - Variation with cytochrome, *J. Am. Chem. Soc.* 113, 6822-6831.

[14] Liang, N., Kang, C. H., Ho, P. S., Margoliash, E., and Hoffman, B. M. (**1986**) Long-range electron-transfer from iron(II)-cytochrome *c* to (zinc-cytochrome-c peroxidase)(+) within the 101 Complex, *J. Am. Chem. Soc.* 108, 4665-4666.

[15] Ho, P. S., Sutoris, C., Liang, N., Margoliash, E., and Hoffman, B. M. (**1985**) Species specificity of long-range electron-transfer within the complex between zinc-substituted cytochrome *c* peroxidase and cytochrome *c* , *J. Am. Chem. Soc.* 107, 1070-1071.

[16] Ho, P. S., Hoffman, B. M., Solomon, N., Kang, C. H., and Margoliash, E. (**1984**) Kinetics and energetics of intramolecular electron-transfer in yeast cytochrome *c* peroxidase, *Biochemistry* 23, 4122-4128.

[17] Seifert, J. L., Pfister, T.D., Nocek, J.M., Lu, Y., Hoffman, B.M. (**2005**) Hopping in the electron-transfer photocycle of the 1:1 complex of Zn-cytochrome *c* peroxidase with cytochrome *c* , *J. Am. Chem. Soc.*

[18] Kang, S. A. C., B.R. (**2005**) Effects of interface mutations on association modes and electron-transfer rates between proteins, *Proc. Natl. Acad. Sci. USA* 102, 15465-15470.

[19] Wallrapp, F. H., Voityuk, A. A., and Guallar, V. (**2013**) In-silico assessment of protein-protein electron transfer. A case study: cytochrome *c* peroxidase - cytochrome *c* , *PLoS Comput. Biol.* 9.

[20] Page, T. R., and Hoffman, B. M. (**2015**) Control of cyclic photoinitiated electron transfer between cytochrome *c* peroxidase (W191F) and cytochrome *c* by formation of dynamic binary and ternary complexes, *Biochemistry* 54, 1188-1197.

[21] Bashir, Q., Volkov, A. N., Ullmann, G. M., and Ubbink, M. (**2010**) Visualization of the encounter ensemble of the transient electron transfer complex of cytochrome *c* and cytochrome *c* peroxidase, *J Am Chem Soc* 132, 241-247.

[22] Volkov, A. N., and van Nuland, N. A. J. (**2013**) Solution NMR study of the yeast cytochrome *c* peroxidase: cytochrome *c* interaction, *J. Biomol. NMR* 56, 255-263.

[23] Volkov, A. N., Worrall, J. A., Holtzmann, E., and Ubbink, M. (**2006**) Solution structure and dynamics of the complex between cytochrome *c* and cytochrome *c* peroxidase determined by paramagnetic NMR, *Proc Natl Acad Sci* 103, 18945-18950.

[24] Pelletier, H., and Kraut, J. (**1992**) Crystal structure of a complex between electron-transfer partners, cytochrome *c* peroxidase and cytochrome-c, *Science* 258, 1748-1755.

[25] Guo, M. L., Bhaskar, B., Li, H. Y., Barrows, T. P., and Poulos, T. L. (**2004**) Crystal

structure and characterization of a cytochrome *c* peroxidase-cytochrome *c* site-specific cross-link, *Proc Natl Acad Sci USA* 101, 5940-5945.

[26] Liang, N., Mauk, A. G., Pielak, G. J., Johnson, J. A., Smith, M., and Hoffman, B. M. (**1988**) Regulation of interprotein electron-transfer by residue 82 of yeast cytochrome-c, *Science* 240, 311-313.

[27] Mei, H. K., Wang, K. F., McKee, S., Wang, X. M., Waldner, J. L., Pielak, G. J., Durham, B., and Millett, F. (**1996**) Control of formation and dissociation of the high-affinity complex between cytochrome *c* and cytochrome *c* peroxidase by ionic strength and the low-affinity binding site, *Biochemistry* 35, 15800-15806.

[28] Nocek, J. M., Hatch, S. L., Seifert, J. L., Hunter, G. W., Thomas, D. D., and Hoffman, B. M. (**2002**) Interprotein electron transfer in a confined space: Uncoupling protein dynamics from electron transfer by sol-gel encapsulation, *J. Am. Chem. Soc.* 124, 9404-9411.

[29] Nocek, J. M., Liang, N., Wallin, S. A., Mauk, A. G., and Hoffman, B. M. (**1990**) Low-temperature conformational transition within the Zn-cytochrome *c* peroxidase, cytochrome-c electron-transfer complex, *J. Am. Chem. Soc.* 112, 1623-1625.

[30] Van de Water, K., Sterckx, Y. G. J., and Volkov, A. N. (**2015**) The low-affinity complex of cytochrome *c* and its peroxidase, *Nat Comm* 6.

[31] Kang, S. A., Hoke, K. R., and Crane, B. R. (**2006**) Solvent isotope effects on interfacial protein electron transfer in crystals and electrode films, *J Am Chem Soc* 128, 2346-2355.

[32] Kang, S. A., Marjavaara, P.J., Crane, B.R. (**2004**) Electron transfer between cytochrome *c* and cytochrome *c* peroxidase in single crystals, *J. Am. Chem. Soc.* 126, 10836-10837.

[33] Liang, Z. X., Nocek, J. M., Huang, K., Hayes, R. T., Kurnikov, I. V., Beratan, D. N., and

Hoffman, B. M. (**2002**) Dynamic docking and electron transfer between Zn-myoglobin and cytochrome b(5), *J. Am. Chem. Soc.* 124, 6849-6859.

[34] Seifert, J. L., Nocek, J. M., Hatch, S. L., and Hoffman, B. M. (**2001**) Study of electron transfer between cytochrome *c* and cytochrome *c* peroxidase by sol-gel encapsulation, *J. Inorg. Biochem.* 86, 425-425.

[35] Cordes, M., and Giese, B. (**2009**) Electron transfer in peptides and proteins, *Chem Soc Rev* 38, 892-901.

[36] Cordes, M., Kottgen, A., Jasper, C., Jacques, O., Boudebous, H., and Giese, B. (**2008**) Influence of amino acid side chains on long-distance electron transfer in peptides: electron hopping via "stepping stones", *Angew Chem* 47, 3461-3463.

[37] Warren, J. J., Ener, M. E., Vlcek, A., Winkler, J. R., and Gray, H. B. (**2012**) Electron hopping through proteins, *Coord. Chem. Rev.* 256, 2478-2487.

[38] Warren, J. J., Winkler, J. R., and Gray, H. B. (**2013**) Hopping maps for photosynthetic reaction centers, *Coord. Chem. Rev.* 257, 165-170.

[39] Lukacs, A., Eker, A. P., Byrdin, M., Brettel, K., and Vos, M. H. (**2008**) Electron hopping through the 15 A triple tryptophan molecular wire in DNA photolyase occurs within 30 ps, *J Am Chem Soc* 130, 14394-14395.

[40] Reece, S. Y., Seyedsayamdost, M. R., Stubbe, J., and Nocera, D. G. (**2007**) Direct observation of a transient tyrosine radical competent for initiating turnover in a photochemical ribonucleotide reductase, *J Am Chem Soc* 129, 13828-13830.

[41] Winkler, J. R., and Gray, H. B. (**2014**) Long-range electron tunneling, *J Am Chem Soc* 136, 2930-2939.

[42] Gray, H. B., and Winkler, J. R. (**2003**) Electron tunneling through proteins, *Q. Rev. Biophys.* 36, 341-372.

[43] Warren, J. J., Winkler, J. R., and Gray, H. B. (**2012**) Redox properties of tyrosine and related molecules, *FEBS Lett* 586, 596-602.

[44] Warren, J. J., Herrera, N., Hill, M. G., Winkler, J. R., and Gray, H. B. (**2013**) Electron flow through nitrotyrosinate in Pseudomonas aeruginosa azurin, *J Am Chem Soc* 135, 11151-11158.

[45] Shih, C., Museth, A. K., Abrahamsson, M., Blanco-Rodriguez, A. M., Di Bilio, A. J., Sudhamsu, J., Crane, B. R., Ronayne, K. L., Towrie, M., Vlcek, A., Jr., Richards, J. H., Winkler, J. R., and Gray, H. B. (**2008**) Tryptophan-accelerated electron flow through proteins, *Science* 320, 1760-1762.

[46] Takematsu, K., Williamson, H., Blanco-Rodriguez, A. M., Sokolova, L., Nikolovski, P., Kaiser, J. T., Towrie, M., Clark, I. P., Vlcek, A., Winkler, J. R., and Gray, H. B. (**2013**) Tryptophan-accelerated electron flow across a protein-protein interface, *J Am Chem Soc* 135, 15515-15525.

[47] Giese, B., Napp, M., Jacques, O., Boudebous, H., Taylor, A. M., and Wirz, J. (**2005**) Multistep electron transfer in oligopeptides: direct observation of radical cation intermediates, *Angew Chem* 44, 4073-4075.

[48] Fitzgerald, M. M., Churchill, M. J., McRee, D. E., and Goodin, D. B. (**1994**) Small molecule binding to an artificially created cavity at the active site of cytochrome *c* peroxidase, *Biochemistry* 33, 3807-3818.

[49] Musah, R. A., Jensen, G. M., Bunte, S. W., Rosenfeld, R. J., and Goodin, D. B. (**2002**) Artificial protein cavities as specific ligand-binding templates: Characterization of an engineered heterocyclic cation-binding site that preserves the evolved specificity of the parent protein, *J Mol Biol* 315, 845-857.

[50] Musah, R. A., and Goodin, D. B. (**1997**) Introduction of novel substrate oxidation into

cytochrome *c* peroxidase by cavity complementation: Oxidation of 2-aminothiazole and covalent modification of the enzyme, *Biochemistry* 36, 11665-11674.

[51] Cao, Y., Musah, R. A., Wilcox, S. K., Goodin, D. B., and McRee, D. E. (**1998**) Protein conformer selection by ligand binding observed with crystallography, *Protein Sci.* 7, 72-78.

[52] Hays Putnam, A. M., Lee, Y. T., and Goodin, D. B. (**2009**) Replacement of an electron transfer pathway in cytochrome *c* peroxidase with a surrogate peptide, *Biochemistry* 48, 1-3.

[53] Putnam, A., Lee, Y. T., and Goodin, D. B. (**2009**) Replacement of an electron transfer pathway in cytochrome *c* peroxidase with a surrogate peptide, *Biochemistry* 48, 1-3.

[54] Panavas, T., Sanders, C., and Butt, T. R. (**2009**) SUMO fusion technology for enhanced protein production in prokaryotic and eukaryotic expression systems, In SUMO Protocols, pp 303-317, *Springer*.

[55] Pollock, W. B. R., Rosell, F. I., Twitchett, M. B., Dumont, M. E., and Mauk, A. G. (**1998**) Bacterial expression of a mitochondrial cytochrome *c* . Trimethylation of Lys72 in yeast iso-1-cytochrome *c* and the alkaline conformational transition, *Biochemistry* 37, 6124-6131.

[56] Yonetani, T. (**1967**) Studies on cytochrome *c* peroxidase X. Crystalline apo-and reconstituted holoenzymes, *J. Biol. Chem.* 242, 5008-5013.

[57] Rabi A. Musah, G. M. J., Steven W. Bunte, Robin J. Rosenfeld, and David B. Goodin. (**2002**) Artificial protein cavities as specific ligand-binding templates: Characterization of an engineered heterocyclic cation-binding site that preserves the evolved specificity of the parent protein, *J. Mol. Biol.* 315, 845 - 857.

[58] Otwinowski, A., and Minor, W. (**1997**) Processing of X-ray diffraction data in oscillation mode., *Methods Enzymol.* 276, 307-325.

[59] Adams, P. D., Afonine, P. V., Bunkoczi, G., Chen, V. B., Davis, I. W., Echols, N., Headd, J. J., Hung, L.-W., Kapral, G. J., and Grosse-Kunstleve, R. W. (**2010**) PHENIX: a comprehensive Python-based system for macromolecular structure solution, *Acta Crystallogr D* 66, 213-221.

[60] Brunger, A. T., Adams, P. D., Clore, G. M., Delano, W. L., Gros, P., Grosse-Kunstleve, R. W., Jiang, J. S., Kuszewski, J., Nilges, M., Pannu, N. S., Read, R. J., Rice, L. M., Simonson, T., and Warren, G. L., . (**1998**) Crystallography and NMR system: a new software suite for macromolecular structure determination., *Acta Crystallogr. D* 54, 905-921.

[61] Emsley, P., and Cowtan, K. (**2004**) Coot: model-building tools for molecular graphics, *Acta Crystallogr D* 60, 2126-2132.

[62] Chae Hee Kang, S. F.-M., and E. Margoliash. (**1977**) Steady State Kinetics and Binding of Euakryotic Cytochromes c with Yeast Cytochrome *c* Peroxidase, *J Biol Chem* 252, 919-926.

[63] English, B. P., Min, W., van Oijen, A. M., Lee, K. T., Luo, G., Sun, H., Cherayil, B. J., Kou, S., and Xie, X. S. (**2005**) Ever-fluctuating single enzyme molecules: Michaelis-Menten equation revisited, *Nat. Chem. Biol.* 2, 87-94.

[64] Barry, B. A., El-Deeb, M. K., Sandusky, P. O., and Babcock, G. T. (**1990**) Tyrosine radicals in photosystem II and related model compounds - Chracterization by isotopic labeling and EPR spectroscopy, *J. Biol. Chem.* 265, 20139-20143.

[65] Miller, M. A., Vitello, L., and Erman, J. E. (**1995**) Regulation of interprotein electron transfer by Trp191 of cytochrome *c* peroxidase, *Biochemistry* 34, 12048-12058.

[66] Snellenburg, J. J., Laptenok, S. P., Seger, R., Mullen, K. M., and van Stokkum, I. H. (**2012**) Glotaran: A java-based graphical user interface for the R package TIMP, *J. Stat. Softw* 49, 1-22.

[67] Erman, J. E., Vitello, L. B., Mauro, J. M., and Kraut, J. (**1989**) Detection of an oxyferryl porphyrin pi-cation radical intermediate in the reaction between hydrogen peroxide and a mutant yeast cytochrome *c* peroxidase - Evidence for tryptophan 191 involvement in the radical site of compound I, *Biochemistry* 28, 7992-7995.

[68] Melissa M. Fitzgerald, R. A. M., Duncan E. McRee, and David B. Goodin. (**1996**) A ligand-gated, hinged loop rearrangement opens a channel to a buried artificial protein cavity, *Nat. Struct. Biol.* 3, 626 - 630.

[69] Finzel, B. C., Poulos, T. L., and Kraut, J. (**1984**) Crystal structure of yeast cytochrome *c* peroxidase refined at 1.7-A resolution, *J. Biol. Chem.* 259, 13027-13036.

[70] Yu, A., Liu, Y. H., Li, Z. C., and Cheng, J. P. (**2007**) Computation of pK(a) values of substituted aniline radical cations in dimethylsulfoxide solution, *J. Phys. Chem. A* 111, 9978-9987.

[71] DeFelippis, M. R., Murthy, C. P., Faraggi, M., and Klapper, M. H. (**1989**) Pulse radiolytic measurement of redox potentials: the tyrosine and tryptophan radicals, *Biochemistry* 28, 4847-4853.

[72] Miller, M. A. (**1996**) A complete mechanism for steady-state oxidation of yeast cytochrome *c* by yeast cytochrome *c* peroxidase, *Biochemistry* 35, 15791-15799.

[73] Volkov, A. N., Bashir, O., Worrall, J. A. R., and Ubbink, M. (**2009**) Binding hot spot in the weak protein complex of physiological redox partners yeast cytochrome *c* and cytochrome *c* peroxidase, *J Mol Biol* 385, 1003-1013.

[74] Yonetani, T. (**1965**) Studies on cytochrome *c* peroxidase II. stoichiometry between enzyme, H_2O_2, and ferrocytochrome *c* and enzymatic determination of extinction coefficients of cytochrome *c* , *J. Biol. Chem.* 240.

[75] Jasion, V. S., Polanco, J. A., Meharenna, Y. T., Li, H. Y., and Poulos, T. L. (**2011**)

Crystal structure of Leishmania major peroxidase and characterization of the compound I tryptophan radical, *J. Biol. Chem.* 286, 24608-24615.

[76] Ivancich, A., Dorlet, P., Goodin, D. B., and Un, S. (**2001**) Multifrequency high-field EPR study of the tryptophanyl and tyrosyl radical intermediates in wild-type and the W191G mutant of cytochrome *c* peroxidase, *J. Am. Chem. Soc.* 123, 5050-5058.

[77] Miner, K. D., Pfister, T. D., Hosseinzadeh, P., Karaduman, N., Donald, L. J., Loewen, P. C., Lu, Y., and Ivancich, A. (**2014**) Identifying the elusive sites of tyrosyl radicals in cytochrome *c* peroxidase: implications for oxidation of substrates bound at a site remote from the heme, *Biochemistry* 53, 3781-3789.

[78] Bernini, C., Arezzini, E., Basosi, R., and Sinicropi, A. (**2014**) In silico spectroscopy of tryptophan and tyrosine radicals involved in the long-range electron transfer of cytochrome *c* peroxidase, *J. Phys. Chem. B* 118, 9525-9537.

[79] Debus, R. J., Barry, B. A., Babcock, G. T., and McIntosh, L. (**1988**) Site-directed mutagenesis identifies a tyrosine radical involved in the photosynthetic oxygen-evolving system, *Proc. Natl. Acad. Sci USA* 85, 427-430.

[80] Wehbi, W. A., Di Bilio, A. J., Crane, B. R., Winkler, J. R., and Gray, H. B. (**2001**) Properties of photogenerated aromatic side-chain radicals in rhenium-modified copper proteins, *J. Inorg. Biochem.* 86, 477-477.

[81] Hazzard, J. T., Poulos, T. L., and Tollin, G. (**1987**) Kinetics of reduction by free flavin semiquinones of the components of the cytochrome *c* -cytochrome *c* peroxidase complex and intracomplex electron transfer, *Biochemistry* 26, 2836-2848.

[82] Miller, M. A., Hazzard, J. T., Mauro, J. M., Edwards, S. L., Simons, P. C., Tollin, G., and Kraut, J. (**1988**) Site-directed mutagenesis of yeast cytochrome *c* peroxidase shows histindine 181 is not required for oxidation of ferrocytochrome *c* , *Biochemistry* 27, 9081-9088.

[83] Liu, R. Q., Miller, M. A., Han, G. W., Hahm, S., Geren, L., Hibdon, S., Kraut, J., Durham, B., and Millett, F. (**1994**) Role of methionine 230 in intramolecular electron transfer between the oxyferryl heme and tryptophan 191 in cytochrome *c* peroxidase compound II, *Biochemistry* 33, 8678-8685.

[84] Stemp, E. D. A., and Hoffman, B. M. (**1993**) Cytochrome-C Peroxidase Binds 2 Molecules of cytochrome *c* - Evidence for a low-affinity, electron transfer active site on cytochrome *c* peroxidase, *Biochemistry* 32, 10848-10865.

[85] Koloczek, H., Horie, T., Yonetani, T., Anni, H., Maniara, G., and Vanderkooi, J. (**1987**) Interaction between cytochrome *c* and cytochrome *c* peroxidase: excited-state reactions of zinc-and tin-substituted derivatives, *Biochemistry* 26, 3142-3148.

[86] Walters, V. A., Depaula, J. C., Jackson, B., Nutaitis, C., Hall, K., Lind, J., Cardozo, K., Chandran, K., Raible, D., and Phillips, C. M. (**1995**) Electronic structure of triplet states of zinc(II) tetraphenylporphyrins, *J. Phys. Chem.* 99, 1166-1171.

[87] van Stokkum, I. H., Larsen, D. S., and van Grondelle, R. (**2004**) Global and target analysis of time-resolved spectra, *BBA-Bioenergetics* 1657, 82-104.

[88] Page, C. C., Moser, C. C., Chen, X. X., and Dutton, P. L. (**1999**) Natural engineering principles of electron tunnelling in biological oxidation-reduction, *Nature* 402, 47-52.

[89] Everest, A. M., Wallin, S. A., Stemp, E. D. A., Nocek, J. M., Mauk, A. G., and Hoffman, B. M. (**1991**) Aromatic hole superexchange through position 82 of cytochrome *c* is not required for intracomplex electron transfer to zinc cytochrome *c* peroxidase, *J. Am. Chem. Soc.* 113, 4337-4338.

[90] DeFelippis, M. R., Murthy, C. P., Broitman, F., Weinraub, D., Faraggi, M., and Klapper, M. H. (**1991**) Electrochemical properties of tyrosine phenoxy and tryptophan indolyl radicals in peptides and amino acid analogs, *J. Phys. Chem.* 95, 3416-3419.

[91] Matelkova, K., Ossberger, K., Hudak, J., Vatral, J., Boca, R., and Linert, W. (**2013**) Redox activity of some non-innocent amino acids, *Mon. Chem.* 144, 937-949.

[92] Battistuzzi, G., Bellei, M., Bortolotti, C. A., and Sola, M. (**2010**) Redox properties of heme peroxidases, *Arch. Biochem. Biophys.* 500, 21-36.

[93] Purcell, W., and Erman, J. E. (**1976**) Cytochrome *c* peroxidase catalyzed oxidations of substitution inert iron (II) complexes, *J Am Chem Soc* 98, 7033-7037.

[94] Mondal, M. S., Fuller, H. A., and Armstrong, F. A. (**1996**) Direct measurement of the reduction potential of catalytically active cytochrome *c* peroxidase compound I: Voltammetric detection of a reversible, cooperative two-electron transfer reaction, *J Am Chem Soc* 118, 263-264.

[95] Stevenson, G. P., Lee, C. Y., Kennedy, G. F., Parkin, A., Baker, R. E., Gillow, K., Armstrong, F. A., Gavaghan, D. J., and Bond, A. M. (**2012**) Theoretical analysis of the two-electron transfer reaction and experimental studies with surface-confined cytochrome *c* peroxidase using large-amplitude fourier transformed AC voltammetry, *Langmuir* 28, 9864-9877.

[96] Barrows, T. P., Bhaskar, B., and Poulos, T. L. (**2004**) Electrostatic control of the tryptophan radical in cytochrome *c* peroxidase, *Biochemistry* 43, 8826-8834.

[97] Miller, M. A., Liu, R. Q., Hahm, S., Geren, L., Hibdon, S., Kraut, J., Durham, B., and Millett, F. (**1994**) Interaction domain for the reaction of cytochrome *c* with the radical and the oxyferryl heme in cytochrome *c* peroxidase compound I, *Biochemistry* 33, 8686-8693.

[98] Lett, C. M., and Guillemette, J. G. (**2002**) Increasing the redox potential of isoform 1 of yeast cytochrome *c* through the modification of select haem interactions, *Biochemical J* 362, 281.

[99] Rafferty, S. P., Pearce, L.L., Barker, P.D., Guillemette, J.G., Kay, C.R., Smith, M.,

Mauk, A.G. (**1990**) Electrochemical, kinetic, and circular dichroic consequences of mutations at position 82 of yeast iso-1-cytochrome *c* , *Biochemistry* 29, 9365-9369.

[100] Machczynski, M. C., Kuhl, K. P., and McGuirl, M. A. (**2007**) Modulation of the electrochemical behavior of tyrosyl radicals by the electrode surface, *Anal. Biochem.* 362, 89-97.

[101] Hoganson, C. W., and Tommos, C. (**2004**) The function and characteristics of tyrosyl radical cofactors, *BBA-Bioenergetics* 1655, 116-122.

[102] Furuta, K., Tanizawa, Y., Horiuchi, H., Hiratsuka, H., and Okutsu, T. (**2008**) Tryptophan neutral radical brings along photochemical crystallization, *Chem. Lett.* 37, 458-459.

[103] Huyett, J. E., Doan, P. E., Gurbiel, R., Houseman, A. L. P., Sivaraja, M., Goodin, D. B., and Hoffman, B. M. (**1995**) Compound ES of cytochrome *c* peroxidase contains a Trp pi-cation radical - Characterization by cw and pulsed Q-band endor spectroscopy, *J Am Chem Soc* 117, 9033-9041.

[104] Bonagura, C. A., Sundaramoorthy, M., Pappa, H. S., Patterson, W. R., and Poulos, T. L. (**1996**) An engineered cation site in cytochrome *c* peroxidase alters the reactivity of the redox active tryptophan, *Biochemistry* 35, 6107-6115.

[105] Bonagura, C. A., Bhaskar, B., Shimizu, H., Li, H. Y., Sundaramoorthy, M., McRee, D. E., Goodin, D. B., and Poulos, T. L. (**2003**) High-resolution crystal structures and spectroscopy of native and compound I cytochrome *c* peroxidase, *Biochemistry* 42, 5600-5608.

[106] Wang, J. M., Mauro, J. M., Edwards, S. L., Oatley, S. J., Fishel, L. A., Ashford, V. A., Xuong, N. H., and Kraut, J. (**1990**) X-ray structures of recombinant yeast cytochrome-c peroxidase and 3 heme-cleft mutants prepared by site-directed mutagenesis, *Biochemistry* 29, 7160-7173.

[107] Ferrer, J. C., Turano, P., Banci, L., Bertini, I., Morris, I. K., Smith, K. M., Smith, M.,

and Mauk, A. G. (**1994**) Active-site coordination chemistry of the cytochrome *c* peroxidase Asp235Ala variant - Spectroscopic and functional characterization, *Biochemistry* 33, 7819-7829.

[108] Fishel, L. A., Farnum, M. F., Mauro, J. M., Miller, M. A., Kraut, J., Liu, Y. J., Tan, X. L., and Scholes, C. P. (**1991**) Compound-I radical in site-directed mutants of cytochrome *c* peroxidase as probed by electron-paramagnetic resonance and electron nuclear double-resonance, *Biochemistry* 30, 1986-1996.

[109] Jonsson, M., Lind, J., Merenyi, G., and Eriksen, T. (**1995**) N-H bond dissociation energies, reduction potentials and pK_{a}'s of multisubstituted anilines and aniline radical cations, *J. Chem. Soc. Perkin Trans* 2, 61-65.

[110] Wardman, P. (**1989**) Reduction potentials of one-electron couples involving free radicals in aqueous solution, *J. Phys. Chem. Ref. Data* 4, 1637-1754.

APPENDIX B

WHITE COLLAR-1: ENDEAVORS TO PREPARE ACTIVE, SOLUBLE PROTEIN

B.1 The primary photoreceptor of White Collar-1

White Collar-1 (WC-1) is a multi-domain blue light photoreceptor in the fungus *Neurospora crassa* that consists of Per-Arnt-Sim (PAS) domains important for protein-protein interactions, a GATA zinc-finger DNA binding domain, and poly-glutamine activation regions (Figure B.1; [1, 2]). Of the three PAS domains in the protein, PAS A has been characterized as a light-oxygen-voltage (LOV) domain that confers photosensitivity to the organism, as determined when researchers constructed a "blind" WC-1 by the introduction of single point mutations to the flavin binding residues [3, 4]. It has also been found to purify with a yellow flavin pigment and has a fluorescence absorption and emission profile characteristic of flavin [4, 5]

WC-1 forms a heterodimeric complex with White Collar-2 (WC-2) known as the White Collar Complex (WCC) and plays an essential role in all light-regulated responses. In particular, WCC activates transcription of the *frequency* gene by binding to the light regulatory element. As levels of Frequency increase, Frequency along with Frequency-Interacting RNA Helicase forms the FFC complex that represses WCC activity. Together these two complexes comprise the positive and negative elements of the organism's circadian clock and generate an oscillatory rhythm. The FFC complex is important for resetting the circadian clock and allows for photoentrainment [6, 7]. VVD also plays a role in responses to increasing intensities of blue light, further repressing WCC activity and conferring sensitivity to changing light levels [8].

Reconstitution of this protein system has been fraught with challenges owing to protein insolubility. WC-1 in particular has a well-behaved PAS C domain that binds to WC-2, but the photoactive LOV domain alone typically purifies out of *E. coli* in inclusion bodies, as the apoprotein tends to be poorly folded without the flavin cofactor. A homology model of WC-1 LOV shows the similarity to its proposed binding partner VVD. However, ligand binding predictions show the PAS domain can easily bind to a molecule of heme and inhibit proper flavin binding (Figure B.2). Incorporation of the flavin exogenously requires denaturation of the inclusion bodies and proper refolding of the protein with the cofactor. Here, we delineate our few successful attempts at reconstituting the WC-1-LOV domain.

Figure B.1: Domain map of White Collar-1.

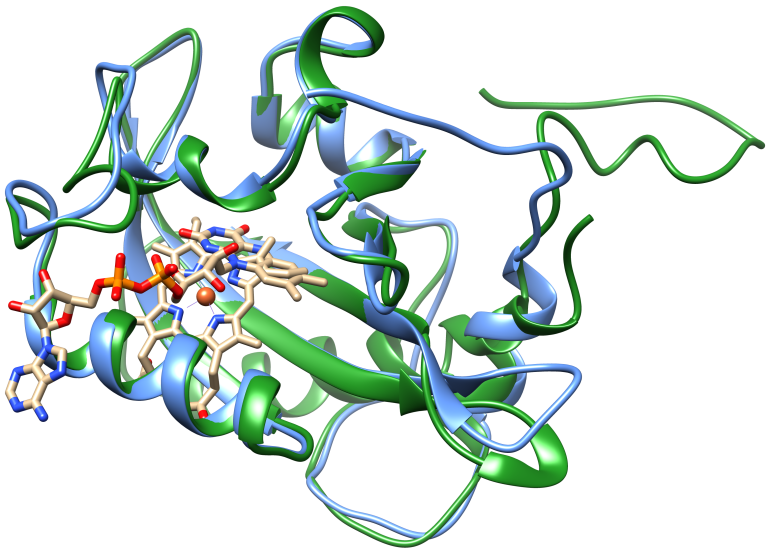

Figure B.2: Comparison of WC-1 (blue) to WT VVD (green; PDB 2PD7). Homology model of WC-1 generated by Phyre 2 [9] using 5VA1, 2PDT, 5SVU, 3UE6, 2WKQ,and 4WUJ, with 96% of the 180 residues modeled at >90% accuracy. Ligand prediction was performed by 3DLigandSite [9] and predicted primarily flavin cofactors. The one heme containing result from *E. coli* direct oxygen sensor (PDB 1S66) illustrates where heme could potentially bind and interfere with the flavin binding pocket. Figures were prepared with Chimera [10].

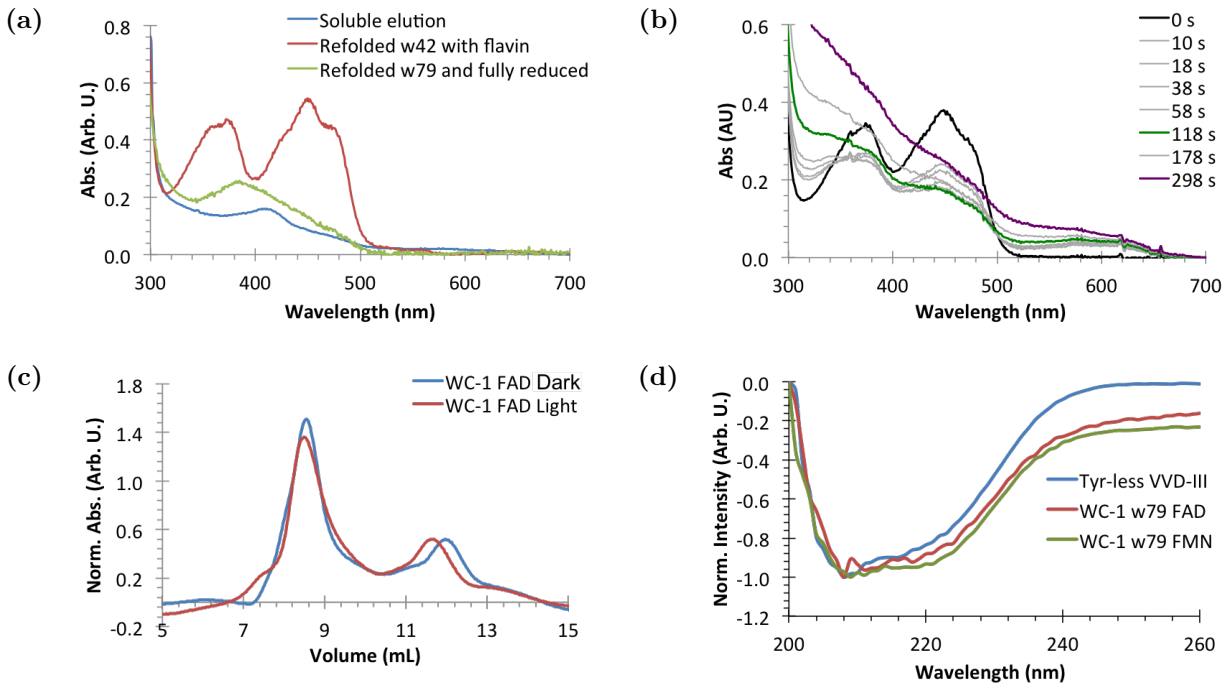

Figure B.3: (a) Comparison of cofactors bound in WC-1 by UV-vis spectroscopy. Solution protein elution typically has nonspecifically bound heme. WC-1(356 − 507; w42) was refolded once with bound flavin, as distinguished by the characteristic peaks. WC-1 (348 − 535; w79) was refolded successfully once and purified out in an adduct state (λ = 390 nm), but did not reoxidize fully. (b) Photoreduction of w42 generates some neutral semiquinone state. Further irradiation results in loss of flavin and protein precipitation, which can be seen by the rising baseline. (c) w79 exhibited a small amount of conformational change in the light by size exclusion chromatography. (d) Circular dichroism indicated refolded WC-1 proteins had a considerable amount of helical content and little random coil. Comparison to Tyr-less VVD-III highlights some differences. Due to uncertain protein concentrations, all spectra were normalized.

B.2 Expression methods

WC-1 constructs (356−507; denoted w42) and (348−535; denoted w79) were ligated into pET-28a vectors and expressed in various *E. coli* cell lines, including a CmpX13 strain modified from *E. coli* C41 (DE3) with a flavin transporter RibM to improve flavin incorporation [11], ArcticExpress, and SoluBL21 cells. No one cell line drastically improved protein yield or flavin incorporation. A variety of construct lengths were tested from (102 − 918) to shorter constructs of solely the LOV domain and synthetic genes were also used in an effort to opti-

mize codon usage. Different affinity tags were also tested, including maltose-binding protein, SUMO, and trxA from pET32, with the idea that tags could increase solubility through a passenger effect or aid in folding [12, 13]. Any soluble protein generally ends up binding nonspecifically to heme (Figure B.3a).

Saccharomyces cerevisiae BY4741 cells were used for co-expressing WC-1 constructs with either VVD or WC-2. The p423Gal1 + p426Gal1 and p423Met25 + p426Met25 vector pairs were used for WC-1 LOV $(297-507)$ + VVD-37 and WC-1 $(102-918)$ + WC-2 $(51-456)$. Co-expressions did not yield useable protein with bound flavin and and indicated that further optimizations would be required. Protein expression by High Five insect cells were also attempted (Kemp Biotechnology), with constructs in pFastBac-HTb vectors. Whereas a significant amount of WC-1 was expressed (as determined by immunoblotting), isolation and purification of the protein resulted in no bound flavin cofactor observed spectroscopically.

B.3 Refolding of the domain with flavin

After multiple failed attempts of soluble, flavin bound protein, cell pellets were dissolved in either 6 M guanidine hydrochloride or urea. Undissolved components were centrifuged down. His-tagged solubilized WC-1 was bound to Ni-NTA resin and isolated. The subsequent elution was steadily dripped into refolding buffer (50 mM sodium phosphate, pH $7-8$, 500 mM NaCl, 10% glycerol, 5 mM DTT) with excess flavin while stirring at 4 °C. After overnight refolding, insoluble proteins were filtered or centrifuged out and soluble protein extracted from the remaining solution by Ni-NTA resin. While bound to the resin, excess flavin was gradually removed by washes with flavin-free buffer, and the refolded protein eluted. Analysis by UV-vis generally shows a lack of bound flavin, though ocassionally the cofactor is partially bound such that blue light irradiation causes reduction of the flavin to

the hydroquinone state, however, no adduct state is observed, except in one case (Figure B.3a). One refolding attempt resulted in properly bound flavin but photoreduction caused formation of the neutral semiquinone state (Figure B.3b). To date, properly bound flavin has been difficult and inconsistent, though refolded protein has a surprising amount of helical content (Figure B.3d). For partially bound flavin, protein conformational changes appear to occur in the presence of light, as determined by size exclusion chromatography (Superdex 75 HR 10/30; Figure B.3c). To reduce the variation in flavin binding, current work is aimed at introducing residues that limit flexibility in the flavin binding pocket and to improve the quantity of residues in contact with the cofactor.

B.4 Acknowledgements

Thanks to Joanne Widom for the extensive years of work she has invested in this project. She has generated countless constructs in the attempt to further our studies of WC-1. Also thanks to Min Dong (Lin group, Cornell University) for insightful discussions on protein expression and help with using the yeast expression system. This work was financially supported by the NIH training grant T32 GM08267 (to E.F.Y.) and NSF grant 1715233 (to B.R.C.).

BIBLIOGRAPHY

(1) Loros, J. *Mol. Microbiol.* **2005**, *56*, 299–302.

(2) Crane, B. R.; Young, M. W. *Annu. Rev. Biochem.* **2014**, *83*, 191–219.

(3) Ballario, P.; Talora, C.; Galli, D.; Linden, H.; Macino, G. *Mol. Microbiol.* **1998**, *29*, 719–729.

(4) Froehlich, A. C.; Liu, Y.; Loros, J. J.; Dunlap, J. C. *Science* **2002**, *297*, 815–819.

(5) He, Q. et al. *Science (80-.).* **2002**, *297*, 840–843.

(6) Cheng, P.; Yang, Y.; Wang, L.; He, Q.; Liu, Y. *J. Biol. Chem.* **2003**, *278*, 3801–3808.

(7) He, Q.; Shu, H.; Cheng, P.; Chen, S.; Wang, L.; Liu, Y. *J. Biol. Chem.* **2005**, *280*, 17526–17532.

(8) Chen, C.-H.; DeMay, B. S.; Gladfelter, A. S.; Dunlap, J. C.; Loros, J. J. *Proc. Natl. Acad. Sci.* **2010**, *107*, 16715–16720.

(9) Wass, M. N.; Kelley, L. A.; Sternberg, M. J. E. *Nucleic Acids Res.* **2010**, *38*, W469–W473.

(10) Pettersen, E. F.; Goddard, T. D.; Huang, C. C.; Couch, G. S.; Greenblatt, D. M.; Meng, E. C.; Ferrin, T. E. *J. Comput. Chem.* **2004**, *25*, 1605–1612.

(11) Mehlhorn, J.; Steinocher, H.; Beck, S.; Kennis, J. T. M.; Hegemann, P.; Mathes, T. *PLoS One* **2013**, *8*, e79006.

(12) Esposito, D.; Chatterjee, D. K. *Curr. Opin. Biotechnol.* **2006**, *17*, 353–358.

(13) Raran-Kurussi, S.; Waugh, D. S. *PLoS One* **2012**, *7*, e49589.